# Investigation of Ultra-Wideband Wireless Communication inside Electromagnetically Ultra Small Confined Environments

Javier Gelabert

Christ Church College

A thesis submitted in partial fulfilment of the requirements for the degree of Doctor of Philosophy at the University of Oxford

Supervised by

Dr. Christopher Stevens
Prof. David Edwards

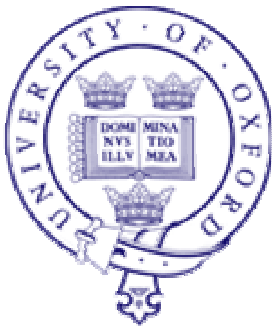


Department of Engineering Science
Parks Road, Oxford OX1 3PJ, UK

October 2011

# Investigation of Ultra-Wideband Wireless Communication inside Electromagnetically Ultra Small Confined Environments

Javier Gelabert
Christ Church College

A thesis submitted in partial fulfilment of the requirements for the degree of Doctor of Philosophy at the University of Oxford

Supervised by Dr. Christopher Stevens and Prof. David Edwards

## Abstract

Ultra-wideband (UWB) communication has been the subject of extensive research in recent years due to its unique capabilities and potential applications, particularly in short-range multiple access wireless communications. However, many important aspects of UWB-based communication systems have not yet been thoroughly investigated. The propagation of UWB signals inside very small enclosed environments is one of the important issues with significant impacts on the future direction, scope, and generally the extent of the success of UWB technology. The objective of this thesis is to obtain a more thorough and comprehensive understanding of ultra-small UWB channels for communication applications and design issues for enhancing the data rate of UWB systems. This works supports the postulation of a high capacity UWB wireless interconnect scheme for communicating devices within conducting enclosures – a wireless "backplane".

This thesis proposes the use of an Ultra-Wide Bandwidth (UWB) ultra-small scale wireless interconnect scheme for use within electrically small enclosures. Such ultra-small environments (size $\leq$ 10 wavelengths) are topologically much more complex, being more cluttered, than typical indoor environments (size $\geq$ 10 wavelengths). The concept is presented through two different scenarios. Firstly, a PC Tower case is presented as a model environment and the work seeks to present the optimum channel performance, where EMI

issues are discussed and problem avoidance proposed. Secondly, in order to extrapolate the different results from the study inside the PC, an investigation is carried out using an Aluminium tower case as a more generic model environment. The analysis is based on the behaviour of box modes within a conducting resonator enclosure and the effective communications bandwidth for UWB systems for different sizes and components within.

From these general considerations the research presents theoretical and experimental results from which are derived the communications metrics measured within enclosures. Simulations of the different scenarios are performed using different techniques such as ray tracing and a full wave model, based on CST Microstripes. Empirical data is recorded using a vector network analyser (VNA)-based wideband channel sounding system where channel measurements are carried out in every scenario regarding different aspects such as frequency response and time domain analysis, evaluation of the channel capacity, power delay study and the nature of the environment.

## Acknowledgements

First of all, I would like to express my gratitude to Dr. Christopher Stevens and Prof. David Edwards for supervising this work, having an excellent experience and knowledge in this field. It is my luck to work closely with them thereby combine their expertise in time domain and RF measurements, communications, wave propagations and antennas. This project could not have been possible without their advice and guidance throughout the project.

Secondly, I should like to acknowledge all the staff in the Communication Research Group who has supported me in so many different ways, with special mention of Vit Sipal who has helped me with some of the experimental campaign; I have been fortunate to have worked closely with him, and learnt from his experience in UWB technology. Also I express my gratitude to Grahame Faulkner for helping me with all the setup for different measurements campaigns.

Thirdly, I would like to thank Dr.Wasim Q.Malik for his support and also, I am indebted to Dr. Athanasios Kavatjikidis for his guidance and advice during my introductory period as a visiting student – his encouragement played a significant role at an early stage.

Finally, but not least, I am grateful to my family, Carmen and the "Foundation Sa Nostra", without whose financial and loving support this project would have not been possible.

Javier Gelabert

Oxford

October 2011

# List of Publications

## Journal Papers

1. **J. Gelabert**, D. J. Edwards, C. J. Stevens, "Resonant Nature of a PC Enclosure for UWB Communication: Wireless Bus Potential", *IEEE Transactions on Antennas and Propagation.* (Under review)
2. **J. Gelabert**, D. J. Edwards, C. J. Stevens, "Experimental Evaluation of UWB Wireless Communication within a PC Case", *Electronic Letters,* June 2011 Vol. 47 No. 13.
3. V. Sipal, **J. Gelabert**, B. Allen, C. Stevens, and D. Edwards, "Frequency-Selective Fading of Ultra wideband Wireless Channels in Confined Environments," *IET Microw. Antennas Propag*. -- Aug. 2011, Vol. 5, Issue 11, p.1328–1335.

## Conference Papers

1. **J. Gelabert**, A. Kavatjikidis, D. J. Edwards, C. J. Stevens, "Experimental UWB Channel Characterisation of an Electromagnetically Small Environment", *LAPC Conference 2009,* Loughborough, UK, Nov. 2009.
2. **J. Gelabert**, D. J. Edwards, C. J. Stevens, "UWB Wireless Interconnect Scheme for Communicating Devices within a Small Conducting Enclosure", *EUCAP Conference 2011,* Rome, Italy, April 2011. (**Finalist for Best Paper Award**)
3. Vit Sipal**, J. Gelabert**, D. J. Edwards, C. J. Stevens, "Frequency Selectivity in Confined Environments", *EUCAP Conference 2011,* Rome, Italy, April 2011.
4. Vit Sipal**, J. Gelabert**, C. J. Stevens, B. Allen, D. J. Edwards, "Impact of Confined Environment on WiMedia UWB Systems", *LAPC Conference 2011,* Loughborough, UK, Nov. 2011.

## Contents

## List of Figures

## List of Tables

# Chapter 1: Introduction

## 1.1. History of Ultra Wideband Communications

Ultra-wideband communications is not a new technology, being first employed by Guglielmo Marconi in 1901 when it was used to transmit Morse code sequences across the Atlantic ocean using spark-gap radio transmitters. However, the potential benefits of large bandwidth transmission, and the capability for implementing multiuser systems provided by electromagnetic pulses, were never realised at the time. Half a century later, the technology of modern pulse-based transmission began to gain momentum in military applications in the form of impulse radars.

The Ultra Wideband (UWB) transmission concept originated from work in time-domain electromagnetics that began in 1962, this describing more fully the transient behaviour of a certain class of microwave networks and their characteristic impulse response [1]. The aim was to characterize a linear time-invariant system by measuring its channel response. The first patent on UWB communications was awarded to Sperry Research Centre in 1973 based on the concepts of nanosecond impulses and matched filtering [2]. Shortly afterwards, a UWB ground-penetrating radar was developed, followed by other sub-surface radar applications. From the 1960s to the 1990s, this technology was restricted to military and Department of Defence (DoD) applications under classified programs, these including highly secure communications [3].

Despite a background in military applications [4], with recent advancements both in microprocessing and fast switching in semiconductor technology, UWB has increasing civilian and commercial applications [5]. Due to the ever-increasing demand for higher data

rates and the paucity of available spectrum, UWB received renewed attention in recent years as a technique for fast communications. Currently, regulatory authorities world-wide are reviewing the viability of UWB systems in the shared frequency spectrum. In February 2002, the FCC approved the First Report and Order (R&O) for commercial use of UWB technology under strict power-emission limits for various devices [6]. Currently, such restrictions have limited UWB transmission to about 10m, this therefore confining UWB technology to short range applications. In this Thesis, the analysis of the use of this technology over a 'very' short range is discussed.

## 1.2. Motivation and Scope of Research

The use of wireless communications has become omnipresent for a variety of military, commercial, and consumer applications. However, the benefit of wireless connectivity inside very small enclosures, such as personal computers or servers, has not been fully investigated.

'Next generation' computing systems, from high performance server farms to mobile devices, consist of multiple microchips on each single PCB substrate. For applications that connect several of these units together, traditional wired bus interconnects will present upper limits on data capacity due to their waveguide nature; at high operation frequencies they also may introduce significant intersymbol interference (ISI) [8]. Furthermore, such bus boards containing many individual bus lines require complex and costly connectors, this both limiting the number of units that may be connected, and increasing the cost for high performance systems such as cell phone base stations.

The idea of replacing part of these buses within small enclosures by the use of wireless systems has become an important study receiving increasing research interest [7-11].

Removing the bus boards from multi-processor systems like cell phone exchanges and parallel computing devices, offers increased data rates between components, improvements in cost and the potential for new system architectures not limited by fixed connections. Finally, it would permit greater flexibility in the overall geometry of both the enclosures and PCBs, with such systems being cooler and therefore more efficient.

The potential for UWB technology to provide very high data rates over short distances has made it an excellent candidate for wireless personal area networks (WPANs). Such a wire-free transmission with the high data rates characteristic of UWB technology lends itself to very small indoor application environments, such as the inner space of a PC tower case, the absence of wires resulting in significant reduction of overall volume and cost. Currently, the bus interfaces which connect hard drives, DVD players and the PCI cards to the mother board (MB) have a maximum reported data rate at the 3-6 Gbps, this using the serial advanced technology attachment (SATA II) [12]. UWB technology, on the other hand, has the potential to increase SATA II data rates and reduce the size and extent of the physical connections between these components.

These "ultra small" channels are inherently topologically more complicated than the typical 'indoor environment' (size $\geq$ 10 wavelengths). Due to the very short range of the wireless channel, overall performance may be compromised by the dense multipath reflections arriving at the receiver. Furthermore, complex structures within the PC tower case – including the Main Board (MB) and the Printed Circuit Boards (PCBs) – are typically metallic and further influence UWB performance. It is well recognised that Central Processing Unit (CPU) clock speeds, of up to 3.4 GHz for single core processors, and the maximum reported 3.8 GHz for multi-core processors [13], lead to interference within the UWB bandwidth. Thus, an essential objective of this study is to characterise this environment and to determine the extent to which UWB technology is able to improve on current bus

interface data rates, accepting the limitations described above. In addition, electromagnetic interference (EMI) along the bandwidth is also considered.

The cavity also supports a number of electromagnetic modes depending on the position of the source, the nature of the excitation and the details of the wall boundary conditions. This phenomenon, as well as the highly scattered environment with very complicated static topology such as a PC box, gives different results which could be difficult to evaluate its physical origins. Therefore, in order to extrapolate some of these results, a more standardised and 'uncomplicated' model is considered to be built. This model consists of a rectangular aluminium shielded cavity which acts as a resonator and has similar dimensions of a personal computer server. Eight printed circuit cards (PCBs) are included inside the confined cavity simulating possible internal parallel microprocessor communication. Different measurements campaigns are carried out inside the box to try to extrapolate results from the PC box to a more general enclosed case. Modifications on the volume of the case and the use of absorbers are also considered. Understanding the behaviour of UWB technology within a more standardised model would contribute to the development of wireless communication inside very small cavities. Electromagnetic simulations of both scenarios are also undertaken with the help of *Microstripes*™ to have a clearer understanding of the wave propagation inside these small cavities.

Thus, the aim of this study is to quantify specific aspects of UWB technology within a 'standard' PC tower case and the Aluminium case, with particular reference to:

(i) Evaluation of fading inside very small confined environments

(ii) Dependency of fade-depth on cavity volume, frequency and bandwidth

(iii) Frequency and time domain study

(iv) Influence of orientation/location of the antennas

(v) Modelling of the power delay profile (PDP)

(vi) Analysis of the ideal channel capacity

Finally, after all this analysis, specific design rules will try to be established for an optimum wireless communication with the use of ultra-wideband (UWB) technology inside this type of channel.

## 1.3. Thesis Organization

The layout of this dissertation is as follows: Chapter 2 presents firstly an overview of Ultra-Wideband technology; its regulations and applications in the merging market and a brief comparison with narrowband and optical communication are also included. Then, an extended report of previous studies in the related field is presented. At the end an insight into bus technology is included to get a better understanding and knowledge in the field.

Chapter 3 describes the setup design of the two different scenarios considered in this study and their implementation. The frequency sweeping technique is the one used in this research, which is based in the use of the Vector Network Analyser (VNA) [14]. Two almost identical bow-tie UWB antennas are the ones used in this study, which its properties are described. Essential propagation parameters and different procedures to characterize the small indoor channel are introduced to have a general understanding of the measurement campaign and analysis of the statistical data. Finally, Electromagnetic Interference (EMI) is evaluated when the PC is running at maximum capacity, and problem avoidance is also discussed.

In Chapter 4, the wave propagation inside very small confined environments is investigated. Firstly, the dependence of fading with bandwidth and size of the environment is demonstrated by a simple two-ray channel model. Ray-tracer simulations of a great number

of different confined environments are conducted to quantify the severity of fading effects as a function of the size of the environment. A hypothesis of a hybrid resonator is also presented, again quantifying the minimum bandwidth required in terms of modal spectrum. Finally, electromagnetic simulations are carried out along the chapter to help us to explain, understand and demonstrate the different statements mentioned before.

Chapter 5 undertakes the analysis of frequency and time domain of the UWB channels. Results come from an extended measurement campaign derived from two different environments, the PC Tower box and the Aluminium small resonator cavity. Proposals to model the power delay profile (PDP) of the channel are presented. Root mean square (rms) delay spread and the Ricean K Factor are included at the end of the chapter to give a better understanding of the nature of these channels.

Investigation of the power-loss and channel capacity of the channels is presented in Chapter 6. Spatial distribution of the power is evaluated as well as the fade depth calculated from empirical data. Study of both large and small scale distribution of the channel is presented. Shannon capacity is identified to have huge values for a pre-established SNR of 25 dB at the source. The optimum location and orientation of the antennas are studied with the help of the Shannon capacity distribution along the different positions of the antennas. The influence among the aggregate capacity of the channel of placing an absorber within the Aluminium cavity is evaluated at the end of the chapter.

Finally, Chapter 7 summarises and concludes with observations the investigation of such small indoor environments. Some design rules and venues for future work are proposed at the end of this chapter.

# Chapter 2: Literature Review

Ultra-wideband (UWB) communication has been the subject of extensive research in recent years due to its unique capabilities and potential applications, particularly in short-range multiple-access wireless communications [5]. This technology is presented in this chapter as well as different studies related in the field in order to give a better understanding and knowledge of UWB wireless communications. This thesis is based in the use of this technology inside very small confined environment such as a Personal Computer (PC); thus, this author considers appropriate to include an overview in backplane and PCI Bus technology at the end of the chapter.

## 2.1. Definition of Ultra-Wideband (UWB)

The distinguishing feature of UWB communications technology is the unrivalled data-rates it provides. A radio communication system is said to be ultra-wideband if either its bandwidth is greater than 500 MHz or its fractional bandwidth[1] (FB) exceeds 20%. Thus, UWB is distinct from other transmissions, which typically occupy 3% of the available bandwidth [5]. However, UWB signals occupy a much wider frequency band than other conventional signals, with a consequent overlap of their transmission spectrum with other systems, and this imposes certain practical restrictions in the application of this technology. In this study, the band is considered to be 3-11 GHz.

[1] Fractional bandwidth classifies signals as narrowband, wideband, or ultra-wideband and is defined by the ratio of bandwidth at 10 dB points to centre frequency, i.e. $FB = \frac{\Delta f}{f_c} = 2\frac{f_h - f_l}{f_h + f_l}$ (2.1) where $f_h$ and $f_l$ are the high and low 10 dB cut-off frequencies respectively, and $f_c = (f_h + f_l)/2$.

### 2.1.1. UWB Operation frequencies (Regulatory issues)

UWB signals have unique and promising properties for future communications [5]. However, since they occupy a very large portion of the spectrum, they need to coexist with other different systems without causing significant interference. In order to benefit from advantages of UWB technology without compromising the performance of others, in February 2002, the Federal Communications Commission (FCC) permitted access to an unprecedented amount of bandwidth for commercial development of UWB technology [6]. After much lobbying on both sides, the FCC agreed to the requests of a wide range of supporters, and a year later, the FCC's release of a 'Memorandum Opinion and Order' (MO&O) further consolidated UWB as a future wireless technology. These supporters span a wide range of interests, from leading companies in the home networking arena to consumer electronics giants[2], UWB developers[3] , as well as the Ground Penetrating Radar Industry Coalition (GPRIC).

After UWB was authorised by the FCC, regulatory efforts have been under way in Europe to approve the use of UWB devices but with certain restrictions. Unfortunately, uniform world-wide regulations have not yet been agreed, with various regulations existing in different parts of the word; in Japan and Europe, the restrictions are more relaxed than those in the USA, for example. In this study, the European (ECC) emission limits are identified in Fig. 2.1. In Europe, the proposals of the Electronic Communications Committee (ECC) were ratified in 2007 by the Radio Spectrum Committee (RSC) of the European Commission (EC) [15].

[2] Philips Electronics, Samsung Electronics, Intel, Texas Instruments and Microsoft

[3] Multispectral Solutions, Pulse~LINK, Staccato Communications, Time Domain Corporation, and XtremeSpectrum

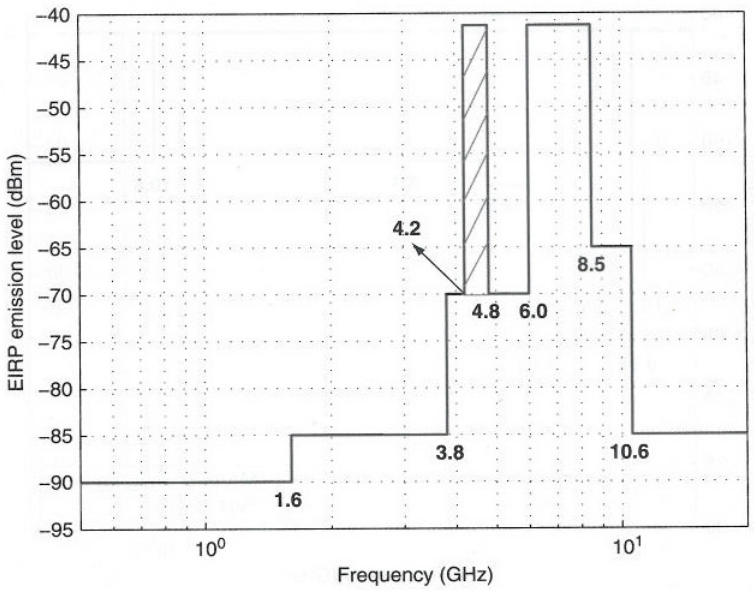




**Fig.2.1. ECC emission limits without appropriate mitigation techniques for indoor UWB devices [16]**

Such UWB systems can transmit at -41.3 dBm/MHz over 6-8.5 GHz band. This limit is also valid for the 4.2-4.8 GHz band until the end of 2010. Once entered in the year 2011, the mean equivalent isotropically radiated power (EIRP) spectral density, meaning the highest signal strength in any direction, is limited to -70 dBm/MHz in that band. Note that FCC in the USA allows an EIRP of -41.3 dBm/MHz over the whole UWB frequency band (3.1-10.6 GHz) [6]. Thus, the EC regulations are more strict that the FCC ones.

### 2.1.2. UWB Applications and Wireless Technologies

Many possible applications have been suggested for UWB technology, but current evidence highlights two main areas for probable application: communications and radar/sensor (e.g. military or aviation) [4]. For both fields the basic UWB system components include transmitter sources, modulators, RF pulse generators, detection receivers and wideband antennas. The fine positioning characteristics of narrow UWB pulses enables them to offer high-resolution radar (within centimetres) for military and civilian applications. In

addition, because of the very wide frequency spectrum band, UWB signals can easily penetrate various obstacles. This property carries great potential for ground-penetrating radar (GPR) and its application such as rescue and recovery of buried casualties in disaster situations (geolocation and positioning) [17, 18]. The required resolution is very high (in order of millimetres) compared with other radars. The bandwidth of GPR is typically in the range of 200 MHz and several GHz. Although there has been a significant amount of research into the development of UWB components in recent years, effective antenna design remains a significant challenge. Loaded dipoles, TEM horns, biconicals and ridged horns [20], spiral and large current antennas have all been proposed each with advantages and disadvantages

The high-data-rate capability of UWB systems for short distances has also numerous applications for home networking and multimedia-rich communications in the form of Wireless Personal Application Networks (WPAN) applications[4]. The demand for high-rate computer communications will yield multiple-access networks with high user density, and also have applications for wireless devices [21, 22, 23]. The Institute of Electrical and Electronics Engineers (IEEE) 802.15 working group is responsible for wireless personal area networks (WPAN) standards. In November 2001, Task Group 3a was formed within IEEE 802.15 to identify a higher speed physical-layer alternative to existing technologies that could support data rates up to 480 Mbps over short ranges of less than 10 meters, in order to enable a broad range of applications such as wireless transmission of video signals [24]. For several years, the IEEE Task Group 3a has been working towards 802.15 UWB Standard (WiMedia UWB) [25, 26, 106]. In Europe, the European Telecommunications Standards Institute (ETSI) has set up a task group to establish emission limits and other regulations for UWB systems [16].

[4] These include wireless links between camcorders, personal computers, DVD players, flat-screen television displays, printers, 3-D gaming equipment, MP3 players and other device

Wi-Fi and Bluetooth [27, 28] are also two well entrenched wireless technologies, so thinking about new technologies for multimedia applications, such as WiMedia UWB [25, 26, 106], could be considered unnecessary. Bluetooth [27] was developed originally for a wireless communication between a mobile phone and a handset. Although usage has expanded to connect several types of devices and peripherals the main limitation is its speed. Even Bluetooth 2.0 tops up to only 3 Mbps. On the other hand, there is Wi-Fi [28], developed primarily to provide wireless access to the internet from personal computers and laptops, giving whole house coverage with data rates no bigger than 54 Mbps. Again this is less than ideal for multimedia streaming due to both lack of bandwidth and quality of service (QoS) provisions. Wimedia's UWB technology was developed to be the ideal technology for implementing WPANs. With data rates of up to 480 Mbps and high QoS is ideal for multimedia applications. Table 2.1 shows a brief comparison between these technologies.

| | **WiMedia UWB** | **Bluetooth 2.0** | **Wi-Fi (802.11.g)** |
|---|---|---|---|
| **Data rate** | 480 Mbps | 3 Mbps | 54 Mbps |
| **Range** | 10 m | 10 m | 30 m |
| **Energy for 1 GB transfer** | 5.4 mWh | 136mWh | 56.6mWh |
| **Time for 1GB transfer** | 82s | 8192s | 409s |
| **Operation frequency** | 3.1-10.6 GHz | 2.4 GHz | 2.4 GHz |

**Table 2.1. Comparison of some wireless technologies [28]**

Thus, each technology has its own strengths and weaknesses. However, for WPAN applications, WiMedia UWB is considered the ideal choice, offering a unique combination of

high speed, low power and ease of use. In the next section 2.1.3 an extended description of this standard is presented.

### 2.1.3. Emerging UWB Standards: WiMedia UWB

Following the acceptance by the FCC for limited use of UWB systems, the IEEE formed a new task group (3a) in order to standardise a new high-speed physical layer (PHY) enhancement amendment to the IEEE 802.15.3 WPAN standard. Originally to a maximum of 55 Mbps, the new standard would enable data rates up to 480 Mbps, permitting imaging and multimedia applications in WPAN. The IEEE 802.15.3a task group studied a number of proposals from different companies, and considered two in detail. The first was based on multiband orthogonal frequency-division multiplexing (MB-OFDM) UWB [29, 31, 106], supported by the WiMedia Alliance [25], and the second being Direct Sequence Code Division Multiple Access (DS-CDMA), supported by the UWB Forum. Unfortunately, a final decision on which technology to use could not be reached and the task-group was dissolved in 2006.

Multi-band systems use OFDM techniques to transmit the information on each of the sub-bands. OFDM has several desirable properties, including high spectral efficiency, inherent resilience to radio frequency (RF) interference, robustness to multipath, and the ability efficiently to capture multipath energy. It is also well understood and has been proven in other commercial technologies (e.g. IEEE 802.11a/g). Furthermore, OFDM offers inherent robustness to multi-path dispersion with a low-complexity receiver. Thus, WiMedia Alliance [25] had the European Computer Manufacturers Association (ECMA) International [30] approve of their WPAN standard based on MB-OFDM UWB technology. According to ECMA standards, which specify a basis for high-speed and short-range WPANs with data rates up to 480 Mbps over short distances (around 2 m).

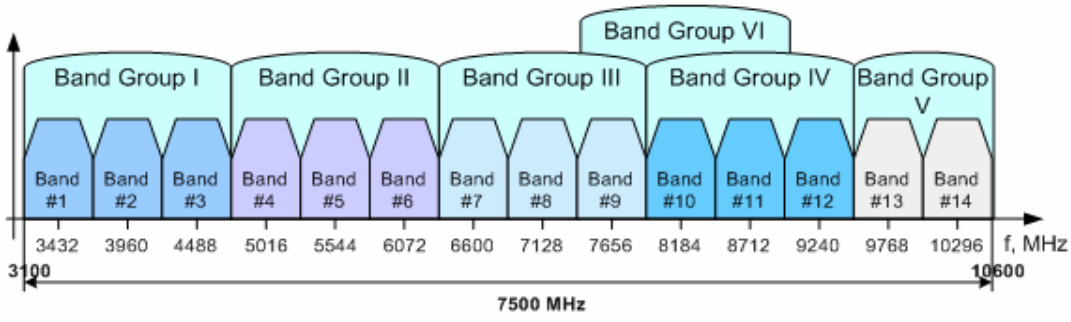


**Fig. 2.2.Allocation of frequency bands according to the ECMA standard [30]**

Fig.2.2 illustrates how frequency band 3.1-10.6 GHz is divided into six frequency bands called band groups. Each one is further divided into three sub-bands (with the exception of group 5 which has two 2), with a 528 MHz period between consecutive centre frequencies [5].The OFDM symbols can hop across sub-bands in each group, but they cannot hop between groups. The OFDM signal consists of 128 subcarriers spaced 4.125 MHz intervals. The multi-band OFDM system enables a UWB communication system which is low power, low in complexity, inexpensive to run, and with the ability to communicate at rates in excess of 110 Mbps over distances beyond 10 meters (depending on the data rate and the channel conditions). In addition, systems based on multi-band OFDM have a high degree of flexibility and can therefore co-exist effectively with existing wireless technologies and adapt to the various regulatory requirements in different regions of the world. An extensive insight of this approach can be found in [31, 106].

In addition to high-rate WPAN applications, UWB signals have also been considered for low-rate WPANs that focus on low power and low complexity devices. Then, in March 2004, the IEEE 802.15 low-rate alternative PHY task group (TG4a) was formed to design an

[5] The centre frequency for the *nth* band, $f_c^{(n)}$, is given by $f_c^{(n)} = 2.904 + 0.528n$ (2.4) for $n$ = 1,…,14. These frequency bands are also classified into six band groups (Fig. 2.2), where, for example the first 3 bands (Band Group 1) are used to transmit information signals.

alternative PHY specification for the already existing IEEE.802.15.4 standard for WPANs [26, 32]. The main objective of this task group was to provide communications and high precisions raging/location capability, high aggregate throughput and ultra-low-power consumption. The TG4a's efforts resulted in the IEEE 802.15.4a standard in 2007 [26]. Now this standard provides facilities for new applications and market opportunities.

## 2.2. Comparison of UWB with Narrowband Communication

Central to UWB technology is the use of short pulses instead of continuous waves to transmit information. Such a pulse directly generates a wide instantaneous bandwidth signal, governed by the time-scaling time properties of the Fourier transform relationship between time, *t,* and frequency, *f.* In contrast, narrowband communication[6] is typically achieved by modulating a sinusoidal carrier with the information to be transmitted. The resultant signal is sinusoidal in nature and occupies a narrowband in the frequency domain (Fig.2.3).

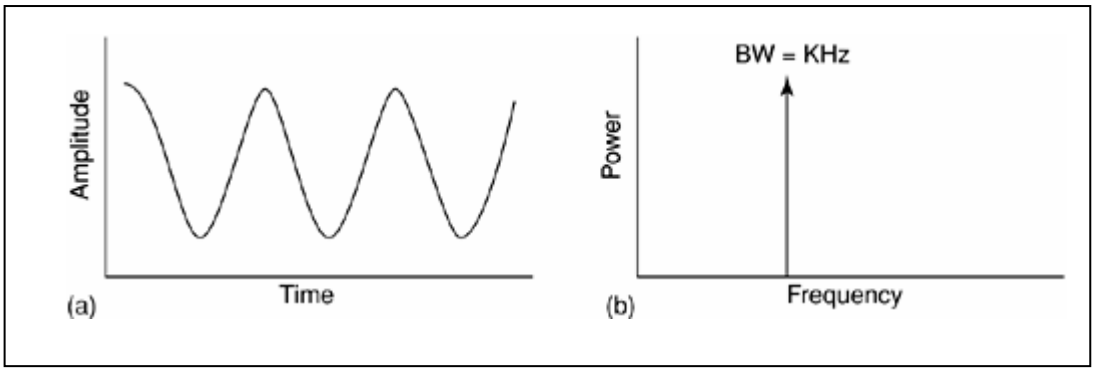


**Fig.2.3.A narrowband signal in (a) time domain and (b) frequency domain**

For UWB applications, any waveform that satisfies the definition for UWB signals can be used. The choice of a specific waveform is determined by both the design and purpose of the application, with consideration given to minimising local interference by choosing the

[6] The classification of signals based on their fractional bandwidth is given as follows: narrowband: FB < 1%, wideband: 1% < FB < 20%, ultra-wideband: FB > 20%.

most suitable UWB waveform [7] [33, 34]. The basic theoretical model for impulse radio uses a class of waveforms known as 'Gaussian waveforms', being very similar to the Gaussian function. Figure 2.4 represents a Gaussian monocycle as an example of a UWB pulse in the time and frequency domains.

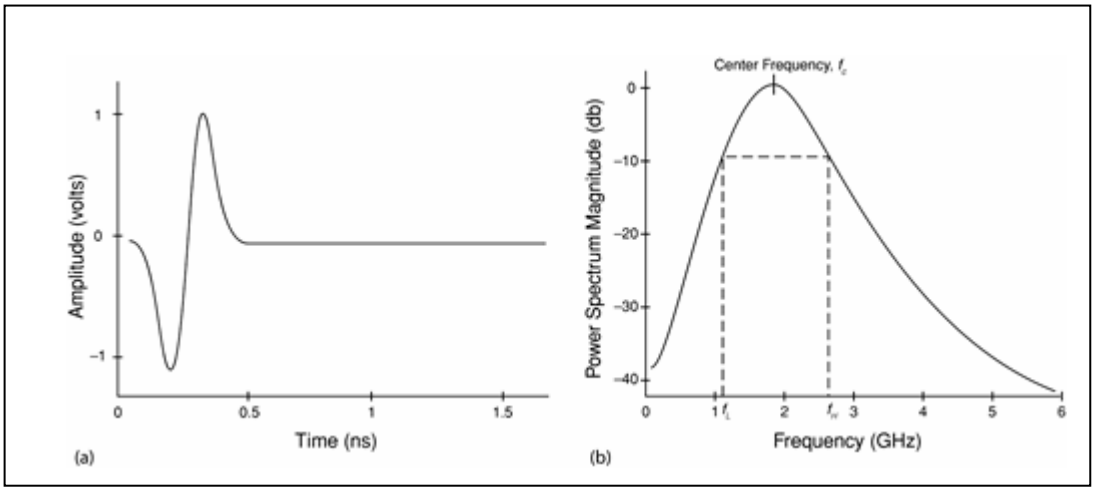


**Fig. 2.4. A 500-picosecond Gaussian monocycle [1] in (a) time and (b) frequency domains**

As shown in Fig.2.4, a 500-picosecond pulse generates a large bandwidth in the frequency domain with a centre frequency of 2 GHz. In Fig.2.4.b, the lowest and highest cut-off frequencies at 10 dB are approximately 1.2 GHz and 2.8 GHz, respectively, which lead to a fractional bandwidth (FB) of 80 percent; this is much larger than the minimum FB required by the FCC. A main advantage of UWB is the ability to share the frequency spectrum, and the power restriction of 75 nanowatts/MHz for UWB systems [6] allows them to reside below the noise floor of a typical narrowband receiver; this enables UWB signals to coexist with current radio services with minimal or no interference. Figure 2.5 illustrates the overlap of bandwidths between UWB, narrowband and wideband. However, despite this ability to share

[7] A UWB signal can be any one of a variety of wideband pulses, such as Gaussian, chirp, wavelet, or Hermite-based short-duration pulses

bandwidth, effective transmission also depends on the form of modulation used for data transfer by UWB.

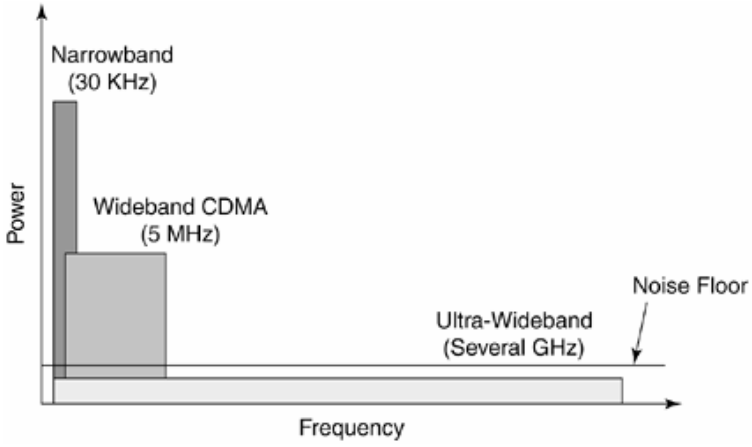


**Fig.2.5. Coexistence of UWB signals with narrowband and wideband signals in the RF spectrum**

A further major advantage of the extended bandwidth for UWB pulses is the improved channel capacity, or data rate. Channel capacity (*C)*[8] is defined as the maximum quantum of data that can be transmitted per second over a communications channel and it linearly increases with bandwidth B [35]. Therefore, having several gigahertz of bandwidth available for UWB signals, a data rate of gigabits per second (Gbps) can be expected. The Hartley-Shannon formula [35] also shows that the channel capacity is logarithmically dependent on signal-to-noise ratio (SNR). Thus, UWB communications systems are capable of working in harsh communication channels with low SNR and yet still offer significant channel capacity as a result of their large bandwidth. Authors in [19] present the coexistence of UWB systems with GSM900, UMTS/WCDMA and GPS systems.

[8] The large channel capacity of UWB communications systems is evident from Hartley-Shannon's capacity formula [35], i.e. $C = B\log_{10}(1+SNR)$ (2.3), where *C* represents the maximum channel capacity, *B* is the bandwidth, and *SNR* is the signal-to-noise power ratio.

### 2.2.1 Multipath interference

Multipath phenomenon is caused by multiple reflections of the transmitted signal from various surfaces such as buildings, trees or people; the phenomenon of multipath interference is unavoidable in wireless communications channels. The straight line between a transmitter and a receiver is the line-of-sight (LOS); the reflected signals from surfaces are non-line-of-sight (NLOS). Figure 2.6 illustrates this phenomenon.

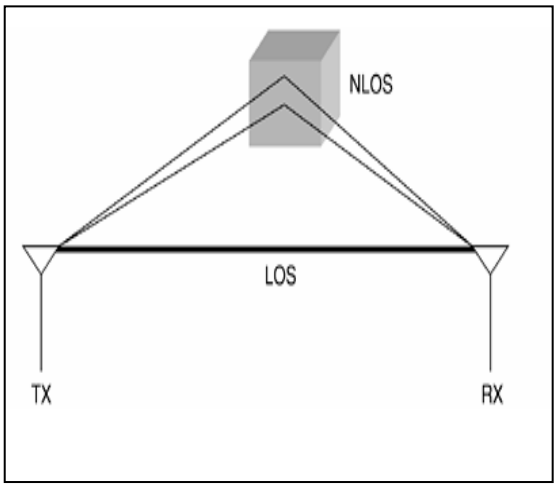


**Fig.2.6. Multipath phenomenon in wireless links**

Unlike narrowband technology, the low frequencies and long wavelengths of the UWB frequency spectrum allows UWB signals to penetrate a variety of materials, including walls. This property makes UWB technology viable for through-the-wall communications and ground-penetrating radars [36], although is only truly viable at the low-frequency portion of the radio spectrum.

For narrowband systems, the properties of the objects, such as reflection and scattering, can be consider as constant with respect to the frequency due to the small frequency band of interest. However, the narrowband systems suffer from non-constant envelope modulation (e.g. OFDM) and need very high linearity and tough filtering to satisfy

out-of-band emission [6, 37, 38]. The challenge of UWB is the frequency dependence of adjacent scattering materials as well as that of transmitter and receiver antennas. In contrast to narrowband systems, in which high efficiency and high Q antennas are easily achievable, design of UWB transmission antenna is complex due to the difficulty in matching antennae over the whole bandwidth.

## 2.3. Radio versus Optical Wireless

Optical wireless communications has been researched over the past 30 years, since the first indoor wireless communication system was developed in 1979 by Gfeller and Bast [39] at IBM in Zurich, including a LOS and diffuse configurations. This technology has become a potentially attractive alternative to RF due to its spectrum is unregulated (except for eye safety) and its extremely large bandwidth available. However, the use of receivers that use incoherent detection leads to a link margin that is many orders of magnitude less favourable that Radio systems, at least at lower frequencies. On top of that, RF systems can be manufactured at low cost, whereas components used in optical wireless can be complex to manufacture. To achieve high data rates, a line of sight channel is desirable in the case of optical wireless. The same disadvantage may also be applied to the new high frequency technologies, such as 60 GHz [40], where blocking causes severe performance limitations due to its beamforming.

Since a PC tower environment contains numerous internal physical obstructions, optical wireless technology was considered to offer no advantages and its possible role was therefore not explored in this study.

## 2.4. Previous Studies in the UWB technology

Many researchers have studied the characterisation of UWB channels in recent years, resulting in more than 5000 research papers on the topic, as well as the development of several communications standards based on UWB technology. Understanding of narrowband technology, as eluded previously, whilst helpful in providing some general understanding in this field, is not applicable to the science of UWB propagation and channel modelling. Of special value is a series of publications by Saleh and Valenzuela (SV) [41], Hashemi [42, 43], Anderson *et al.* [44], Durgin and Rappaport [45-48]. The primary objective of these researchers has been to develop models that describe the system performance adequately, with successful characterisation requiring extensive and accurate measurements. Due to the rapidly growing interest in UWB communications, the development of robust channel models has attracted great interest. Cassioli and A. Molisch [49-51] have presented results for UWB indoor communications, where statistical models of a UWB propagation channel are proposed.

More recently, A. Molisch *et al.* [26] have created the final report of IEEE 802.15.4a channel model for ultra-wideband channels which recommends using the SV model that defines the ray arrival in clusters. This one provides UWB models covering the frequency range from 2-10 GHz, including models for indoor residential, indoor office, industrial, outdoor, and open outdoor environments. Also for the frequency range of 2-6 GHz provides a model for body area networks. However, this author aims to demonstrate that a much simpler model could define these ultra small wideband environments (Chapter 5).

### 2.4.1. Wideband Channel Measurements

Three core wideband measurement techniques have been described in [13]. The two time-domain measurements techniques include the Direct Pulse (DP) and the Spread

spectrum sliding Correlator (SC) technique. The third technique based on frequency measurement is the Frequency Sweeping (FS) technique, also know as the vector network analyser (VNA) based channel sounding method [14].

The most notable UWB time-domain measurement campaign is that by the Ultra Lab group conducted at the University of South California (USC), in collaboration with the Time Domain Corporation [52]. Their measurements were performed using a sampling oscilloscope, a pulse generator and wideband antennas. The results of these measurements were used to develop further models [50, 53], but no information on the pulse shape and the characteristics of the antennas used in their measurements are provided. Both DP and SC techniques have been used in office, laboratory and residential environments in literature [32], but this research is focused on the FS technique.

The Frequency Sweeping (FS) approach for UWB channel characterisation is to perform propagation measurements in the frequency domain and convert the results to the time domain by means of inverse Fourier transform [54, 55]. The advantage of this approach is that the sensitivity of the equipment used, particularly the vector network analyzer (VNA), is much higher than that of the time-domain measurement equipment (i.e. sampling oscilloscope). The chief disadvantage of frequency-domain measurements is that long high-quality RF cables are required for connecting the network analyzer to both transmitting and receiving antennas [56]. These cables represent a major limitation for long distance measurements, although they are acceptable in the small environment used in this study.

Another limitation with this system would be the non-real-time nature of the measurement, where in time varying channels, the channel frequency response would change rapidly, giving an erroneous impulse response measurement. One approach to abrogate this effect is to employ faster sweep times to limit the total swept frequency response interval, but this would impair temporal resolution and lead to an excess delay range in time domain. In

the study described herein, the testing environment is *stationary*, and these factors are therefore immaterial.

A number of different research groups have studied UWB channel propagation using frequency-domain measurements, including Ghassemmzadeh *et al.* [56], Prettie *et al.* [57], Keignart and Daniele [58], Kunisch and Pamp [59], and Hovinen *et al.* [60]. Only Ghassemmzadeh *et al.* [56] used substantially long cables (up to 45m), while most others who have described their measurement setups have used much shorter cables. They have also used different bandwidths in their measurements. Prettie *et al.* [57] and Hovinen *et al.* [60] have used a frequency range of 2 GHz to 8 GHz. Keignart *et al.* [58] have used a smaller frequency range from 2 GHz to 6 GHz, while Kunisch and Pamp [59] conducted UWB channel measurements in the range of 1 GHz to 11 GHz. Ghassemmzadeh *et al.* [56] have presented extensive frequency-domain measurements in 23 residential homes. No multipath component was observed in their measurements beyond 70 ns of excess delay with a 30 dB threshold. These measurements were used by Turin *et al.* [61] to develop an autoregressive model for an indoor UWB Channel. Cramer *et al.* [3, 53] demonstrated that multipath components result in an extended channel impulse response. The study suggested a window of 300 ns to account for all multipath components which contain an appreciable amount of power. In this thesis, due to the reduced volume of the environments, a shorter period of time is expected to contain sufficient power.

### 2.4.2. Short Range UWB Wireless Channels

Currently there is much interest in short-range applications. One of the basic issues of such small confined environments is the fact that their wave propagation properties are fundamentally different where a high number of multipath components are expected due to the reduced size of the environments. Wireless communication more often occurs in a type of

these confined environments such as aircrafts [62-64], spacecrafts [7], road vehicles [65-69, 117] and even electronic enclosures like Magnetic Resonance Imaging (MRI) [70]. There is a special increase in the study of UWB channel modelling for intra-vehicle environments [65], where larger cluster arrivals occurs in contrast to indoor or outdoor environments where the path decay are smaller. In addition, the root mean square (RMS) delay rate is also less, indicating potential for smaller symbol duration when avoiding ISI, and hence the potential for higher data rates. These phenomena are expected to be similar inside the small cavities analysed in this research. Furthermore, due to the potential effective data rates, airlines have also been interested in setting up UWB systems, for example on video for demand applications. In [62] a measurement campaign is conducted on board an Airbus 319 cabin in the frequency range of 3-8 GHz, where a modified Saleh-Valenzuela (SV) cluster model [41] is presented.

As stated in the previous paragraph, the effect of size reduction reflects an increased number of multipaths, and so if this number appears to be so large, the environment itself may act as a resonator. Early studies inside small reverberating chambers were reported like the one from Huang and Edwards [71, 72] and Corona *et a.l* [73], who described the radiated power behaviour inside a reverberating chamber (RVC) in the microwave range. Sorrentino *et al.* [74] demonstrated how to emulate a Line of Sight (LOS) and propagation channels by different absorber configurations. The LOS channels were characterised by the Ricean K-Factor [75] and results showed that K is not only dependant on the number of absorbers but also on their configuration inside the chamber.

Potential applications of UWB have also been pursued by the astronautic industry, in particular by the Institute of Space and Astronomical Science in Japan [7]. UWB carries the advantages of reducing cable weight - and thus launching costs - as well as greater flexibility in the layout of spacecraft subsystems. In their study, they placed different volumes of radio

absorber strips and measured the different fading depth, presented as a function of the radio absorber. Unsurprisingly, the higher the volume of the absorber the greater enhance of the energy losses.

Another emerging area is 'Wireless Body Area Network' (WBAN), which examines the feasibility of wearable computing devices. Such systems envisage UWB wireless communication between miniaturised Body Sensor Units (BSU) and a single Body Central Unit (BCU) worn on the human body, with such a WBAN system using WPAN wireless technologies as a portal to reach longer ranges. UWB measurements around the human body with wearable antennas have been carried out by various researchers [76], with special attention to medical applications [77].

More relevant are the studies similar to the study carried out in this thesis. Special mention to the ones carried out by P. Chiang *et al.* [8], Z. Chen [9], Karendal *et al.* [10], and S. Redfield *et al.* [11] where a measurement campaign is carried out inside a computer chassis. P. Chiang *et al.* [8] describes the significant design challenges of placing very small UWB transceivers in Complementary metal-oxide-semiconductor (CMOS) technology inside the cavity. Some of the challenges are latency, fault tolerance or platform clocks. Also a very interesting comparison with alternative interconnect technologies is shown, where optical links are rejected for similar reasons stated in section 2.3. Again no particular model of the environment is presented, where only three measurements were carried out inside the PC. In contrast, in this thesis, in order to have a deeper understanding of the channel and establish a possible model of the confined environment, an extensive campaign of grid measurements is carried out at different parts of the PC, such as next to the MB, CD slot or PCI cards.

A PC box with inter-chip wireless communication channels is described by Z. Chen *et al.* [9]. Two experiments are undertaken, one with the housing open and another with it closed. Data shows that a significant portion of energy escapes out of the case with the

remaining portion being reflected internally and attenuated. The difference in path loss between case closed and open increases when distance between antennas increases. Although this conclusion is good for general knowledge, the measurement campaign when the case is open is not considered in this study since the purpose of this research is to characterize a confined/shielded scenario. However, interesting analyses are shown like the small scale analysis, where as a result, the lognormal distribution is taken to model the small scale distribution. This thesis examines this contribution and makes a case instead using Nakagami-m distribution for this type of small scale analysis. Comparison between both distributions is also presented.

Karendal *et al.* [10] presents results of a measurement campaign inside two desktop computers analysing the possibility of board-to-board communication. In this case the use Nakagami-m distribution to fit the small scale fading, where there is no observation of large-scale fading effects. They determined that for the range of 3.1-10.6 GHz, orientation and the location of the terminals has no significant effect on the results. A further and more detailed study of this matter is presented in Chapter 6, where the actual election of antennas positions, the central frequency and bandwidth selection does play a dominant role.

Finally, Redfield *et al.* [11] presents a reasonably good model of the computer chassis based in the IEEE 802.15.4a standard model. However, in this thesis a much simpler model is investigated in Chapter 5 where the path decay can be modelled only as the inter-cluster decay.

Thus, with an increasing number of applications for UWB plus the great amount of investigations carried out in very short-range channels, like computer chassis, it is believed that this research is a valuable contribution to this emerging field. Furthermore, any researcher will have to consider extending these UWB measurements campaigns to different

and simpler cubical environments, like an Aluminium box, to try to extrapolate possible results and design rules for this type of small enclosures.

## 2.5. Overview of Backplane and PCI Bus Technology

Recently there has been a trend in the telecomm and datacomm market of rapidly increasing bandwidth with particular growth in systems which are I/O intensive rather than computing intensive. This is driven by customer demands for data-routing (rather than data processing), highly fault tolerant and physically robust systems. Meeting these requirements has raised an awareness of backplane interconnectivity which currently uses copper and operates at a variety of different bit rates and protocols.

Data rate requirements for backplane connectors and systems began to increase in the 1990s and increased from 644 Mbps to 2.5 Gbps at the end of the century. With technology currently capable of reaching up to 5 Gbps, the backplane interconnect industry is now striving to meet the 10 Gbps needs of its customers' next-generation platforms. When the peripheral component interface (PCI) bus [78] was first introduced in the early 1990s, it had a unifying effect on the plethora of input/output (I/O) buses available on PCs at that time, such as the VESA local bus, EISA, ISA, and Micro Channel. It was first implemented as a chip-to-chip interconnect and a replacement for the fragmented ISA bus. During these early years, the 33 MHz PCI bus was a good match for the I/O bandwidth requirements of mainstream peripherals. Today, the demand has changed: processor and memory frequencies have raised several-fold, with processor speeds increasing at the highest rate. At the same time, the PCI bus has increased in frequency from 33 to 66 MHz, while processor speeds have increased from 33 MHz to 3 GHz.

Although PCI has enjoyed great success, it now faces a series of challenges, including bandwidth limitations, host pin-count limitations, the lack of real-time data transfer services,

and the lack of features to meet next-generation I/O requirements (quality of service, power management, and I/O virtualisation). Since the introduction of PCI, there have been several revisions to the PCI specification to meet the ever increasing I/O demands. These are summarised in Table 2.2 [79].

| PCI Bus Bandwidth (bits) | Bus Clock Frequency (MHz) | Bandwidth (MB/s) | Market |
|---|---|---|---|
| 32 | 33 | 132 | Desktop/mobile |
| 32 | 66 | 264 | Server |
| 64 | 33 | 264 | Server |
| 64 | 66 | 512 | Server |

**Table 2.2. PCI Bandwidth and Market Use [79]**

The usable bandwidth of the PCI bus and its derivatives can be significantly less than the theoretical bandwidth due to protocol overhead and bus topology. On the PCI bus, the available bandwidth is shared among all devices on the bus, meaning a decrease in bandwidth as more devices are included. One of the solutions to this problem was PCI Express [79], the next-generation of the PCI bus, introduced in 2004. Today, most PCs are built with a combination of PCI and PCI Express slots, although in time the PCI bus will become old-fashioned. A second popular technology is the wireless PCI card, an insertable device with an antenna to enable fast wireless networking, file uploading and downloading. A wireless PCI card, readily inserted into the back of a PC tower unit, eliminates many of the previously encountered problems with networking via a PCI card, these include speed and the need for extensive cabling (see Fig.2.7 as a graphic example).

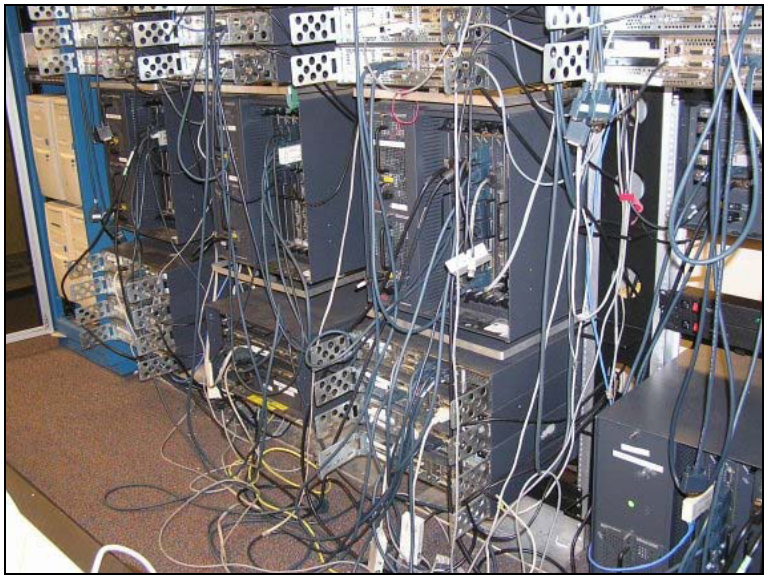

**Fig.2.7. Graphic example of the extensive cabling connecting different devices**

This thesis presents an investigation of another possible solution to the problems addressed before, and aims to characterize and have a deeper understanding of the nature of small confined environment for possible wire-free data transmission. Thus, this work examines the potential for high capacity UWB wireless interconnectivity inside very small confined cavities, with potential applications beyond a standard PC tower model.

# Chapter 3: Materials, Methods and Measurement Design

## 3.1. Introduction

The objective of the following sections in this chapter is to describe the experiment protocols and measurement setup for the different campaigns conducted inside the two electromagnetically small indoor UWB scenarios, these being a standard PC box and an Aluminium rectangular cavity. The apparatus used to perform these measurements were assembled and tested by this author in the Department of Electrical Engineering at Oxford University. To permit measurement repeatability, all aspects of the hardware set-up are described.

Two very similar printed bow-tie antennas [80, 83, 84, 86] were used to carry out the measurements; the rationale for their inclusion, their properties along the selected ultra wideband, and their radiation pattern are all described, in addition to their selected orientation (polarisation) within the cavities. In the complex environment of a PC tower case, a high degree of internal signal reflectivity is expected by the tower, chiefly by the boundary walls, Main Board (MB) and the PCI cards which are typically made from metallic and dielectric materials. Thus, the positioning of one or both of the antennas for optimal signal transmission and reception may be critically dependent on the distance from adjacent components, and it is this relative positioning of antennas and PC tower components one of the sections this study seeks to examine.

As described in section 2.4.1, three wideband measurement techniques are recognized [48]. In this study, the Frequency Sweep (FS) approach was employed, this is based upon the classic vector network analyzer (VNA) method [14]. The sweeper scans a particular frequency band across discrete frequencies, and thus both the number and periodicity of these

frequency steps influence the temporal resolution. This approach is able to measure both the magnitude and the phase of the electromagnetic response, and is used to analyze the properties associated with the reflection and transmission of electrical signals which are known as scattering parameters (S-parameters). The frequency domain thereby obtained is converted to time domain using inverse discrete Fourier transform (IDTF) processing [54, 55], giving a band-limited version of the impulse response.

Finally, empirical data was statistically analysed using methods including power delays profiles (PDPs), cumulative distribution functions (CDFs) of Ricean K factor and root mean square delay (RMS), channel capacity and fading. The definitions of these methods appear in this Chapter. The last section describes the confounding effect of Electromagnetic Interference (EMI) within the PC tower, and approaches to limit its effect. The results of time and frequency domain are presented in Chapter 5. Fading and channel capacity results appear in Chapter 6.

## 3.2. Measurement Setup and Description of Different Scenarios

The vector network analyser (VNA)-based channel sounder was used for all the wideband channel measurements. A vector network analyzer (HP8722ES) was utilised for performing swept frequency measurements connected to a computer by an IEE448/GPIB card. Port 1 was connected to the transmitter antenna and the receiver was connected through port 2 with UWB cables of around 2 metres long. The VNA swept the frequency within the band of interest, which in this case was between 3-11 GHz. This band was chosen as it affords accurate time resolution due to the number of multipaths possible in such short range. The transmitter port of the VNA was setup to transmit a swept frequency signal at a power level of -10 dBm. The complex transfer functions were recorded by sounding the channel at

$n_f$ = 1601 discrete frequencies, with a frequency resolution of 5 MHz, creating a data matrix of *Nx* x *Ny* x $F_p$ .[1]

Ultra wideband propagation measurements were conducted in each of two antenna polarizations, these being with each *co-orientated* horizontally (TH-RH), and with each polarised vertically (TV-RV). With an acceptable input reflection coefficient in the range of -10 dB to -15 dB (within the measurement band (3-11 GHz)), these antennas were well-suited for these experiments [80, 81]. The positioning of the transmitter antenna (TX) was determined by an X-Y positioning arm whose movement across a virtual array was controlled by *LabVIEW* $^{TM}$ graphical development software. This code controlled the movement of the motors and the number of measurement points by setting the appropriate stepping points.

The receiver (RX) was fixed in specific locations within the PC Tower while the TX was moved by the positioning arm. In the case of the Aluminium cavity, the RX position could either be fixed or be moved at the same time as moving TX, with both attached to the Positioning Arm. In order to calibrate the system, both cables were connected together via a semi-rigid cable of 18 cm distance (2 x distance of the semi rigid cable linked to the bow-tie antennas).

A very detailed description of both scenarios of the PC Tower Box and the Aluminium case are presented in following sections. Figure 3.1 shows two pictures of the overall measurement setup for both scenarios.

[1] *Nx* represents the number of measurement points at the x-axis, *Ny* the number of points at the y-axis, and $F_p$ the number of frequency points selected in the whole band. $F_p$ is always 1601 in our experiments, which corresponds with the maximum number which the VNA can support for an established bandwidth.

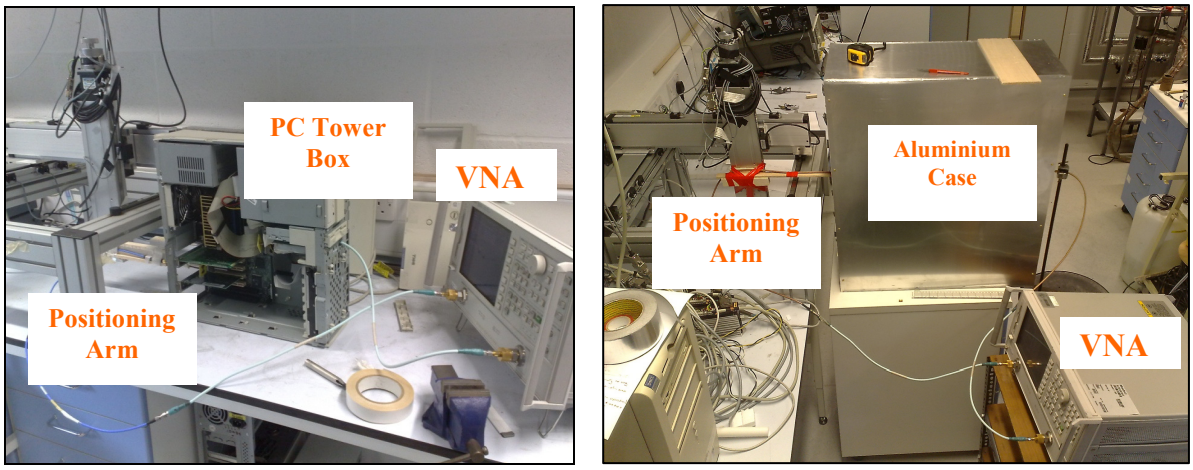


**(a)** **(b)**

**Fig.3.1. Both scenarios with their measurement setups**

**(a) PC Box, VNA, X-Y Positioner, UWB Cables and UWB Antennas**

**(b) Aluminium Case, VNA, X-Y Positioner, UWB Cables and UWB Antennas**

### 3.2.1. Personal Computer (PC) Environment

Firstly, a UWB Propagation measurement was conducted using UWB signals inside a standard PC Tower box. As previously noted, a motor-driven X-Y positing arm was utilised to mobilise the TX between both PCI cards, covering a specific area in the y-x plane. The VNA was used to measure the $S_{21}$ scattering parameters in each position. Irrespective of the location of RX, the TX was mobilised within the same square grid by the Positioning Arm, permitting an accurate measurement of the distance between TX points and the RX location. This arrangement allowed the author to establish a transmitter grid which included defined strategic points for a possible wireless link, involving the area next to the MB and the PCI cards. A schematic diagram of the distribution of the PC Tower box scenario is presented in Fig.3.2.a and the top view of the PC box is illustrated in Fig.3.2.b.

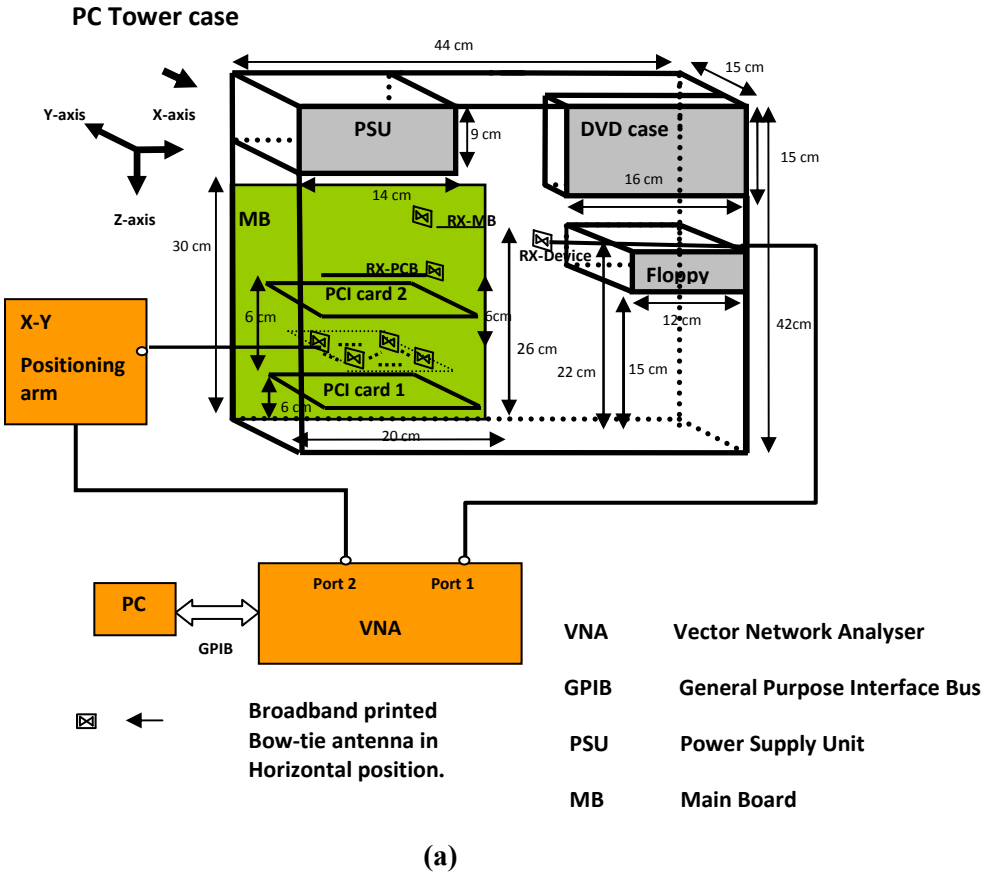


(a)

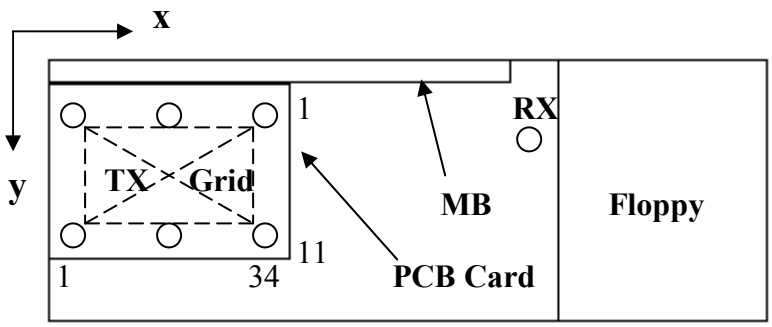


(b)

**Fig.3.2. Schematic diagram of a standard PC Box (a), and the top view of the PC Tower box when RX-Device (b)**

The TX adopts 34x11 positions, separated 5 mm each, which covers an area of 99 cm² in the x-y plane. The TX is always located in between both PCB cards of the computer. The RX locations cover different areas inside the PC case as it is appreciated in Fig.3.2.a. Three different fixed locations are selected: RX-Device, RX-PCB and RX-MB. RX-Device

represents the RX located next to floppy disk and DVD case area, RX-PCB is the one situated just below the edge of the PCI card and RX-MB is the one situated almost on top of the MB, very near to the micro-processor. Higher electromagnetic interference is expected in this situation, where also an increase of NLOS nature might occur due to the shadowing of different elements, like the fan or cables. On the other hand, when the receiver (RX) is located at RX-Device or RX-PCB, a higher LOS scenario is founded, where the only device blocking the signal is the PCI cards. Thus, each position of the RX aims to represent possible locations where a receiver antenna could be located to interconnect different devices inside the PC, with a view to replacement of SATA cables or buses by such a wireless arrangement. An example of the arrangement of antennas within the PC box is shown in Fig.3.3. The orange points represent the many possible locations where the TX is located in the measurement grid and the bow-tie antennas are horizontally polarised.

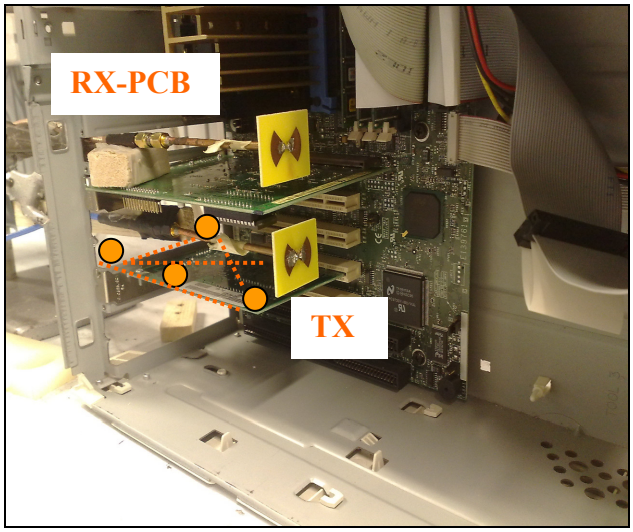


**Fig.3.3. TX and RX-PCB in Horizontal Polarisation inside the PC case**

### 3.2.2. Small Aluminium Resonator Case

The other environment explored in this UWB measurement study is a small rectangular Aluminium case. The purpose of conducting such a study within a more basic

structure is to observe the behaviour of UWB within an 'optimum' environment whose internal dimensions are similar to a personal server or PC, but is devoid of internally complex structures such as cables or MB. Only eight real PCBs are placed in parallel distribution inside the cavity at the back wall as shown in Fig.3.4.b, in an attempt to simulate parallel communication between possible microprocessors inside a very small resonant cavity. Same antennas are used, adopting two different polarisations. Antenna location is determined by the X-Y positioning arm, allowing the positioning of antennas to be varied inside the box in same plane coordinates (x-y axis), but different level (z-axis). Finally, the same VNA is used to measure the $S_{21}$ scattering parameter (transmission) between the transmitter (TX) and receiver (RX) antennas in each position.

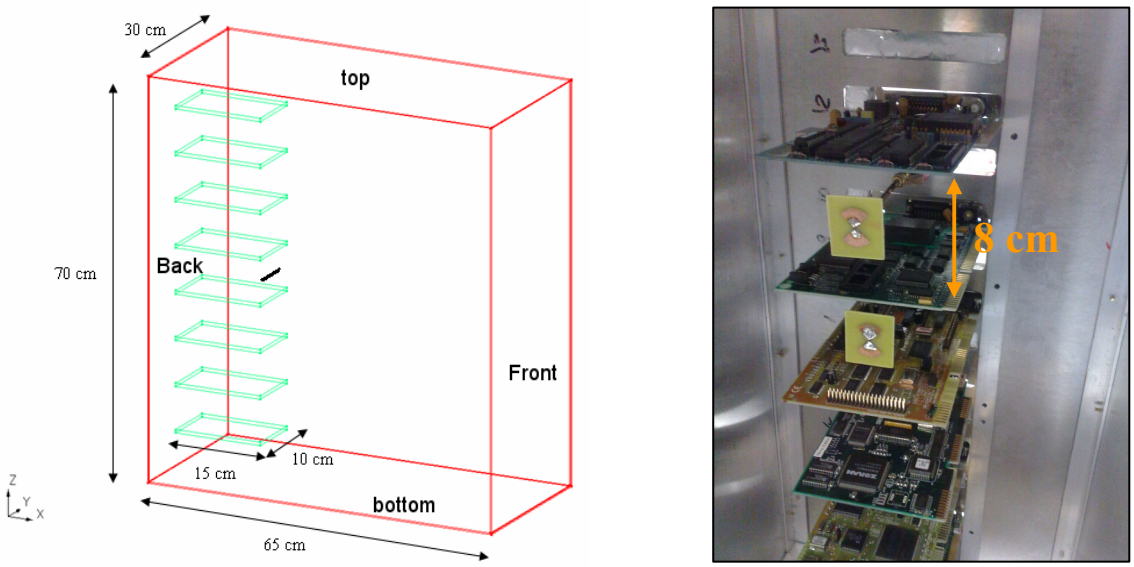


**(a)** **(b)**

**Fig.3.4. Schematic diagram of the Aluminium case (a) and a picture of the parallel distribution of the PCI cards inside the cavity (b)**

The same bow-tie antennas are used, adopting two different polarisations. Again the availability to move them relies on the X-Y positioning arm, allowing the positioning of antennas to be varied inside the box in the same plane coordinates (x-y axis), but different

levels (z-axis). The same VNA is used to measure the $S_{21}$ scattering parameter (transmission) between the transmitter (TX) and receiver (RX) antennas in each position.

Several different experimental paradigms were explored within this confined resonating environment, with both the TX and the RX in different positions (i.e. the RX was not always fixed). This was done in order to determine the different power distribution capacity and fading effects, with antennas located at different positions on top of the PCB cards. A graphical explanation of this is given in Fig.3.5.

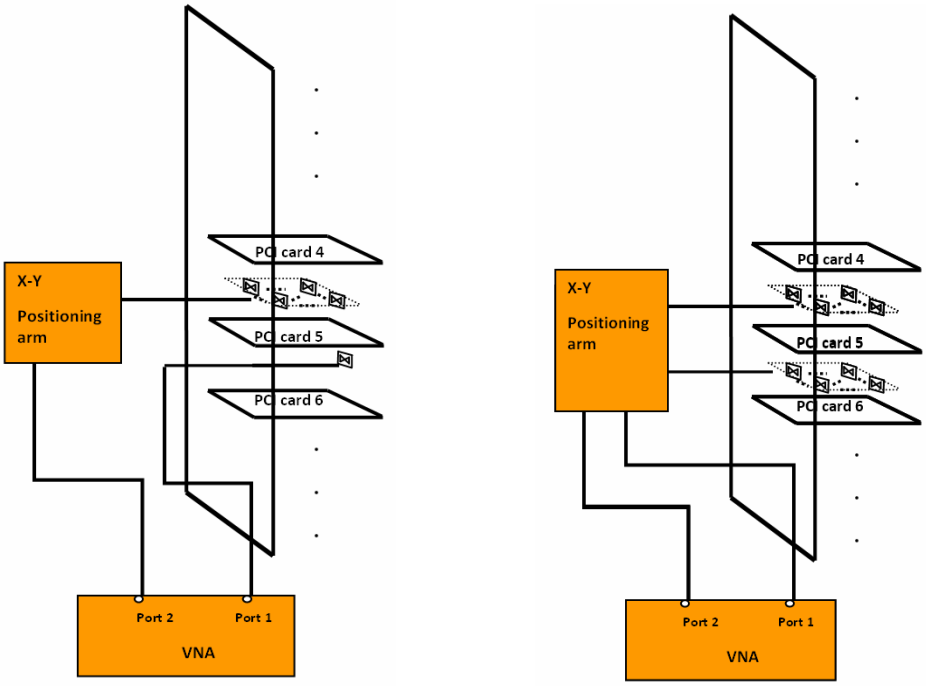


**(a)** **(b)**

**Fig.3.5. Schematic diagram of both scenarios inside the Aluminium case**

**(a) RX is fixed in one position and TX moved with Positioning Arm**

**(b) Both TX and RX are moved with Positioning Arm at same location of the grid but different levels**

The first scenario (Fig.3.5.a) consists on fixing the RX antenna at several points on top of a PCI card and then moving the TX along a grid of measurement points in a different level. This experiment is very similar to the one when the receiver is at RX-PCB inside the

PC box. However, this time the scanned area of the TX is slightly reduced to 75 $cm^2$ (15x5 points separated 1cm each). It is considered sufficient to cover this area (i.e. half of the total) as the remaining area, being symmetrical, would yield the same results. Thus, for the sake of time (10s per measurement at each point) it was decided to scan only half of the possible locations on top of the card. The second scenario (Fig.3.5.b) presents both TX and RX antennas fixed one on top of the other separated by a PCI card and then both moved at the same time over the same points at the measurement grid. This situation will be referred from now on as a 'First level' due to the separation between antennas is by one PCB card. Other scenarios would be 'Second Level' and 'Third Level' where the terminals this time are separated by two and three adjacent cards respectively. A graphical representation of this setup is shown in next Fig.3.6.

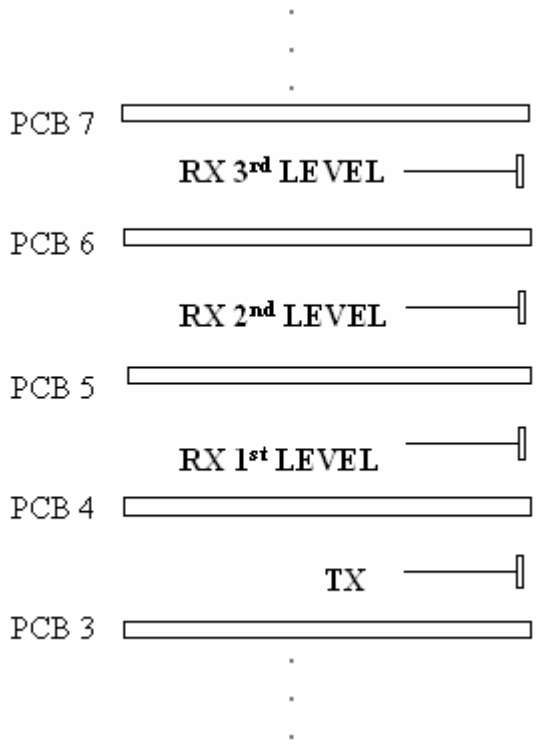


**Fig.3.6. Schematic diagram of different the different positions 'Levels' of the RX inside the Aluminium Case**

It is important to note that the *majority* of measurement cases antennas are in non-line-of-sight (NLOS), as the cards obstruct the direct path between the antennas. Only when the antennas are located at the inner edge of the cards as shown in Fig.3.6, furthest from the back of the box, a slightly LOS scenario is presented.

A further objective is to determine the influence of tower size on UWB behaviour. The greatest advantage of this environment is the possibility to engineer it. The Aluminium box is designed in a way that one of the walls can be moved forward and backwards in three different positions. This wall is in the x-y plane. The aim is to have a different volume and geometry of the cavity and see the implications on the experiments. Figure 3.7 shows a graphical example of these configurations.

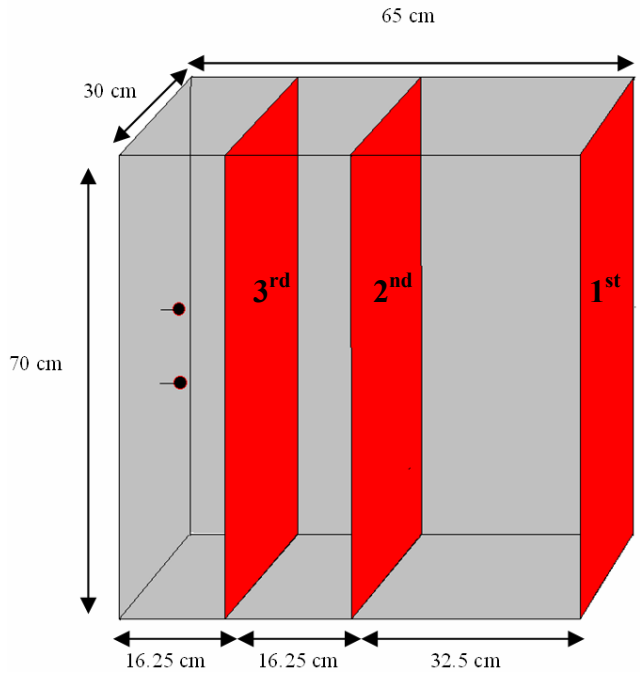


**Fig.3.7. Schematic diagram of different positions of the cavity's front wall**

The anterior surface of the casing is shown in red, with possible antenna locations shown by the black points. By moving the front wall from the 1st to the 2nd position, the volume of the cavity is reduced by half, and by a further half by moving it to the 3rd position. The nomenclature used to denote the cavity is as follows:

1st = Full case

2nd = 1/2 Full case

3rd = 1/4 Full case

Finally, covering the front wall of the Aluminium cavity with an electromagnetic absorber[2] is also investigated. The objective is to check how much the inclusion of an absorber affects the system, especially in terms of small scale fading and multipath detection.

## 3.3. The UWB Antennas

For a wireless system, microstrip patch antennas are a good choice because they have the advantages of low volume, weight and profile, and are inexpensive to make [82]. Three dimensional structures such as bicones, discones and volcano antennas [81, 129] have relatively good radiation properties for the broad band in question, but their size and cost effectively bar them from the experiments described in this study. In the past, the pursuit of increased bandwidth led to the development of a special class of patch antennas. These include tapered slot, spiral, or bowtie antennas [80-86]. In this section, one type of these antennas is described: the Bow-tie antenna [80, 83, 84, 86]. Certain properties, such as their radiation patterns and return loss, make them particularly suitable for this study, and the aim is not to customise them as 'UWB antennas', but to demonstrate their effectiveness in this UWB research.

Vector network analyzer (VNA) calibration is achieved using a standard procedure in which transmitter and receiver are interconnected by cables. Elimination of the antenna effects is more difficult, as they have complex antenna patterns that vary both with frequency and direction; furthermore, gain is frequency dependent and can be different for each

[2] 3M 5050 Absorber tape, attenuation at of ~2.5 dB at selected frequencies (3-11 GHz)

considered direction. Thus, it was decided not to perform antenna calibration at all, but to present the measurements without adjustment for the antennas for each channel measured. However, standard calibration of the cables was done connecting both of them by a semi rigid cable of 18 cm distance (2 x 9 cm length of the semi rigid cable linked to the bow-tie antennas).

Two polarisation modes are adopted by the antennas: horizontal and vertical co-polarisation. Polarisation refers to the direction of the antennas in an empty space, where both of them may be parallel or perpendicular to the respective walls of the environment. The polarisation of both antennas depends on their respective orientation. When both are horizontal (*x-axis = 0*), the wave adapts a *Horizontal polarisation.* If mounted vertically (*z-axis = 0*), the wave moves in the H-plane resulting in *Vertical polarisation.* Therefore, in this study, both horizontal (TH-RH) and vertical (TV-RV) polarisations are described. Although cross-polarised measurements were also performed, a significant decrease of transmitted power made such an arrangement impractical for the study. Figure 3.8 shows an example simulation of the 3D radiation patterns of an UWB antenna [87] once it is vertically polarised (TV-RV) along the z-axis (Fig.3.8.a), and for horizontal polarisation (TH-RH) along the y-axis (Fig.3.8.b).

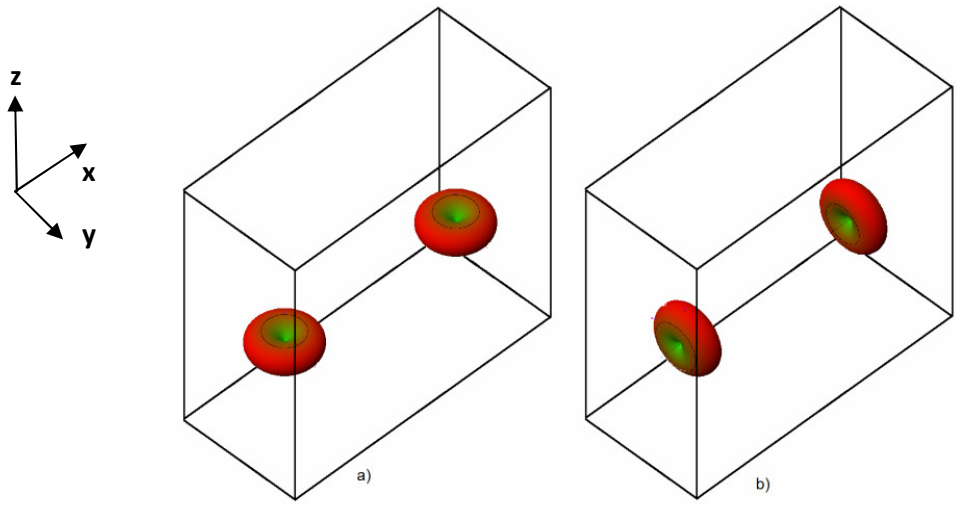


**Fig.3.8. Antenna radiation patters for TV-RV (a) and TH-RH (b) inside the enclosure [87]**

In this particular set-up of the antennas inside the cavity the main difference is that, for the horizontal polarisation (TH-RH), there is almost no energy transmitted through the direct path and the communication should be established through multipath reflections. Such case is attractive e.g. for situation where an obstacle will block the direct line-of-sight. This situation gives an idea of the importance of polarization of the antennas in order to establish the desired communication, i.e. via line-of-sight (LOS) or via reflections (multipaths).

In this thesis, only dual polarisation was considered for each location of the antennas, helping to excite more modes than a single-polarised diversity. These ones will give a good scope of the overall performance of the channel and better insight than the single polarisation model often employed [8-10]. However, different orientations of the antennas could all usefully be considered where the permutations are immense.

### 3.3.1. Triangular Bow-tie Antennas

Two portable bi-directional printed bow-tie antennas with circular-end are used as TX and RX antennas, operating in a frequency range of 3-11 GHz. The antenna geometry is shown in Fig. 3.9.

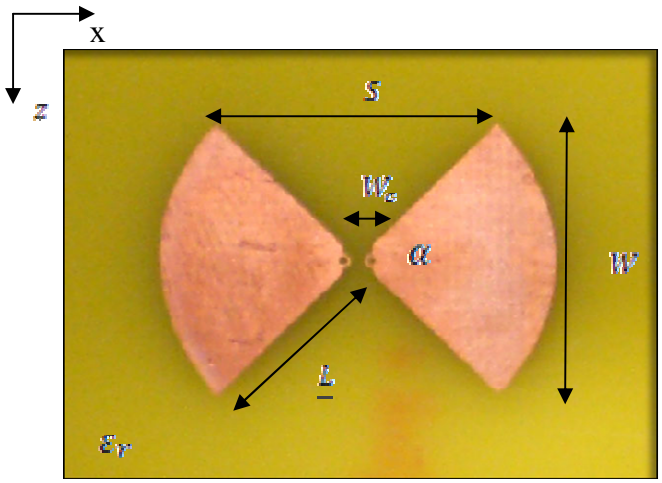


**Fig.3.9. Geometry of the printed bow-tie antenna**

The antenna had a single metallic layer with a flare angle α of 90°, printed on a substrate of thickness h =1.59 mm and with a relative permittivity, $\varepsilon_r$, of 4.5 (FR4). The printed bow-tie antenna was characterised by $W = S = 15\ mm$ and $W_c = 1\ mm$. With all these parameters and antenna dimensions of x = 30 mm and z = 25 mm, a small UWB antenna suitable for this experiment was available.

An essential antenna characteristic for this type of study is an acceptable $S_{11}$ magnitude, also referred to as Return Loss (RL), across the whole UWB band. RL is a measure of the effectiveness of power delivery from a transmission line to a load such as an antenna [88]. Figure 3.10 shows this characteristic of both antennas after measuring the $S_{11}(f)$ ($S_{11}$ versus frequency) parameter with the VNA. The apparatus was calibrated prior to the measurement to remove the attenuation, delay and phase distortion of the cables. $S_{11}(f)$ is studied to derive the reflection coefficient $\Gamma(f)$, which yields the antenna return loss in logarithmic scale often used to characterise the radiation performance of an antenna over a given frequency band.

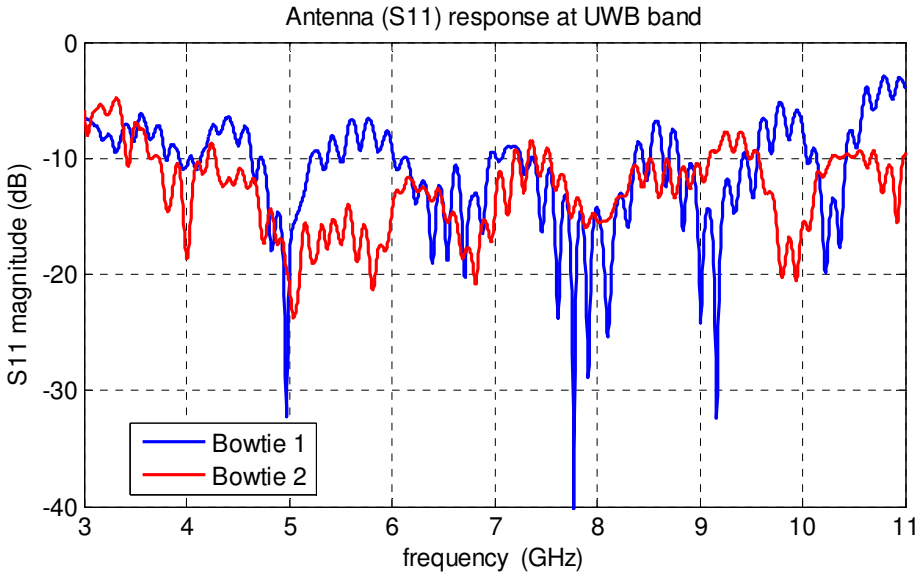


**Fig.3.10. Return Loss of both bow-tie antennas in the studied frequency band**

Figure 3.10 shows that the response of both antennas becomes smaller than -10 dB across almost all the bandwidth, showing that the antenna radiation efficiency is higher than 90% over the selected frequency spectrum. For these studies, in addition to their small size, this is an essential characteristic for an internal environment. The small resonance appearing in each antenna every 150 MHz is mainly introduced by the SMA connector attached with semi rigid cables which are linked to the back of each antenna. Their length is 9 cm (almost 10 cm including the SMA connector), which made measurements relatively straight forward. The resonance frequency has a wavelength corresponding to two times the distance of the semi rigid cable. Thus, a proportion of the signal is internally reflected between the antenna and the SMA connector, creating small resonance behaviour across the bandwidth. This behaviour is due to imperfection of the links between antenna and semi rigid + SMA connectors which is difficult to avoid.

Another analysis of interest is to check the energy levels of transmission between both bow-tie antennas for the studied band inside a free space environment (anechoic chamber). These measurements were carried out in a same plane (y-axis) once the antennas, horizontally orientated, were moved across in steps of 5 cm to from almost 0 cm to 20 cm of separation. Figure 3.11 presents the averaging of the frequency response of the transmitted signal inside the UWB band measured inside the anechoic chamber.

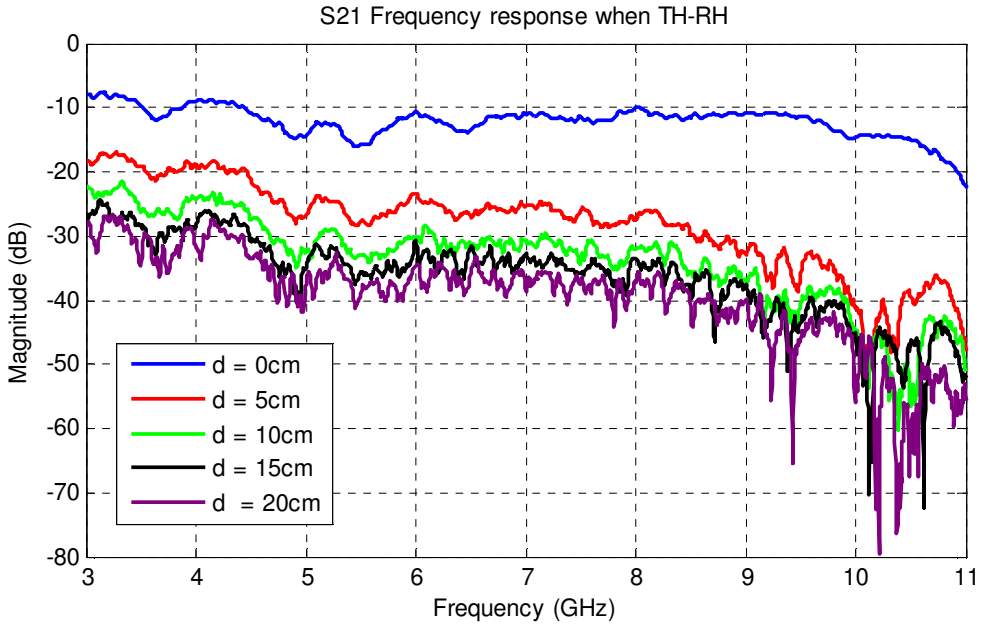


**Fig.3.11. Frequency response in a free space scenario for different separations of the antennas**

It is clear that once two antennas are almost touching each other (0cm) there is still a reasonable amount of power loss of 10 dB across the band. That means that radiated power in other directions than those captured by the RX is lost. It would reasonably be expected that there should be almost no loss; a possible explanation might be that placing the antennas in their near field zone modifies their radiation patter due to proximity. Thus, placing the antennas very close to each other, to walls or electric plates might affect their radiation behaviour. Thus, placement of bow-tie antennas within their near field zone is probably not desirable.

In the other separations between the antennas there is a mean power decay of 20-30 dB difference in decay compared to the first scenario. It looks as though, once the antennas are separated more that 5cm, the average loss in power corresponds to -40 dB. Also, for higher frequencies, there is a slightly extra decay of 10 dB after 9 GHz. The possible explanation of this is related with the RL of one of the antennas, where after 9 GHz its $S_{11}(f)$ becomes considerably worse than the rest of the band (60-70% of the power is radiated in different directions). These observations show that the antennas do not transmit a large

amount of power, and thus, if another type of antenna was employed, a higher power transmission could probably be achieved. However, the purpose of this study was to characterise UWB in a small confined environment using suitable UWB antennas that were capable of radiating an average of 90% of power across the selected bandwidth. Chapter 7 presents in future studies the possibility of the use of alternative UWB antennas with higher power gain (Vivaldi antennas [91] or discone antennas [129]).

Finally, to ensure our antennas have a well defined bi-directional behaviour, their radiation pattern for each polarisation was investigated. This is presented in Fig.3.12 and Fig.3.13 for different frequencies between 3-11 GHz, each with a 1.5 GHz frequency step. Measurements were also undertaken inside the anechoic chamber, simulating a free space environment and avoiding any unwanted reflections, where both antennas were located at a distance of 2 m each in the same plane.

From inspection of Fig.3.12 it is identified that the bi-directional behaviour where the mean lobe beams are in the x-direction is where the most affected radiation patterns are (the ones at higher frequencies). Figure 3.13, the radiation patterns change substantially where now they present less directionality, hence being *omni-directional*. It has been shown in [89] that real UWB antennas will not provide true omni-directional performance. Then, substantially different results from both polarisations can be expected, where the internal distribution of the different devices inside the cavities play a dominant role. Thus both polarisations are considered enough to evaluate the channel characteristics inside these confined environments. Clearly, numerous different polarisations could be adopted and the last chapter (‘Future work’) considers the question of polarisation diversity as well as different types of UWB antennas.

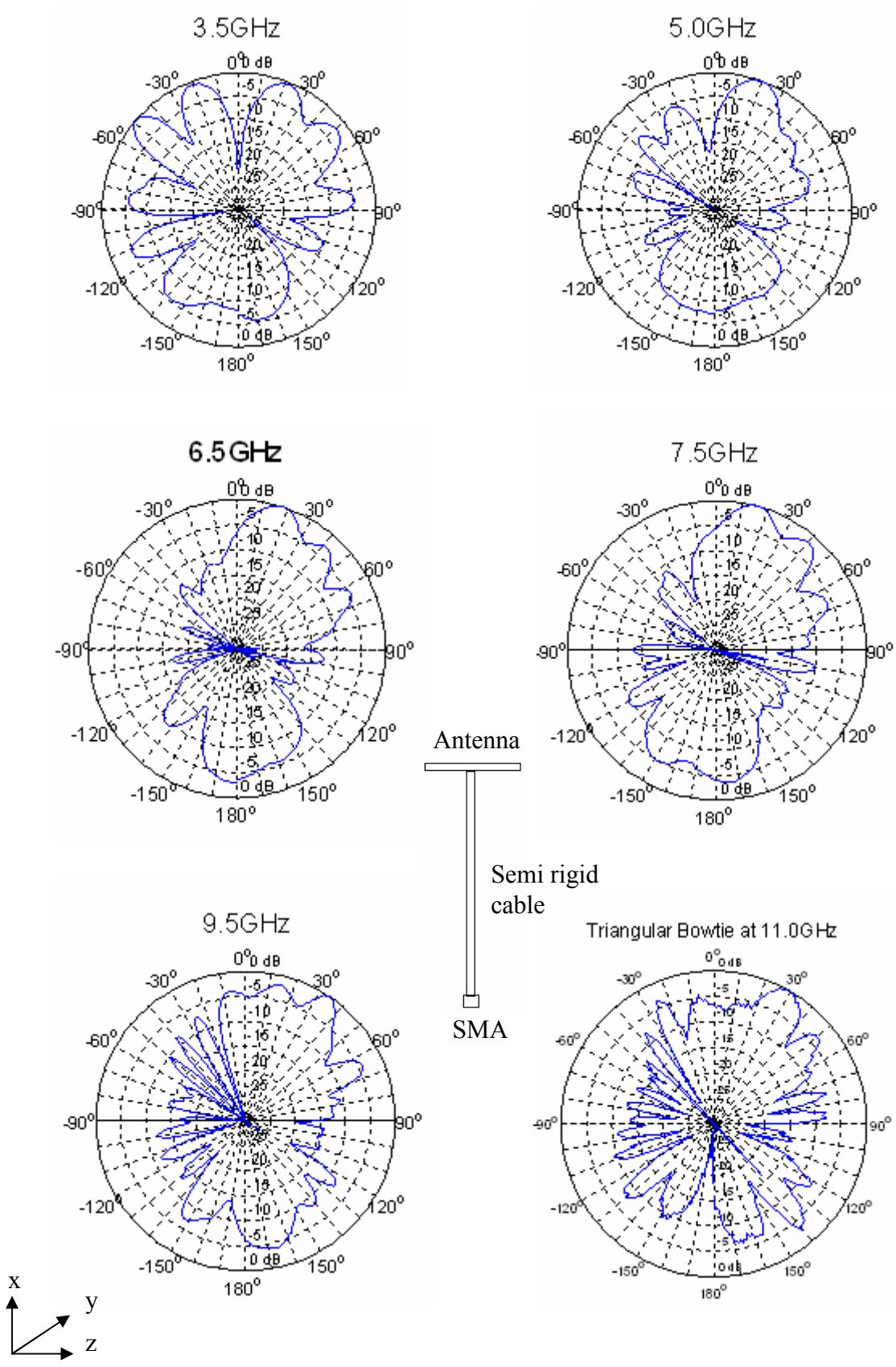


**Fig.3.12.The measured radiation patterns of the triangular bowtie antenna in TH-RH (y-z plane).**

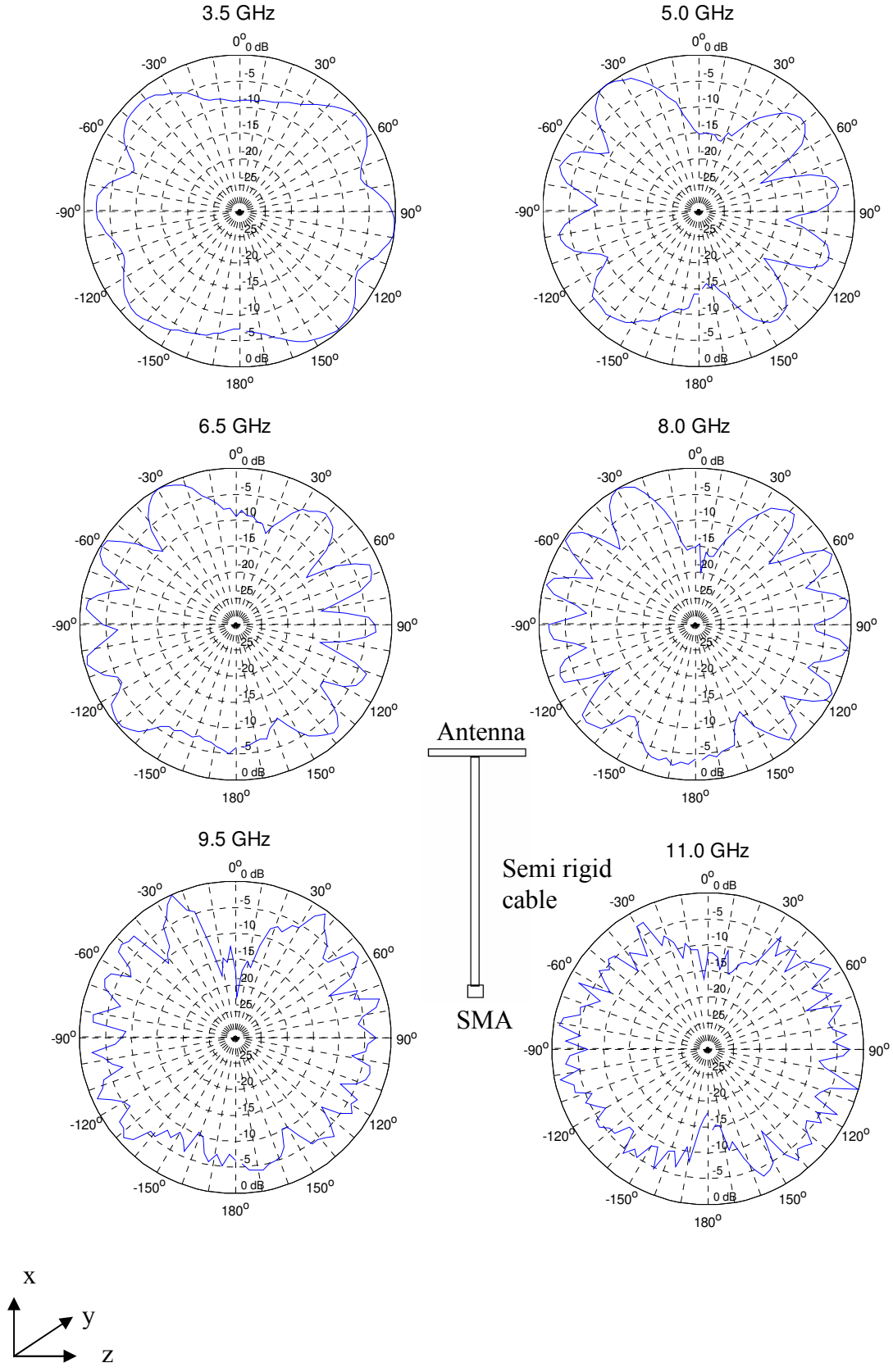


**Fig.3.13.The measured radiation patterns of the triangular bowtie antenna in TV-RV (z-y plane).**

## 3.4. Essential Propagation Parameters and Procedures to Characterize the Channel

The $S_{21}$ data is recorded from the VNA and then stored in a text format into the computer. Then it is processed in MATLAB software by producing a 3D matrix of *Nx* x *Ny* x $F_p$ (e.g. for 125 points in each direction, the matrix would be *125 x 125 x 1601*). In this way each direction can be processed for all the frequencies respectively. The following sections present the definitions of the different procedures and types of analyses carried out to characterize the UWB channel. This section included the definitions of the channel impulse response (CIR), root-mean-square (RMS) time dispersion parameter, path loss (PL), small scale fading, Ricean K-Factor and Shannon's capacity.

### 3.4.1. Multipath Channel Impulse Response (CIR)

When the channel is excited with a pulse, the received waveform is a summation of modified pulses with different attenuation factors and time delays. The received waveform is referred to as multipath profile and the individual pulses are referred to as multipath components because they arrive at the receiver via different paths. In the scenarios encountered in the study, the vast majority of the energy comes from these multipath components from signal reflections. The complex channel transfer function at each grid location is recorded according to:

$$H(x,y,f) = \alpha_{x,y,f} e^{j\gamma_{x,y,f}} \tag{3.1}$$

where $\alpha_{x,y,f}$ and $\gamma_{x,y,f}$ are the measured magnitude and phase responses at frequency *f* on grid position of the antenna *(x,y)*. This complex transfer function is then converted to the impulse response using the Inverse Fourier transformation [54, 55], i.e.

$$h(x,y,\tau) = \alpha_{x,y,\tau}\delta(\tau - \tau_{x,y,\tau})e^{j\gamma_{x,y,\tau}} \quad (3.2)$$

where $\tau_{x,y,\tau}$ is the time delay at every location in the grid and δ is the Dirac delta function [90]. The Power delay profile (APDP) is the spatial average of $|h(x,y,\tau)|^2$ over a local area. By making several local area measurements (TX grid) in different locations, it is possible to build an ensemble of power delay profiles, each one representing a possible small-scale multipath channel state [48].

One model to characterize the multipath channel is the discrete-time impulse response model. In this model, the delay of the multipath defined as τ is segmented into equal time delays called bins [42]. Each bin has a time delay equal to $\Lambda_\tau = \tau_{i+1} - \tau_i$. Any numbers of multipath components received within the *i*th bin are represented by a single resolvable multipath, having a delay $\tau_i$ [48]. The relative delay of the *i*th multipath as compared to the first arriving component is called *excess delay* and if the total number of possible multipaths is *N*, the maximum excess delay would be *N* x $\Lambda_\tau$. The reasonable bin size is the specific measurement's time resolution since two paths arriving within a bin cannot be resolved as a distinct path. Our frequency band is between 3-11 GHz, meaning a time resolution of 125 ps.

In terms of multipath detection in the PDP, Fig.3.14 shows an example of this phenomenon in between an established threshold of 50 dB from the first detected path. This threshold is established once the received power becomes negligent. Figure 3.15 shows an example of power delay profile (PDP) in its first 6ns, where it can be appreciated in this time resolution. However, the 125 ps of time resolution do not correspond to the actual multipath detection established by our MATLAB code. In this code a path is only considered detected when the signal has greater magnitude than the previous and following paths. This path is

called “maxima multipath”. This is to make the detection simpler, where a multipath energy capture can be used as a basic measure of rake receiver’s [92] performance.

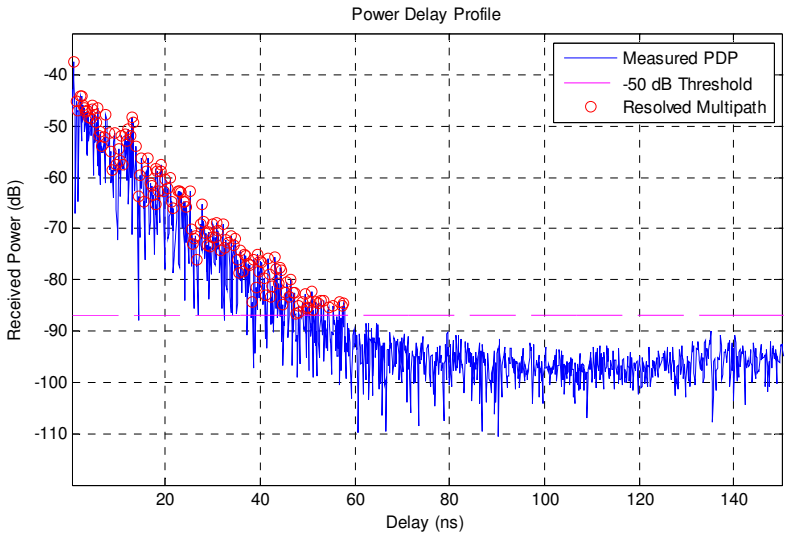


**Fig.3.14. An example of detection of the multipath inside an established threshold**

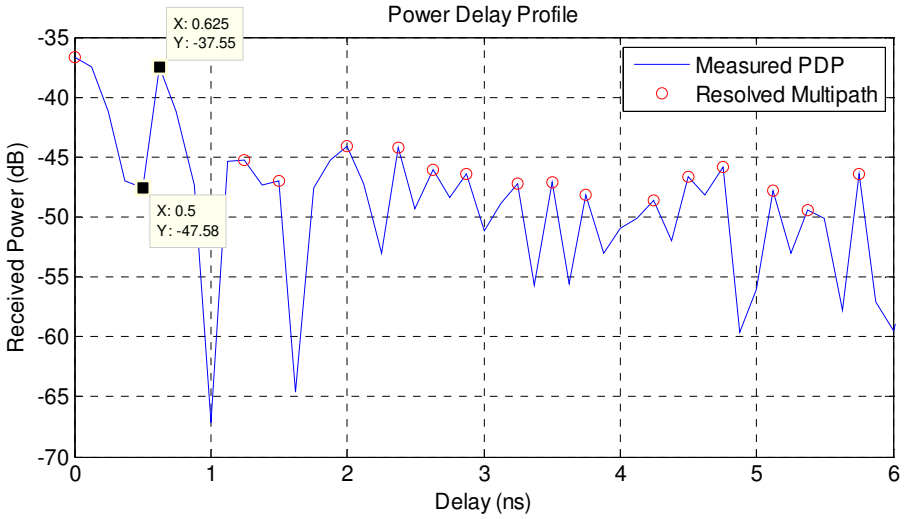


**Fig.3.15. Example of PDP in its first 6 ns of multipath detection**

### 3.4.2. Time Dispersion Parameters

One of the most common time dispersion parameters is the *mean excess delay,* defined as the first moment of the Power Delay Profile (PDP) [93], i.e.

$$\bar{\tau} = \frac{\sum_{i=0}^{N-1} \alpha^2{}_i \tau_i}{\sum_{i=0}^{N-1} \alpha^2{}_i} \tag{3.3}$$

where $\alpha_i$ in Equation (3.3) are the $\alpha_{x,y,f}$ in Equation (3.1). Another parameter is the *RMS delay spread*, defined as the square root of the second central moment of the power delay profile [93]:

$$\tau_{RMS} = \sqrt{(\overline{\tau^2} - \bar{\tau}^2)} \tag{3.4}$$

Different authors in UWB measurement campaigns only employ the delay spread $\tau_{RMS}$ to evaluate the time dispersion of the UWB pulses [94-96]. Thus, $\tau_{RMS}$ will be the only time dispersion parameter considered to present in this study. UWB measurements, such as the ones in [56, 94-96], show that this parameter increases with the increasing of the TX-RX separation distance. This phenomenon is discussed in Chapter 5.

### 3.4.3. Channel Fading: Power Loss Characteristics

#### *3.4.3.1. Path Loss (PL)*

Path Loss (PL) results from an increasing surface area of a wave with propagation outwards from the TX antenna compounded by the scattering behaviour of objects distributed between both antennas (in addition to refraction, reflection, diffraction and/or absorption). PL is defined as the inverse of path gain, i.e. the transmitted power divided by the average received power at the RX antenna.

The propagation of path loss (PL) depends on the distance between TX and RX ($d$) and the transmitted frequency ($f$). Path loss modelling can be simplified by assuming that the frequency and distance dependence are independent of each other [11, 26, 48, 97, 98]:

$$PL(f,d) = PL(f)PL(d) \tag{3.5}$$

The frequency dependence of the path loss is given as [11, 26, 48]:

$$\sqrt{PL(f)} = f^{-2k} \tag{3.6}$$

where $k$ is the decay factor.The distance dependence is usually modelled as power decay law:

$$PL(d) = PL(d_0)(\frac{d}{d_o})^{-n} \tag{3.7}$$

where $n$ and $PL_0$ are respectively the path-loss exponent which shows the rate at which the PL increases with distance $d$ (TX-RX separation) and the intercept point which is the PL at $d_0$ (a reference distance). This path loss exponent ($n$) depends on the environment, therefore depending on the nature of the scenario (NLOS or LOS), this value will vary among different ranges. Although Molisch *et al.* demonstrated in their IEEE 802.15.4a channel model [26] that this PL model of Eq (3.7) fits all different types of environments, it is considered that in a smaller and more complex encasement, this model might be unhelpful. PL results are investigated in Chapter 6.

#### *3.4.3.2. Small Scale fading*

Small-scale fading describes the fluctuations of the received amplitude, phases, or multipath delays of a radio signal over a short duration or in the spatial neighbourhood at the moving antennas' location, so that the large-scale path loss effects may be ignored [48]. This definition can be applied to UWB communication as constructive and destructive interference of the multipath components due to a small change in the location of the antenna. In UWB small-scale measurements it is shown that the UWB channel's small scale-fading depends mostly on environment type and the bandwidth of the signal, where different distributions can be applied [74]. In Chapter 4 a very detailed explanation of this phenomenon inside very

small confined environments is presented and Chapter 6 contents the empirical results of this phenomenon.

For UWB channels the IEEE 802.15.4a model proposes that the m-Nakagami distribution is suitable for modelling the radio links [26]. The probability density function of the m-Nakagami distribution is given as follows:

$$pdf(x) = \frac{2}{\Gamma(m)}\left(\frac{m}{\Omega}\right)^{m} x^{2m-1} e^{-\left(\frac{m}{\Omega}x^{2}\right)} \tag{3.8}$$

where $x$ represents the relative attenuation of the channel compared to the local mean, $m \geq 1/2$ is the Nakagami m-factor, $\Omega$ is the mean-square value of the amplitude and $\Gamma(m)$ is the gamma function. The Nakagami distribution covers a wide range of fading conditions; when m = 1/2, it is a one-sided Gaussian distribution and, when m =1, it is a Rayleigh distribution [48]. So this study, in order to model a given set of empirical data, the *m-parameter* from data will have to be calculated as follows:

$$m = \frac{\Omega^{2}}{E[\left(X - \Omega^{2}\right)]} \tag{3.9}$$

where the *m-parameter* typically decreases with delay, but to simplify the description, it is chosen deterministically. This means, that for a given bandwidth, a constant *m-parameter* is calculated.

### 3.4.4. Shannon's Capacity

Shannon has shown that, theoretically, it is possible to transmit information over a given channel with an arbitrary small error probability if the data rate is not higher than the channel capacity [35, 62]. Today, with coded modulation schemes it is possible to transmit

with data rates quite close to channel capacity. Therefore, channel capacity $C$ is one of the most important parameters of a transmission system, which is calculated as [99]:

$$C = \sum_{n=1}^{N} B \log_2(1 + SNR_{source} \times |H(n)|^2) \tag{3.10}$$

where $B$ is the bandwidth used in each frequency point (8GHz/1601 points = 5 MHz), $|H(n)|^2$ represents the $S_{21}$ magnitude measured with the VNA and *SNR* is the Signal to Noise ratio at the source, considered in this study to be 25 dB due to the possible electromagnetic interference (EMI). However, a higher value of *SNR* would be also quite realistic for higher frequencies where clock signals and their harmonics are weak (see section 3.5). This author is aware of that noise should be associated with detector rather than the source. However, the way to calculate channel capacity in Eq.(3.10) is sufficient and used by other authors [99].

### 3.4.5. Ratio between Dominant Path and Reflections (Ricean K-Factor)

The Ricean K-factor was utilised to discriminate between line-of-sight (LOS) or dominant path and non-light-of sight (NLOS) scenarios in this study (reflections). It is defined as the ratio of the power received in the fixed component, to the total power received via indirect scattered paths. Knowledge of the Ricean K Factor is important in the understanding of wireless channels: low K values indicate high signal reflection, whilst high K values occur in the setting of a free space path where only the direct components exist. The link between Ricean K-Factor and multipath suggests a link between performance and path geometry [75]. It will be presented using Cumulative Distribution Functions (CDFs), which describe the probability that a real-valued random variable 'x', with a given probability distribution, will be found at a value less than or equal to 'x'.

## 3.5. Electromagnetic Interference (EMI)

This last section of the chapter aims to show the influence of, and solutions to, Electromagnetic Interference (EMI) on the bandwidth used in this study. Background EMI originating within the chassis can limit the wireless link budget and therefore the maximum channel capacity achievable. To evaluate the magnitude of the interference, a bench test was run that fully stressed the I/O interfaces (ie. all resources utilised maximally), flooding the environment with the maximum possible radiated interference. A spectrum analyser was utilised to evaluate the generated interference levels from 0-6 GHz once the computer was off and again once powered on. The bow-tie antenna was located in the three different positions inside the PC where the RX is placed for the whole measurement campaign. In addition, the RX antenna was located in a fourth location just outside the PC in the back wall to measure the possible interference and radiation emitted by the PC. Figure 3.16 shows these EMI effects.

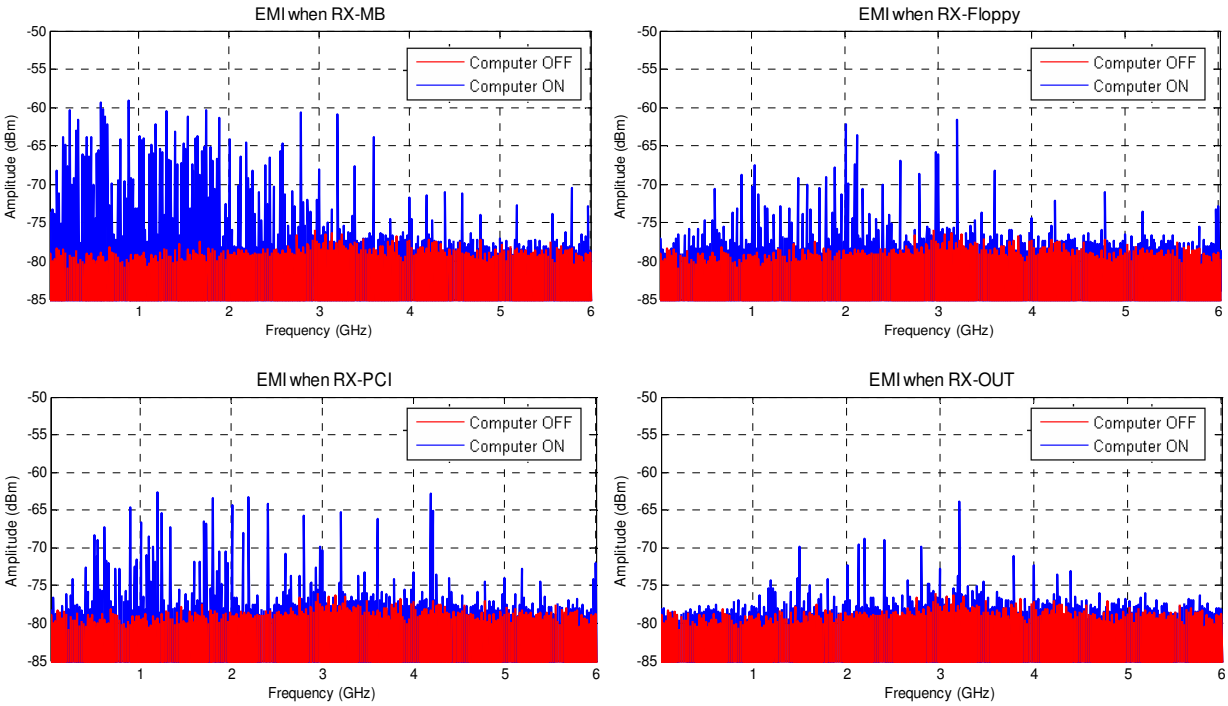


**Fig.3.16. Measured EMI from 0-6 GHz for different locations of RX when computer on/off**

Figure 3.16 shows that narrowband interference was found mainly between 0.3-3.2 GHz, with the largest signal peak occurring at 3.2 GHz (-60 dBm). A second peak was noted

at 3.2 GHz, corresponding with the clock frequency of the microprocessor. Subsequent interference patterns were harmonic, corresponding to multiples of the 0.3-3.2 GHz band, such us 4 GHz, 4.2 GHz, 4.4 GHz and 4.8 GHz. However, even the multiple harmonics of the 3.2 GHz frequency appeared negligible in terms of signal interference.

Entirely as expected, the degree of interference is highest with the RX placed adjacent to Microprocessor (MB), where the RX is in the near field of the MB, and lower when located next to the Floppy disk. No more than -60dBm of power noise is detected, equivalent to <1nW of power. One solution to avoid this background noise power would be to transmit the UWB signal with a much higher power, such as 1mW (0 dBm). This would correspond to a SNR of 60 dB. Since the standard Bluetooth case 3 for reception within a range of 1m [27, 28] uses this power to transmit, it does not look unachievable at all to use this power for transmissions. Even 1μW (-30dBm) would suffice, since the experiments in this study show a tolerance of a SNR of 25 dB.

Figure 3.16 also demonstrates that background EMI attenuates at frequencies higher than ~ 4 GHz, suggesting that beyond this level UWB transceivers will encounter significantly less interference, and supporting the use of higher frequencies for wireless communication inside an enclosed PC environment. A final observation is that, with the RX located just outside of the PC, very little EMI is detected, the only narrowband interference being that corresponding to the clock frequency of the microprocessor at -65 dBm.

This author is aware that future standard PCs might have more powerful microprocessors which could translate to interference at higher frequencies within the UWB wireless bus bandwidth. Therefore, another possible solution could be to use a mask that eliminates the narrowband interference after these become significantly high (i.e. -70 dBm). The actual interference harmonics have a bandwidth of 20 MHz, thus we could create a mask of 50 MHz. In the case of EMI when RX-Floppy, there are 3 strong interference peaks within

the bandwidth with greater power than -70 dBm, therefore this mask should be applied three times. This means a reduction of the overall bandwidth of 150 MHz. Since the calculated Shannon capacity in (3.10) depends of the bandwidth, a reduction of the maxima data rate will appear. However, this has an almost negligible effect to the overall aggregate capacity where the use of this mask reduces the bandwidth by less than 1%. Therefore, the use of a mask at the receiver could be a good solution to avoid the EMI, which has minimal effect on the maxima capacity of the channel when high bandwidths are used. In contrast, complexity of the design of the transceiver would be increased substantially for these purposes.

# Chapter 4: Wave Propagation in Small Confined Environments

## 4.1. Introduction

One of the basic issues of such small confined environments (<10 wavelengths) is the fact that their wave propagation properties are fundamentally different due to the high number of multipath components. The main study in which this chapter is focused on is the issue of frequency selective fading in this type of environments, especially on the general dependency of fading as a function of size of the environment. Another proposal presented is the hypothesis that the confined environment acts as a resonator. Once the size of the environment is reduced to the level when the dimensions are comparable to the individual wavelengths (<10λ), the number of multipaths becomes so large that the environment acts as a resonator. Therefore, this chapter explores the relationship between the performance of a communication system and the combination of the size of an environment, the transmission frequency and bandwidth.

The structure of this section is as follows. Firstly, the dependence of fading with bandwidth is demonstrated by a simple two-ray channel model. Then, the change of fading's impact with the size of the environment is quantified. Ray-tracer simulations for 4600 different confined environments are conducted to quantify the severity of fading effects as a function of the size of cubic environments. The hypothesis of a hybrid resonator is also presented, again quantifying the minimum bandwidth required in terms of modal spectrum. Finally, electromagnetic simulations are also performed to further quantify these various influences.

## 4.2. Size-Dependent Modelling of Fade Depth

### 4.2.1. Introduction

In wireless communications, fading represents the main contributor towards frequency selectivity. Defined as the measure of the channel energy's variability over a small region in space, fading is caused by the superposition of multipath components at the receiver [100]. In most applications, it is desirable that the data rate should not change for small movements of the TX or RX [101], and it is therefore essential that fading within the system is reduced to a minimum. Many researches have shown that fading is less severe for wideband systems due to the fact that fading is due to interference between arriving multipaths [102-105], where the further increase in bandwidth the greater multipath resolution is obtained and therefore the time-of-arrival estimate for the direct path becomes progressively more accurate; thus, the impact of fading is least for larger bandwidth systems.

A popular way to manage the impact of fading and frequency selectivity is to include a fade margin into the link budget. By doing so, the receiver still has an acceptable signal-to-noise ratio (SNR) - even in the case of terminals located at a minimum in the channel transfer function – and the required fade margin is inversely proportionate to the transmission bandwidth. Thus, UWB wireless systems are inherently less affected by frequency-selective fading than narrowband transmission, this effect being known as 'fade depth scaling'.

Fade depth scaling relates the variation of the channel energy to the signal bandwidth. Malik *et al.* defines fade depth in [102-105] as three times the standard deviation of channel energy for a small spatial variation of the receiver/transmitter. If this value is included as a fade margin to the link budget, in more than 99% of cases the receiver energy will be sufficient.

Another solution to reduce the impact of fading is also the use of spreading over frequency. As explained in Chapter 2, WiMedia alliance uses Orthogonal Frequency Division Modulation (OFDM), where one information bit is modulated onto several carriers [31, 106]. Such techniques improve performance through exploiting increased frequency diversity and also help to protect against the frequency selectivity of the channel.

In conclusion, fading is a well known phenomenon, but the relationship between its severity and the size of the environment is an interesting area not fully understood; this section therefore explores the limitations on environment size imposed by frequency selectivity.

### 4.2.2. The severity of Fade Depth in Small Confined Environments

In this section, a model is developed to investigate the influence of bandwidth and size of the environment on frequency selective fading. The simplest such UWB wireless link model consists of two pulses arriving at the receiver as illustrated in Fig. 4.1, which shows the normalized impulse response of such channel.

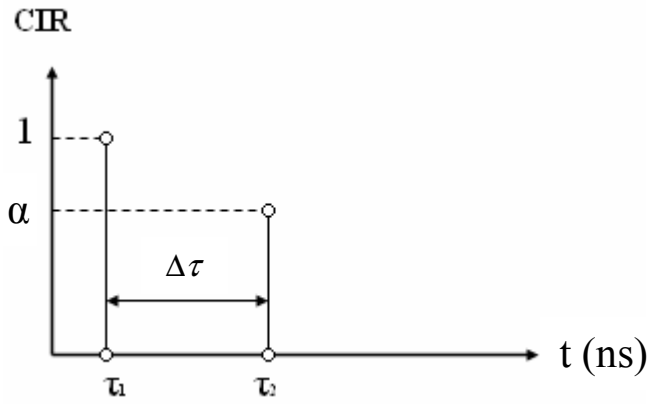


**Fig. 4.1 Two-pulse model - channel impulse response**

where $\Delta\tau$ is the delay between rays, and (1 – α) describes attenuation of the second pulse relative to the first as a result of $\Delta\tau$ (note, this can be a negative value). The square modulus of the transfer function of such a channel for an arbitrary frequency is given as follows:

$$|H(f)|^2 = |1+\alpha e^{j2\pi f\Delta\tau}|^2 = 1+\alpha^2+2\alpha\cos(2\pi f\Delta\tau) \tag{4.1}$$

Then, for a wideband wireless channel, the energy can be calculated as:

$$\int_{f_c-BW/2}^{f_c+BW/2}|H(f)|^2 df = BW(1+\alpha^2)+\frac{\alpha}{\pi\Delta\tau}\{\sin(2\pi\Delta\tau(f_c+BW/2)-\sin(2\pi\Delta\tau(f_c-BW/2))\} =$$

$$= BW\{(1+\alpha^2)+\frac{2\alpha}{\pi\Delta\tau}(\sin(\pi\Delta\tau BW)\cos(2\pi\Delta\tau f_c)) =$$
$$= BW\{(1+\alpha^2)+2\alpha\{\sin c(\pi BW\Delta\tau)\cos(2\pi f_c\Delta\tau)\} \tag{4.2}$$

where $BW$ represents the bandwidth of the channel around the centre frequency $f_c$. The physical reason for fading can be visualized from the last part of the Eq. (4.2). If a small displacement of the transmitter or the receiver occurs, the delay between the two rays will change, having an impact on the channel energy because the value of the cosines and *sinc*-term changes. Changes of the coefficient α will not be considered because, by definition, fading is a random variation of energy for small displacements, which is too small to result in a significant variation of the path loss. Thus, α is approximately constant and its effect is negligible compared to the delay $\Delta\tau$. The first term inside the braces, $(1+\alpha^2)$, is independent on bandwidth $BW$. The second term, $2\alpha\{\sin c(\pi BW\Delta\tau)\cos(2\pi f_c\Delta\tau)$, depends on $BW$ and as the bandwidth increases, its contribution to the sum is reduced with the amplitude of the *sinc*-

function[1]. In contrast, if $BW$ gets smaller (product ($\pi BW\Delta\tau$) approaching zero), the value of the *sinc*-function approaches one. Therefore, the maximum variation of the channel energy due to the variation of $\Delta\tau$ is given by the ratio $2\alpha/(1+\alpha^2)$. Moreover, the parameter α, which describes the relative attenuation of the second ray, will be higher, increasing the variation of the channel energy. The attenuation will be higher in a small confined environment because the reflection losses of the metallic walls will be lower than in other cases where walls are made of concrete or brick. Also, the reduced delay between the two rays contributes to the relative increase of α. Thus, relative increases of this factor also contribute, according to Eq.(4.2), to the increase of severity of fading.

In contrast to the above theoretical model, in a real set up a higher number of multipath components would be expected, this increasing the complexity of the analyses given above Eq.(4.1)-(4.2). Nevertheless, for an estimation of the effect of environment size on fading, the two pulse model is sufficient because it corresponds well to a previously published investigation [107].

In small confined environments, the average delay between the rays is reduced due to the smaller inherent internal dimensions. Therefore, to reduce the effect of fading, a larger bandwidth is required. Whilst the effect of fading is negligible for an infinite bandwidth, it is of interest to consider the relationship between the minimum possible bandwidth ($BW_{\min}$) to maintain fading below a certain level for a given environment size. The mean delay between two consecutive pulses will define the largest $BW_{\min}$. From a simple geometrical consideration, this delay will increase linearly with the size of the room, since wavefronts travel longer distances to reach their destination. Considering enclosure volume, *V,* the dependency can be expected to be proportional to $\sqrt[3]{V}$. As a result, it can be concluded that

[1] $\sin cx = \dfrac{\sin(\pi x)}{\pi x}$

the $BW_{\min}$ required to resolve all multipaths is inversely proportional to cubic root of the volume of the environment. Thus:

$$BW_{\min} \propto \frac{1}{\Delta\tau} \propto \frac{1}{\sqrt[3]{V}} \tag{4.3}$$

To conclude, the simple two-ray model confirms that, in confined environments, the effect of fading will be more severe than in other, larger, indoor environments. In order to prove this statement, in the following section a ray tracing study is conducted to quantify the severity of fading as a function of environment size.

## 4.3. Ray-Tracing Study: Tiling technique

The basic model used to study wave propagation is ray tracing, and while this approach has been used for indoor radio propagation in indoor [108-111], the majority of these involve narrowband systems, and only limited attempts have been made to predict the UWB characteristics in indoor environments [112].

In this section, a simple model to approximate our scenario is constructed using a 3D ray tracing technique [113]. This ray tracing technique is a ray optical method that assumes quasi-optical propagation of radio waves, so this assumption is fulfilled if the wavelength is much smaller than the size of the reflecting objects. Simple indoor radio propagation models usually consider only reflection [114]. A simple rectangular box is considered with reflective walls whose reflection coefficient 'r' can be varied to model the losses. The fact that the wavelength has to be much smaller than the objects presented inside the cavity mean that

very small pieces were not considered to be included since our smallest wavelength is 3 cm. The terminals are not located at anytime in their near field area[2].

The setup of the ray tracing model is based on the *tiling* technique [113]. In this method, virtual rooms extend in an infinite 3D space containing virtual sources which represent the actual source reflected in the cavity's walls. Rays up to 6 bounces are considered using this tiling algorithm, in which copies of the rectangular case are used to determine the impulse response of the channel in the time domain. The magnitude of these impulse responses is given by the multiplication of two factors: one is the distance *d* that the wave travels from TX to RX, given by the power square law [115], and the other is the number of reflections taken by the propagating waves before reaching the RX. The ray tracing algorithm is described in more detail in [113].

To test the hypothesis that frequency selective fading becomes more severe in confined environments, extensive ray tracing simulations of small confined environments are conducted. A total of 4,600 environments were modelled, with each environment consisting of a rectangular box. The dimensions of the box are given as: $rand_1 b \times rand_2 b \times b$ where $rand_i$ are random variables with uniform distribution from the interval (1,2). In total, 100 different pairs of $rand_1$ and $rand_2$ are generated. The length parameter *b* is swept in 45 steps from 0.25 m to 4 m, where the steps are logarithmically distributed.

The position of the transmitter and receiver is selected as follows: the RX is placed to a position *[0.25b; 0.9b; 0.5b]*. The TX selected varied in a square grid in the horizontal *x-y* plane of 20×20 points spaced by 1 cm. The centre of the grid was at *[0.75b; 0.65b; 0.4b]*. The transfer functions are determined for the frequencies 1 - 11 GHz. Then the fade depth

[2] $R = \frac{2D^2}{\lambda}$ where *R* is the distance between antennas, $D$ is the antenna diameter and λ is the measurement wavelength (longest of the ones tested)

scaling with bandwidth is determined at centre frequency of 6 GHz in the way as it was presented in [102-105]. The CIR for a given bandwidth is calculated for each position of the receiver.

The local area in this study is defined by maximum displacement of 4 cm in both directions, thus 81 measurement points. It must be noted that the selection of the local area is essential. It cannot be too large because while movement by 4 cm is negligible for $b$ larger than 2 m in terms of change in path loss for the direct path, it is significant for the smallest $b$ = 0.25 m. On the other hand, if the area is too small, the area will not contain the full variation of the path loss caused by the multipath superposition.

In selecting the reflection coefficient 'r', an estimated value of 0.9 was chosen, where a very high reflective environment is expected due to the metallic structure of the walls (i.e. PC Tower case). For the sake of simplicity, the reflection coefficient is assumed to be constant for the whole band, where in real scenarios this might not be the case, but this simplification reduces significantly the computational effort with no significant impact on the results.

Among all of that, more exhaustive ray-tracing methods could provide a more accurate estimate of the channel, but again these are computationally intensive and thus impractical for simulating very complex structures such as PCs. That means that, even though the obtained solutions are not fully exact, the channel behaviour can be still modelled in a realistic way.

### 4.3.1. Analysis of Simulations

The first simulation examines fade depth calculations for several rectangular cavities, or rooms, these are characterised by their volume ($V = b^3$), and presented in Fig. 4.2.

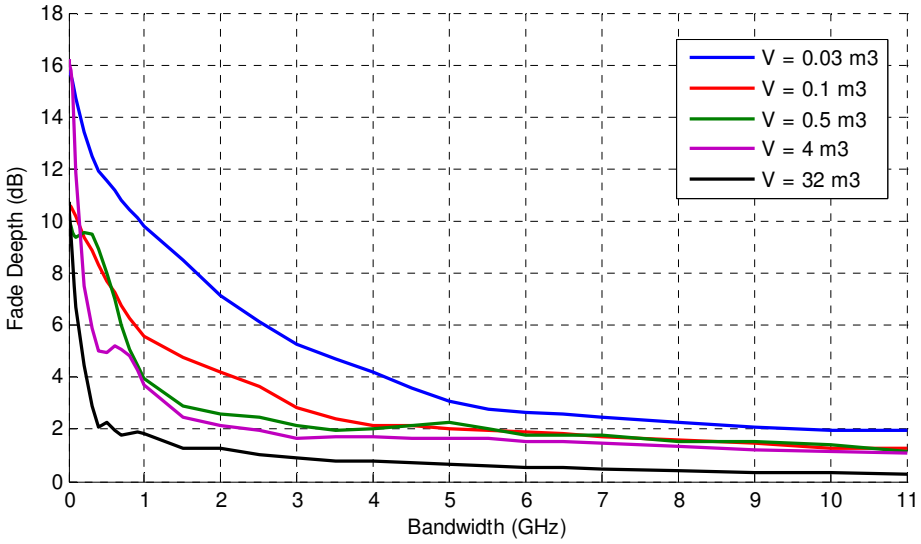


**Fig. 4.2 Fade depth scaling with variable bandwidth for varying room size**

Firstly, it can be appreciated in Fig.4.2 that for smaller volumes of the rectangular cavities there is an increase in fade depth, which verifies the statement of previous section 4.2.2. Also, it is important to note the decrease of this factor as the bandwidth increases. For the case of V = 0.03 $m^3$, which roughly corresponds to the volume of standard PC Tower case, the fade depth for 500 MHz of bandwidth (i.e. wideband) is around 11 dB, which is much higher than the corresponding ones in ECMA UWB standards (0-6 dB) for similar volumes [116]. Therefore, the results suggest that for very small confined environments such as computers, new standards with increased fade margins might have to be developed to mitigate the issue of frequency selective fading, as it was confirmed by tests in [117].

The model for fade depth scaling is presented in [105, 107] and in this section it is used to study the dependencies on the room size in more detail. For the sake of clarity, the model from [85] is shortly introduced. The fade depth scaling with bandwidth can be modelled with the following formula:

$$FD = A + \frac{B}{1 + C \times BW} \tag{4.4}$$

where *BW* stands for the variable bandwidth; *A*, *B* and *C* are model parameters.

The model and the meaning of parameters is presented in Fig. 4.3, using data taken from [105, 107], which shows the measured fade depth as a function of bandwidth and the fit according to the model from Eq. (4.4).

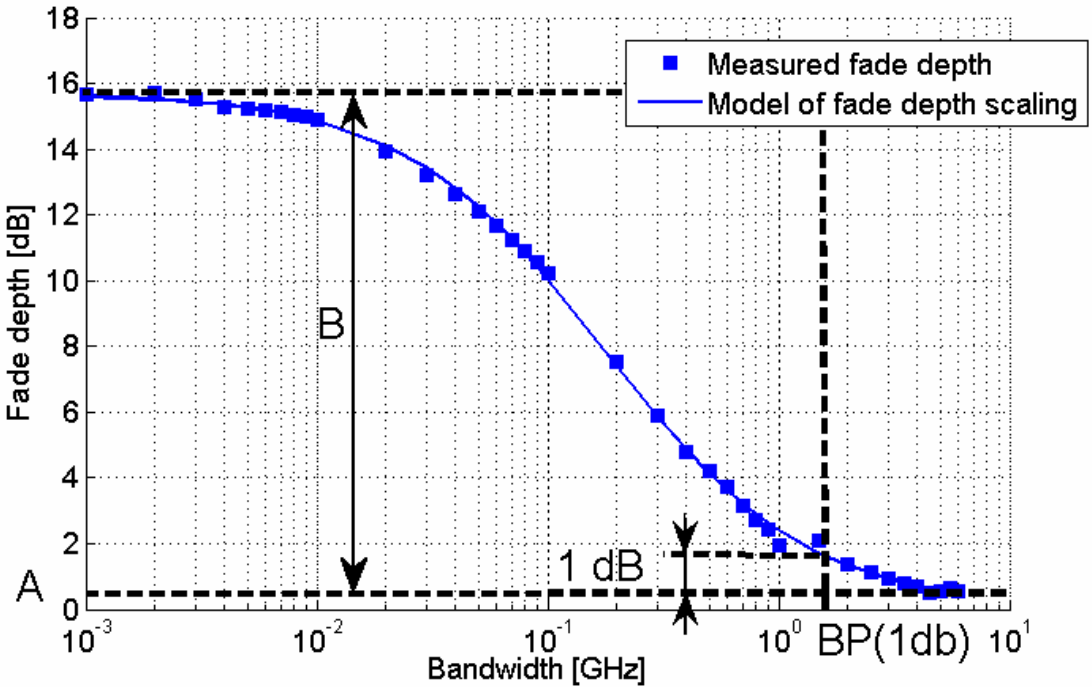


**Fig.4.3. Fade depth scaling model (data set is from [105, 107])**

The parameter *A* represents the minimum fade depth for infinite bandwidth. The second parameter *B* describes the difference in fade depth between narrowband and wideband channels. It can be understood as a penalty that narrowband channels have to pay in the form of fade margin that must be included in the link budget. Reference [105] identifies another important parameter: 1 dB breakpoint bandwidth. This is the bandwidth at which the fade depth increases to 1 dB above the minimum level given by parameter *A* (see Fig. 4.3). It defines the bandwidth above which the channel behaves as a wideband channel with minimum influence from fading.

$$BP(1dB) = \frac{B-1}{C} \tag{4.5}$$

The resulting dependency of the minimum fade depth on the volume of a room as determined by simulation is presented in Fig. 4.4.

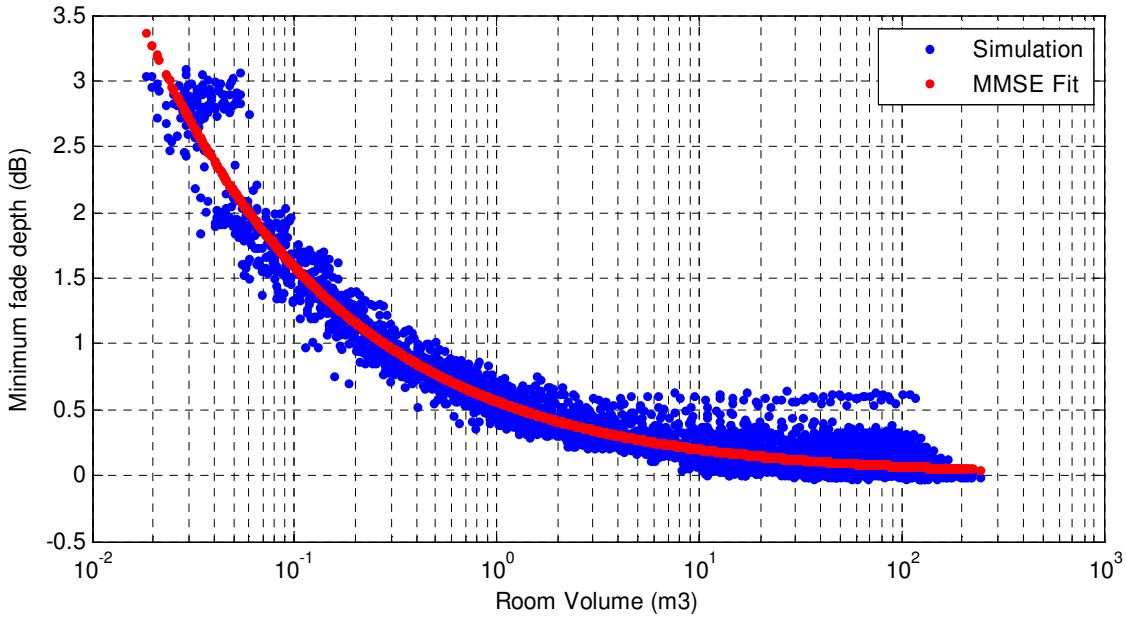


**Fig.4.4. Dependency of minimum fade depth on room volume**

From Fig. 4.4, the minimum level of fading increases exponentially as the room volume is decreased. There are two data plots in Fig. 4.4. The blue dots represent the values obtained for all the 4,600 rooms sorted by their volume. The red dots are the best fit of the data based on minimum mean square error (MMSE) fitting. This fit is used to emphasize the trend of the data. Then, the equation of the fit is:

$$A = 1.21V^{-0.292} \tag{4.6}$$

The increase of the minimum fade depth for small rooms may be attributed to the fact that for the smallest room, the fixed local area of 81 points already contains the impact of path loss dependency on distance whereas this dependency is negligible for larger rooms.

Furthermore, for smaller rooms, larger bandwidth is required to reach the minimum fade depth.

The ray tracing model results vary. This is because the relative positions of transmitter and receivers to the walls, and other reflectors, are random, and therefore so too are the fade depth scaling curves. Parameter *A* is used to quantify a random curve; hence it is a random variable also with mean and variance.

The dependency of the parameter *B* on room volume is presented in Fig.4.5

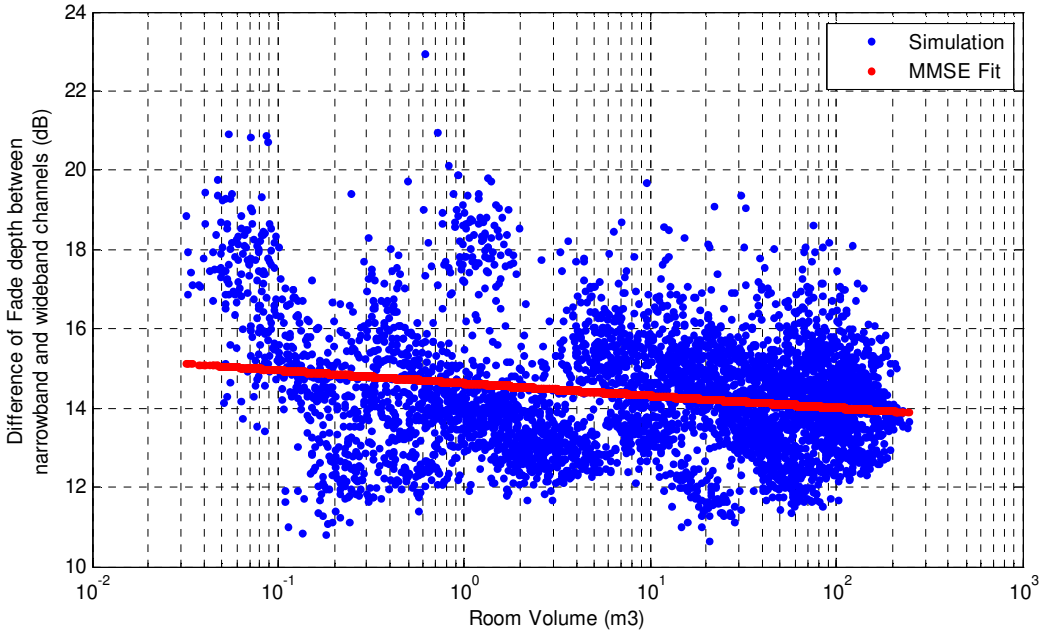


**Fig.4.5. Dependency of fade depth increase on room volume**

Apart from slight deviations from the trend for very small rooms (volumes below 1 $m^3$), this parameter is almost independent on the room volume with dependency given by:

$$B = 14.48V^{-0.009} \tag{4.7}$$

The dependency of the breakpoint bandwidth *BP(1dB)* on the size of the room is presented in Fig. 4.6.

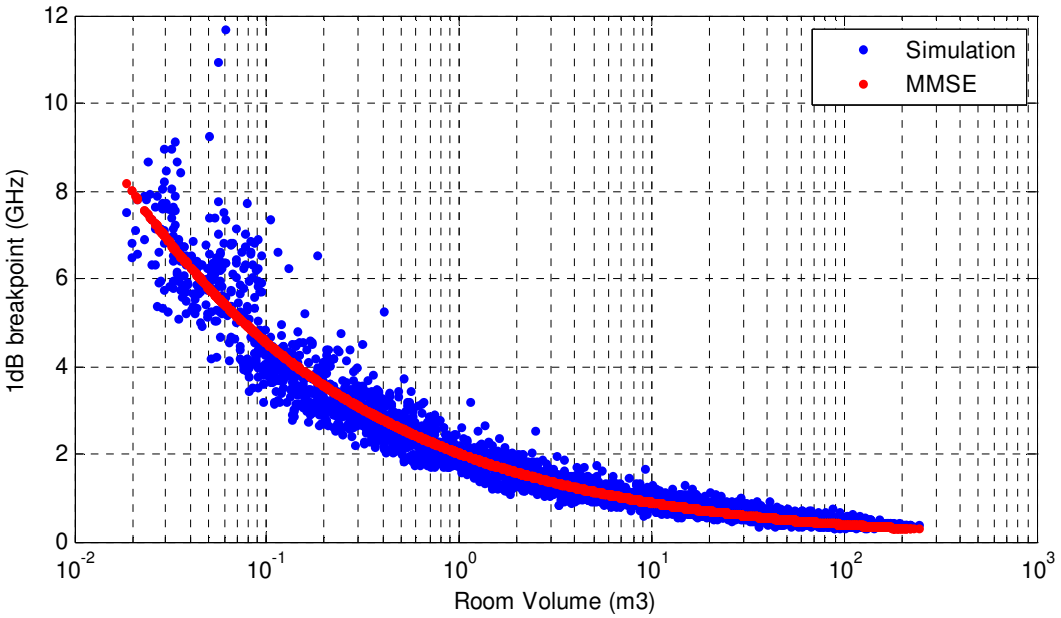


**Fig.4.6. Dependency of bandwidth break point BP (1dB) on room volume**

It can be seen in Fig.4.6 that the bandwidth required for minimizing the effects of fading significantly increases for confined environments. In our case of a PC box with a volume of 0.03 $m^3$ ($\sim 10^{-1.5}$), the bandwidth necessary to minimise the effects of fading would be 6 GHz. However, this assumes an empty PC case, and the optimum bandwidth could be affected by items within the case. For the empty Aluminium case environment, the measurement results are discussed subsequently in Chapter 6.

The trend of the minimum mean square fit (MMSE) is given as:

$$BP(1dB) = 2.02V^{-0.351} \tag{4.8}$$

which corresponds well to the initial model expectation of minimum bandwidth being scaled proportionally to $V^{-0.33}$.

## 4.4. Modal Frequency Selectivity

The preceding section examined frequency selective fading. However, confined environments can also act as a resonator, and this is associated with a second form of frequency selectivity, modal frequency selectivity, which does not occur in electrically large environments. Resonance can affect the performance of a communication system, the determining parameters being the relative ratios between the size of the environment, frequency used and bandwidth used [101], as discussed below.

### 4.4.1. Hypothesis of a Hybrid Resonator

The effect of size reduction implies an increase of the number of multipath components and a reduced delay between consecutive rays. Then, if the size of the environment is further reduced to the level when the dimensions are comparable to the individual wavelengths, the number of multipaths becomes so large that the environment acts as a resonator. This leads to an interesting ambiguity related to the physical size of an environment. On one side, there are environments large compared to the wavelengths ($>10\lambda$) where the wave propagation is well understood as a set of individual rays [26]. On the other hand, when these environments become smaller ($<10\lambda$) then they might act as resonators. Resonator theory is well understood in other fields (for example, electromagnetism [101]). Essentially, a cavity resonator is a hollow conductor blocked at both ends and along which an electromagnetic wave can be supported, and can be viewed as a waveguide short-circuited at both ends. In a resonator, the waves cannot propagate in the standard way. Instead, the transmitter (TX) pumps energy into the resonator, which stores it in the form of electromagnetic field and then the RX draws the energy out of the resonator. As a result, some positions or polarizations of the antennas can hinder proper channel communication; if the

terminals are located at the resonator null point or Node (N), little or no energy transfer occurs, with the converse occurring when terminals are located at the point of maximum interference (A = Antinode). A useful illustration of this is presented in Fig.4.7.

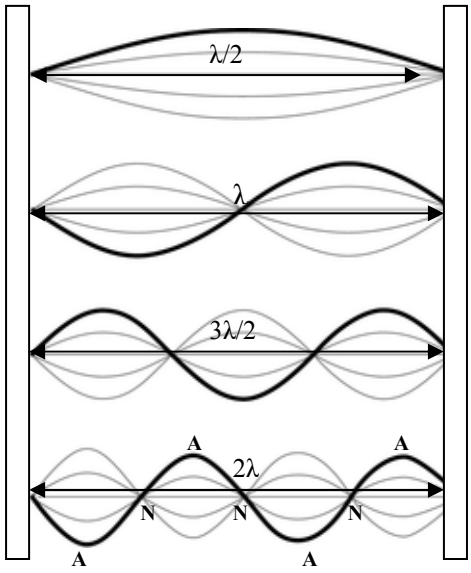


**Fig.4.7. Example of different modes adopted by standing waves inside a cavity**

The behavior of the waves at points of minimum and maximum vibrations (nodes and antinodes) causes constructive interference and results in resonant standing waves. The term 'standing wave' is often applied to a resonant mode of an extended vibrating object, and is caused by constructive interference of two waves traveling in opposite directions. An important aspect of this phenomenon of 'standing waves' is that the wavefront changes phase upon reflection from a fixed surface. Under these conditions, the medium appears to vibrate in segments or regions and the fact that these vibrations are made up of travelling waves is not apparent - hence the term 'standing waves' [118].

'Borderline' environments will act as a hybrid between a resonator and a large environment with wave propagation. Understanding these two influences on the channel is essential, as they may have an impact on the design of future radio systems.

### 4.4.2. Theory of Cube Resonators

To examine resonator behaviour, an ideal lossless cubical resonator is studied with walls with *a* length, which size $S = a$, and the dielectric inside the resonator is air. The resonator frequencies of such cubical resonator can be calculated using the well known relation [101]:

$$f_s = c_0\sqrt{(\frac{m}{2a})^2+(\frac{n}{2a})^2+(\frac{q}{2a})^2} = \frac{c_0}{2}\sqrt{(\frac{m}{S})^2+(\frac{n}{S})^2+(\frac{q}{S})^2} \tag{4.9}$$

where *m* ,*n, q* are integer mode descriptors, *S* is the size of the cubical resonator, $f_r$ is the resonator frequency and $c_0$ is the speed of light in the air. Figure 4.8 shows the possible number of resonant frequencies in a cubic environment across the whole UWB band (3-11 GHz).

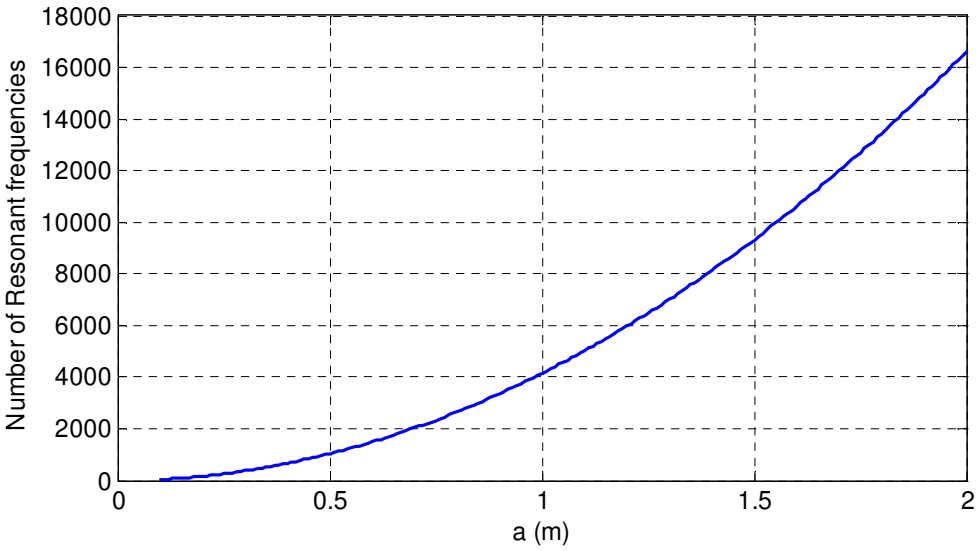


**Fig.4.8. Number of $f_s$ inside a cube cavity for different *a* lengths**

Figure 4.8 is demonstrates the exponential increase in resonant modes with increasing cavity volume. The previous Fig.4.7 showed how difficult good channel communication becomes with decreasing environment size as fewer modes are excited inside the cavity. It

follows that the probability of an antenna being located in a resonator node is larger for smaller cavities.

Now, if *c* and *S* are transformed to the left-hand side, Eq. (4.9) reads as follows:

$$\frac{S}{\lambda_r} = \frac{1}{2}\sqrt{(m^2 + n^2 + q^2)} \tag{4.10}$$

The Eq. (4.10) limits the number of resonator frequencies in the resonator cube. Figure 4.9 presents a graphical plot of the spacing of the individual resonances. For a resonator of relative size $S/\lambda_r$, all the arrows below the value of $S/\lambda_r$ represent modes that can be excited and the frequency distance between them. Arrows above the given size of the environment $S/\lambda_r$ cannot be excited as the resonator is too small for them. The number of excitable modes is represented as Dirac impulse lines.

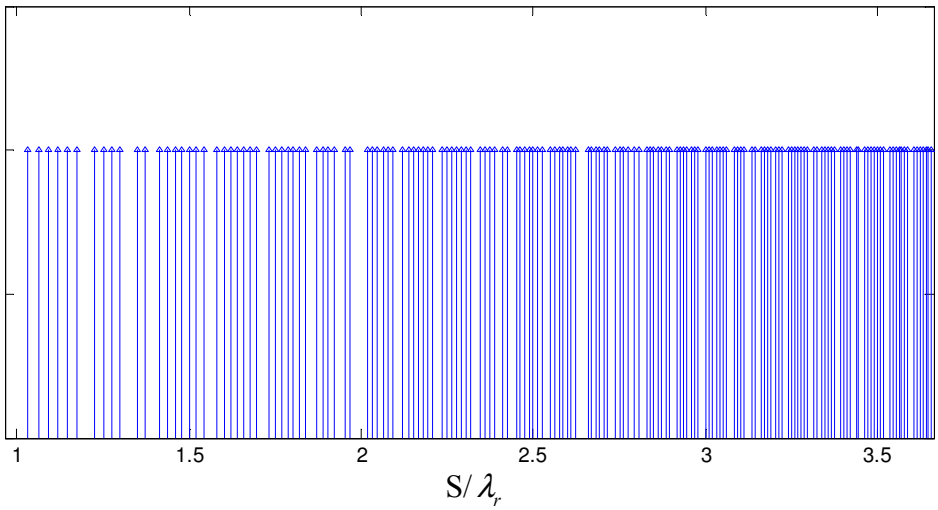


**Fig.4.9.Distribution of the excitable modes relative to the scaled size of the confined environment**

It can be observed from Fig.4.9 that the number of excitable modes, once the relative size of the environment increases, increases, hence the frequency gap between consecutives modes is reduced. This is crucial for the impact on the performance of a communication

system operating in such environment. In an ideal lossless resonator, the electromagnetic field can only be excited at the resonator frequencies. The performance of a communication system depends on the mutual combination of its frequency and bandwidth. Thus, the problem in the communication system is stated as follows with possible solutions to solve it:

- Problems:
    - If the bandwidth and the frequency are such that the spectrum they represent falls between the mode lines (as in Fig. 4.9), then the environment does not act as a resonator, it cannot be excited and no communication can be established.
    - If however the bandwidth and the frequency are such that, the spectrum they represent contains one mode line, then the environment acts as a resonator, and can be excited. However there is a risk that either the TX and/or RX might adopt a mismatched polarisation or occupy a resonant node, and thus be unable to excite the electromagnetic field. As a result, there is a high risk that the communication will fail.
- Solutions:
    - By increasing the number of modes within the spectrum, the probability of the antennas occupying a resonator node or being incorrectly polarised decreases (i.e., the system demonstrates hybrid behaviour).
    - Changing from a small confined environment to a typical environment, (i.e., above $10/\lambda$) significantly increases the number of mode lines within the spectrum such that wave propagation can occur in a standard ray-like manor.

Thus, for a given environment size, these problems identify minimum bandwidth requirements ($BW_{\min}$) to enable effective communication, at least for certain antenna

positions and polarisations. The requisite bandwidth must be larger than the distance between resonances closest to the frequency of the system $f_s$. Thus, if we call $f_{s+1}$ the nearest higher resonance frequency, and $f_{s-1}$ the nearest lower resonant frequency, the $BW_{\min}$ can be calculated as follows:

$$BW_{\min} > f_{s+1} - f_{s-1} \tag{4.11}$$

If we substitute now Eq.(4.10) in Eq.(4.11):

$$BW_{\min} > \frac{c}{2S}\sqrt{(m_{s+1})^2 + (n_{s+1})^2 + (q_{s+1})^2} - \sqrt{(m_{s-1})^2 + (n_{s-1})^2 + (q_{s-1})^2} \tag{4.12}$$

where $m_{s-1} + n_{s-1} + q_{s-1}$ and $m_{s-1} + n_{s-1} + q_{s-1}$ are the mode descriptors for the closest resonance frequencies above and below system frequency $f_s$ respectively. Fig.4.10 illustrates an example of the bandwidth $BW_{\min}$ required to establish a communication in dependency on the system frequency for a fixed size of the environment, where $a$ = 0.5m and $a$ = 1m.

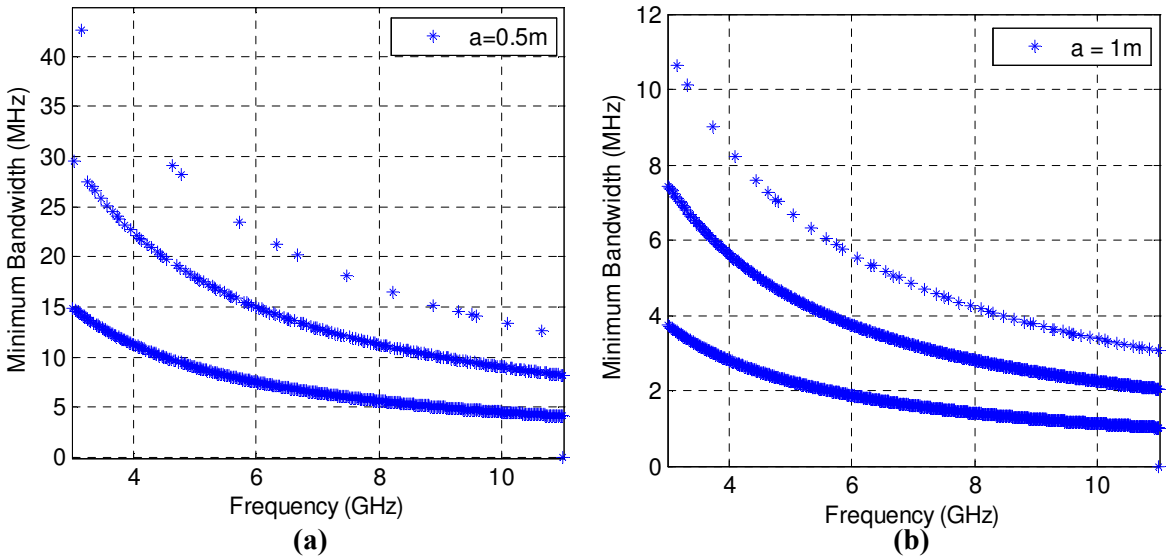


**Fig.4.10. Minimum bandwidth required to establish communication at selected frequencies for a = 0.5 m (a), and a = 1m (b)**

Figure 4.10 does not present one curve; it rather presents three curves for each case. This is due to the fact that the distance between resonances is not monotonously decreasing. This is caused by limited number of the combinations of the three integer modal descriptor. This can be seen even as a 'clustering' of modal lines in Fig.4.9. It can be observed that for larger sizes of the environment (Fig.4.10.b) a smaller $BW_{\min}$ is required in order to establish a communication, due to less frequency resonances being excited inside the case.

For a 'general shape' resonator, the form of Eq. (4.9) – (4.12) will be slightly more complex, although again, for effective communication the spectrum should include at least one modal line (seen in Fig. 4.9), and not fall *between* two modal lines. Although the positions of the mode lines will be different to those for an ideal lossless cubical resonator, the inverse relationship between the mean distance between the mode lines and the relative size of the resonator still holds true [101].

Similar losses would also occur in a general shape, although the modal lines, which are Dirac impulses in the lossless case, are replaced by resonance curves corresponding to the resonator's quality factor (Q). For a high Q, the resonance curves will be narrow and high, and thus the behaviour will essentially be the same. A low quality factor results in greater losses, and the curves will be wider and lower and thus the channel performance would be attenuated.

## 4.5. Electromagnetic Simulations of Confined Environments

In view of the complexity of the PC case scenario, in which channel behaviour is affected by both the case and its components, in this section a more realistic model using a 3D electromagnetic simulator is considered. The confined environment of a PC Tower box and a rectangular Aluminium cavity is used to study both wave propagation and resonator

behaviour. The effect of variables such as the size and position of different simulated absorbing materials within the case, in addition to the location of the exciting field, are also studied.

### 4.5.1. Description of the Electromagnetic Models

A more exact model is constructed using a 3D electromagnetic simulator (CST MicroStripes). In this method, an accurate geometric model of a real computer tower case (*44cm x 18cm x 42cm*) and the chassis of the Aluminium enclosure (*65cm x 30cm x 70cm*) are built, their external and internal component dimensions being very similar to an actual PC set-up (section 3.2). The inner enclosure includes the power supply, drive enclosures, the Main Board (MB) and PCI peripheral cards as shown in Fig.4.11.a. The power supply and drive enclosures are represented with small metallic boxes, whereas the MB and PCB cards, being 6 cm apart, are each modelled as a pair of flat plates (relative permittivity εr = 4.5 and loss tangent[3] of 0.3) separated by a very thin metal core in between, modelling the ground plane (best way considered to simulate PCBs). Cards are separated by 6cm. Dimensions of the PC box and different parts are almost identical to the ones from the real environment (standard PC box).

The second model is a simple rectangular case made from aluminium which includes PCB cards (see Fig.4.11.b), similarly modelled to the PC box setup, but with a loss tangent of only 0.1 for each PCB card. The cards are stacked one above another at 8 cm intervals. The difference in loss tangent for each is applied because, in a real PC, various other components (in addition to the PCI cards and MB) also act as absorbers. Such items include cables, casing

---

[3] $\tan\delta = \frac{we^{ii} + \rho}{we^{i}}$ where $w$ is the angular frequency, $\rho$ is the conductivity, and permittivity (ε) is defined as the measure of the resistance that is encountered when forming an electric field in a medium, and can have real and imaginary components such that $\varepsilon = e^{i} + je^{ii}$.

plastics, venting, fans, etc; which, for the sake of simplicity of the model, and time of simulation (14h), are not included. Therefore, for the model to behave realistically (in terms of power decay), different loss tangent values were chosen for each environment which match the power decay observed from statistical data. Figure 4.11 shows both models implemented with the MicroStripes Simulator; the yellow box inside both diagrams represents the field of analysis.

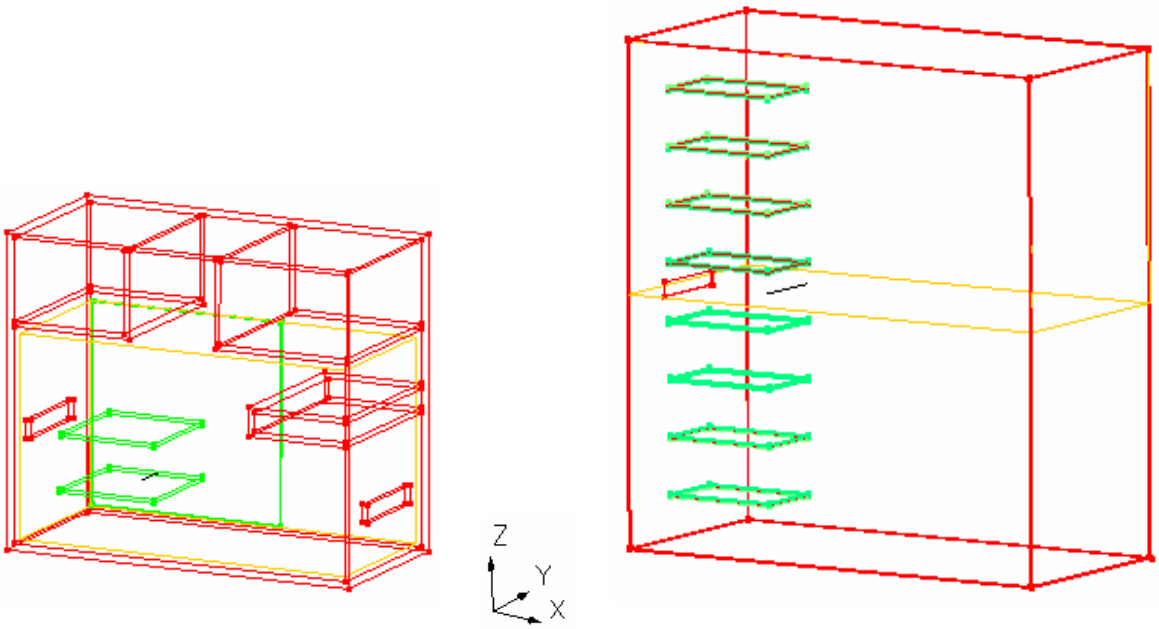


**(a)** **(b)**

**Fig.4.11. Simulated PC box (a) and simulated Aluminium box (b)**

The excitation type is an initial field excitation of 1V/m Electric field (E), located in between the PCB cards, to simulate the location where our TX antenna in real measurements would be located most of the time (see Fig.3.2). Both horizontal (direction of y-axis) and vertical polarisation (direction of z-axis) of the dipole are considered, where the excited field is broadband with frequencies ranging from 3-9 GHz. Examining the behaviour of higher frequencies proved impractical due to the processing time and computational power required to accommodate the significantly higher number of grids, this being the case even for the Aluminium case alone.

The following sections present different electric field distributions at varying frequencies, represented as the Root Mean Square (RMS) value of the electric field within the PC box and Aluminium cavity. The objective was to demonstrate well the modal frequency described in section 4.4 and compare it between the different environments.

### 4.5.2. Wave Propagation inside the PC Box

The results for different frequency regions and polarisations of the RMS electric field (E) of the region described in section 4.5.1 are presented in the following Fig.4.12. The x-y plane is located just above of the lower PCB card, with the other two planes approximating to the walls of the PC box. The resonator like behaviour of the channel is demonstrated by variation in the field strength, with a range of 20-30 dB seen between the lowest and highest frequencies (Fig.4.12). Spatial fading is also very clear for both polarisations, where fade depth [103-105] is slightly lower for higher frequencies (almost 1 dB difference between 3 GHz and 9 GHz), and it is not surprising that, as the relative size of the environment becomes larger, fading is reduced. The maximum standard variation ($\sigma$) of the RMS electric field is approximately 11 dB, giving an indication of wide energy distribution across the whole channel.

For low frequencies (f = 3 GHz and f = 5 GHz), the relative size of the environment is smaller; thus, the modal lines are not so dense. There is a higher risk that terminals will fall either between the modal lines or the risk of weak excitation due to antenna position/polarisation in a resonance node (N) that is not supported by the resonance. Of interest is the finding that a standing wave occurs above the floppy disk between 2 metallic walls, and therefore an antenna in this position could well fall in a resonant zero position. In contrast, the electric field variations in the region of the PCB cards are less marked.

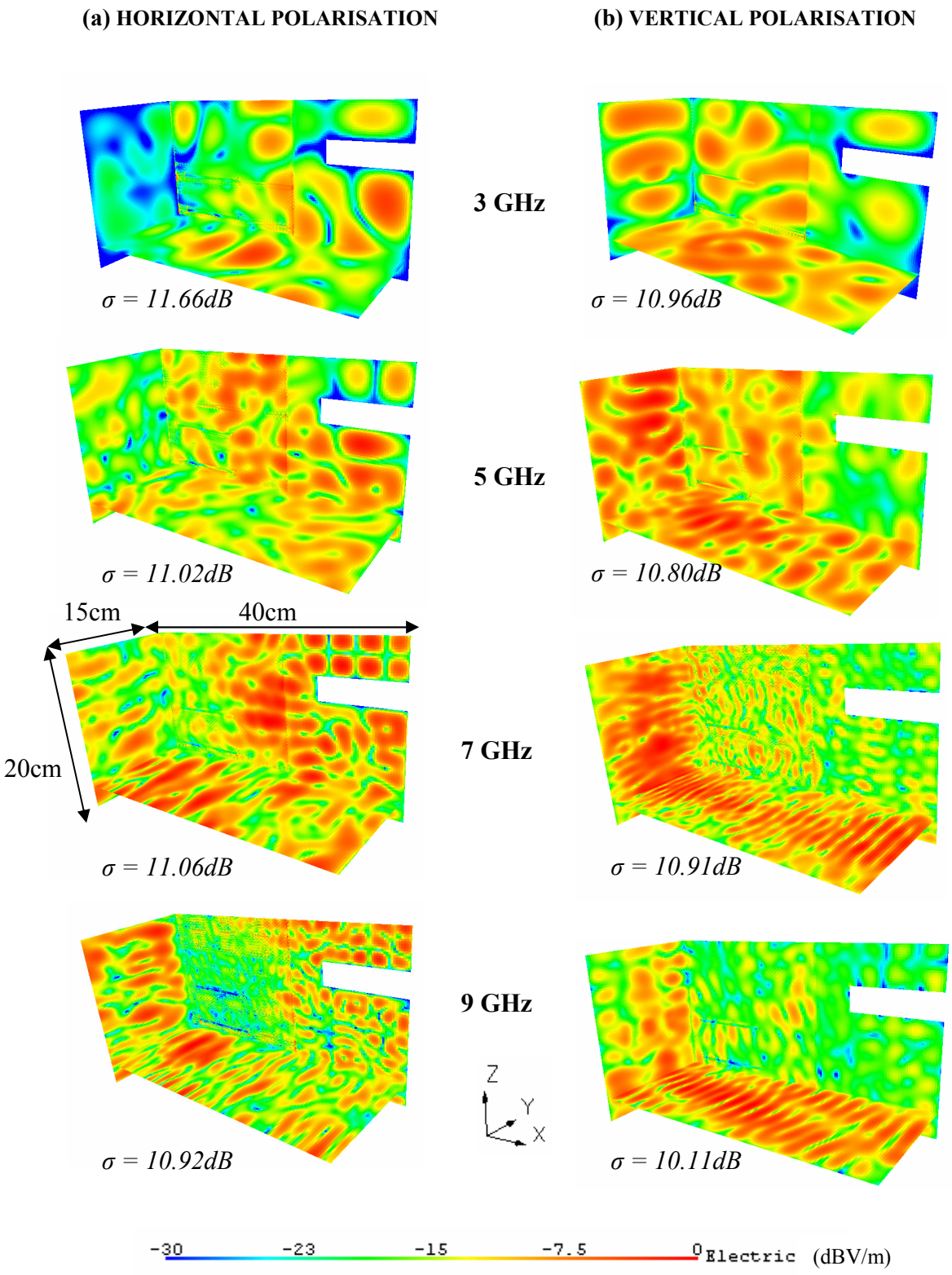


**Fig.4.12. Electric field distribution of different frequency regions inside the PC Box**

**(a) Horizontal polarisation of the exciting dipole**

**(b) Vertical polarisation of the exciting dipole**

The corresponding wavelength of the higher frequencies (f = 7GHz and f = 9 GHz), are relatively small compared to the environment. The two polarisations exhibit similar behaviour but the horizontal arrangement has lower mean field strength due to interactions with the PCI and MB surfaces. This behaviour is due to the radiation generated by the dipole; a different pattern would occur with polarisation in the x-direction. The resonator patterns with these wavelengths are periodic in the plane where the separation between the modes coincides with half of the wavelength.

The objective of these simulations is to attempt to demonstrate increased efficiency of a communication channel with decreasing wavelengths, where the probability of positioning the antenna in a resonant zero (node), or incorrect choice of antenna, is inversely proportional to the environment size. However, it is difficult to determine the optimum location of the antennas within the box in view of the many other absorbing and scattering components not included within the model but which exist in a PC box, and which would affect resonant behaviour in a wireless set-up.

### 4.5.3. Wave Propagation inside the Aluminium Case

The same procedure as for the previous analysis in section 4.5.2 is performed using an Aluminium box as described in section 4.5.1. Fig.4.13 shows the 3 dimensional RMS electric field distributions (yellow box) inside the Aluminium box for different frequencies and polarisations of the dipole. Being symmetrical about its vertical midpoint, only the bottom half of the Aluminium box is considered. The location of the dipole is between the $4^{th}$ and the $5^{th}$ PCB card, and the x-y plane is located adjacent to the $7^{th}$ PCB to determine the effect of an electric field close to the PCB cards. With this outer casing model, which would contain no scattering components as described for a PC environment, a much better approximation to a ‘real’ environment, in terms of wave propagation, is anticipated.

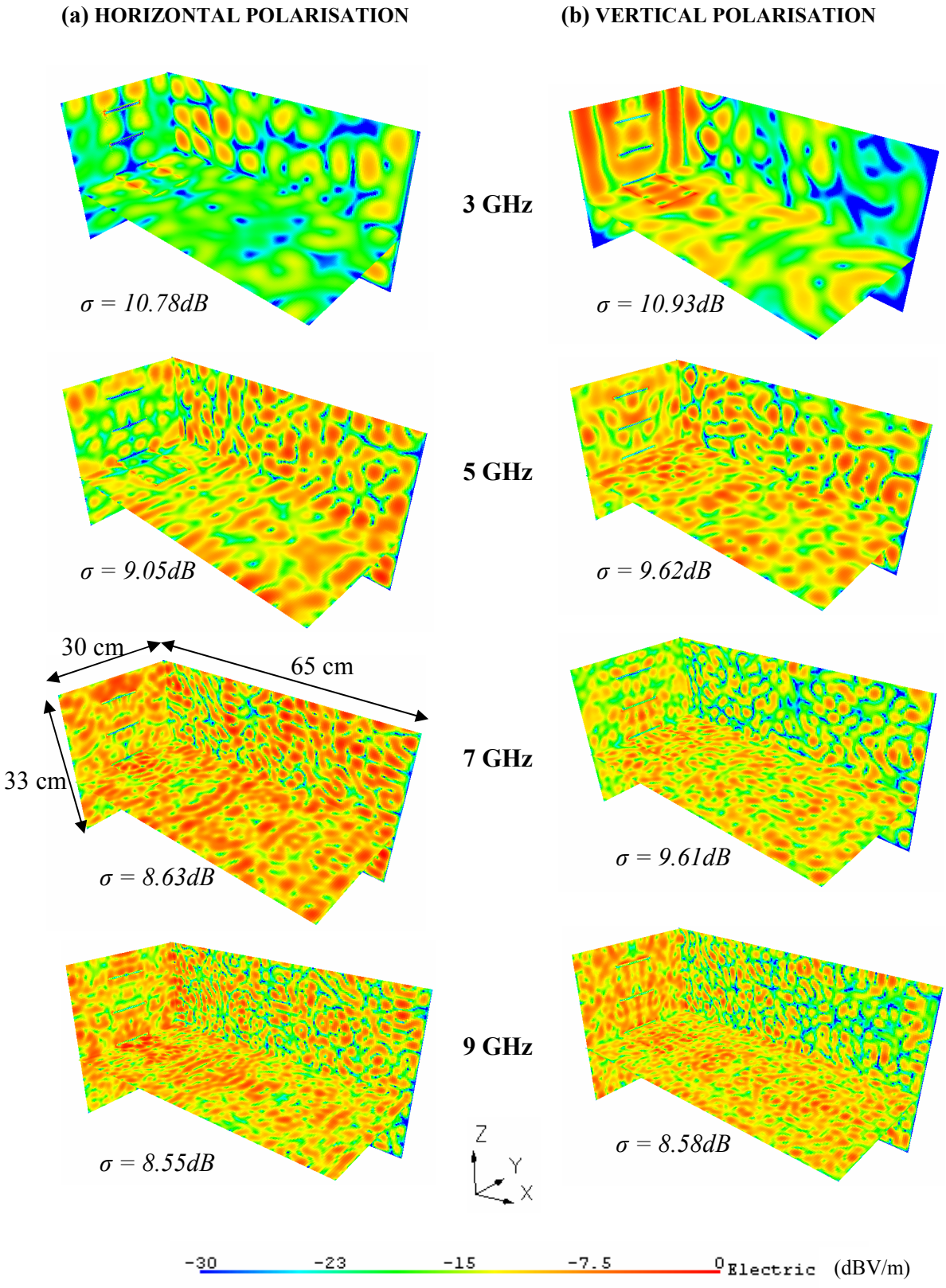


**Fig.4.13. Electric field distribution of different frequency regions inside the Aluminium Case**

**(a) Horizontal polarisation of the exciting dipole**

**(b) Vertical polarisation of the exciting dipole**

As expected, a similar trend is observed within the aluminium box in terms of resonance (Fig.4.12 vs. Fig.4.13), with a range of 20-30 dB in field strength variation across different TX positions. The fade depth in this scenario is slightly larger (by 3dB) than that observed in Fig.4.1 due to less internal scattering and higher internal reflectivity. However, again, the standard variation ($\sigma$) of the RMS electric field also decreases with frequency (~2.5 dB between lower and higher frequency). This is because the relative size of the environment becomes larger, where there is an exponentially decrease of minimum fade depth once the size of environment increases (see Fig.4.5). Thus, diversity in polarisation becomes less important in terms of fading if many modes are excited in one dimension. Furthermore, the effect of polarisation also becomes negligible for higher frequencies, where so many modes are excited in each dimension. This gives an idea of how diversity in polarisation becomes less important for fading mitigation once so many modes are excited in one dimension.

In the case of vertical polarisation for f = 3 GHz in Fig.4.13, a well-defined standing wave is noted in the direction of the dipole's polarisation where the PCBs are located. An open waveguide [118] is created across the y-z plane in the gap between the walls and the PCBs, whose width is 10 cm, corresponding to wavelength width for this frequency (f = 3GHz). This demonstrates how parallel placement of PCB cards inside the structure can create waveguide behaviour within certain parts of the box, depending on the frequency broadcast by the dipole and its location and polarisation. By extrapolation, this phenomenon has potential for good parallel communication between cards, where a high capacity link could be established between all of them *if* terminals are placed in the optimum location - preferably on the edges of the cards, at least according to the findings from this study. This phenomenon will be verified in the later section of Chapter 5 and 6 by statistical data from measurement campaigns inside the cavity.

## 4.6. Conclusions

This Chapter has explored the phenomenon of frequency-selective fading, which degrades signal characteristics, in a confined environment. The communication channel has been shown to be a hybrid of a ray-like channel observed in large environments (>10λ) and a resonator-like channel in which communication can occur through coupling[4].

The two-ray model predicted that in small confined environments the frequency selective fading will be a more severe issue. This model predicts that bandwidth required to resolve all multipaths is scaled proportionally to $V^{-0.333}$ where $V$ is the volume of the environment; ray tracing simulation predicts scaling proportional to $V^{-0.293}$.

One of the main determinants of performance is bandwidth: for a narrowband system, there is a significant effect of the spatial variation of the field strength which can be up to 30 dB. Should either the receiver or transmitter be positioned in one of the resonant zeros, communication would be severely attenuated or nil. For a wideband system (>500 MHz), this is less problematic because such a system relies on frequency diversity – that is, spreading information over a larger bandwidth alleviates the impact of the resonator-like behaviour because more energy excites more modes.

In contrast, higher frequencies are associated with less fading inside a confined environment (with a relative increase in environment size-to-frequency ratio). The difference in the standard deviation of the RMS electric field of the channel was around 1-3 dB, and an interesting study would be to compare fading statistics of the simulated results with real measurements inside the PC Box and aluminium cavity (Chapter 6).

[4] Coupling is defined as the desirable or undesirable transfer of energy from one medium to another medium

One approach to improving signal strength appears to be through optimal polarisation of the receivers and transmitters. By using antennas with dual or even triple polarisation would allow excitation of more modes than a single-polarised antenna, with a reduced likelihood that either TX or RX is positioned in a null point (resonator zero), as more mode lines are available as the number of polarisations is increased. In addition, this solution also does not compromise the spectral efficiency.

Finally, another alternative would be to engineer the environment with a view to minimising fading and resonance. Fading inside the Aluminium case appeared to be slightly bigger than in the PC Tower box (~3 dB). Therefore, the use of absorbers would mitigate against the number of multipaths, and the system would be less resonant. As a result, even the issue with inter-symbol-interference in wideband systems could be resolved or mitigated. Note however that as many multipaths are attenuated, only the energy of the LOS remains available for transmission, which paradoxically reduces the SNR and ultimately compromises the spectral efficiency.

# Chapter 5: Frequency and Time Domain Analysis

## 5.1. Introduction

This Chapter presents analysis of the frequency and time response of the empirical data collected inside both confined environments (PC Tower and Aluminium case). This chapter is divided as follows. Firstly, the analysis of the frequency domain inside the PC Tower and then the Aluminium case (with its different versions) are presented; secondly, there is the time domain analysis which includes the channel impulse response (CIR) carried out again in both scenarios. Two different approaches to model the power delay profile (PDP) are presented and this is followed by the RMS delay spread investigation for each environment. Finally, the Ricean K-factor, confirming the dominant NLOS nature of the environments, is summarised.

## 5.2. Frequency Domain Analysis

The first analysis in this chapter corresponds to the frequency domain of the different enclosures. Empirical data is recorded with the VNA in this format, where each point (of a total of 1601) includes the magnitude and phase for the corresponding frequency. The bandwidth is 8 GHz (3-11 GHz), which corresponds to a frequency resolution of 5 MHz. Although higher resolution could have been achieved by splitting the bandwidth into defined bands for each measurement, and then joining them, this approach was not adopted due to time restraints.

Single point measurements are subject to strong variations due to fading effects. Therefore the frequency responses for all different cases are presented using the average value all points from the TX grid for each frequency point.

### 5.2.1. Frequency response inside the PC Tower Box

Figure 5.1 presents the different frequency responses inside the PC Tower for both polarisations, once the RX is located at its three different fixed positions (Rx-Device, RX-PCB and RX-MB). The objective is to show how the frequency response is affected by both polarisations and location of the antenna inside the PC Tower case.

**(a)**

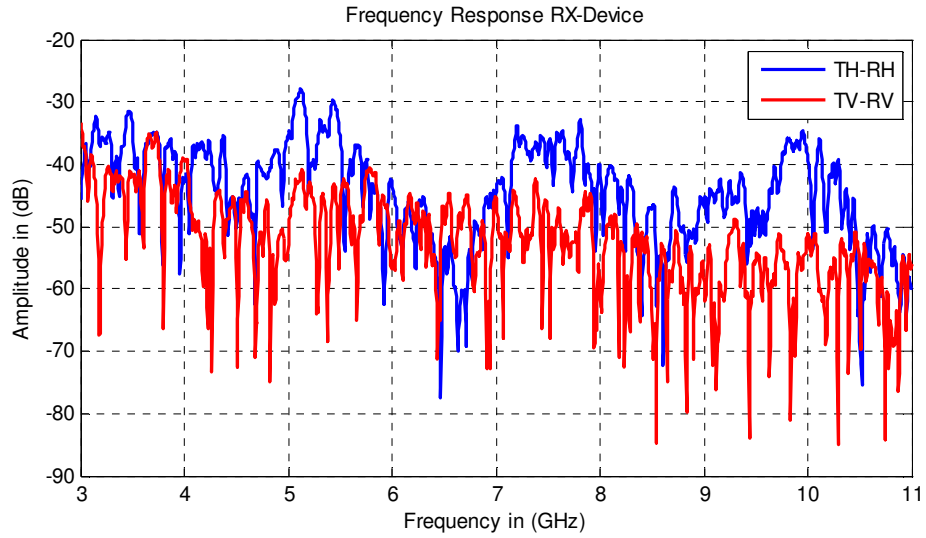


**(b)**

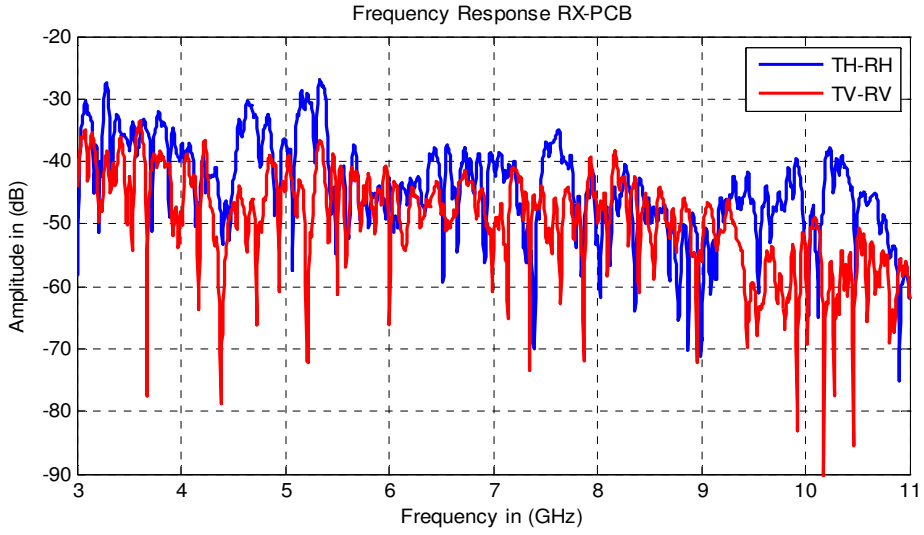

(c)

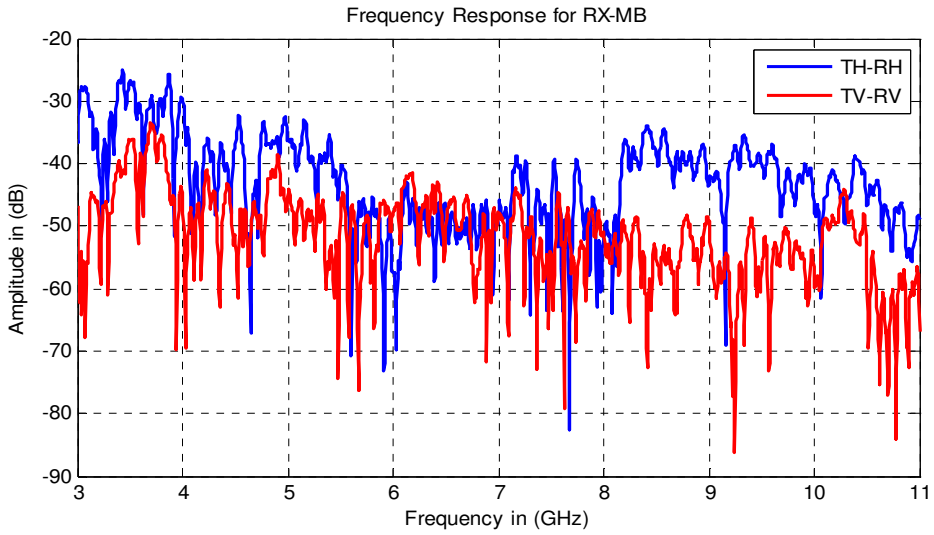


**Fig.5.1. Frequency Responses for both polarisations inside the PC Tower case when the receiver is located in:**

**(a) the RX-Device**

**(b) the RX-PCB**

**(c) the RX-MB**

It is apparent from Fig.5.1 that the horizontal polarisation (TH-RH) presents a slightly better response in terms of mean power over the whole band. The mean power transmitted for the full-band for TH-RH is around -44 dB, whereas the mean power for TV-RV is -51 dB, both for RX-Device and RX-PCB. Only in the case of RX-MB these mean power values for each polarisation are slightly lower (~1.5 dB). The explanation for that might due to higher shadowing at the receiver when located in the proximities of the main board (MB). Both polarisations in *all* the cases have similar standard deviation of power of ~7.5 dB. It is an interesting finding from Fig.5.1 that the actual distribution of the antennas inside the box does not affect significantly the overall mean power, these having very similar values for each case. This makes sense in part due to the fact that the difference in distance between the different RX positions is not large, hence the variance in path loss over distance ($PL(d)$) might not be very significant. A deeper study of this phenomenon is presented in Chapter 6.

The polarisation adopted by the antennas does, however, play a dominant role. Several factors could account for this. Firstly, with a change in antenna orientation, the gain and therefore radiation pattern changes. A change in power with antenna polarisation can excite different PC components lying in the path of transmission, which may themselves absorb part of the transmission energy. To confirm this, the frequency response inside the Aluminium cavity could be examined with differing antenna orientations (without a MB included to simplify the model). The other explanation for the difference of mean power between polarisations is related to the different modes excited inside the cavity due to its different size and shape once the polarisation is changed from horizontal to vertical. Due to the hybrid-resonance nature of the cavity, different standing waves are excited across the channel depending on the frequency selectivity. If the terminals are located in zones where the standing waves cause destructive interference (resonant zeros), part or no energy is received by the RX.

The most important characteristic to point out is the non-continuous decay of energy in TH-RH along the band, where in specific frequency areas there appears an abrupt increase of energy (peaks). This behaviour is easy to spot in Fig.5.1.a and Fig.5.1.b, where three peaks appear around specific frequencies. These peaks correspond to 5 GHz, 7.5 GHz and 10 GHz. Therefore, it appears that there is a constructive interference every 2.5 GHz, which in terms of wavelength is 12 cm. This distance corresponds to double the distance between the PCB cards ($d = 6cm$) and also the distance between the second PCB card and the bottom wall. Thus, it seems that the radiation patterns of the antennas horizontally polarised excite a strong waveguide [118] in the z-axis. Furthermore, a Bragg's diffraction phenomenon [119] may occur due to the regular arrangement of the PCB cards. This could result in constructive interference every $2d$ once the wave hits the structures with an angle of incidence of 90°. Bragg's Law [119] is expressed as follows:

$$n\lambda = 2d\sin\theta \tag{5.1}$$

where $n$ is an integer, $\lambda$ is the wavelength of incident wave, $d$ is the spacing between the PCBs, and $\theta$ is the angle between the incident ray and the scattering planes. Thus, if the angle of incidence is 90°, meaning that the signal is incident perpendicularly on the structure (PCB), wavefronts of constructive interference appear every 2.5 GHz along the band. This discovery explains the association between frequency selectivity and PCB separation distance.

It would be of interest to investigate this effect within the new Aluminium case which simulated a possible Personal Server and in which the separation between PCBs is different ($d$ =*8cm*), in order to verify that such constructive interference occurs in a simpler structure in which the only scattering/absorbing objects are the parallel PCBs themselves.

### 5.2.2. Frequency response inside the Aluminium Case

The aim of this section is to verify the non-homogeneous frequency response, observed in the previous section 5.2.1, from a similar environment such as a rectangular Aluminium case. This time, however, the separation between the PCBs is different ($d$ =*8 cm*). Figure 5.2 shows the frequency response of both polarisations where the response is an average of all points inside the transmitter (TX) grid. The RX in Fig.5.2 is fixed on top of an adjacent parallel PCB card (‘First Level’) which corresponds to a very similar scenario presented inside the PC box when RX-PCB (see section 3.2.1).

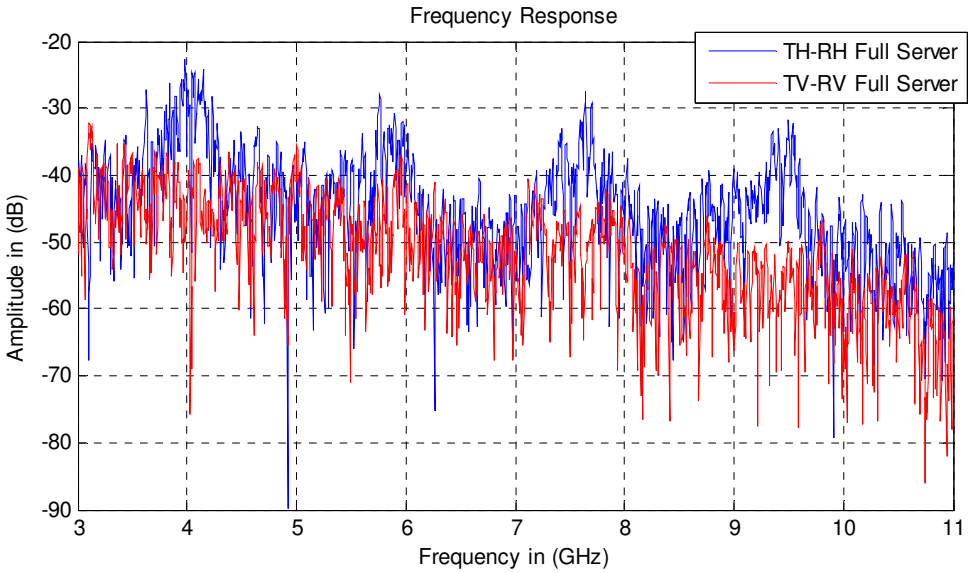


**Fig.5.2.Comparison of frequency responses for both polarisations inside the Aluminium case containing the PCBs**

This time the peaks in Fig.5.2 for TH-RH are clearer, where the constructive interference now appears at different frequencies. These frequencies are around 4 GHz, 5.8 GHz, 7.6 GHz and 9.4 GHz. Thus, the interval is 1.8 GHz, corresponding to a wavelength of ~16cm, which is again double the distance between the cards ($\lambda = 2d$). The fact that this resonance starts at 4 GHz is related to the fact that the first resonance appears when $\lambda = 2d$. Although the inter-plate distance is 8 cm, there are different components integrated into each card which, depending where the antenna is located in the TX grid, might slightly reduce the distance between cards. In contrast, the trend followed by the TV-RV is similar to that found inside the PC, where a more homogeneous decay of energy along the band is seen. The explanation of this is similar to the one obtained from the PC Tower, where the radiation patterns of TV-RV do not interact in the same way with the devices present in the case.

The total mean power transmitted for TH-RH is slightly smaller (~ -42 dB) than the one from PC Tower (~ -44 dB), with a similar standard deviation of 8 dB. This time, however, the average difference in mean power between polarisations decreases substantially to only 1-2 dB, where the mean power for the TV-RV case is around (~ -44 dB). Therefore, it

seems that the highly complex environment presented in the PC Tower case, as well as the change in size of the enclosure, might also play a substantial role in overall performance.

A higher number of frequency response spikes is also seen in the Aluminium case model (Fig.5.2) compared to the PC Box (Fig.5.1); apart from the absorbing and scattering effects of the 8 PCB cards, the Aluminium case has high internal reflectivity. Furthermore, a higher number of frequency modes are excited due to the higher volume of the cavity (see Fig.4.8), hence the number of frequency points. In order to evaluate these phenomena, Fig.5.3 shows a comparison of frequency responses between the three different sizes adopted by the Aluminium case, for TH-RH alone (empty and filled cavities). The inclusion of the results of TV-RV (as well as the ones from an extra absorber) were considered irrelevant in this section since the purpose of this last study was to examine the reduction of frequency resolution with case size.

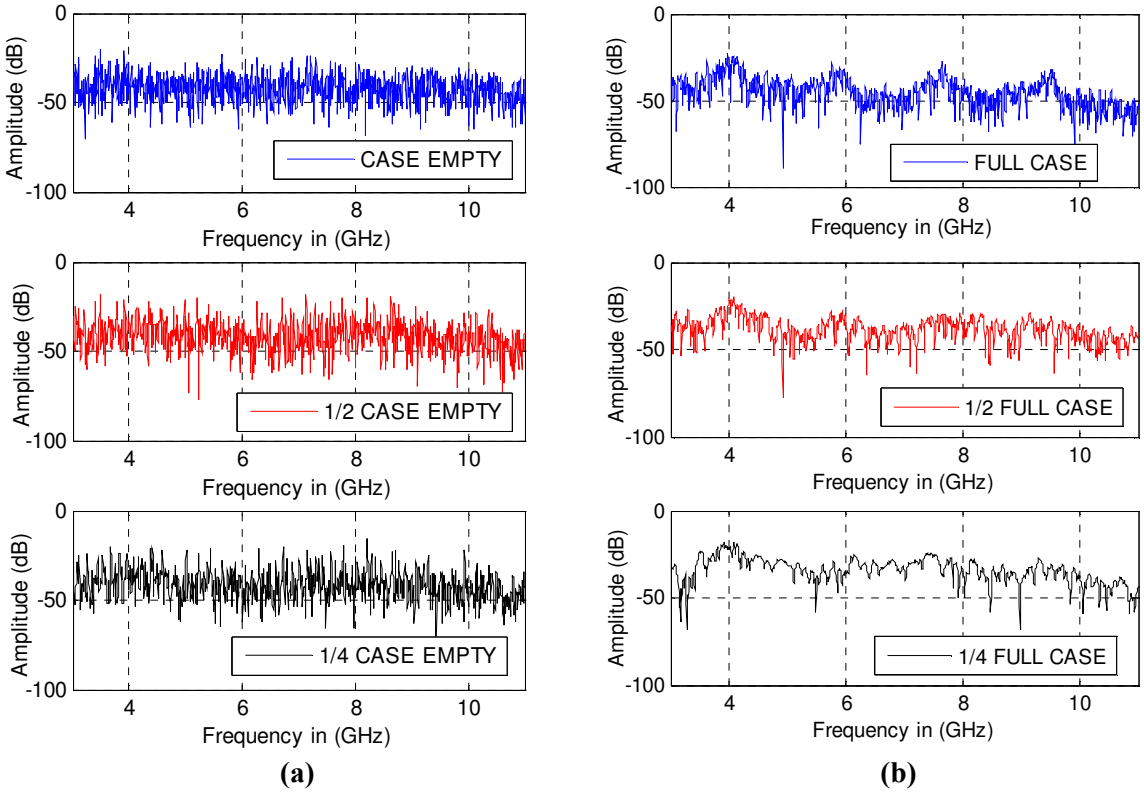


**Fig.5.3. Comparison of frequency response for TH-RH for different volumes of the Aluminium Case when**

**(a) Empty Case** **(b) Full Case ( inclusion of 8 PCB cards)**

Figure 5.3 shows that, once devices are included within the cavity, the frequency response changes significantly along the bandwidth. Figure 5.3.b illustrates resonant behaviour every 1.8 GHz occurring as a result of device distribution and polarisation. When the case is empty (Fig.5.5.a), this resonant behaviour is absent.

A huge number of frequency spikes are detected in this scenario ('Empty case'), where, decreasing the size of environment, does not really affect the overall behaviour of the frequency, in part due to the same polarisation of the antennas being present for each size of the case. However, once the PCBs are included inside the case (Fig.5.3.b), it is quite clear how the reduced volume affects the performance. The resonant peaks become less easy to identify, hence less resolution in frequency appears due to fewer modes being excited inside the cavity with the presence of the PCBs. This phenomenon becomes stronger once the volume of the aluminium cavity is reduced to 75% ('1/4 Full case'), where the ratio between the volume and the surface area of the structures increases substantially. This indicates that the more populated the environment becomes, the less resonance occurs in the overall system.

Finally, path loss in terms of frequency ( $PL(f)$ ) becomes very difficult to model due to the clear resonant behaviour appearing across the bandwidth, like the TH-RH case. In other words, the overall architecture inside these complex environments becomes crucial, where there is a strong correlation between the radiation patterns of the antennas and the distribution of the devices inside the PC Tower case. Authors in a very similar environment [11] modeled the *PL(f)* as $f^{-2k}$ [11, 26, 48] with a decay factor $k$ of 1.47 for the far-field scenario. However, this frequency dependency model of the path loss (*PL(f)*) becomes inappropriate since the *PL(f)* cannot be fitted to linear decay, especially for the TH-RH case. Therefore, path loss over frequency seems not to be a very useful parameter to model for this type of channel. It is known from [26] that the propagation loss of the channel is a function

of both transmitted frequency and distance between antennas. Chapter 6 analyses the distance-dependence of path loss ($PL(d)$) in more detail to check whether this particular parameter is suitable to model the channel behaviour.

## 5.3. Time Domain Analysis

This section is divided into different subsection described as follows:

i. The first two sections examine the different Average Power Delay Profiles (APDP) of the different measurement campaigns inside the PC Tower box and Aluminium case respectively.

ii. Secondly, simulations of the PDP, calculated from the electromagnetic models presented in section 4.5, are presented.

iii. Later, two different simple approaches are used in order to evaluate the APDP. The first is based in the reflection coefficient of the environment, trying to establish a correlation between the volume of the case and the different reflection coefficients 'r'. The ray tracing model explained in section 4.3 is used in this section. The second approach treats the power decay as a geometric series for a given number of multipaths inside of a threshold.

iv. Finally, the RMS delay spread [48] is calculated and predicted by the geometric model explained in previous section (iii).

### 5.3.1. APDP Results of PC Tower Box

This first section presents different APDPs calculated inside the PC Tower case for different polarisations and location of the RX antenna. Figure 5.4 shows these different APDPs.

(a)

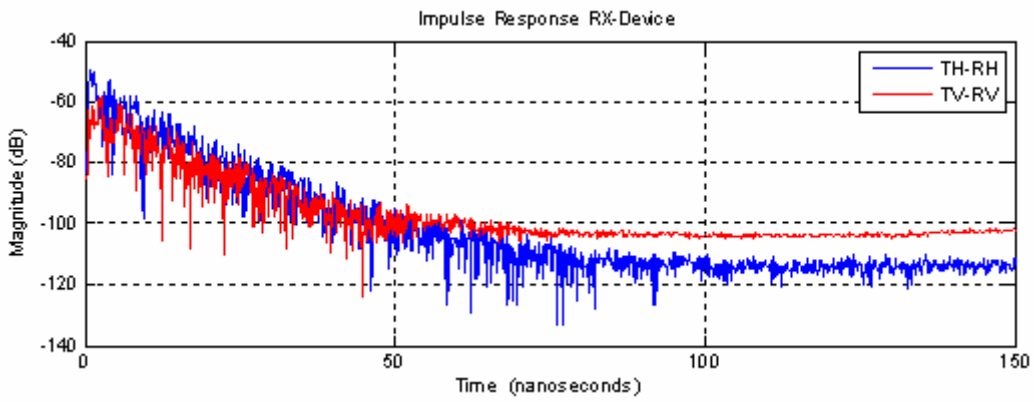


(b)

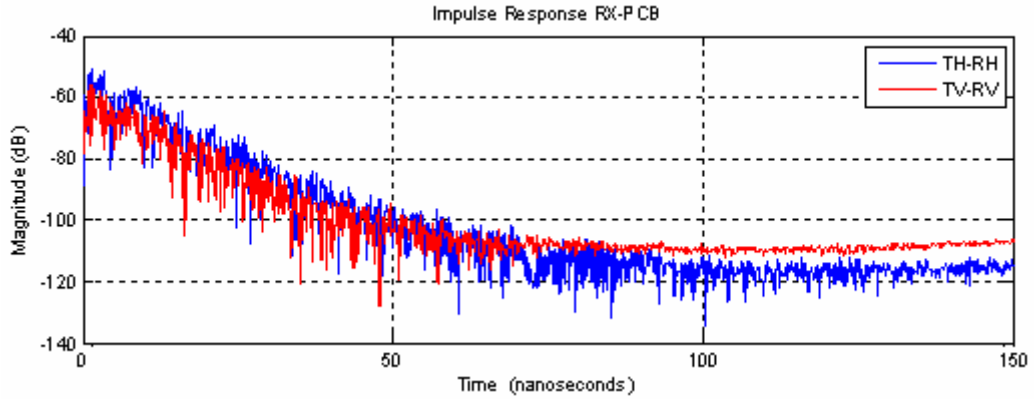


(c)

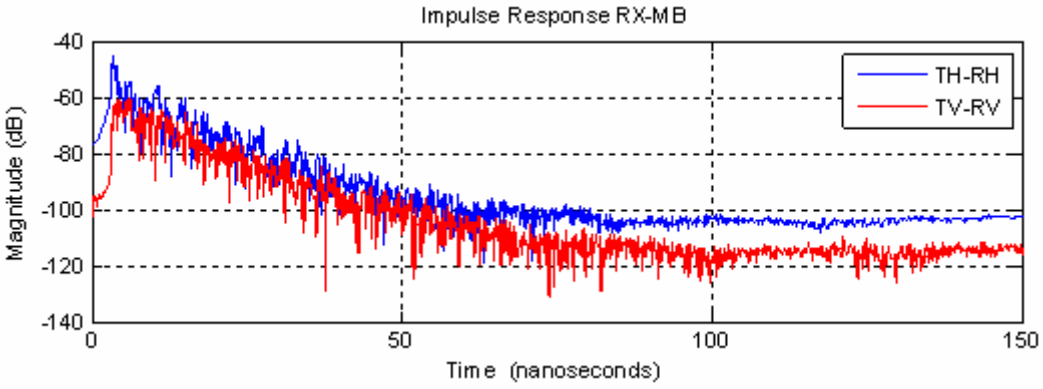


**Fig.5.4. APDPs comparison between both polarisations inside the PC Box when**

**(a) RX-Device**

**(b) RX-PCB**

**(c) RX-MB**

This author considers it important to remind the reader in this section that APDP is calculated as follows [7]:

$$APDP = \frac{1}{N}\frac{1}{M}\sum_{x=1}^{N}\sum_{y=1}^{M}\left|h(x,y,\tau)\right|^2 \tag{5.1}$$

where *M* and *N* are the total number of *x, y* points of the TX grid respectively, $|h(x, y, \tau)|$ is the channel impulse response (CIR) calculated at each point of the TX grid, and $\tau$ is the relative delay of the *i*th multipath as compared to the first arriving component (excess delay) [48].

A difference in mean power decay of 7 dB is detected between polarisations. Again, the reasons stated in previous section 5.2 might explain this behaviour, where the antenna orientation plays a dominant role.

Once the receiver (RX) is placed next to the Main Board (MB) (Fig.5.4.c), a significantly different behaviour appears between polarisations. Firstly, the first path arrives after 3 ns, which means the signal bounces around the case covering a distance of almost 1m before reaching the receiver. In other words, this situation becomes a very high NLOS situation where the strongest path received does not correspond with to the LOS path. This is because in this experiment the RX was placed in a location where objects from the MB, such as the fan, were shadowing the signal completely. In contrast, a great deal of similarity is observed between Fig.5.4.a and Fig.5.4.b, where although the RX is located in totally different spots inside the PC Tower box, not very dramatic changes appear. This indicates that once the RX is *not* being shadowed completely by other objects, it does not really matter where to place the RX in terms of mean power decay.

Another important characteristic to note is the rapid decay of the signal with time in each scenario. Every case from Fig.5.5 presents linear decay on a logarithmic scale in the first 50-60 ns (exponential decay in a linear scale), where after a threshold of 45-50 dB from first arrival, no more relevant changes in power transmission appear. This is translated to an average decay of power of 50 dB/50 ns (1 dB/ns), if the slope is considered linear throughout the time. The slope of the APDP is believed to change if certain factors are modified, of which the most important are cavity size and population. In other words, either placing or

removing devices inside the confined environment, or modifying their volumes or shapes would significantly affect the APDP. Section 5.3.2 presents various APDP examples calculated in different scenarios inside the Aluminium case for different situations.

### 5.3.2. APDP Results of Aluminium Cavity

This section presents different APDPs from the empirical data measured inside the Aluminium case. Figure.5.5 shows a comparison between different APDP for different dimensions of the Aluminium case; this time only TH-RH is included in the graphs due to the small difference between both polarisations in terms of power decay.

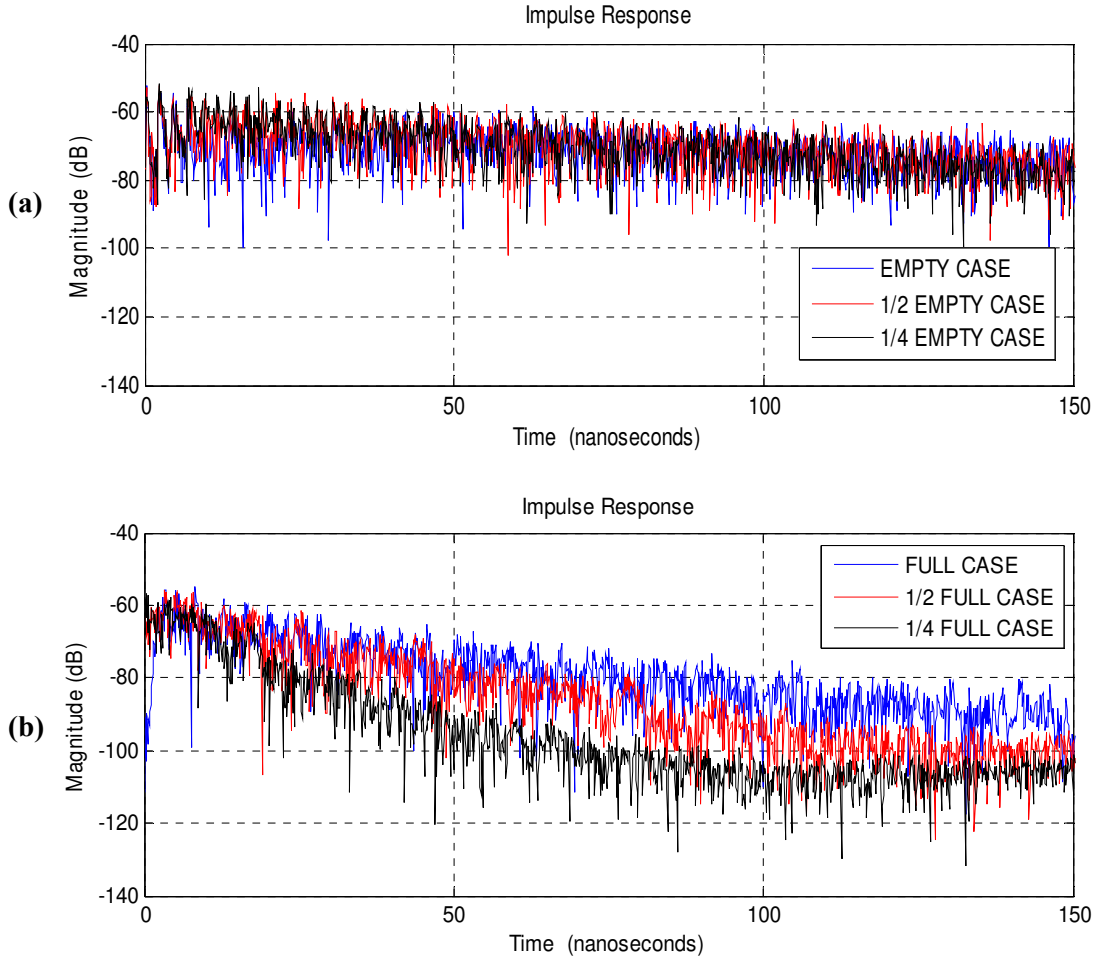

(c)

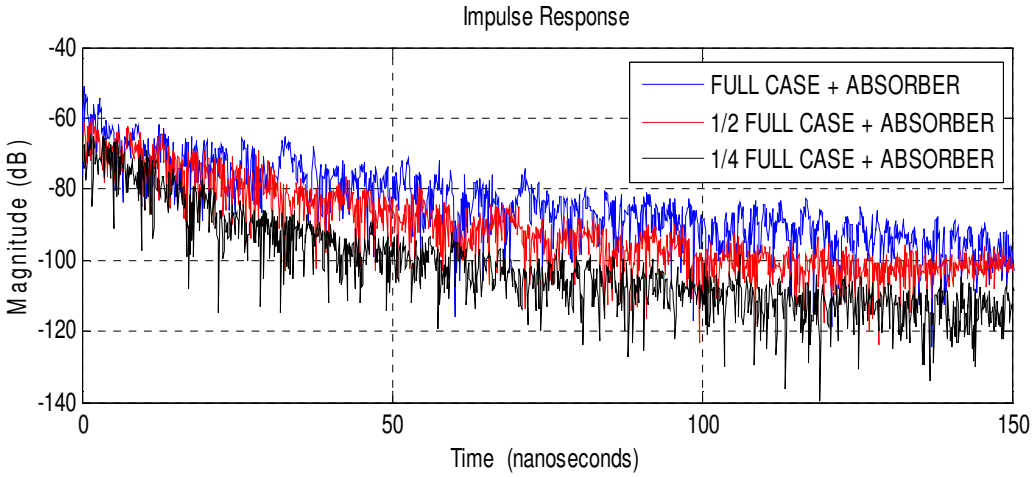


**Fig.5.5. APDPs comparison between three different volumes of the Aluminium case when**

**(a) Empty case**

**(b) Full case**

**(c) Full case + Absorber**

It is easy to appreciate the increase in the slope of APDP once the size of the cavity is reduced, especially when the cavity is filled with PCB cards (Fig.5.5.b) and with an absorber (Fig.5.5.c). This emphasises the effect these devices have inside the cavity in terms of power loss. The decay in power observed for the 'Empty case' scenario (Fig.5.5.a) is almost negligible (~5dB/50ns), where the power arrives from reflections practically without any attenuation due to high internal reflectivity. Only after 100ns is a slight change in the slope of the APDP between different sizes appreciated, where multipaths take a shorter time to reach the RX. This phenomenon is more abrupt with the presence of absorbers inside the cavity, such as PCBs and a 3M 3030 Absorber, where multipath components coming from reflections with these devices result in greater power loss. Internal topology of the case will also interfere with the received signal due to shadowing.

In terms of power decay, the 'Full case' scenario resulted in a decay of ~10dB/50ns and a slightly steeper slope once the absorber is placed inside. The difference is greater between the smallest version of the 'Full case + Absorber' and the 'Empty case', this being

more than 30 dB in power loss per unit time over the same period. This is because of the change in ratio between size and absorption for the larger versions of the case.

Particular attention is given to Fig.5.5.a, where a well-defined clustering[1] is noted every 2 ns for the first 25 ns. This phenomenon is easy to recognise for a perfect resonator environment where very clear standing waves can be excited without the presence of any scatters/absorbers. However, once the environment is filled with different structures, fewer waveguides modes are excited, hence the presence of well-defined clusters is reduced. This phenomenon is further analysed in section 5.3.4.

### 5.3.3. APDP of Electromagnetic (EM) Simulations

This part shows the APDP of simulations of the electromagnetic (EM) models of the PC Box and Aluminium Case built in *Microstripes*$^{TM}$. The aim of this part is to determine whether the simulated EM models follow the same behaviour in power decay as the ones calculated from empirical data.

Figure.5.6 presents the APDP of each environment both empty and then populated with different devices. In the case of the PC Box, the devices are the MB and two PCBs, and in the Aluminium Box, 8 PCBs. The description of the setup was previously given in section 4.5.1.

[1] Cluster is defined as a group of the same or similar elements gathered or occurring closely together

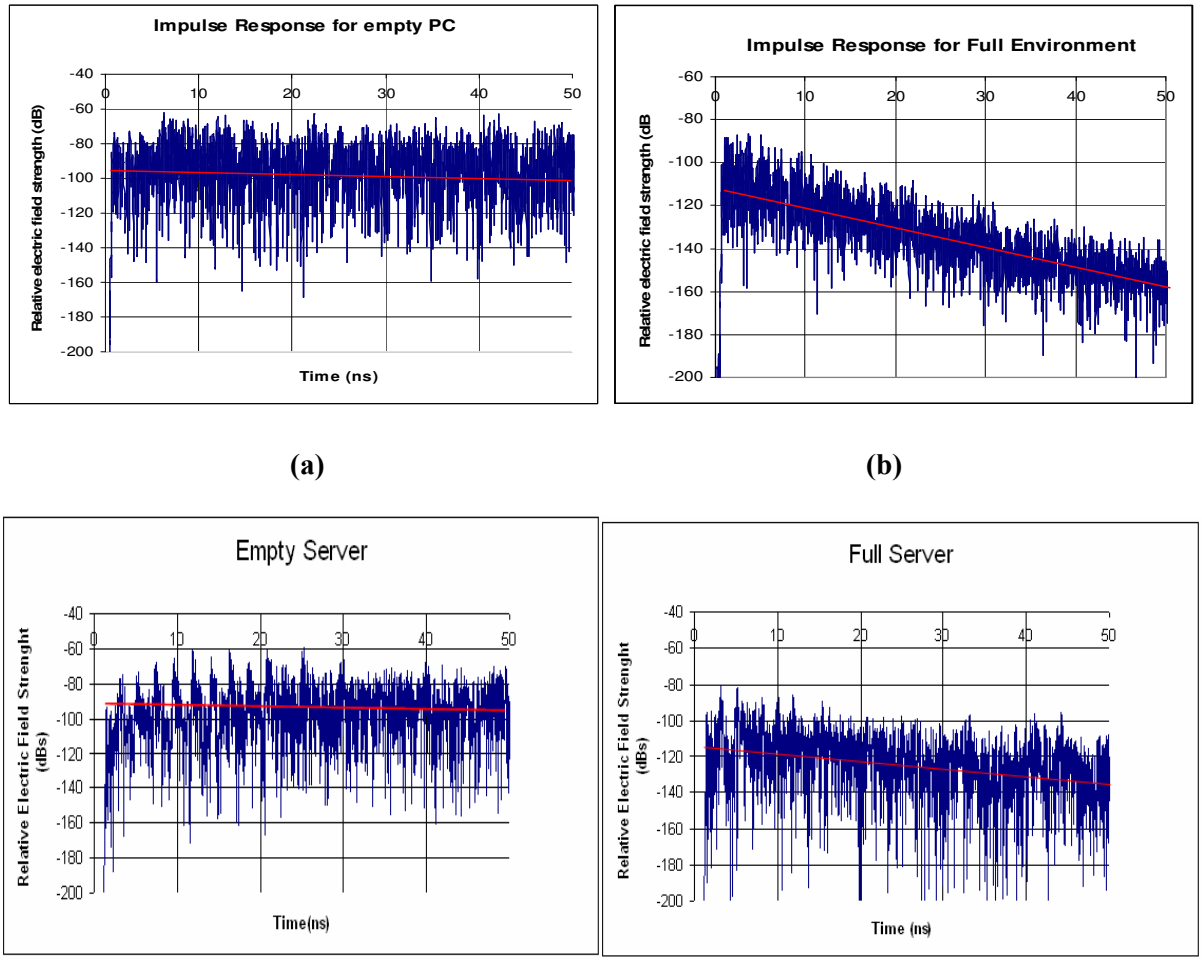


**(a)** **(b)**

**(c)** **(d)**

**Fig.5.6. Predicted Performance for Microstripes Simulator showing the different decay for**

**(a) Empty PC** **(c) Empty Aluminium Case**

**(b) Full Aluminium Case** **(d) Full PC Box**

As expected, without the MB and PCI cards, high internal reflection (Fig.5.6.a) results in little or no decay of signal power. Once the absorbing components are included (MB and PCBs), the slope of power increases to 0.9 dB/ns (Fig.5.6.b), being very close to the real APDP measured from empirical data (~ 1dB/ns from Fig.5.5). A similar trend is experienced inside the Aluminium Case, in which highly reverberant behaviour is observed in Fig.5.9.c and almost no decay appears due to internal reflections. With the only potential irregularity and point of energy loss being the hole in the back wall required for antenna placement.

Interestingly, the same resonator pattern deduced from the empirical data (Fig.5.5a) appears in the first 25 ns every 2 ns. Once the PCBs cards are included in the cavity, a higher absorption of power is observed. This power decay of 0.2 dB/ns is again very similar with the real slope measured from empirical data (Fig.5.8.b), which presented a slope of 20dB/100ns. The difference in power decay curves with time between 'Full case' and 'Full PC' is due to the smaller dimensions of the PC, in which multipath reflections take a shorter time to arrive to the RX. Furthermore, the ratio between size and absorption is higher.

The aim of this section was to demonstrate how different components placed inside the cavities, with different absorbing properties (loss tangent), dramatically affect the overall system performance. This power decay study is not only important in terms of the analysis of the losses, but crucial for the design of structures intended to receive the information carried by the signal. On the other hand, these simulated APDP from EM models fit reasonably well with empirical data and therefore these models are considered to be reasonable simulations of the real environments.

### 5.3.4. Model Parameterization of the APDP

According to the Saleh-Valenzuela (SV) model [41] for indoor propagation, the impulse response (complex in baseband) is given in general as

$$h(t) = \sum_{k,l} \alpha_{kl} e^{j\theta_{kl}} \delta(t - T_l - \tau_{kl}) \tag{5.2}$$

where $l$ is the cluster index, $k$ denotes the $k$th ray of the $l$th cluster, $\alpha_{kl}$ and $\theta_{kl}$ are the multipath gain and phase of the $k$th path of the $l$th cluster component, respectively; $\tau_{kl}$ is the delay of the $k$th path of the $l$th cluster relative to the $l$th cluster arrival $T_l$. The cluster arrival time and the ray arrival time within each cluster are modeled as a Poisson distribution with

arrival rates $\Lambda$ and $\lambda$, respectively, with $\Lambda > \lambda$. The amplitudes of the multipath components $\alpha_{kl}$ follow a Nakagami-m distribution. The phase term $\theta_{kl}$ is uniformly distributed between 0 and $2\pi$. In the channel model, the number of clusters, $L$, is a Poisson-distributed random variable with probability density function (PDF) given by the model 802.15.4a [26], with mean $\overline{L}$:

$$pdf_L(l) = \frac{\overline{L}^l e^{(-\overline{L})}}{L!} \tag{5.3}$$

Cluster inter-arrival times are exponentially distributed with cluster arrival rate of $\Lambda$ (5.4) and so is the intra-arrival time of the rays, $\lambda$, within each cluster (5.5).

$$p(T_l \mid T_{l-1}) = \Lambda e^{-\Lambda(T_l - T_{l-1})} \tag{5.4}$$

$$p(\tau_{kl} \mid \tau_{k(l-1)}) = \lambda e^{-\lambda(\tau_{kl} - \tau_{k(l-1)})} \tag{5.5}$$

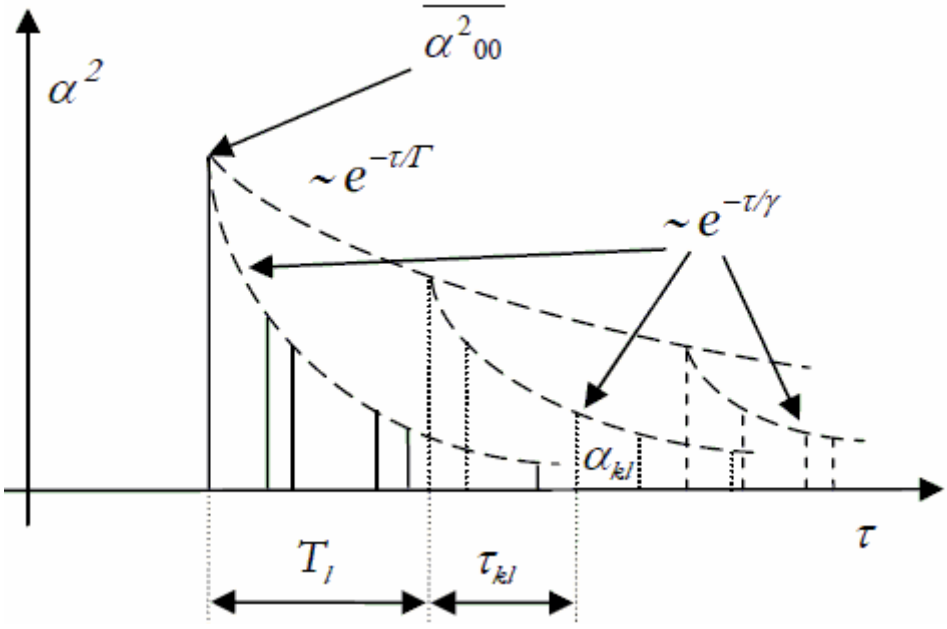


**Fig.5.7. Graphical representation taken from [120] of the Saleh-Valenzuela (SV) model [41]**

The mean square values of the gain are calculated as follows

$$\overline{\alpha_{kl}{}^2} = \overline{\alpha_{00}{}^2} e^{-T_l/\Gamma} e^{-\tau_{kl}/\gamma} \tag{5.6}$$

where $\overline{\alpha_{00}{}^2}$ is the average power gain of the first ray of the first cluster, and $\Gamma$ and $\gamma$ are power-decay constants for the clusters and rays, respectively. Due to the discrepancy in the fitting for the indoor residential, and indoor and outdoor office environments, the IEEE TG4a proposed to model ray arrival times with mixtures of two Poisson processes [26].

The environments analysed in this thesis are also considered indoor environments, although their properties differ substantially from the typical indoor environments (>10 λ). Thus, analysis of the APDP inside the PC Tower case and Aluminium box becomes relevant to determine if the SV model is still appropriate. Firstly, Fig.5.8 shows an example of APDP calculated inside the 'Empty Aluminium case', considered to have almost perfect resonator behaviour. The power decay with time is expected to be very low in this scenario.

**(a)**

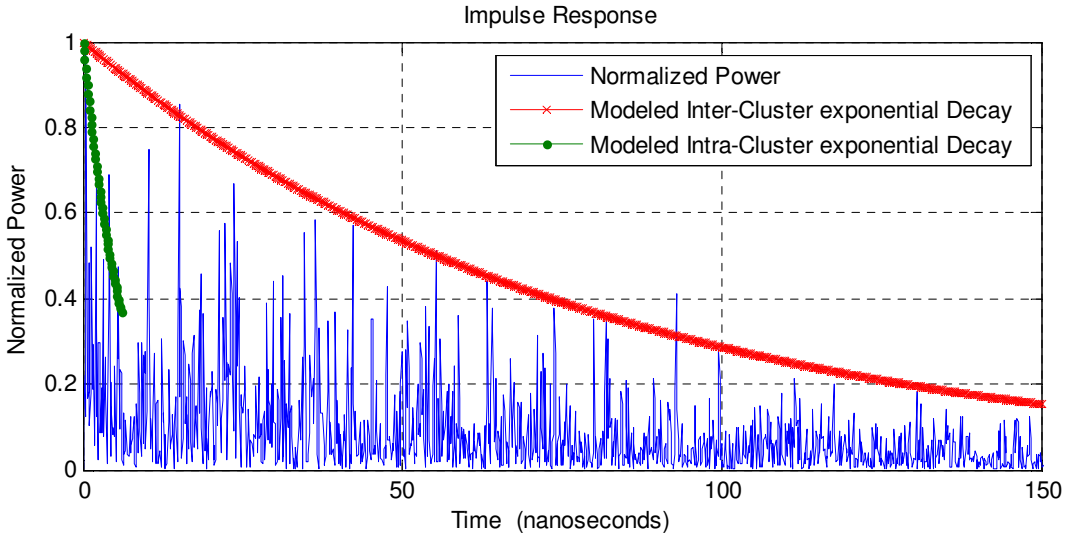

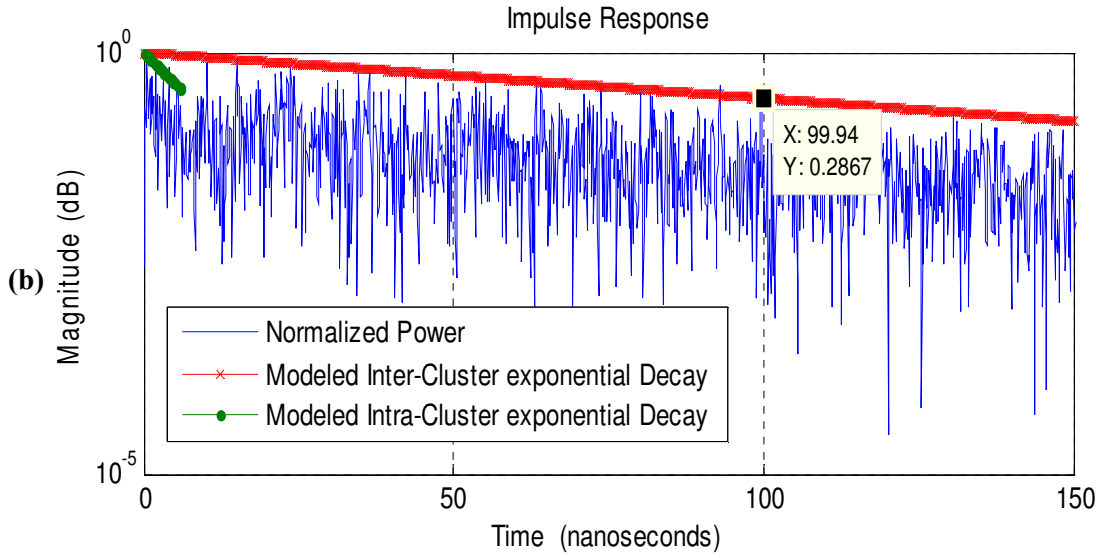


**Fig.5.8. Normalised APDP of the Empty case on linear scale (a) and in semi-logarithmic scale(b)**

Figure 5.8 presents both modeled inter-cluster and intra-cluster exponential decay fitted of the APDP of the 'Aluminium empty case', both in linear (Fig.5.8.a) and semi-logarithmic scale (Fig.5.8.b). A very clearly different exponential decay in Fig.5.8.a is observed between clusters ($\Gamma$ = 80 ns) and rays inside the cluster ($\gamma$ = 6 ns). These clusters are selected manually by visual inspection [26]. Clustering identification employing statistical techniques such as clustering algorithms are inappropriate for these applications due to the higher difficulty to develop a robust algorithm for the automatic identification of cluster regions [26]. Therefore, the modeled intra-cluster exponential decay ($\gamma$) might not be a representative model of the channel. This parameter ($\gamma$) becomes even harder to identify once the cavity is populated due to a rapid decay of power with time, and also the hybrid resonator-ray like behaviour. An example of that is shown in Fig.5.9, where the APDP is calculated inside the PC Tower case when the receiver is at RX-Device.

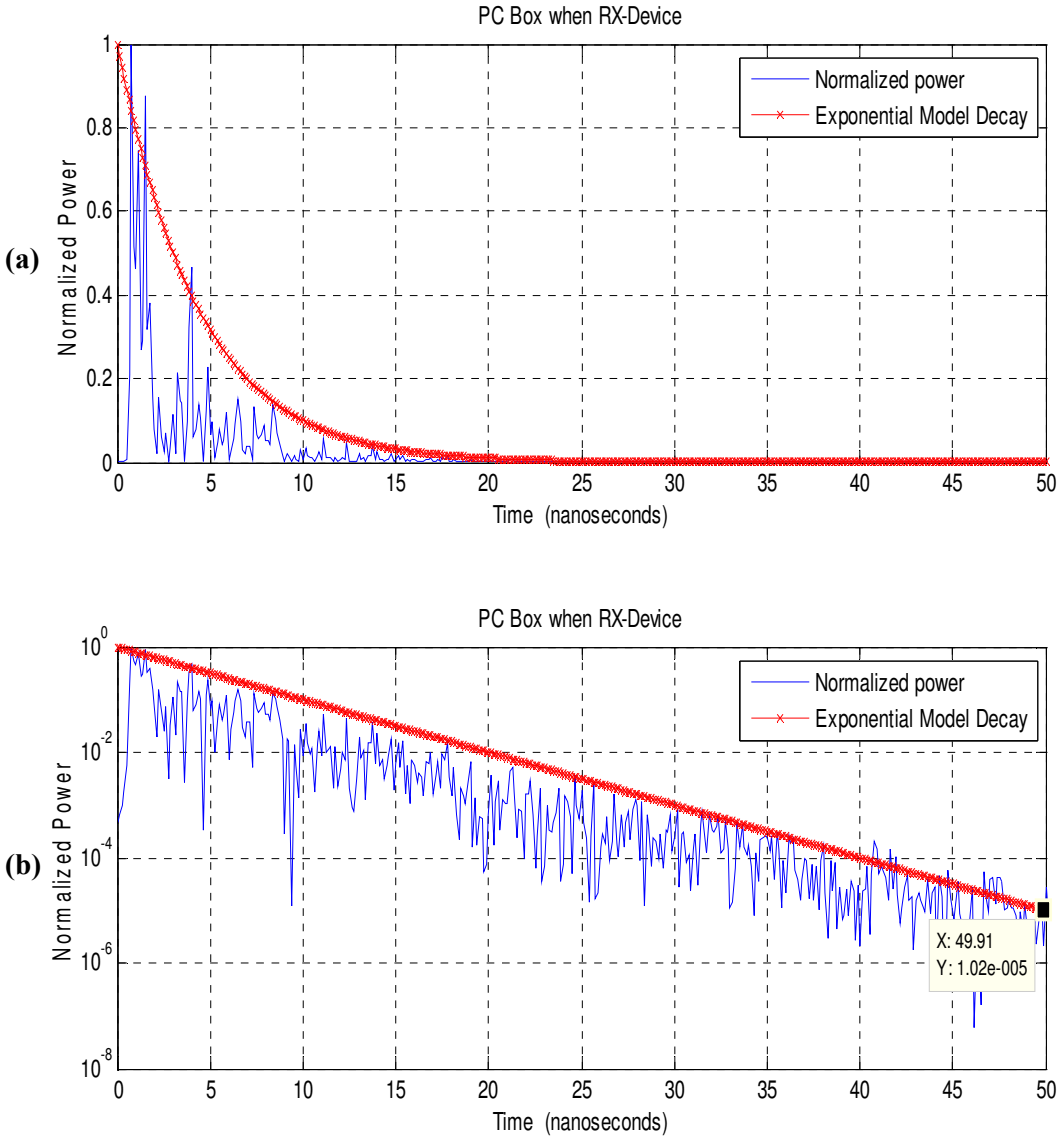


**Fig.5.9. Normalised APDP of the PC Tower, (a) on a linear scale and (b) semi-logarithmic scale**

One parameter of small enclosures under scrutiny is the density of multipaths resulting from the reduced environment size, and the effect this has on the ability of RX to distinguish between these different components within clusters. Furthermore, due to the rapid decay of power inside the cavities (less than 20 ns), the typical identification of clusters by visual inspection [26] becomes impossible. Figure 5.9 illustrates a single exponential model decay which represents the decay of the overall power (inter-cluster decay). This power decay in linear scale (Fig.5.9.a) is found to be 4.34 ns and is very close to the 5.44 ns and

3.49 ns values previously calculated in [10]. This author, like Karendal *et.al* [10], believes that a single exponential decay model is sufficient as a simpler approach to the APDP; thus

$$APDP \propto e^{-\tau/\Gamma} \tag{5.7}$$

Figure 5.9.b and Figure 5.8.b illustrate the power decay on a semi-logarithmic scale, which is presented as a linear decay. The values included inside the plot represent a power decay of 0.05 dB/ns for an empty aluminium box, and 1 dB/ns for the PC Box. These values of the modeled exponential decay correspond very well to the ones established by visualisation in sections 5.3.1 and 5.3.2.

The next section investigates two different linear approaches of the APDP in order to prove that this linear decay (exponential decay on a linear scale) is a sufficient and valuable approach to modelling the power decay, even when the cavity presents almost perfect resonance ('Empty Case' scenario).

### 5.3.5. Possible Approaches to Evaluate the APDP

Two different approaches are considered in this section with the aim of modelling the power delay profile. The main physical reasons for decay are reflectivity and enclosure size. The antennas themselves and their orientation also play an important role in this matter as shown in previous sections 5.3.1 and 5.3.2. In those sections, however, the polarisation adopted by the antennas was not taken into account.

Firstly, a study of reflectivity using simulations of the environments created by ray tracing (tiling model) is presented in addition to real measurements inside the aluminium cavity to try to explain the familiar linear decay profile (as seen on a semi-logarithmic scale). Secondly, a simple geometrical model is considered as a preferred approach to the APDP.

#### *5.3.5.1 Reflectivity Approach*

In this section a model based on the reflectivity of the environment is presented using the tiling algorithm explained in section 4.3. A very detailed description of the model used also appears elsewhere [113]. However, for these simulations, certain changes are included, related to power decay as the inverse of the square of the distance ($1/d^2$) [115]. This expectation is also explained by the Friis equation [115].

As explained in Chapter 4, when an electromagnetic field is excited inside a small rectangular conducting chamber, the chamber can be considered as a resonant cavity [107]. As such, this cavity will support a number of modes depending on the position and frequency of excitation, and the physical properties of the walls. Such a resonator will support waveguides modes which form standing waves [118], these distributing energy throughout the chamber according to the modal distribution. These waves travelling along the case might create constructive or destructive (fading) interference [103-105]. As a result, the path loss (PL) can vary significantly even for small displacements, meaning that these variations cannot be explained by the variation in path loss with distance. Thus the only losses taken into account in this tiling model for ultra small environments are due to the variations of the given value of the reflectivity coefficient ('r'), where PL due to distance is not considered.

In order to prove that assumption, a comparison between both hypotheses (the Friis Model - expectation of $1/d^2$ fall-off power - and the Non-Friis Model), and experimental data from the 'Empty Aluminium case' are presented (Fig.5.10). A deterministic value of 'r' (0.985) is used to fit the linear decay (semi-logarithmic scale). This high r coefficient is reasonable because the aluminium case is almost perfectly reflective, with the only possible losses being due to the apertures in the walls of the server for locating the antennas. It is

known that the ‘r’ coefficient is inversely proportional with power decay; the less reflective the environment becomes (small ‘r’ values), the more rapid loss in power is expected.

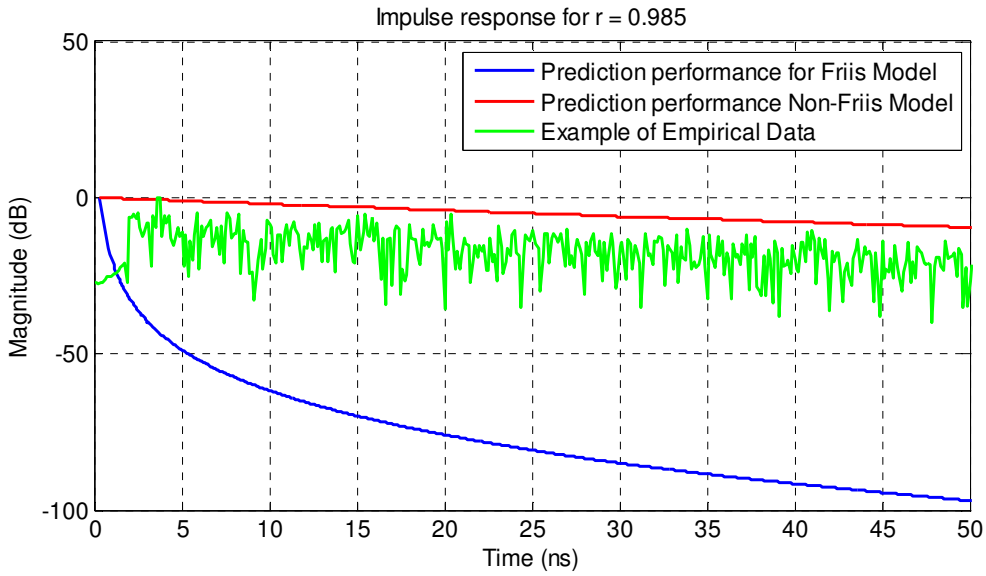


**Fig.5.10. Comparison between different reflectivity model hypotheses and the APDP measured inside the ‘Empty Aluminium Case’**

Figure 5.10 shows that the prediction of the non-Friis model is the best fit of the two. This could be due to the formation of standing waves within these very small cavities, and that the (slow) power loss can only be due to internal reflections.

A simulation of this phenomenon is illustrated in Figure 5.11, where different reflection coefficients are given for the volume (in this case the volume of the PC Tower case).

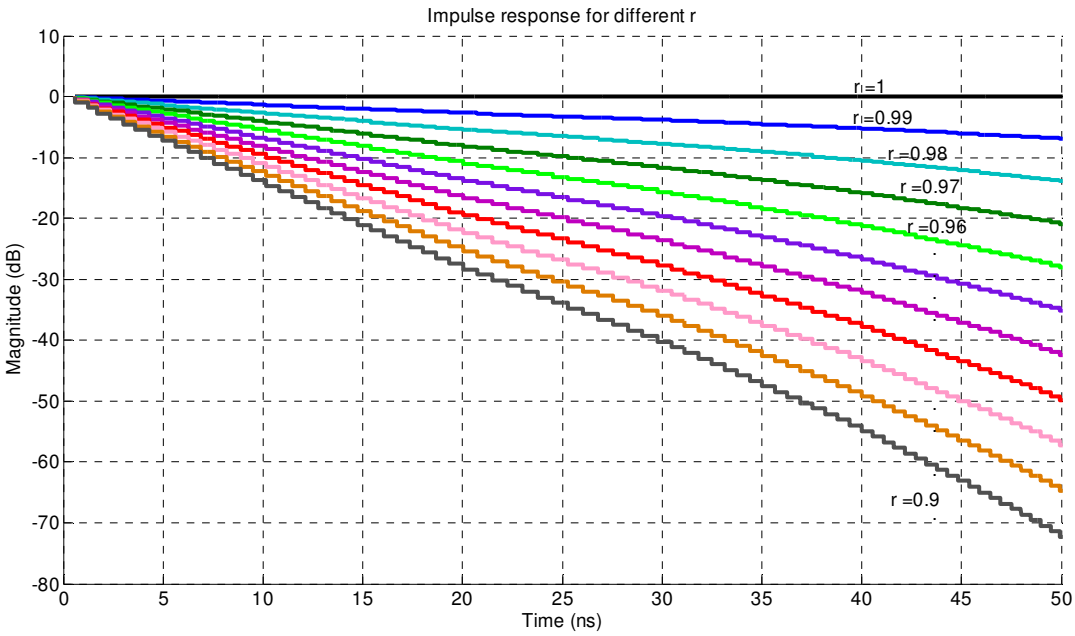


**Fig.5.11. Predicted performance from ray tracing simulation, showing different APDP decays once the reflection coefficient decreases**

It appears that in Fig 5.11 for the given volume of the PC Tower case (44 x 42 x 15 $cm^3$), the decay follows a pattern of ~7 dB decay per hundredth of 'r'. This means that the decay of ~1 dB/ns (or 50dB/50ns) calculated in section 5.3.1, corresponds with a reflection coefficient of r = 0.93. Thus, the PC Tower box could be modeled as an empty reflective environment with an 'r' of 0.93. For a theoretical environment where r = 1 ('perfect' internal reflectivity) there is no power loss, and the decay profile is flat.

In the case of the Aluminium Box, the volume of our server is different (65 x 70 x 30 $cm^3$), and a different decay pattern will therefore be observed: for a given 'r' value, different power decays occur with different volumes. A graphical example of this phenomenon is presented in Fig.5.12 for a given reflection coefficient of r = 0.97.

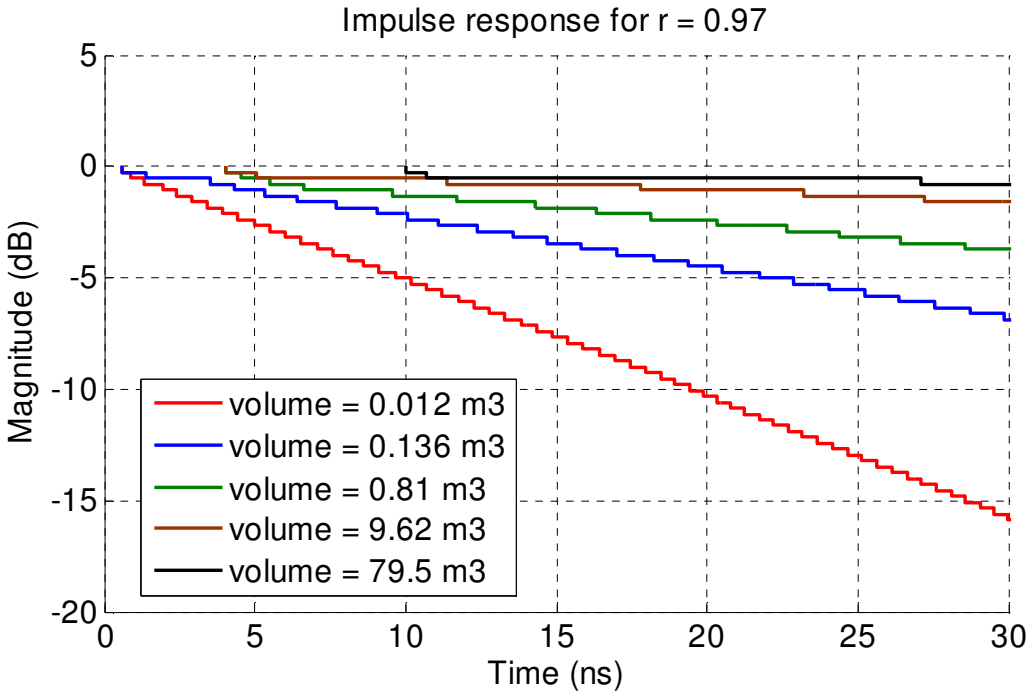


**Fig.5.12. Predicted decay of power for different internal volumes with a reflection coefficient 'r' of 0.97**

This data shows that decay is quicker in smaller environments – for example, a decay of 5dB takes twice as long in a volume of 0.136 $m^3$ as it does in a volume a tenth of the size (0.012 $m^3$). Note, both take the same number of reflections to decay to the same magnitude (dB), but over a different time course. Thus, Fig.5.12 presents a graphical simulation of the variation in the power decay with volume (for a given 'r' coefficient).

A further observation is the variation in times of arrival of the first path. In the largest case (79.5 $m^3$), the first path arrives after 10 ns, corresponding to a distance of 3 m between the virtual source and the RX. In contrast, for the lower volume, the first path arrives after 2 ns, corresponding to a distance of 60 cm, this is due to a smaller path length in the smaller environment. This relatively simple model confirms the hypothesis that the higher the volume of a cubic case, the lower the decay in the magnitude of the power.

These results were then compared with actual data taken from measurements inside the 'Empty Aluminium case'. Various empirical volumes were adopted (with a constant 'r'

value) and the results were compared with simulated values for the same volumes. Figure 5.13.a shows the different APDP for each volume of the 'Empty Aluminium case' and its linear fits of power decay in the first 150 ns. Figure.5.13.b illustrates a comparison between the linear fits (semi-logarithmic scale) of the normalized APDP of the empirical data taken from Fig.5.13.a and the ray tracing model fits for the corresponding volume of each cubic case (dashed lines).

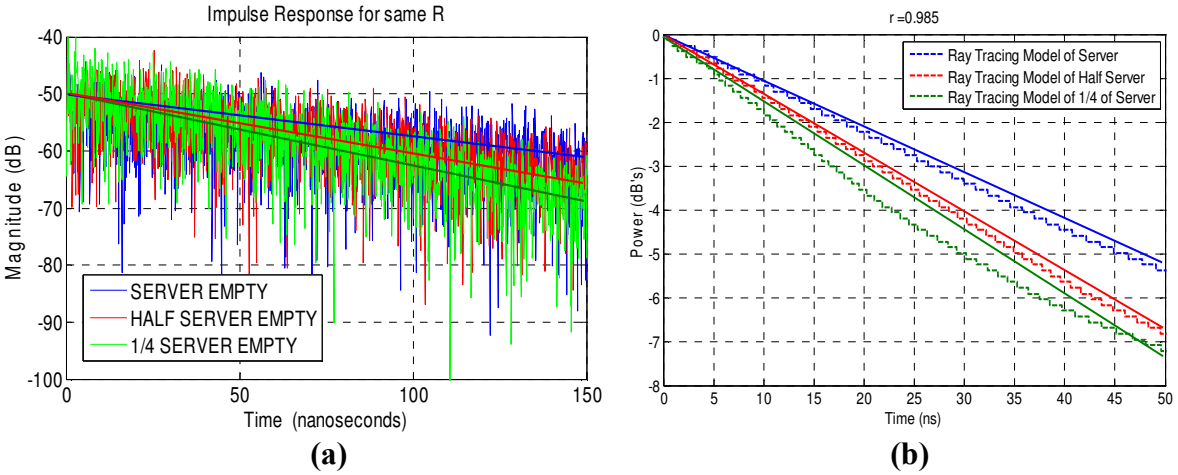


**Fig.5.13. Comparison of the APDP for each volume of the 'Empty Aluminium case' with:**
**(a) linear fits to the data in semi-logarithmic scale**
**(b) the comparison of these normalised fits with the ray tracing model of power decay using inside identical volumes of the cubic cases (dashed lines)**

The actual difference between volumes in Fig.5.13 is not large, although is enough to demonstrate that the smaller the volume, the faster the power decay rate (higher decay constant). Figure 5.13.b shows a very similar trend between simulations with an r = 0.985 and the empirical results, making the tiling model a good approach for the 'Empty' cubic cases.

The model becomes less accurate once the cubic case is populated with different devices (e.g. MB, PCB cards, and cables). This is in part due to the decreasing ratio between cavity and card volume once the case gets smaller. Thus, the reflectivity nature of the cavity

changes considerably, making this model an inappropriate choice for this kind of scenario. An example of this phenomenon is shown in Fig.5.14, where the Aluminium case is now filled in with the 8 PCB cards ('Full Case').

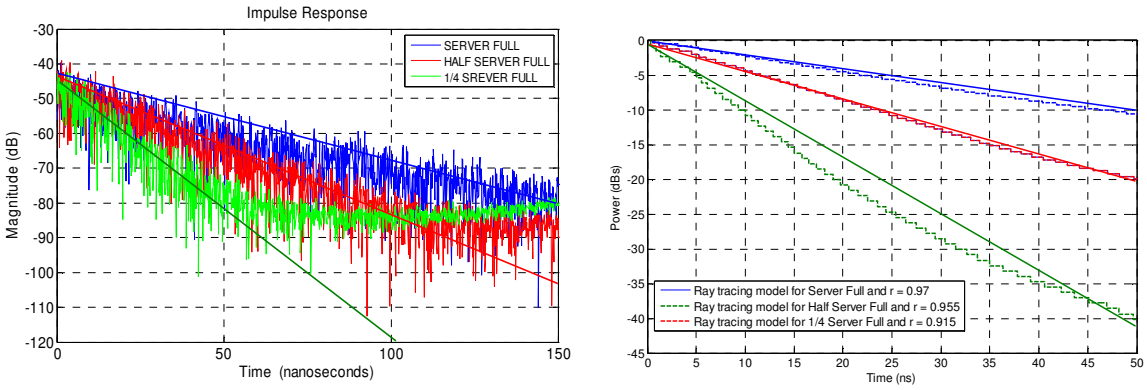


**(a)** **(b)**

**Fig.5.14. Comparison of the APDP for each volume of the 'Full case' with:**

**(a) linear fits to the data in semi-logarithmic scale**

**(b) the comparison of these normalised fits with the ray tracing model of power decay using inside identical volumes of the cubic cases (dashed lines)**

Figure 5.14.a shows a similar trend to that observed in 5.13.a, where the lower the volume the steeper the slope of power. This time the difference between decays is higher compared to the one in Fig.5.13.a, due to the presence of absorbing materials (PCBs). Figure.5.14.b includes different ray tracing fits according to the different sizes of the case. This time, different values of 'r' are needed to model the empirical results of APDP. This is because each volume, populated with different devices (PCBs, MB, cables) with different physical properties will have a different impact on the channel.

In order to fit the APDP of the 'Full Case', a reflection coefficient of 0.97 is needed. In contrast, once the 'Full case' is reduced to a half size, the 'r' value needs to be decreased to 0.955 to achieve a satisfactory fit of the APDP to the empirical data. Therefore, once the cavity becomes populated with its different size versions, prediction of the reflection coefficient becomes very difficult.

Finally, this model is only appropriate for small empty resonator cases, where small volume variations do not affect the reflectivity. Once the case gets larger, this model becomes inappropriate since, at that point, path loss over distance is no longer irrelevant (i.e. ray-like behaviour).

#### *5.3.4.2. Geometric Model Approach*

The second approach considered to model the APDP consists of a simple geometric model in which the power decay is believed to follow a geometric series. A geometric series is one in which there is a common ratio between each element and the one preceding it [76]:

$$a + ar + ar^2 + ar^3 + .. + ar^{N-1} = \sum_{i=0}^{N-1} ar^i = a\frac{1-r^N}{1-r} \tag{5.8}$$

where $a$ is the first term of the series, $r$ is the common ratio and $N$ is the number of multipath components.

In order to evaluate these values the behaviour of the PDP from empirical data has to be evaluated in more detail. Hence the PDP is averaged (and normalised) from all the measurements made on the grid for all different RX positions and polarisations. Then, the mean and standard deviation of APDP and excess delay can be calculated. This study is presented in Fig.5.15.

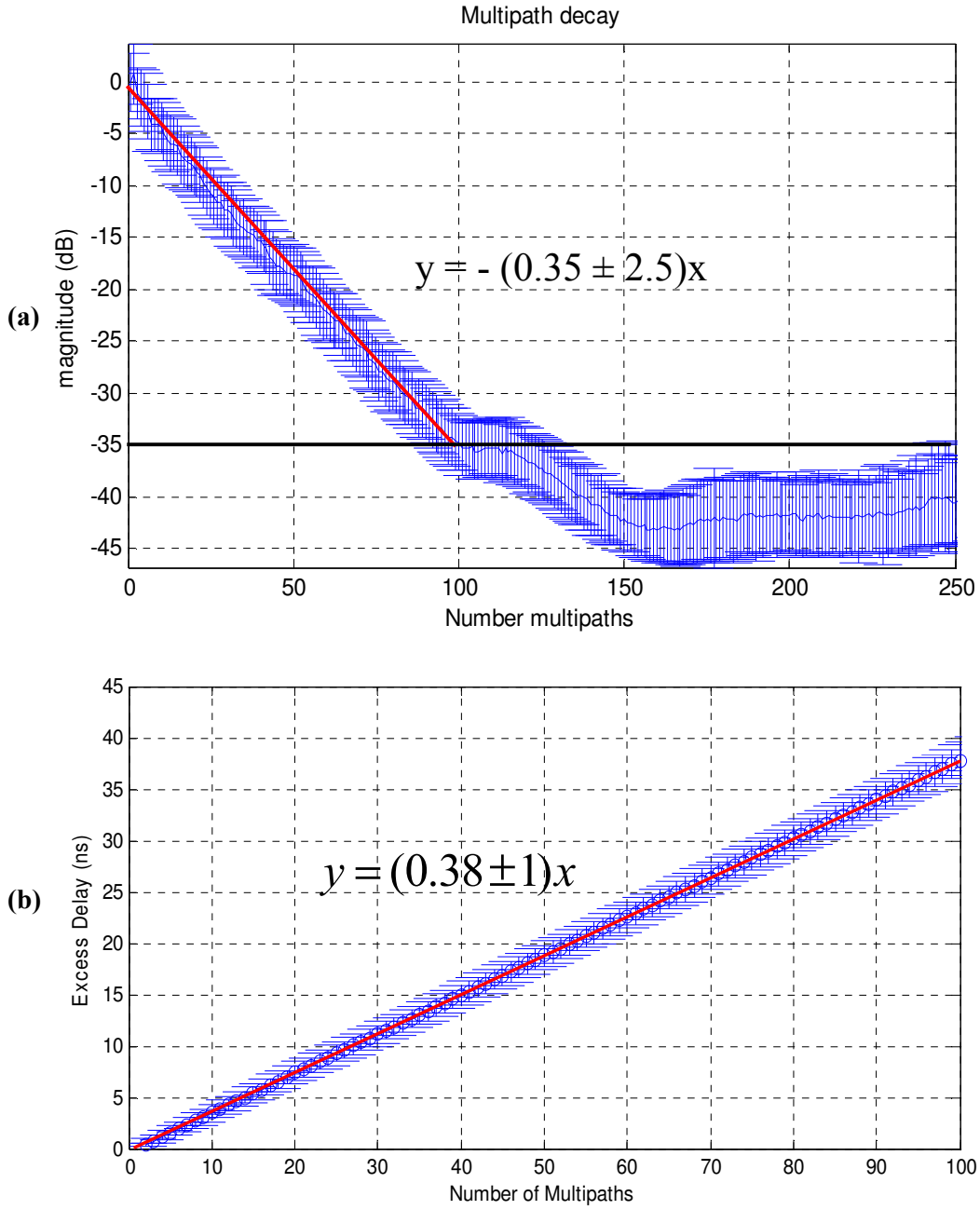


**Fig.5.15. (a) Average and standard deviation of normalised APDP and (b) excess delay for the first 100 resolved multipaths**

An almost perfect linear decay (on a semi-logarithmic scale) is observed in Fig.5.15.a for the first 100 multipaths, indicating that the power decay does indeed follow a geometrical series, at least initially. The averaged power decay presents a normal distribution of 0.35 dB per multipath resolved, with a mean standard deviation of 2.5 dB. However, after about 100 resolved multipaths, power transmission is considered irrelevant. The excess delay appears

normally distributed with a mean delay of 0.38 ns and with a mean standard deviation of 1ns. For the sake of simplicity, a 0.38 ns/multipath constant value is taken as the delay between consecutive multipath. The same occurs with APDP, where decay (ζ) is 0.35 dB/multipath. Thus, the power decay in dB/ns units is calculated as follows:

$$power\_decay(dB/ns) = \frac{decay\_time\_cte(dB/mult)}{delay(ns/mult)} = \frac{\zeta(dB/mult)}{\Delta\tau(ns/mult)} \tag{5.9}$$

Then, the power decay inside the PC Tower case is 0.92 dB/ns, which is reasonably close to the calculated one of ~1dB/ns. A graphical representation of the geometrical model of the power decay per multipath is presented in Fig.5.16 giving a demonstration of the decay behaviour of the power on a semi-logarithmic scale:

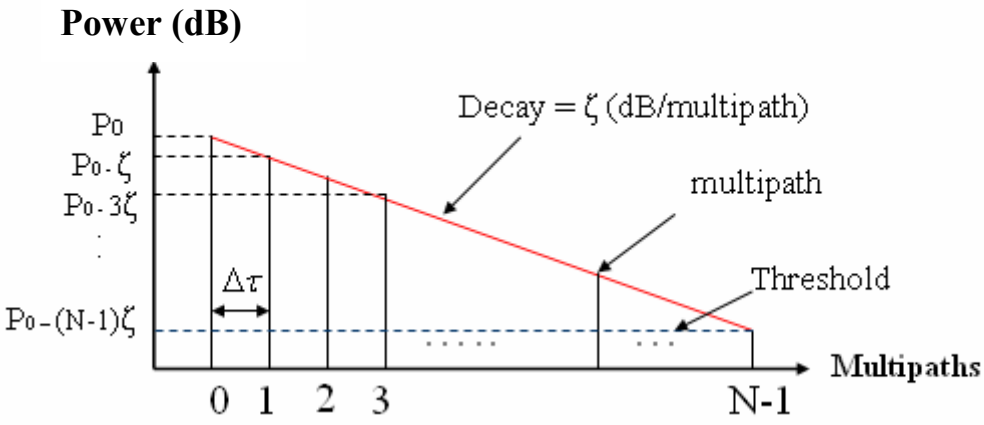


**Fig.5.16. Graphical representation of the power decay per resolved multipath**

where $P_0$ is the Power of the first path detected, which represents the first term of the series. Then the total power is the sum of the calculated detected multipaths until the threshold is reached, which in this case is translated to the first $N = 100$ multipaths. Thus, the power is represented as follows:

$$P_{total} = P_0 + (P_0 - \zeta) + (P_0 - 2\zeta) + (P_0 - 3\zeta) + ... + (P_0 - (N-1)\zeta) \tag{5.10}$$

Now, for the sake of simplicity, the decay will be presented in linear scale by γ, hence $\gamma = 10^{\zeta/10}$ (dB transformation of the decay in log scale ζ). Also, $P_0$ is considered to be 0 dB (normalised power). Then, Eq (5.10) can be written in linear scale as:

$$P_{total\_linear} = 1 + 10^{-\frac{\zeta}{10}} + 10^{-(\frac{\zeta}{10})^2} + 10^{-(\frac{\zeta}{10})^3} + ... + 10^{-(\frac{\zeta}{10})^{N-1}} = \\ P_{total\_linear} = 1 + \gamma + \gamma^2 + \gamma^3 + ... + \gamma^{N-1} \quad (5.11)$$

Eq (5.11) follows the same geometric series patterns as shown in equation (5.8), where the common ratio *r* is represented by the constant linear decay $\gamma = 10^{\zeta/10}$. The first term of the series *a* is considered to be unity. Thus, we can rewrite the equation (5.11) as follows:

$$P_{total\_linear} = \sum_{i=0}^{N-1} ar^i = \sum_{i=0}^{N-1} (10^{-(\frac{\zeta}{10})})^i = \sum_{i=0}^{N-1} (\gamma)^i = \frac{1-(\gamma)^{N-1}}{1-\gamma} \quad (5.12)$$

where $\gamma$ is the linear power decay per each detected multipath and *N* is the total number of multipaths. It is important not to forget that if our decay was expressed in terms of dB/ns, the decay might be multiplied by the constant delay 0.38 ns.

Once the total power is defined in equation (5.12), an interesting study would be to predict the increase of this power per multipath, or in other words, to analyse the number of multipaths necessary to approach the maximum value of the power. This type of analysis is very useful for future implementations of rake receivers [121]. Figure.5.17 presents a comparison of the normalised accumulated power calculated by the geometrical model and from empirical data from measurements inside the PC Tower.

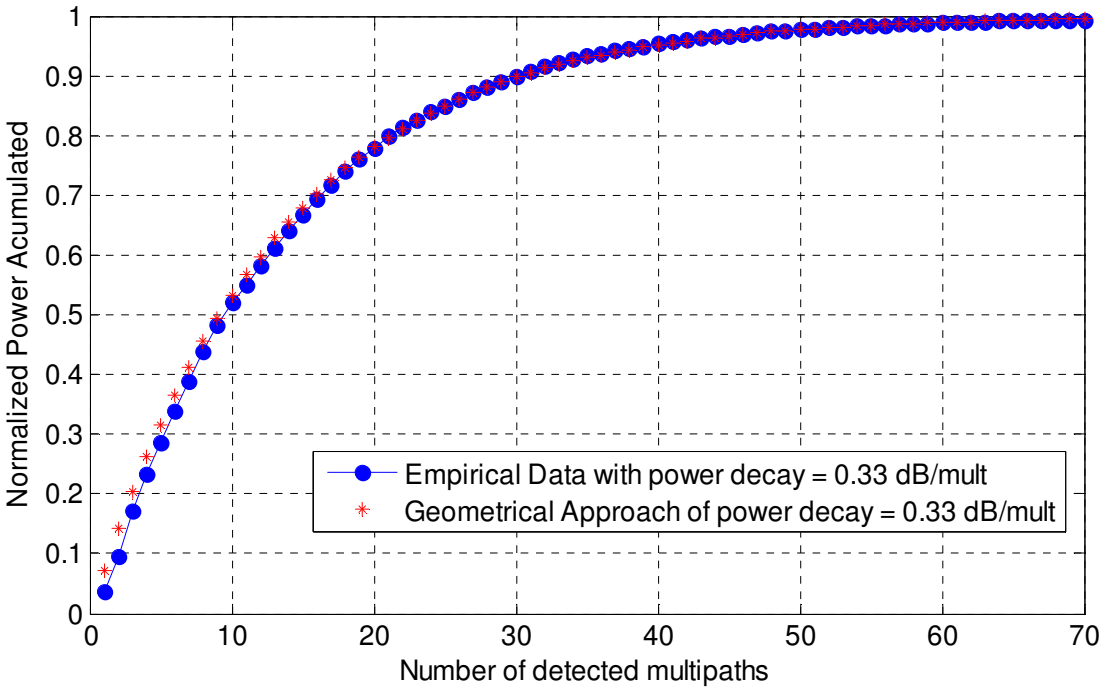


**Fig.5.17.A comparison of normalised power accumulation per resolved multipath between an example of empirical data measured inside PC Box, and the simulation from the geometrical model**

Figure.5.17 illustrates how a very similar trend in terms of power accumulation is followed by the geometrical model in comparison with the real data. The ratio assumed for the geometrical model is 0.33 dB/mult (~1dB/ns), corresponding to the real scenario of the PC case. This discovery verifies the assumption of the APDP following a geometric model, where the prediction of a linear decay (on a semi-logarithmic scale) is confirmed by the model. The slight difference between both lines might be due to the fact that in order to normalise the geometric model, the power accumulated by each multipath is divided by its limit of the geometrical series. This limit is calculated as follows:

$$\lim_{i\to\infty}\frac{1-\gamma^{i}}{1-\gamma}=\frac{1}{1-\gamma} \tag{5.13}$$

where $\gamma$ is the linear power decay. Thus, the normalised accumulated power from the geometrical series is calculated as:

$$\frac{Power\_accumulated}{Total\_Power} = \frac{\frac{1-\gamma^{N-1}}{1-\gamma}}{\frac{1}{1-\gamma}} = 1-\gamma^{N-1} \tag{5.14}$$

where the *Power_accumulated* comes from Eq (5.12) and the *Total_power* comes from the established limit of power in Eq (5.13), where the number of *N* multipaths is set to infinity.

To conclude this section it is important to bear in mind that from this model different investigation can be undertaken, such as investigating the ideal decay for a given volume, in order to simplify receiver architectures without losing too much energy. Prediction of the RMS delay spread and Ricean K-Factor for a given linear power decay would be very useful to know; hence they are presented at the end of this chapter.

### 5.3.6. RMS Delay Spread

The time dispersion of a channel is characterised in terms of the time delay spread, which depends on the location and composition of scatterers and the overall geometry of the propagation environment. The delay parameters are extracted directly from the power delay profile (PDP). The RMS delay spread ($\tau_{RMS}$) is the square root of the second central moment of the power delay profile [48]. As mentioned in Chapter 3, only the calculations of the RMS delay spread are presented in this section due to the fact it is considered sufficient in terms of the analysis of time dispersion. This parameter has been found to vary with distance [26], but due to the reduced distance between antennas within the enclosures, the mean value $E\{\tau_{RMS}\}$ could be considered sufficient to characterise $\tau_{RMS}$. However, Fig.5.18 shows the cumulative distribution function (CDF) of the RMS delay for each receiver location and polarisation in order to evaluate its variation.

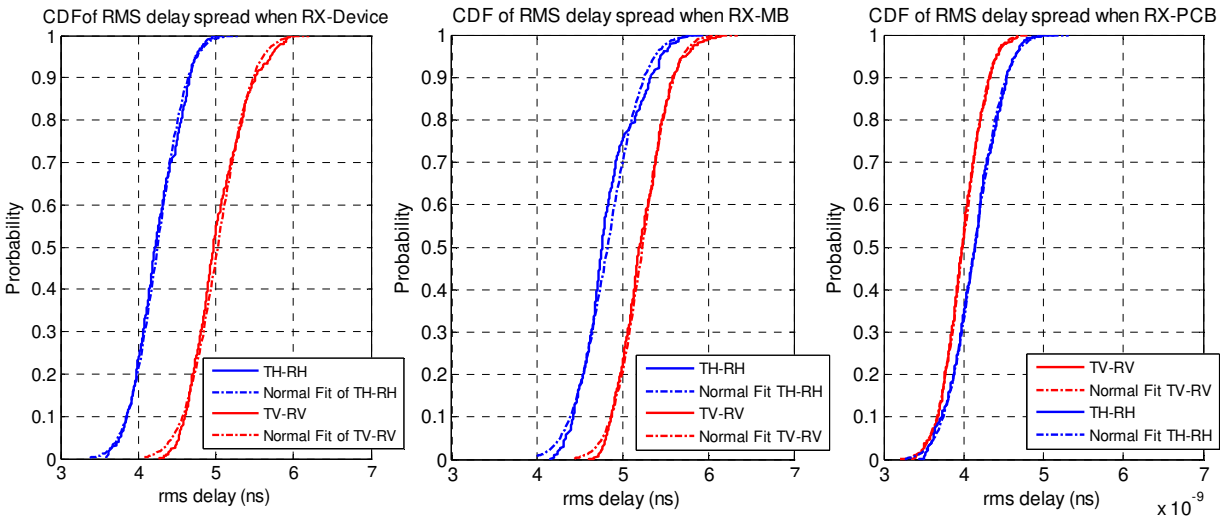


**(a)** **(b)** **(c)**

**Fig.5.18. CDF of RMS delay Spread across the whole grid when the receiver is located at**

**a) RX-Device**

**b) RX-MB**

**c) RX-PCB**

All cases in Fig.5.18 present similar values between both polarisations, where the median difference is less than 1 ns. In terms of time dispersion difference between RX positions, the TH-RH case does not change significantly between scenarios. In contrast, in the TV-RV case in Fig.5.18.c, there is a significant change of more than 1ns in comparison with Fig.5.18.a and Fig.5.18.b. The possible explanation for this is the higher proximity of both antennas in this case (see Fig.3.3.a). An average RMS delay spread is found to be around 4-5 ns, and it appears as though that polarisation does not have a dramatic effect. In practice, values of the $\tau_{RMS}$ depend on the choice of noise threshold used to process the PDP [48]. If this noise threshold is set too low, noise could be processed as multipath, thus giving higher values of the parameter. The threshold established to calculate $\tau_{RMS}$ is 35 dB, although it is reckoned that less than that would be enough to process the multipaths (20 dB) [26].

Subsequently, the values of the mean and standard deviation of $\tau_{RMS}$ for all different scenarios (PC Tower case and Aluminium Box) were calculated and presented in Table 5.1.

| RMS Delay spread *(ns)* | Scenario | Horizontal Polarisation (TH-RH) | | Vertical Polarisation (TV-RV) | |
|---|---|---|---|---|---|
| | | **Mean** | **Std.** | **Mean** | **Std.** |
| **PC Box** | RX-MB | 4.818 | 0.339 | 5.228 | 0.286 |
| | RX-Device | 4.248 | 0.308 | 5.025 | 0.354 |
| | RX-PCB | 4.137 | 0.307 | 4.001 | 0.255 |
| **Aluminium Box (Full + Absorber)** | Case | 12.16 | 1.213 | 13.17 | 1.677 |
| | ½ Case | 7.078 | 0.537 | 7.118 | 0.335 |
| | ¼ Case | 4.916 | 0.463 | 4.390 | 0.405 |
| **Aluminium Box (Empty)** | Case | 39.47 | 0.643 | 38.84 | 0.612 |
| | ½ Case | 34.22 | 0.903 | 34.17 | 0.846 |
| | ¼ Case | 28.61 | 0.705 | 28.59 | 0.665 |
| **Aluminium Box (Full)** | Case | 19.69 | 0.643 | 19.70 | 0.612 |
| | ½ Case | 10.82 | 0.404 | 10.41 | 0.317 |
| | ¼ Case | 6.601 | 0.609 | 6.522 | 0.349 |

**Table 5.1. Measured full-band UWB channel time dispersion statistics**

As mentioned previously, the mean value for the calculated delay inside the PC box varies between 4-5 ns without substantial variations in mean and standard deviation (around 0.3 ns) between polarisations. The same trend is followed by the other cases, where the difference in values between polarisations is negligible. However, the difference in $\tau_{RMS}$ between scenarios is very significant: an example is when the mean value $E\{\tau_{RMS}\}$ = 39.47 ns of the Aluminium empty box compared with a difference of more than 20 ns once this same scenario becomes populated with PCBs and absorber (12.16 ns). Once the size the enclosure is reduced, a substantial drop in delay also appears. It seems that the higher the resonance of the environment, the higher the value of $\tau_{RMS}$; hence, $\tau_{RMS}$ *could* be an indicator of resonance within these small enclosures. This makes sense since the values of $\tau_{RMS}$ depend on the actual slope of the power over time. Of special interested is the fact that once the size of the Aluminium is reduced (to a similar volume to a standard PC), with the inclusion of the PCBs and EM absorber, the value of the RMS delay becomes reasonably close to the one calculated

inside the PC Tower case. Thus, similar power decays in both scenarios are expected to be found.

The different values of $\tau_{RMS}$ differ substantially across the various scenarios, and their validation becomes an important issue. Of note is the value calculated inside the PC Tower case. This has a mean $\tau_{RMS}$ of ~ 4.5 ns, which differs substantially from a mean $\tau_{RMS}$ of ~ 23 ns reported previously in a similar scenario [11]. Due to this significant difference between values of this parameter, the author believes that a prediction of $\tau_{RMS}$ for a given power decay (dB/mult) becomes substantially useful to check if the empirical values are logical. In order to verify this prediction, the RMS delay spread was calculated using the APDP geometric model presented in section 5.3.4.2. Figure 5.19 presents this prediction where the real values of $\tau_{RMS}$ from Table 5.1 are also included.

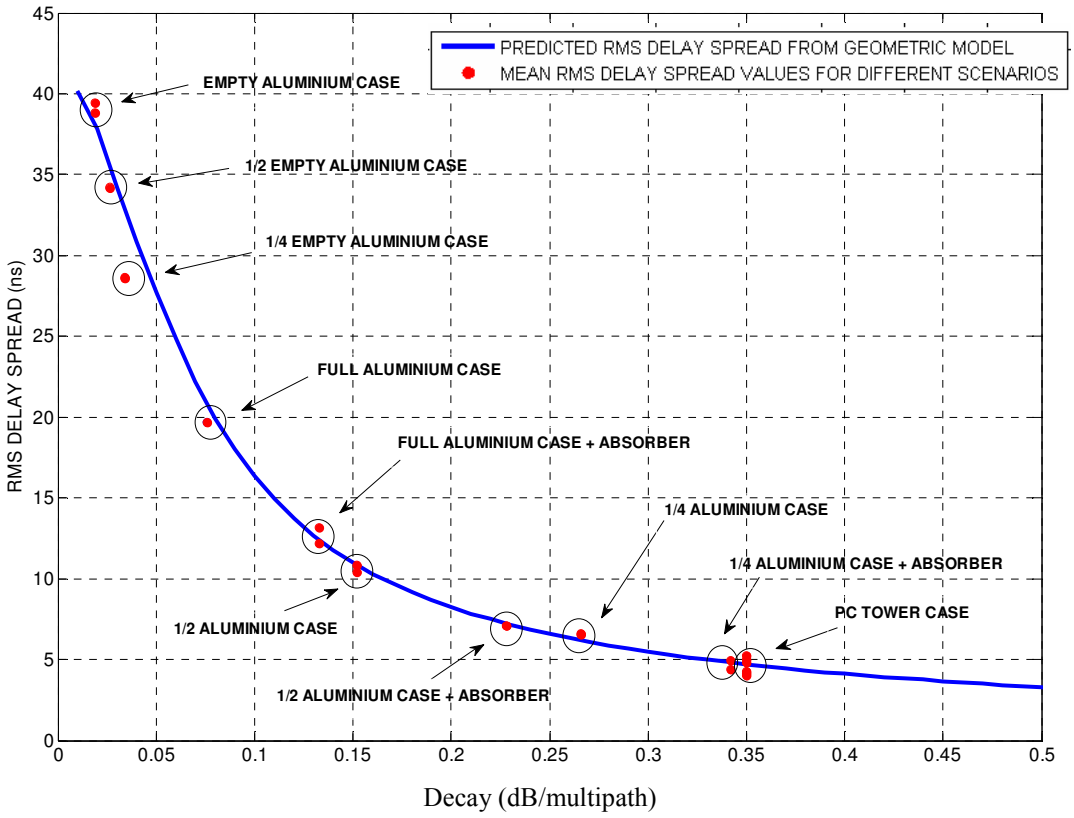


**Fig.5.19. Predicted RMS delay spread from geometric model for a given power decay (dB/multipath). Red dots represent the different mean RMS delay values calculated from empirical data**

Figure 5.19 shows the predicted exponential decay (on a semi-logarithmic scale) of the RMS delay spread for a given power decay (dB/mult) and the correlation with the real values calculated from measurement sets. A very good match between both trends is observed and the error between them is negligible; hence Fig.5.19 verifies the results calculated inside the cavities. Furthermore, it shows that the geometric model is a very good approach to modelling the APDP in these kinds of environments.

## 5.4. Ratio between Dominant Path and Reflections (Ricean K-Factor)

Considering that line-of-sight (LOS) paths are present inside the enclosures, the aim of this analysis is to give an idea of the nature of these confined environment. Low K values indicate that the majority of the received signals are reflected; high values indicate a free space path where only the direct components exist. Firstly, Fig.5.20 presents the different CDFs of the K-Factor inside the PC Tower box in order to evaluate its nature.

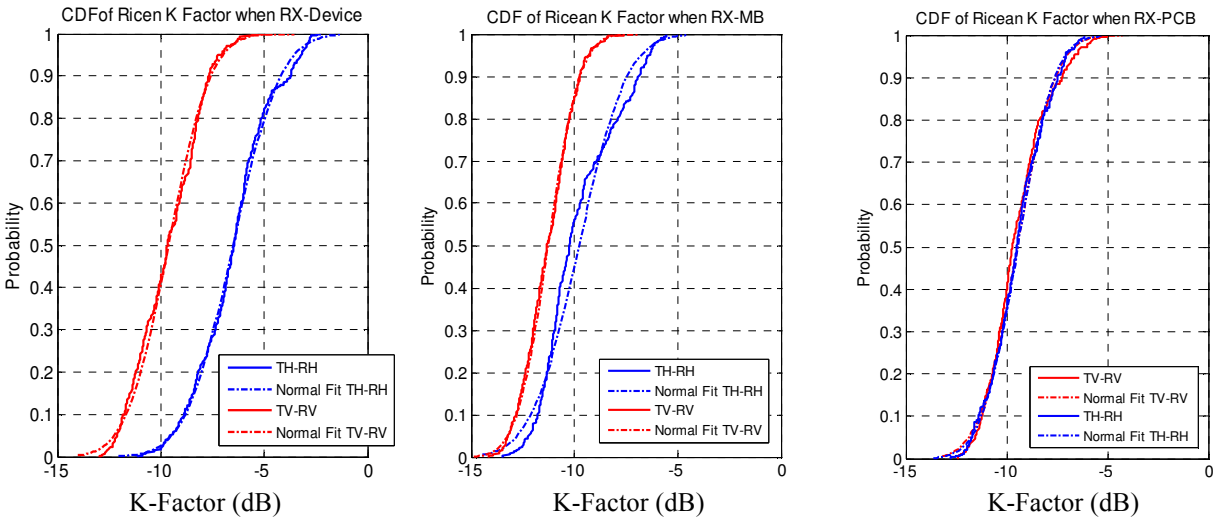


**(a)** **(b)** **(c)**

**Fig.5.20. CDF of Ricean K-Factor across the grid points when the receiver is located at**

**(a) RX-Device**

**(b) RX-MB**

**(c) RX-PCB**

The first impression from Fig.5.20 is that almost all situations have a mean K-Factor value of -10 dB. This corresponds to a transmission of only 10% of the total energy by the direct path, the remainder coming from multipath reflections. Furthermore, once the receiver antenna is located in RX-MB (Fig.5.20.b), some of the values of K-Factor only transmit 5% of the energy by the LOS path. Again, this can be accounted for by the shadowing effect of components of the MB. Figure 5.20.a shows that only once the antennas are horizontally orientated (TH-RH), does a significant proportion (almost 25%) of the energy come from the direct path. The line-of-sight (LOS) nature gets stronger due to the bi-directional pattern of the antennas, especially once the TX adopts positions on the edge of the PCB cards where less shadowing between the antennas occurs. The actual analysis of the spatial distribution of the power transmitted is investigated in Chapter 6.

After the analysis of the Ricean K-Factor inside the PC box, it becomes apparent that this confined environment presents a highly non-line-of-sight (NLOS) nature, where an average of 90% of the energy comes from scattered paths. This conclusion indicates how reflective and scattering this environment truly is. Thus, if the antennas do not present a LOS configuration, the total energy received by the antenna relies entirely on multipath components (reflections). Ultimately, this presents certain challenges since complex receivers would have to be installed to detect all the indispensable reflected multipaths in order to capture the transmitted energy.

For this reason, the inclusion of absorbers inside these cavities becomes desirable. It is known that in order to increase the K-factor the $Q$ (Quality Factor) needs to be lowered by placing absorbers within the chamber [122]. This is because a higher number of absorbers decrease the number of reflections, and thus the LOS path becomes more valuable. In order to verify this phenomenon, Table.5.2 presents the different values of this parameter for all the different scenarios.

| Ricean K-Factor *(dBs)* | Scenario | Horizontal Polarisation (TH-RH) | | Vertical Polarisation (TV-RV) | |
|---|---|---|---|---|---|
| | | Mean | Std. | Mean | Std. |
| **PC Box** | RX-MB | -9.779 | 1.825 | -11.27 | 1.197 |
| | RX-Device | -6.501 | 1.807 | -9.629 | 1.594 |
| | RX-PCB | -9.441 | 1.416 | -9.470 | 1.472 |
| **Aluminium Box (Full + Absorber)** | Case | -9.561 | 3.343 | -9.656 | 2.342 |
| | ½ Case | -12.24 | 1.229 | -11.97 | 1.323 |
| | ¼ Case | -10.04 | 1.368 | -9.920 | 1.314 |
| **Aluminium Box (Full)** | Case | -12.15 | 3.377 | -11.35 | 2.213 |
| | ½ Case | -13.77 | 1.017 | -12.41 | 2.064 |
| | ¼ Case | -11.89 | 1.172 | -11.53 | 1.354 |
| **Aluminium Box (Empty)** | Case | -14.29 | 2.187 | -16.25 | 1.868 |
| | ½ Case | -14.05 | 1.675 | -17.96 | 1.250 |
| | ¼ Case | -14.49 | 1.758 | -16.33 | 1.380 |

**Table 5.2. Measured full-band UWB channel Ricean K-Factor statistics**

Ricean K-Factor values for a perfect resonator (Aluminium Box Empty) are very low, especially for TV-RV, where an extremely NLOS nature is noted: less than 3% of the power comes from direct paths, and the actual environment size appears not to influence the K values. This reiterates how important multipath components become for energy transmission. In contrast, as the Aluminium box becomes populated with PCBs, there is, as expected, a reduction of the K-Factor. Special attention is drawn to the standard deviation of the results for the 'Full case' scenario (> 3 dBs), in which certain grid points transmit almost 15% of the energy by a LOS path, and others only just above 3%.

Results for the Aluminium Box including the EMC absorber AB-5050 (plus the PCBs), supports a previous report [122], in which the greater the number of absorbing materials, the higher the value of the K Factor. The actual increase is an average of 2 dB in respect of the scenario without the absorber, with a median value of -10 dB. The results

including the PCBs plus absorber are actually very similar to the ones calculated inside the PC Box.

Finally, a comparison between the general trend of the Ricean K-factor predicted by the geometrical model of the APDP and the empirical values from this factor is presented in Fig.5.21.

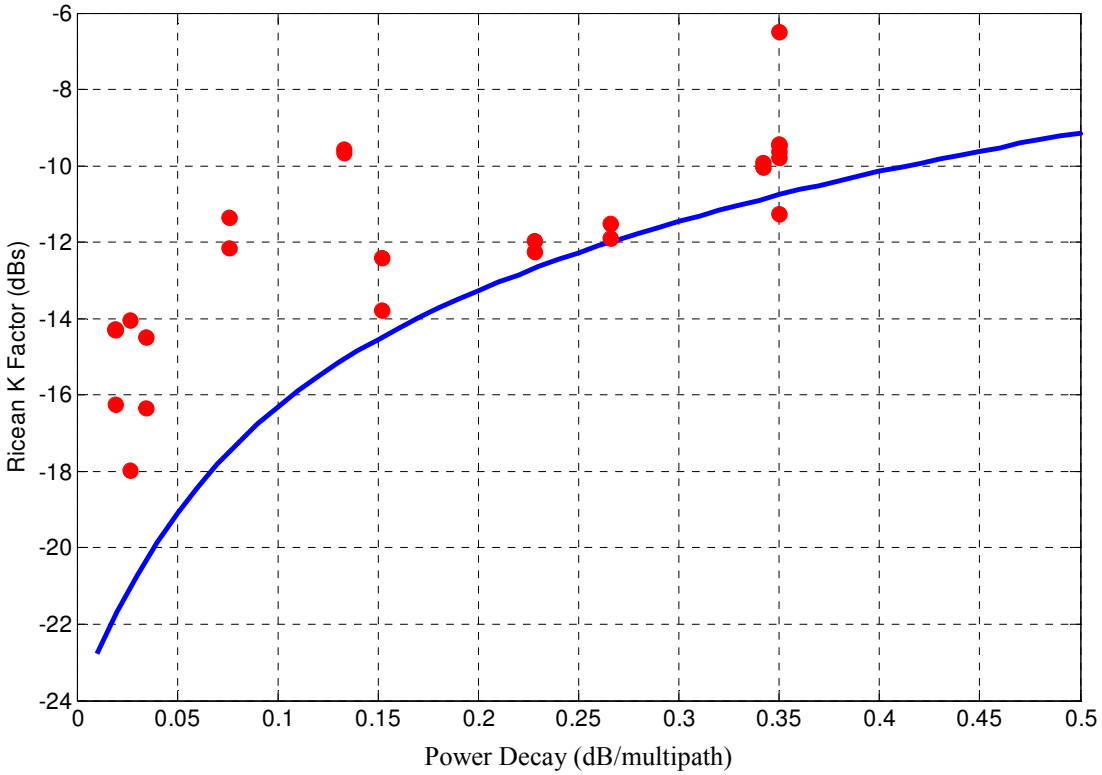


**Fig.5.21. Predicted Ratio between Dominant Path and Reflections (Ricean K-Factor) from geometric model for a given power decay (dB/multipath). Red dots represent the different Ricean K-Factor values calculated from empirical data.**

This time the match between the predicted ratio between dominant path and reflections (Ricean K-Factor) and the values from empirical data is less close, especially for the cases in which there is lower power decay (i.e. higher resonance). One of the reasons is the influence of antenna polarisation inside the cavities, where the radiation patterns of the antennas is a factor which is not represented by the actual geometric model. This emphasises the effect of antenna polarisation on the results, and finding the best approach to model this type of environment becomes extremely complex. However, the maximum error is around 6

dB for the '1/4 Full Case', which represents a difference of 1% in the power transmitted by LOS path. Thus, even in that case, the actual geometrical model describes the predicted Ricean K-Factor performance reasonably well.

## 5.5. Summary of Findings

This chapter has presented the frequency and time domain analysis of the measurement campaigns inside the PC Box and Aluminium case. Based on the analysis of the results, certain deductions can be made:

i. A difference in mean power received (~7 dB) is noted between different polarisations inside the PC Tower. In contrast, the difference of mean power inside a less complex Aluminium case is almost negligent. This gives an idea of the influence of antenna radiation patterns on the internal orientation of the electronic components (i.e. MB). However, positions of the RX inside the metallic structures did not affect significantly the mean power transmission once the RX is not adjacent to the MB.

ii. Frequency responses of the environments showed a resonator pattern along the band for horizontal polarisation (TH-RH), which this author believes is due to constructive interference created by a Bragg distribution [119] of the devices inside both cavities. This pattern disappears once polarisation of the antennas and/or the size of the environment are modified. This discovery explains the association between frequency selectivity and PCB separation distance. Results also showed that the more populated the environment becomes, the less resonance occurs in the overall system.

iii. Due to the reduced size of these enclosed environments and their internal reflectivity, very dense multipath reflections arrive in a very short period of time. Therefore, the

mean power decay depends very considerably on the actual size and reflectivity of the environment, it is steeper than the decay seen in a typical indoor environment, and it is reduced once the cavity becomes more resonant. Simulations of the power delay profile (PDP) of the environments modeled by *Microstripes*$^{TM}$ fitted very well with real measurements.

iv. Reflectivity is fairly uniform across the different scenarios. Thus, ray tracing simulations, for a range of reflection coefficients, showed a good match to the actual PDP. They verified that the standard $1/d^2$ power decay over distance is no longer expected. However, inclusions of absorbing materials were not considered in these simulations, thus correlation between coefficient reflections and engineered enclosures became significantly complex.

v. Averaged power (APDP) follows very similar exponential decay to the model from [26]. However, density of clusters encountered in these environments is extremely high due to the reflectivity of the metallic surroundings and the small dimensions of the enclosures. Thus, differentiation of clusters and ray arrivals inside each cluster cannot be distinguished by visual inspection. This author believes that a simpler model than the one presented by [11, 26] can represent the APDP of these channels. This model is based on a geometric series where the 'common ratio' is the power decay. A geometrical fit was considered because the APDP decreases monotonically – and the power decay of each subsequent multipath could be treated as a ratio of the previous one. This model was found to predict, with some precision, the results from time dispersion and Ricean K-factor.

*vi.* Time dispersion was interpreted by the RMS delay spread. Because of the small distance between antennas, this parameter varies greatly, and the mean value is

sufficient to characterise it. This factor was noted to be in the order of nanoseconds due to the reduced size of the enclosures, where its values are correlated strongly with the power decay of the channel (i.e. resonance of the channel).

*vii.* Finally, The Ricean K-Factor showed the dominant non-light-of-sight (NLOS) nature of the environments. Only best scenarios presented a 25% energy transmission via direct ray whereas in the majority of the scenarios, no more than 10% of the energy arrived by LOS path. This show how important the selection of the antennas (radiation patterns) might be if the transmission relies on reflections or direct path. Ricean K-factor results in [122] show that K is not generally dependent only on the number of absorbers in a reverberating chamber but also on their configuration. Therefore, for future studies, is not only important how many absorbers one includes inside the confined environment, but actually where these are located.

# Chapter 6: Power Loss and Capacity of the Channels

## 6.1. Introduction

This Chapter examines power loss and channel capacity of the confined environments of a PC Box and an Aluminium Resonator Cavity, and is divided as follows:

i. An in depth study of *large scale fading* (path loss) within the two small scale environments is performed.

ii. A more significant study of fading with reference to environment dimension is performed (small scale fading). In this section, spatial distribution (and standard deviation) of power is discussed. Simulation results from the fade depth model [105, 107] presented in chapter 4 are compared with the results from this empirical data.

iii. In the second half of the chapter the channel capacity is analysed. This is calculated for the whole bandwidth (3-11 GHz) with an assumed SNR of 25 dB at the source. At the beginning an aggregate capacity per multipath is compared to the overall data rate of SATA and PCI buses. This comparison is followed by an extended study of the ideal locations of the antennas inside both environments, where the spatial distribution of channel capacity for the full-band is presented for different scenarios inside the PC Box and Aluminium case. At the end of this part, a very interesting evaluation of the variation of the aggregate capacity once the aluminium case is engineered (change of size and absorber inclusion) is also included.

iv. A summary of the entire study is presented.

## 6.2. Path Loss over Distance

Path Loss (PL), defined as the division between the averaged received power and the transmitted power, depends on the distance (*d*) between TX and RX and the transmitted frequency (*f*). Path loss modelling can be simplified by assuming that frequency and distance act as independent variables with respect to the effect on PL [26, 48, 97, 98]:

$$PL(f,d) = PL(f)PL(d) \tag{6.1}$$

The frequency dependence of the Path loss is given as [26, 48, 97, 98]:

$$PL(f) \propto f^{-2k} \tag{6.2}$$

where *k* is the decay factor. The analysis of *PL(f)* was already studied in section 5.2. Thus, this section only covers the distance dependence of the path loss, usually modelled as power decay law:

$$PL(d) = PL(d_0)(\frac{d}{d_o})^{-n} \tag{6.3}$$

where *n* is the path loss exponent and $d_0$ is the reference distance in this research which is considered to be 1cm. This path loss exponent (*n*) depends on whether the propagating wave is NLOS or LOS and therefore varies according to the internal environment. LOS path loss exponents in indoor environments vary from 1 in a corridor [123] to about 2 in an office environment. In contrast, NLOS *n* exponents typically range from 3-7 [26]. Figure 6.1 presents the different PL(d) once the receiver antenna (RX) is located in its three different locations inside the computer for both polarisations. A linear regression fit for PL is given for each case.

**(a)**

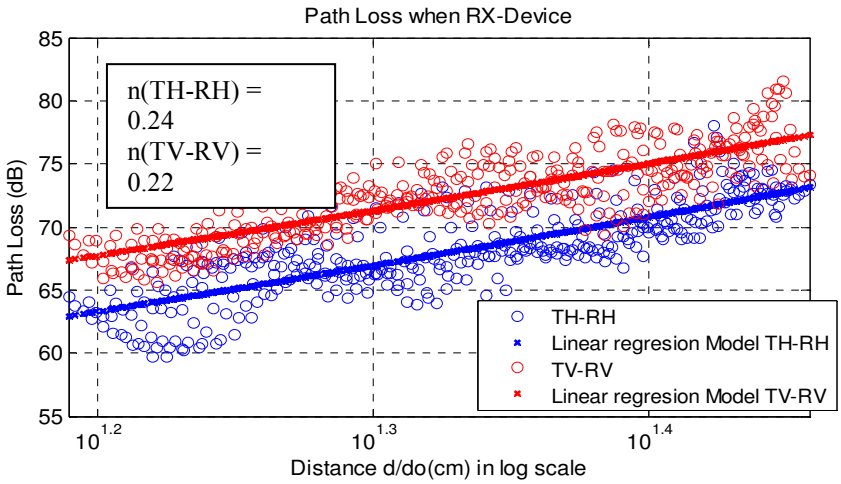


**(b)**

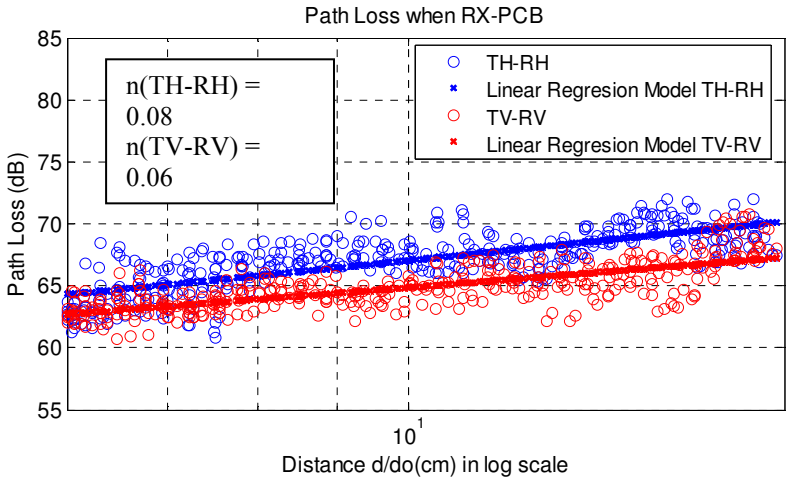


**(c)**

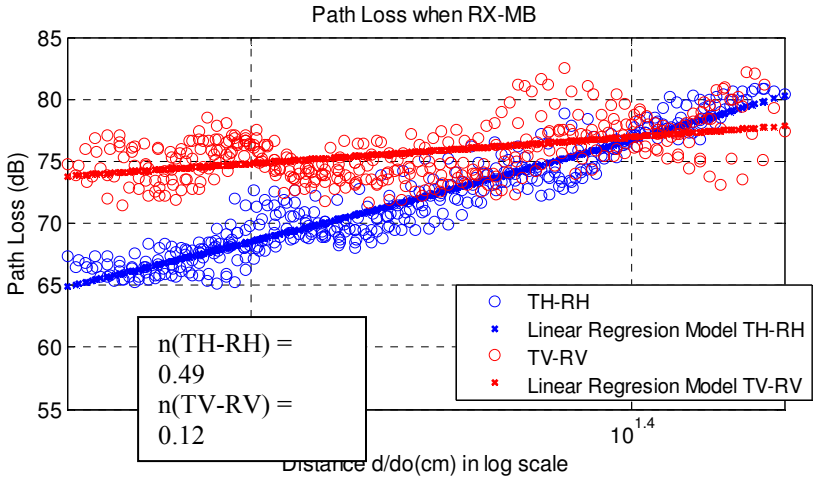


**Fig.6.1.Path loss (PL) comparison between both polarisations inside the PC Box with the receiver positioned at:**

**(a) RX-Device**

**(b) RX-PCB**

**(c) RX-MB**

Although the TX always adopts the same locations in the grid, the distance between terminals is different as the RX is located at the three different points inside the PC. These distances, ranging between 6cm and no more than 28 cm, all represent a far-field scenario, (near-field being slightly less than 1 cm)[1]. That is the reason, in order to separate between near and far field, that *1cm* was chosen as the reference distance ( $d_0$ ) in the *PL(d)* analysis.

From inspection of Fig.6.1 a similar behaviour between polarisations is detected once the receiver antenna is located at the RX-Device and RX-PCB (Fig.6.1.a and Fig.6.1.b respectively). Furthermore, PL(d) seems to have a slightly homogeneous difference between polarisations across the range of distances studied. The exception is when RX is at the MB (Fig.6.1.c), where the deviation between polarisations is substantially different. With TH-RH, a steeper averaged PL is observed than for the vertical polarisation case, thus the path loss becomes less negligible than in the other cases. A possible explanation is the highly shadowing effect by the elements on the MB, where once the TX is closer to the RX, higher possibilities of line-of-sight (LOS) nature might be identified due to the radiation pattern of the terminals.

The plots presented in Fig.6.1 are fitted by semi logarithmic linear regression as previously described [26], although this fit may not be appropriate for a complex internal environment. Figure 6.1.c in particular identifies waveguide behaviour which it is expected from the theory previously described (Chapter 4), where a semi-hybrid scenario is found inside the PC and waveguide modes can appear along the case due to the resonator-like behaviour. Previous authors have attempted to model the PL of a very similar scenario with a regression line and noted that not all points fitted onto the logarithmic linear regression line [9].

---

[1] $R = \frac{2D^2}{\lambda_{\max}} = \frac{2(2cm)^2}{10cm} = 0.8cm$

A more in depth study of the PL is also carried out inside the Aluminium box. Although it is recognised that simple linear regression is not adequate to model PL, Table 6.1 presents the values which *would* define the PL(d) from Eq.(6.3), on a logarithmic scale for different scenarios and both polarisations.

| Path Loss *(dB)* | Scenario | Horizontal Polarisation (TH-RH) | | | Vertical Polarisation (TV-RV) | | |
|---|---|---|---|---|---|---|---|
| | | n | Std. | PL(d) | n | Std. | PL (d) |
| **PC Box** | RX-MB | 0.49 | 4.27 | 15.78 | 0.12 | 2.17 | 51.90 |
| | RX-Device | 0.24 | 3.50 | 32.41 | 0.22 | 3.27 | 36.76 |
| | RX-PCB | 0.08 | 2.40 | 55.40 | 0.06 | 1.87 | 55.65 |
| **Aluminium Box (Full + Absorber)** | Case | 0.11 | 6.66 | 54.43 | 0.05 | 6.47 | 61.79 |
| | ½ Case | 0.1 | 7.23 | 44.94 | 0.06 | 5.98 | 43.83 |
| | ¼ Case | 0.25 | 7.29 | 27.87 | 0.01 | 5.18 | 51.73 |
| **Aluminium Box (Full)** | Case | 0.09 | 2.81 | 53.31 | 0.04 | 1.49 | 59.91 |
| | ½ Case | 0.09 | 2.80 | 41.19 | 0.03 | 1.48 | 46.72 |
| | ¼ Case | 0.37 | 6.61 | 18.88 | 0.06 | 1.83 | 41.96 |
| **Aluminium Box (Empty)** | Case | 0.07 | 1.53 | 51.97 | 0.1 | 1.96 | 48.63 |
| | ½ Case | 0.06 | 1.36 | 52.06 | 0.1 | 1.93 | 45.64 |
| | ¼ Case | 0.05 | 1.30 | 52.48 | 0.08 | 1.87 | 47.55 |

**Table 6.1. Measured full-band UWB channel Path Loss**

Table 6.1 shows that the path loss exponent *n* is less than 0.5 for all scenarios. This agrees with a previous report [11] where *n* is approximately 0.11 once both antennas are in the far-field. This value is significantly lower than any previously reported data [26], where the variation of PL(d) inside these small environments is almost flat. The explanation for this is likely to be due to reduced distance antennas inside the selected enclosed environments, and their highly reflective nature, where almost all the energy emitted is reflected back to the RX. Very little variation of *n* (and therefore standard deviation) is observed between the different scenarios inside the Aluminium box, except for when the Aluminium box is at its

smallest and most cluttered version. Again, the difference could be due to the higher shadowing nature caused by the PCB cards and that the moving wall being located just next to the PCB cards (a higher NLOS scenario). In other words, now the signal does not have as much free-space to bounce around the case in respect to others situations, where bigger gaps formed between PCBs and front wall used to appear. In addition, fewer resonant modes are excited due to the dimensions and topography of the system, which is translated to a higher difference in power decay depending on the antenna separations.

A great difference in *n* appears between both polarisations when RX-MB inside the PC Box. This author believes that this great variation might be due to the fact that, in this location, the RX is really blocked by different elements from the MB (i.e, fan), where the change of polarisation has a great impact in the PL exponent. This is an example where the linear fit of the PL does not appear to be a great approach to model this parameter.

Finally, PL(d) does not appear to obey the 802.15.4a standard model previously established [26] and the greatest influences appear to be antenna location and polarisation. Therefore, the normal relationship between PL and distance does not appear to hold true for this internal environment, where small scale fading appears to have a greater influence than large scale fading. As discussed in Chapter 4, in a small environment, minor antenna displacements towards, or into, resonant zeros can result in an abrupt change in energy.

## 6.3. Small Scale Fading Analysis

Power variation for small displacements of the TX within the grid is investigated using a small scale analysis. Malik *et al* define fade depth as three times the standard deviation of channel energy for a small spatial variation of the receiver/transmitter [103-105]. In order to calculate the fade depth it must be noted that the selection of the local area is essential. In order to remove the path loss effect, smaller areas of the grid are considered to

calculate the fading, where even a value of $4cm^2$ means a very small area, it becomes quite significant in our small environment. However, such an area must of course be large enough to contain the full variation of the energy caused by the multipath superposition.

### 6.3.1. Fade Depth Results

This section examines the fade depth calculations, derived from empirical data to determine its relationship between frequency, signal bandwidth, and environment size. Figure 6.2 presents the spatial distribution and standard deviation of power across the TX grid inside the PC Box for both low (3 GHz) and high (9 GHz) frequencies.

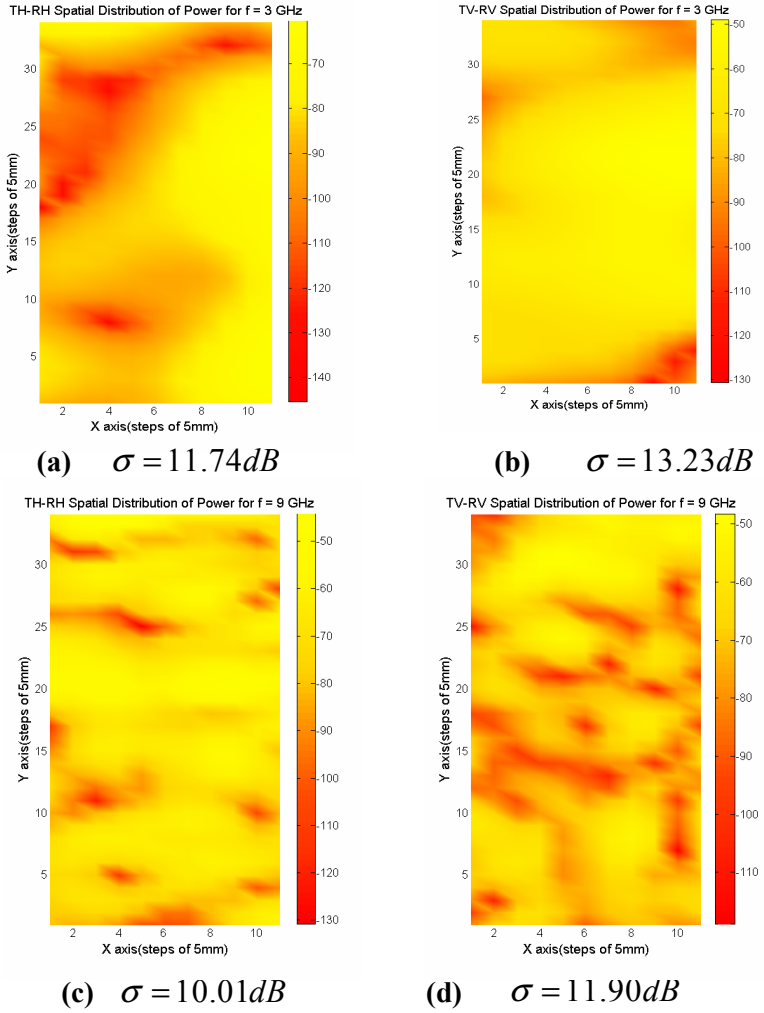


**(a)** $\sigma = 11.74dB$ **(b)** $\sigma = 13.23dB$

**(c)** $\sigma = 10.01dB$ **(d)** $\sigma = 11.90dB$

**Fig.6.2. Spatial distribution of Power inside the PC Box and its standard deviation when**
**(a) f = 3 GHz for horizontal polarisation** **(c) f = 9 GHz for horizontal polarisation**
**(b) f = 3 GHz for vertical polarisation** **(d) f = 9 GHz vertical polarisation**

Figure 6.2 clearly demonstrates the difference in signal distribution between lower and higher frequencies. The wavelengths of low frequencies (Fig.6.2.a and Fig.6.2.b) are much larger than the elements in the channel, and the relative size of the environment becomes smaller. Consequently, the resonant modes are sparse in frequency and there is a higher risk that a particular frequency will fall either between the resonances or there will be a risk of weak excitation due to antenna position in a resonant zero**.** Furthermore, power enhancement appears to occur when the antenna is closer to the aluminium wall, where almost all the emitted power is reflected. The fact that there is a gap between the aluminium wall and the TX grid also somehow excites waveguide modes of the empty section.

In contrast, with high frequencies (the shortest wavelength being 3.3 cm for 9 GHz, Fig.6.2.c and Fig.6.2.d), the scenario is different as the wavelength gets relative smaller in comparison to the environment. Many nodes appear this time well scattered across the grid.

The highest standard deviation of energy ($\sigma$) occurs at the lower frequency (3GHz), where $\sigma$ differs by ~1.5 dB between vertical and horizontal polarisations. Fade depth also decreases for larger frequencies, with a similar $\sigma$ decrease of ~1.5 dB seen between low and high frequencies for both polarisations, evidence that fade depth [103-105] decreases for larger frequencies [107]. This result is close to the ~1 dB difference from simulations in section 4.5.2.

Table 6.2 shows the different values of $\sigma$ for both PC Box and Aluminium Case as a function of signal frequency, these being 3 GHz, 5 GHz, 7 GHz and 9 GHz, as used in section 4.5.

| Standard Deviation of Power ($\sigma$ ($dB$)) | Frequency | Horizontal Polarisation (TH-RH) | Vertical Polarisation (TV-RV) |
|---|---|---|---|
| **PC Box** | 3 GHz | 11.74 | 13.23 |
| | 5 GHz | 11.53 | 13.21 |
| | 7 GHz | 10.43 | 12.36 |
| | 9 GHz | 10.01 | 11.90 |
| **Aluminium Box (Full + Absorber)** | 3 GHz | 12.97 | 13.15 |
| | 5 GHz | 11.55 | 12.25 |
| | 7 GHz | 11.53 | 12.35 |
| | 9 GHz | 11.36 | 11.89 |
| **Aluminium Box (Full)** | 3 GHz | 12.72 | 13.19 |
| | 5 GHz | 12.32 | 12.48 |
| | 7 GHz | 10.41 | 12.22 |
| | 9 GHz | 11.09 | 12.08 |
| **Aluminium Box (Empty)** | 3 GHz | 10.92 | 12.00 |
| | 5 GHz | 11.11 | 11.67 |
| | 7 GHz | 10.68 | 11.36 |
| | 9 GHz | 9.36 | 10.93 |

**Table 6.2. Standard deviation of Power for the increase of Frequency**

Table 6.2 shows that, in all cases, there is an inverse relationship between the standard variation of power and signal frequency, that is, fading is attenuated with increasing frequency. Fade depth ($3x\sigma$) [103-105] is similar across the different scenarios, with a reduction of 1-2 dB only when the Aluminium case is empty. This is a paradoxical finding because the more populated the environment, the fewer the multipaths and the less the environment behaves as a resonator. A plausible explanation is that the chaotic environment of the enclosure actually creates substantial random signal *propagation* with constructive interference resulting due to the location of the PCBs. That being said, all results remain fairly similar with maximum variation of no more than 3.5 dB.

For a narrowband system, there is a significant risk that the spectrum is not able to excite the electric field due to the antenna position/orientation or due to resonator properties. This means the bit-error-rate increases significantly due to the decrease of the SNR. This is

the reason behind the high values of the standard deviation of the power from Table 6.2, where even increasing the central frequency, the fade depth of the power of the channel is still reasonably high (mean standard deviation of ~12 dB).

Fade depth becomes less significant in a wideband system (> 500 MHz) inherently relying on frequency diversity. Spreading information over a larger bandwidth alleviates the impact of resonator-like behaviour due to more energy exciting more modes. Figure 6.3 shows the decrease of fade depth once the bandwidth is increased for all different scenarios and polarisations of the antennas.

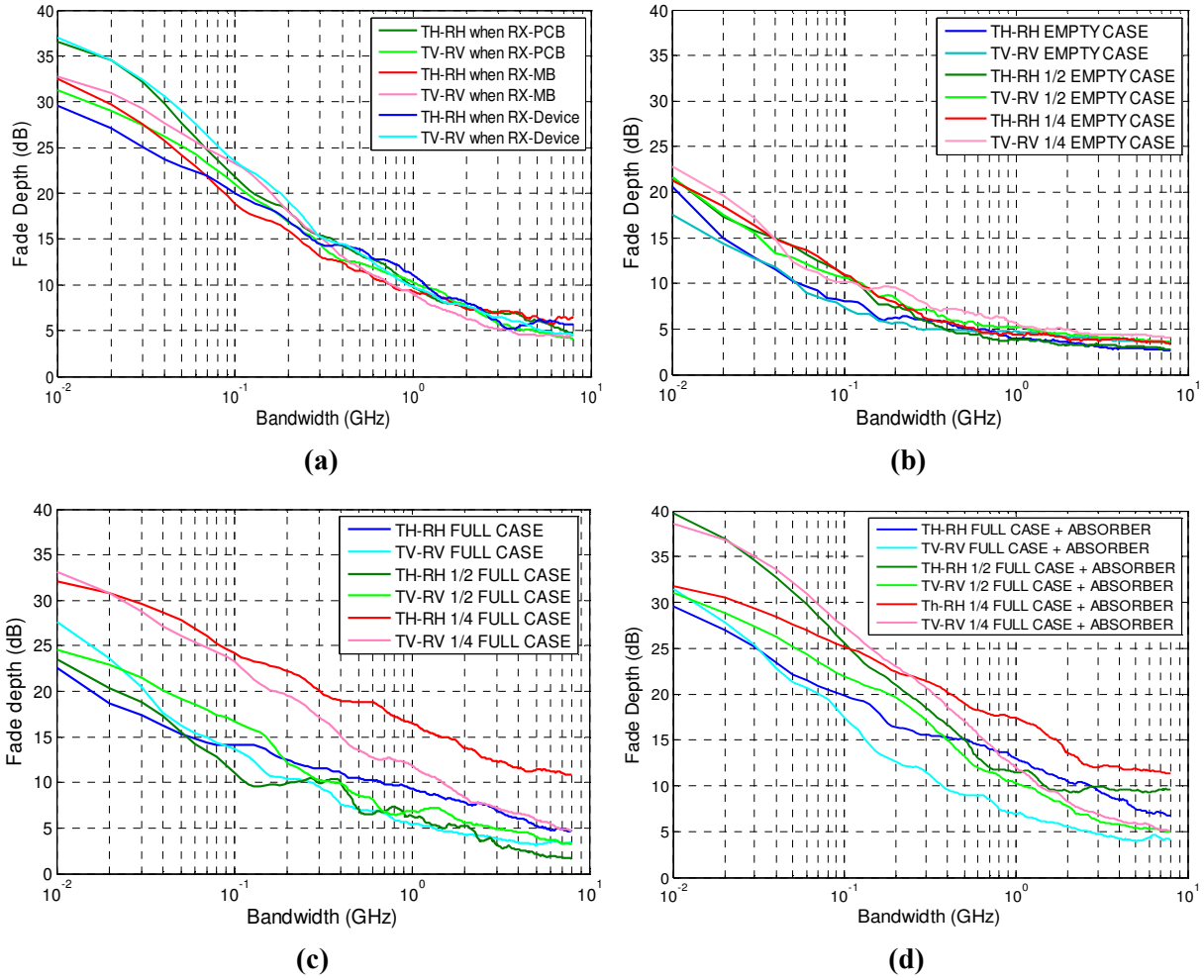


**Fig.6.3. Decrease of Fade Depth of the PC Box with the increase of bandwidth inside**

**(a) PC Box**

**(b) Empty Aluminium Case**

**(c) Full Aluminium Case**

**(d) Full Aluminium Case + Absorber**

A number of deductions can be made from the plots in Figure 6.3:

i. Variation of RX position (Fig.6.3.a) does not appear to affect massively the overall trend of fade depth, except for vertically polarised terminals which are associated with increased maxima values of fade depth for narrow bandwidths. This could be attributed to the influence of vertically orientated components within the MB.

ii. Fade depth maxima and minima differ substantially between different cases. Only with the empty aluminium box (Fig.6.3.b) does fade depth show little change between different scenarios with decreasing box dimensions. This finding becomes very important since the reduction of the empty environment seems not to affect dramatically the fade depth. Thus, diminishing the size of the Aluminium case (with a consequent reduction of resonant modes), does not cause a significant increase in fade depth.

iii. The fade depth values in this case match the simulated values (section 4.3.2) reasonably well, where fade depth was fitted by a model for enclosed environments. The volume for the Aluminium empty case is $0.136\,m^3$; thus, following the fade depth model calculated from ray tracing simulations, the different parameters are calculated as

$$\begin{aligned} BP &= 2.02V^{-0.351} = 4.07GHz \\ A &= 1.21V^{-0.292} = 2.16dB \\ B &= 10.51V^{+0.002} = 10.52dB \end{aligned} \tag{6.4}$$

where these values are close to the empirical results of Fig.6.3.b. Unfortunately, once the box is populated by different devices (MB, PCBs, cables, absorbers), the fade depth model from chapter 4 does not fit well to the different empirical results. This model was created from ray tracing simulations (with 'empty' enclosures) with a reflection coefficient of 0.9. This time, the environments are much more dense and

complex, and fitting the general trend of fade depth becomes very difficult. This is especially noted in Fig.6.3.c and 6.3.d, where the Aluminium case is engineered to contain PCBs and Absorber, and the actual behaviour of fade depth between different sizes of the box and polarisations of the terminals becomes less predictable.

iv. For all cases, an inverse relationship is noted between fade depth and bandwidth and, for bandwidths greater than 500 MHz (wideband), fade depth decreases by about 50% when compared to narrowband. Note is made of Fig.6.3.d where, for the smallest version of the Aluminium case for TV-RV, fade depth reduction approaches 35 dB between maxima and minimum values (around 85% of fade depth). This abrupt difference might be due to the reduced size of the environment, where time arrivals between multipaths are heavily reduced, hence a higher probability of interference between wavefronts (see section 4.2.2) for narrowband than for broadband systems.

v. Smaller Aluminium case scenarios are associated with the worst fade depth values for narrow bandwidth, this is verified in Figure 6.3 a/b/c/d. Furthermore, simulations in Chapter 4 (Fig.4.6) indicated an optimum bandwidth of about 6 GHz to minimise the effects of fading, and this is supported by the results from this part of the study. However, the minimum fade depth is larger than expected from simulations (~5-10 dB), and the fade depth difference between narrowband and wideband is especially different (100% larger than expected).

### 6.3.2. Small Scale Fading Distribution

Previous authors have considered that the best distribution to fit the amplitude to all measurements of each TX/RX pair is the Nakagami-m distribution [10, 26], with other authors considering a lognormal distribution to be better than the various alternatives, these including Gamma, Nakagami-m, Normal, Rayleigh, Rician and Weibull distributions [9]. In

this study only the Nakagami-m and lognormal distributions are considered to use to fit the amplitudes, which are Nakagami-m and lognormal distribution. A common hypothesis test called Kolmogorov-Smirnov is performed to compare the considered distributions [51]. Figure 6.4 shows an example of data fitted to both distributions.

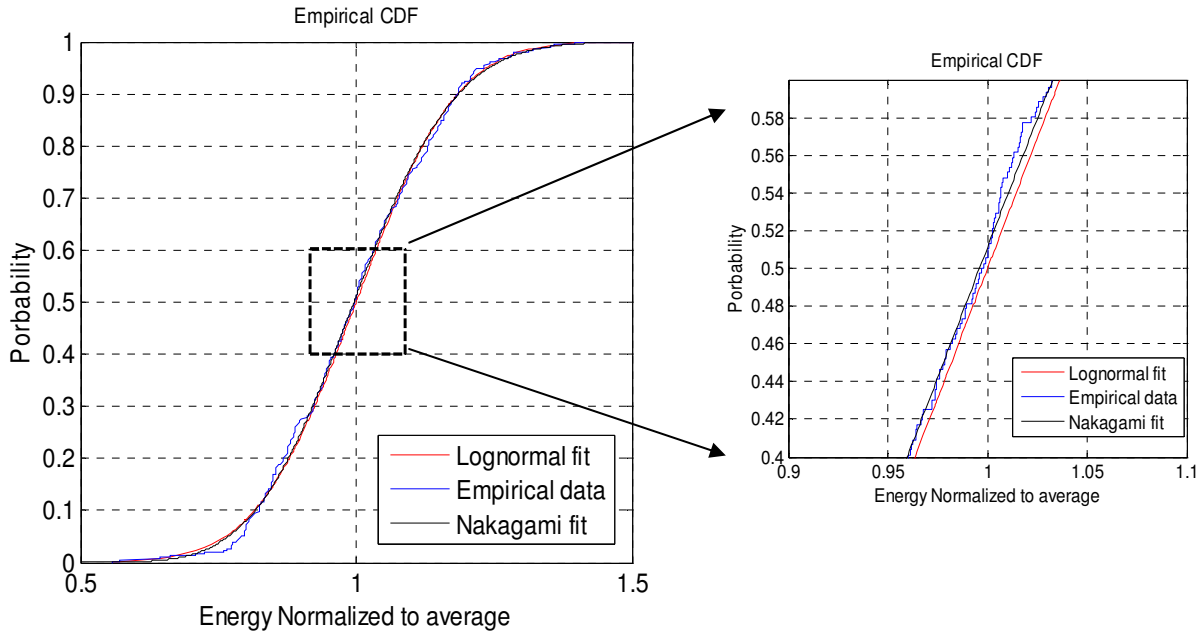


**Fig.6.4. CDF of normalised energy to average, fitted by Lognormal and Nakagami-m distributions**

For the majority of cases, a good fit was achieved with the Nakagami-m distribution. However, as it is appreciated from Fig.6.4, both fits are almost identical, where only once the CDF of the normalized energy is zoomed in, it is deducted that Nakagami-m distribution is actually a better fit than the lognormal one. Furthermore, the Nakagami-m distribution passed the Kolmogorov-Smirnov test in the vast majority of cases whereas lognormal distribution did not. This study confirms the findings of other authors [26], with the lognormal model for small scale distribution seeming less appropriate, as noted elsewhere [9].

Previous studies have evaluated the different values of the *m* parameter and the *omega* parameter ($\Omega$) across time [10]. The published literature [103-105] describes an inverse relationship between bandwidth and fading due to the effect of multipaths, and an

increase in bandwidth therefore leads to a reduction in bit errors. The dependency of these values on *actual* bandwidth has been investigated, with complete signal loss reported for lower bandwidths, but a low risk of attenuation for larger bandwidths [124]. Figure 6.5 shows the impact of bandwidth on actual *m* and Ω parameters for logarithmically-spaced bandwidths between 8 MHz - 7 GHz, with a centre frequency of 7 GHz for each scenario in the PC Box.

**(a)**

**(b)**

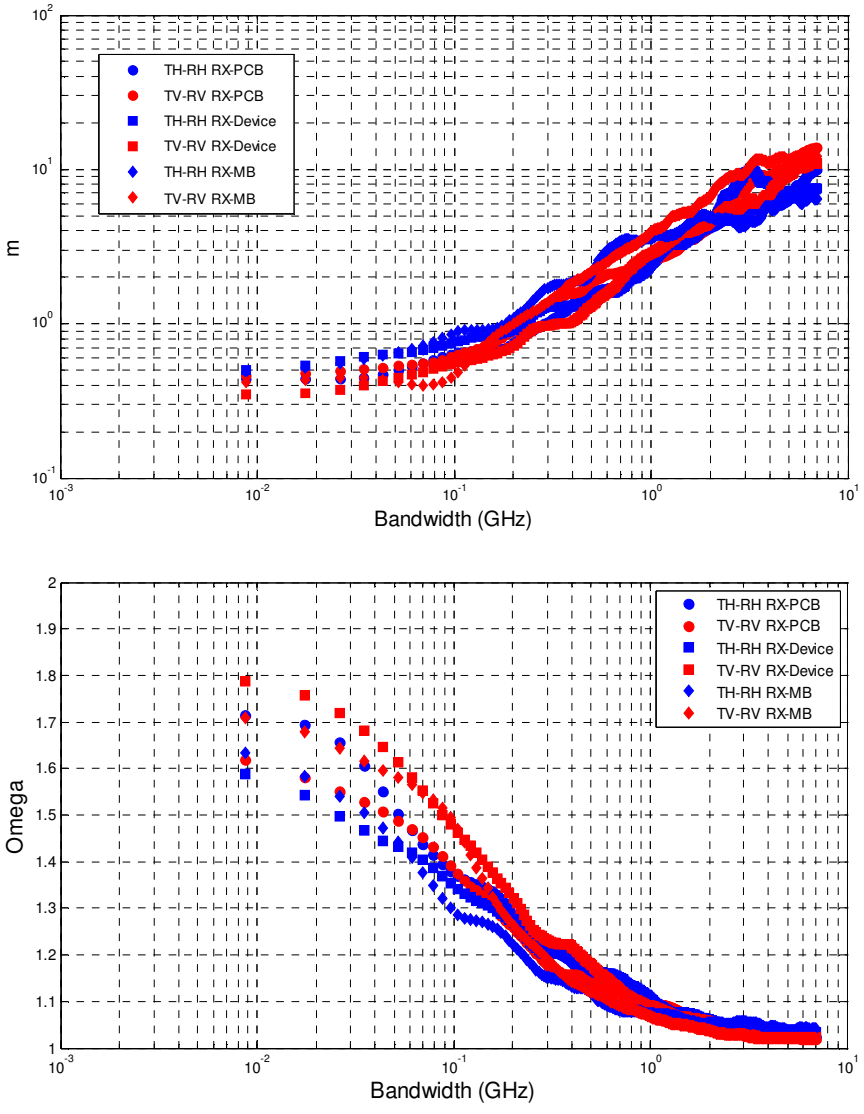


**Fig.6.5. Dependency of m and omega parameters on bandwidth**

**(a) *m* parameter**

**(b) Omega Parameter**

Figure 6.5 shows that for *m* and omega, the respective values are similar across the different scenarios due to the short distance between antennas. These are random parameters and therefore with a lognormal distribution there are occasional dips in the trend, as previously reported [70]. Thus, for certain combinations of bandwidths, the parameters may diverge from the general trend for distance and centre frequencies**.**

Further analysis of the wideband region (bandwidth greater than 500 MHz) reveals that the *m* values are greater than 1.2, and Ω values less than 1.15. Table 6.3 presents the different values of *m* parameter and Ω for every case for the full-band UWB channel (3-11 GHz).

| **Small Scale Fading** | **Scenario** | **Horizontal Polarisation (TH-RH)** | | **Vertical Polarisation (TV-RV)** | |
|---|---|---|---|---|---|
| | | **m** | **Ω** | **m** | **Ω** |
| **PC Box** | RX-MB | 6.458 | 1.041 | 12.20 | 1.021 |
| | RX-Device | 7.474 | 1.034 | 10.91 | 1.023 |
| | RX-PCB | 10.02 | 1.025 | 13.88 | 1.018 |
| **Aluminium Box (Full + Absorber)** | Case | 3.609 | 1.055 | 15.54 | 1.017 |
| | ½ Case | 1.387 | 1.115 | 8.791 | 1.027 |
| | ¼ Case | 0.963 | 1.169 | 7.991 | 1.029 |
| **Aluminium Box (Full)** | Case | 8.018 | 1.026 | 23.46 | 1.011 |
| | ½ Case | 3.243 | 1.051 | 23.09 | 1.011 |
| | ¼ Case | 1.566 | 1.128 | 10.03 | 1.024 |
| **Aluminium Box (Empty)** | Case | 33.74 | 1.007 | 21.40 | 1.012 |
| | ½ Case | 34.40 | 1.007 | 21.40 | 1.012 |
| | ¼ Case | 23.03 | 1.011 | 15.27 | 1.016 |

**Table 6.3. Measured full-band UWB channel Nakagami- m and Omega statistics**

From Table 6.3, it is apparent that the values for Ω are tightly clustered between 1 and 1.17. In contrast, variation of the *m*-parameter is significant across the different scenarios, ranging from 1.387 for a normal sized, full Aluminium box with absorber, to 34.4

for a half-sized empty box. Note is made of the results from an empty Aluminium box, which has a very high resonance. With increasing population of the enclosure, when optimum polarisation becomes critical for transmission, the *m* parameter decreases in value.

## 6.4. Evaluation of the Channel Capacity

The section is divided into two studies. The first calculates the aggregate channel capacity inside both the PC Tower case and Aluminium case for a given SNR at the source (25 dB), and compares the results with actual data rates achieved by current PCs buses (SATA II and PCI bus) [12, 78, 79].

The second study analyses the spatial distribution of channel capacity across the grid for different internal locations of RX, with the objective of identifying areas of enhanced channel capacity, these being probable best locations for antenna placement.

### 6.4.1. Comparison with Standard Data Rates of PCs

Within a conventional PC enclosure there exist numerous interconnecting cables and line buses, a number of which connect the Mother Board (MB) to devices such as CD-ROM or floppy disk. These wired buses have a maximum data rate of 3 Gbps using the Serial Advanced Technology Attachment (SATA II) [12]. Closer inspection reveals other, finer cables, interconnecting the MB and Peripheral Cards (PCBs) with other subordinate microchips, with a standard date rate for 32-bit communication not exceeding 1Gbps [78,79]. Such necessary physical interconnections require a huge amount of space, where further improvements of data rate are limited by the confines of the casing (ever smaller casing being driven by demand). Unsurprisingly therefore, the study of wireless communications within such environments is attracting increasing research interest [7-11].

The results of the aggregate Shannon capacity [35, 99] for an SNR of 25 dB at source are presented in Fig.6.6. Two threshold lines are included at 1 and 3 Gbps representing the standard data rate for PCI Bus and SATA II respectively.

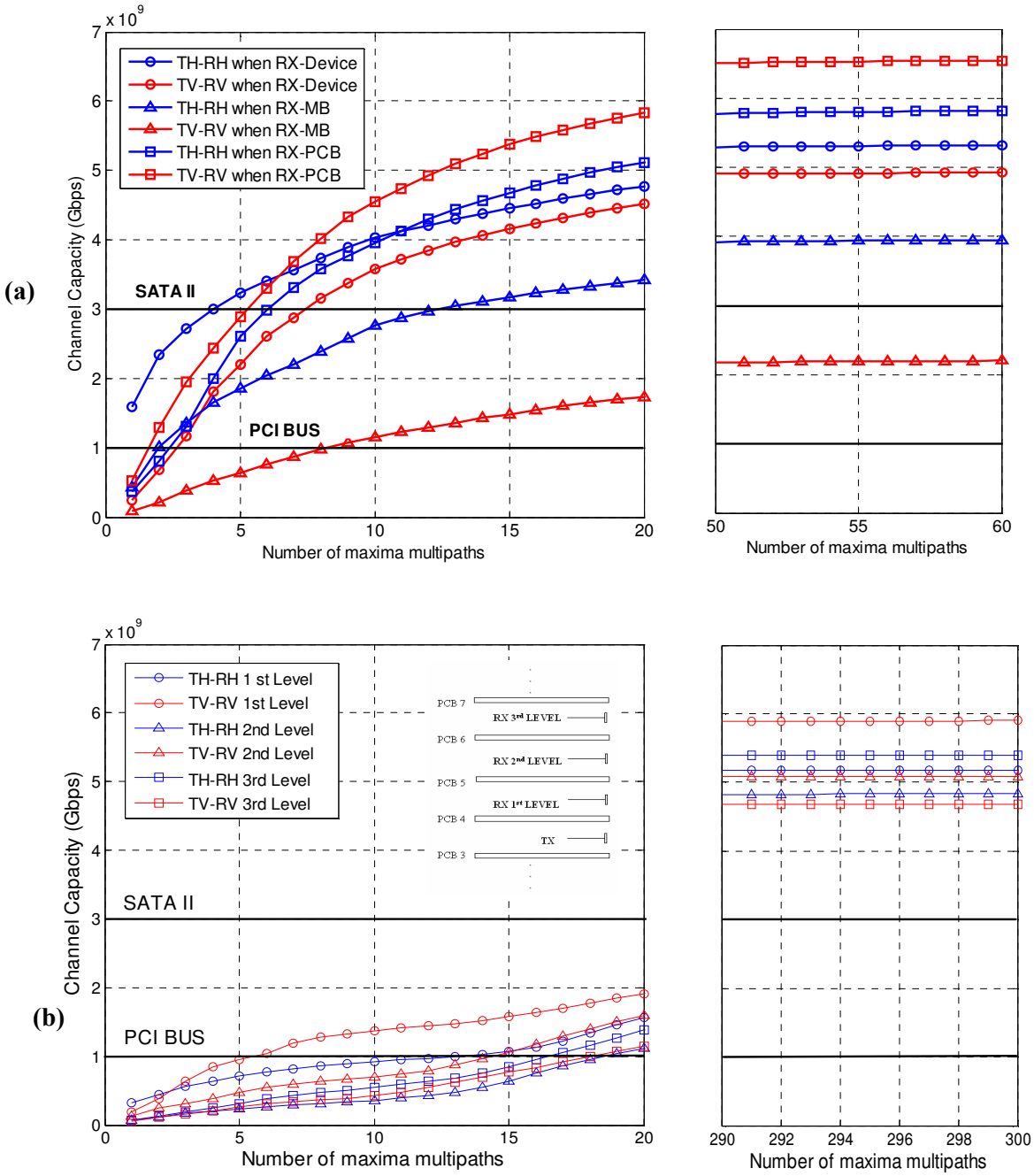


**Fig.6.6. Aggregate channel capacity comparison between different scenarios inside**

**(a) The PC Tower box**

**(b) The Aluminium case**

Figure 6.6.a presents the Shannon capacity results calculated inside the PC Box for each polarisation and fixed location of the RX, whereas Fig.6.6.b presents the channel capacity measured inside the Aluminium Box with *eight* PCB cards. Each detected multipath is the averaged channel capacity of the whole locations adopted by the TX. Both figures are divided into two subplots for a better resolution of the multipath components.

Figure 6.6 clearly indicates a significant difference in the aggregate capacity in the first 20 multipaths between both enclosures. For the case of the PC Box measurements (Fig.6.6.a), the number of multipaths needed to overcome the wiring standard data rates is 1-2 for the PCI bus rate, and 5-7 to achieve SATA II data rate. The scenario when the receiver is located at RX-Device for TH-RH appears to be the best, with the first path already achieving 1.5 Gbps. The explanation for this might be that an average better LOS nature is present in this case, where the first path corresponds with the maxima path. *Vertical* polarisation (TV-RV) in all cases appears to have the worst performance, presumably related to the absorbing influence of the MB and its vertically orientated components. The lowest channel capacity is observed when the RX is placed at the MB (especially if vertically orientated), where channel capacity decreases substantially, and more than twice the number of multipaths are required to achieve data rates similar to the other scenarios. Factors accounting for these results are likely to be the absorption by the (adjacent) MB, and the shadowing created by its surface elements (fan, electronics, etc). Indeed, the maximum capacity (2.2 Gbps) is achieved only after 50 multipaths, this contrasting with a maximum of 6.5 Gbps in the best scenario.

The Aluminium case scenario (Fig.6.6.b) differs considerably from the PC Box (Fig.6.6.a) in the first 20 multipaths in a number of regards:

i. In the former, the number of multipaths required to attain a data rate of 1 Gbps is up to 18 (TH-RH 2$^{nd}$ level), this is compared to the same data rate achieved with no

multipath for all of the scenarios in the PC Box, and an impressive 5.5 Gbps achieved with18 multipaths for 'TV-RV when RX-PCB' (Fig. 6.6.a)

ii. Only once both terminals are vertically orientated, and separated by only 1 PCB card, is this result improved (and still underperforms significantly compared to the same set up in the PC Box).

iii. In terms of maximum possible capacity achieved (bit rate plateau with increasing multipaths), similar results are achieved, with the average maxima being approximately 5 Gbps.

iv. Finally, the optimum capacity of 5.9 Gbps is achieved once the separation between terminals is minimum ('First level') and they are vertically orientated.

Several deductions can be drawn from these observations. The first relates to enclosure size: the Aluminium box in this analysis has a larger volume and more reflective than the PC Box, and multipaths take longer to arrive to the RX. In addition, a higher number of multipaths are expected due to the 'perfect' internal reflectivity of the casing. This effect is most clear in the second subplot of Fig.6.6.b, where 5 times the number of multipaths is required to match the maximal channel capacity seen in Fig.6.6.a. The second observation is that the influence of RX location on overall maximum capacity is smaller for the Aluminium box than it is for the PC box. This is probably due to the irregular population of the PC box, which contains many different components (devices, absorbing materials, electronics, cables, etc). In a static environment, these can generate a highly random complex channel, with the actual location and orientation of the antennas markedly influencing the maximum data rate. The optimum location for antennas in a wireless UWB setup is studied in sections 6.4.2 and 6.4.3 that follow.

### 6.4.2. Optimum antenna location in PC Tower Box

The spatial diagram of the distribution of channel capacity across the TX grid (11x34 points in steps of 5 mm) for different RX locations inside the PC box is investigated in this section. Again, the calculated capacity uses the established SNR of 25 dB at source and the full-band (3-11GHz), avoiding small scale fading with the use of wide bandwidth (> 500MHz). The aim is to investigate the grid for areas of increased Shannon capacity to locate optimum antenna positioning.

Figure 6.7 and Figure 6.8 present this data, derived empirically for horizontal and vertical polarisation (TH-RH and TV-RV), with RX located at three different locations within the PC Box (see section 3.2.1). In each plot, higher points in the Y-axis (18-34 points) represent the locations where the TX is closer to the edge of the PCB, which is also closer to the RX fixed positions. Lower points (1-17 points) are those located closer to the back wall of the PC and represent locations further to the RX (see Fig.3.3).

The results clearly show that, as discussed in previous sections, TH-RH (Fig.6.7) has a better performance inside the PC than TV-RV (Fig.6.8). Only when the receiver antenna is at RX-PCB is the maximum Shannon capacity similar to that in TH-RH. Thus, in almost every case, and as expected, grid locations closer to the edge of the PCB show higher Shannon capacity values. This of course is due to the reduced distance between antennas, and that the line-of-sight (LOS) path is less obscured by other devices. Conversely, antenna placement at the rear of the PC results in a transmitted signal being absorbed and scattered by the MB and PCBs, with over 50% attenuation in channel capacity compared to the 'RX-PCB' setup.

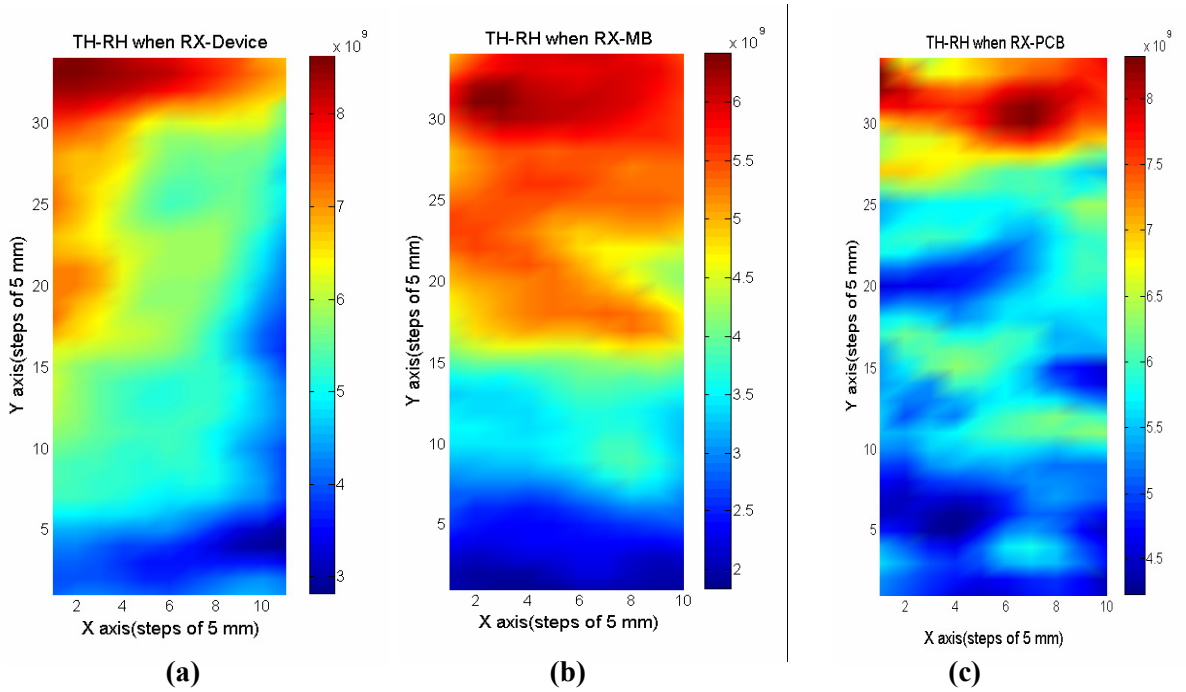


(a) (b) (c)

**Fig.6.7. Spatial diagram of channel capacity for Horizontal polarisation in different scenarios inside the PC Box when**

**(a) RX-Device**

**(b) RX- MB**

**(c) RX-PCB**

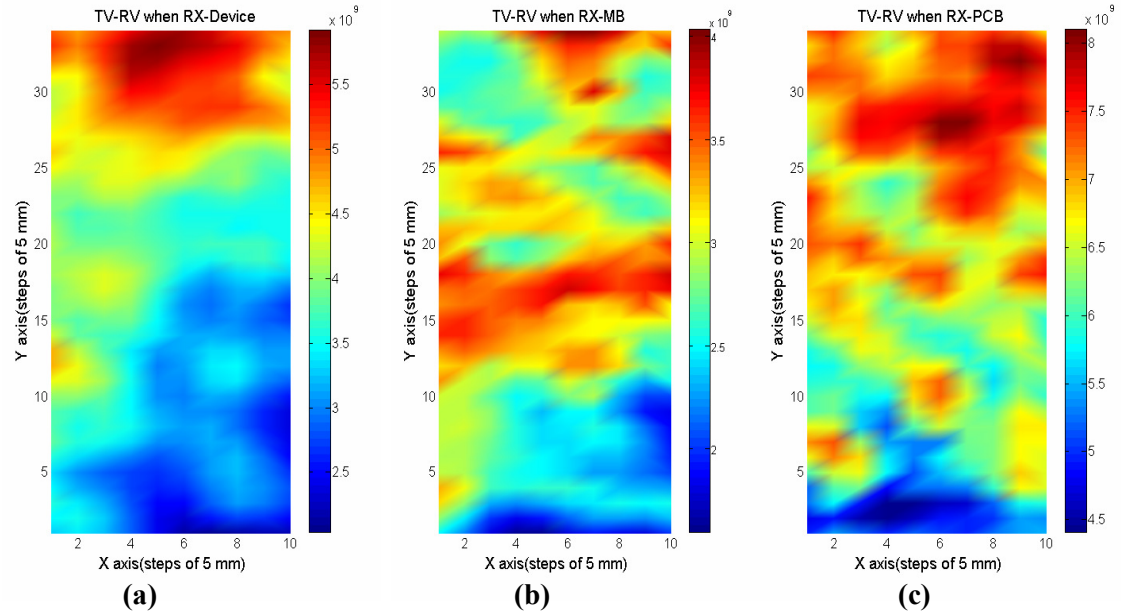


(a) (b) (c)

**Fig.6.8. Spatial diagram of channel capacity for Vertical polarisation in different scenarios inside the PC Box when**

**(a) RX-Device**

**(b) RX- MB**

**(c) RX-PCB**

An interesting finding occurs when the receiver is at RX-PCB (Fig.6.7.c and Fig.6.8.c). Although locations of the TX antenna close to the edge of the PCBs (17-34 y-axis points) still give the best performance, polarisation of the antennas appears to have a relatively small influence on overall channel capacity. The reason could be a short path length, and it is recognised that multipath components cannot travel long distances across the PC box, where each one might suffer a reduction of its power due to absorption. Therefore, the situation when the RX is located on the PCB appears to be the optimum arrangement. In order to investigate this situation further, a more detailed study of antenna location on top of the PCBs is conducted inside the Aluminium box, with a similar distribution of the PCBs inside of it. The aim will be to extrapolate results from the measurements and compare them with the actual ones inside the PC Box.

### 6.4.3. Optimum antenna location in the Aluminium case

The Aluminium Case is built to simulate a personal server with eight PCB cards placed in parallel above one another at the rear wall (see Fig.3.4). This simulates parallel - communication between devices (microprocessors) in which the antennas would be integrated on the boards - being placed on top of the boards in the simulated model. Shannon capacity distribution is assessed across the TX grid to determine best antenna position.

#### *6.4.3.1. One fixed Antenna*

The first scenario contains bow-tie antennas placed on the top surface of a pair of adjacent PCBs one above another**.** In each respective measurement campaign, the RX is fixed while the TX is moved across the grid. Half of the actual board is used due to the symmetry along the x-y plane of the system, and 15x5 points, separated by 1cm, are plotted. Figure.6.9 and Figure.6.10 show the spatial diagrams of channel capacity computed over the whole bandwidth (3-11 GHz) for horizontal and vertical polarisation respectively.

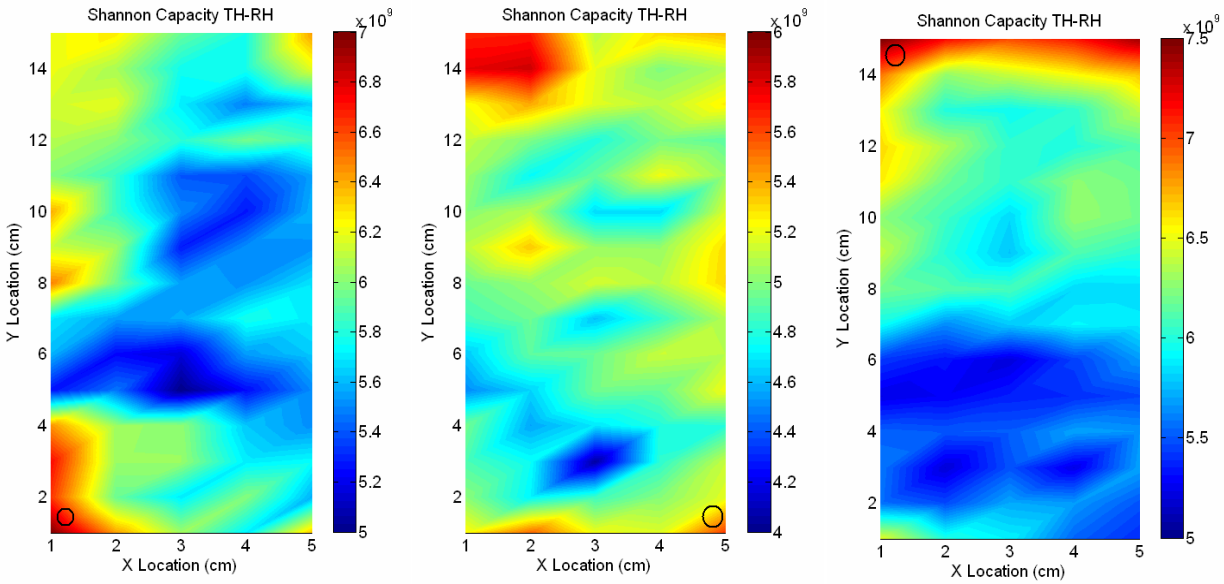


**Fig.6.9. Spatial diagram of channel capacity for TH-RH inside the Aluminium Case when Rx in different fixed positions (black circle)**

**(a) RX at back edge of PCB card (1,1)**

**(b) RX at back half of PCB card (5,1)**

**(c) RX at front edge of PCB card (15,1)**

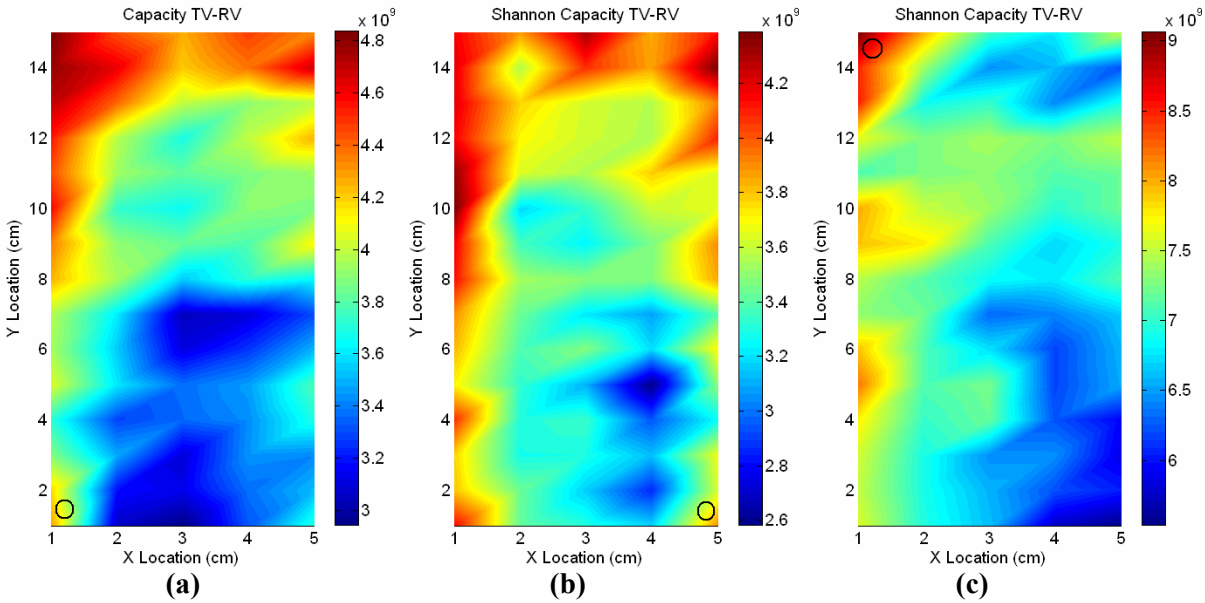


**Fig.6.10. Spatial diagram of channel capacity for TV-RV inside the Aluminium Case when Rx is at different fixed positions (black circle) at a different level of the TX.**

**(a) RX at back edge of PCB card (1,1)**

**(b) RX at back half of PCB card (5,1)**

**(c) RX at front edge of PCB card (15,1)**

Three plots are presented in each figure, where the RX (black circle) represents the different fixed locations adopted by the receiver. Point (1,1) corresponds to the back edge of the card, point (15,1) to the front edge, and (5,1) to the back half of the PCB (see Fig. 3.5.a). These locations are chosen for practical reasons, a bus antenna being easier to site in these positions than in the centre of the cards.

The maximum difference in channel capacity between the three fixed RX positions with TH-RH is relatively small (~ 1 Gbps), but rises to about 4 Gbps once the RX is moved to the front of the PCB with transmitter polarisation switched to TV-RV. However, an increase in Shannon capacity is seen for *both* polarisations when the RX is moved to the edges of the cards. This may be due to a higher available peak in the first path with a LOS path between the wall of the cavity and the edges of the PCB. In contrast, by moving the RX to position (5,1), a loss of energy occurs, due to a non-LOS (NLOS) arrangement with multipaths deflected between, and absorbed by, the cards. For example, with TV-RV polarisation, low data rates (~ 4.5 Gbps) are achieved when the RX is at the rear of the cards, but a two-fold rise in capacity to about 9 Gbps is seen when the RX is placed at the front of the cards. These examples clearly demonstrate the impact of antenna orientation and location on overall channel capacity, despite the fact that fading is minimal in small-environment wideband systems.

Finally, the areas of the TX grid on the adjacent PCB, where the fixed RX is located, usually present the highest values of channel capacity. Therefore, it seems the right choice to locate the terminals on the same location of the adjacent PCBs. Also, for architectural purposes, it makes more sense to integrate the terminals at the same location of each board. The next section (6.4.3.2) evaluates the channel capacity of the system once the terminals adopt the same location on top of different parallel PCB cards.

#### *6.4.3.2. Both Antennas fixed above one another*

Although the optimum antenna location appears to be on matching positions of the boards, the effect of increasing the number of boards *between* antennas remains unknown. This section therefore investigates the effect of increasingly distant antenna spacing on the spatial distribution of Shannon capacity. Separation of the antennas by one board is termed "First level" separation, two boards is referred to as "Second level", and three boards "Third level".

The results are shown in Figure.6.11 and Figure.6.12 for horizontal and vertical polarisations respectively, the RX being located *on top of* three different PCBs. This time the RX is moved across the RX grid, with the TX also variously positioned using the Positioning arm (see Fig.3.5.b). To limit the number of variables, the inter-anntenna distances are kept unchanged at 8, 16 and 24 cm respectively for each of the three different levels, irrespective of their individual positions on the boards (see Fig.3.6).

From the spatial density plots in Fig.6.11 and Fig.6.12, the maximum channel capacity is achieved once *both* terminals are positioned close to the card edges, this arrangement allowing a line-of-sight (LOS) channel between the boards and the walls. In contrast, with antennas located at the back of the boards adjacent to the aluminium wall, a lower capacity is seen because without a LOS path, transmission can only occur via reflected multipath components.

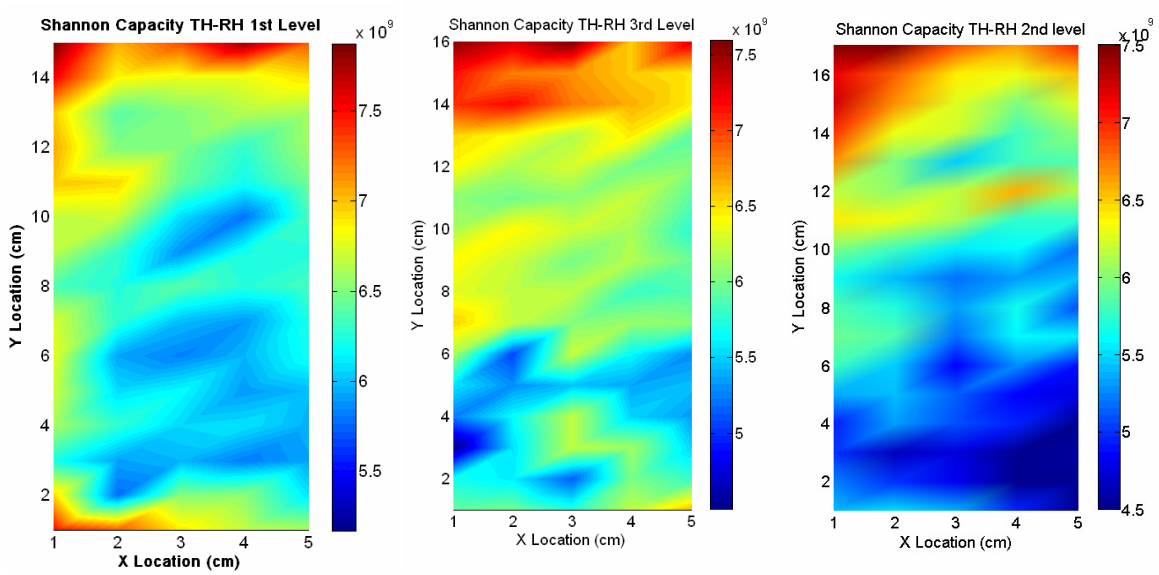


(a) (b) (c)

**Fig.6.11. Spatial diagram of channel capacity for TH-RH inside the Aluminium Case when Rx is at three different levels.**

**(a) Rx at 'First level' (8 cm)**

**(b) Rx at 'Second level' (16 cm)**

**(c) Rx at 'Third level' (24 cm)**

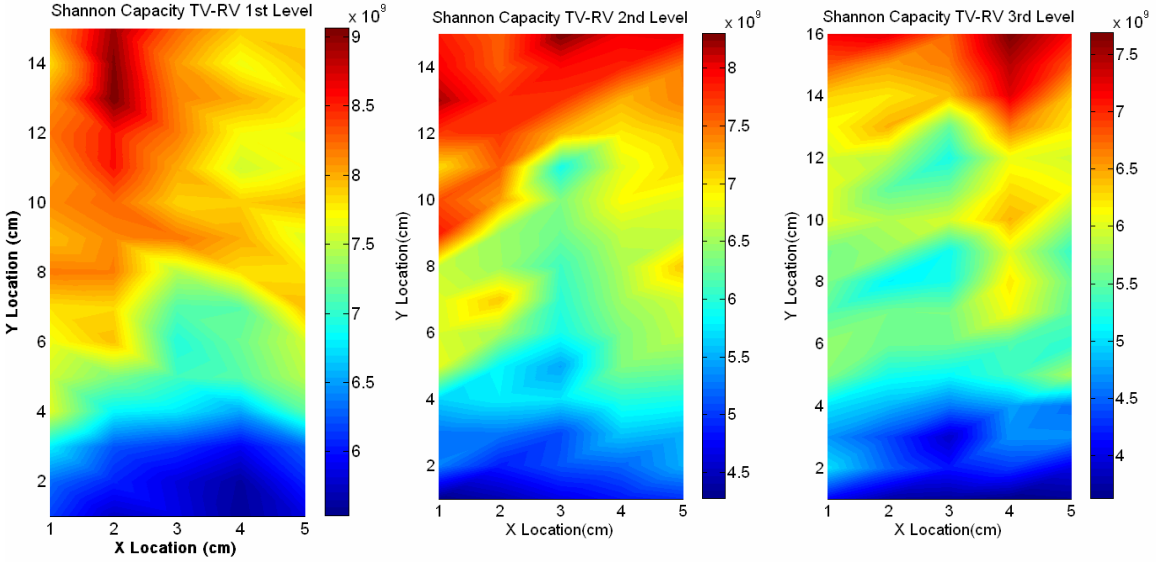


(a) (b) (c)

**Fig.6.12. Spatial diagram of channel capacity for TV-RV inside the Aluminium Case when Rx is at three different levels.**

**(a) Rx at 'First level' (8 cm)**

**(b) Rx at 'Second level' (16 cm)**

**(c) Rx at 'Third level' (24 cm)**

Vertical polarisation has a slightly better performance than horizontal, where the maximum capacity is achieved at the "First level" (~ 9 Gbps). With increasing separation, a decrease in capacity is observed, probably due to absorption by the parallel boards which absorb part of the energy. Interestingly, there is almost no change in maximum channel capacity values with TH-RH antenna polarisation. This is most probably due to the fact that the peak radiation gain is in the z-axis, and waveguide modes can be excited in that direction without shadowing when the antennas are at the edge of the cards.

Thus, when the antennas are at the front or edges of the cards, the LOS nature increases the overall channel capacity. In addition, waveguide modes are excited between the vacant sections between walls and cards – this possibly accounting for the common *maximum* capacity in the three different scenarios. The lack of extra absorbers inside the cavity (apart from the PCBs themselves) accounts for the finding that similar maximum data rates are achieved for each card. Of course, in a more realistic scenario the actual position and distances between antennas have a significant impact (section 6.4.2).

Ideally, exact antenna placement would not influence channel capacity. The highly simplistic model described above contained only 8 PCBs positioned equidistant and in parallel on the rear wall. Since the walls are 'perfectly' reflective, the total energy (allowing for a small coefficient of absorption by the cards) will arrive at the receiving antenna both via LOS transmission and multipaths (allowing for any destructive interference between sets of multipaths). When, in a NLOS scenario, communication relies on multipath components, the fewer the number of multipaths for data transmission the better, and this is achieved by reducing the channel size and avoiding a reflective environment. Section 6.4.4 explores the relationship between channel capacity variation per multipath with environment size, and the influence of an EMC absorber on one of the cavity walls.

### 6.4.4. Channel Capacity of the Engineered Aluminium Case

This final investigation into channel capacity evaluates the relationship between environment size with and without an EMC absorber on the aggregate Shannon capacity (see Fig.3.7). Similarly, channel capacity is calculated for the full-bandwidth (3-11 GHz) and a SNR of 25 dB at source. This time the RX is always fixed at the 'First level' on the front edge of the card. This is because this author believes that, after all previous analysis, this location is the optimum one among the other locations presented in the study.

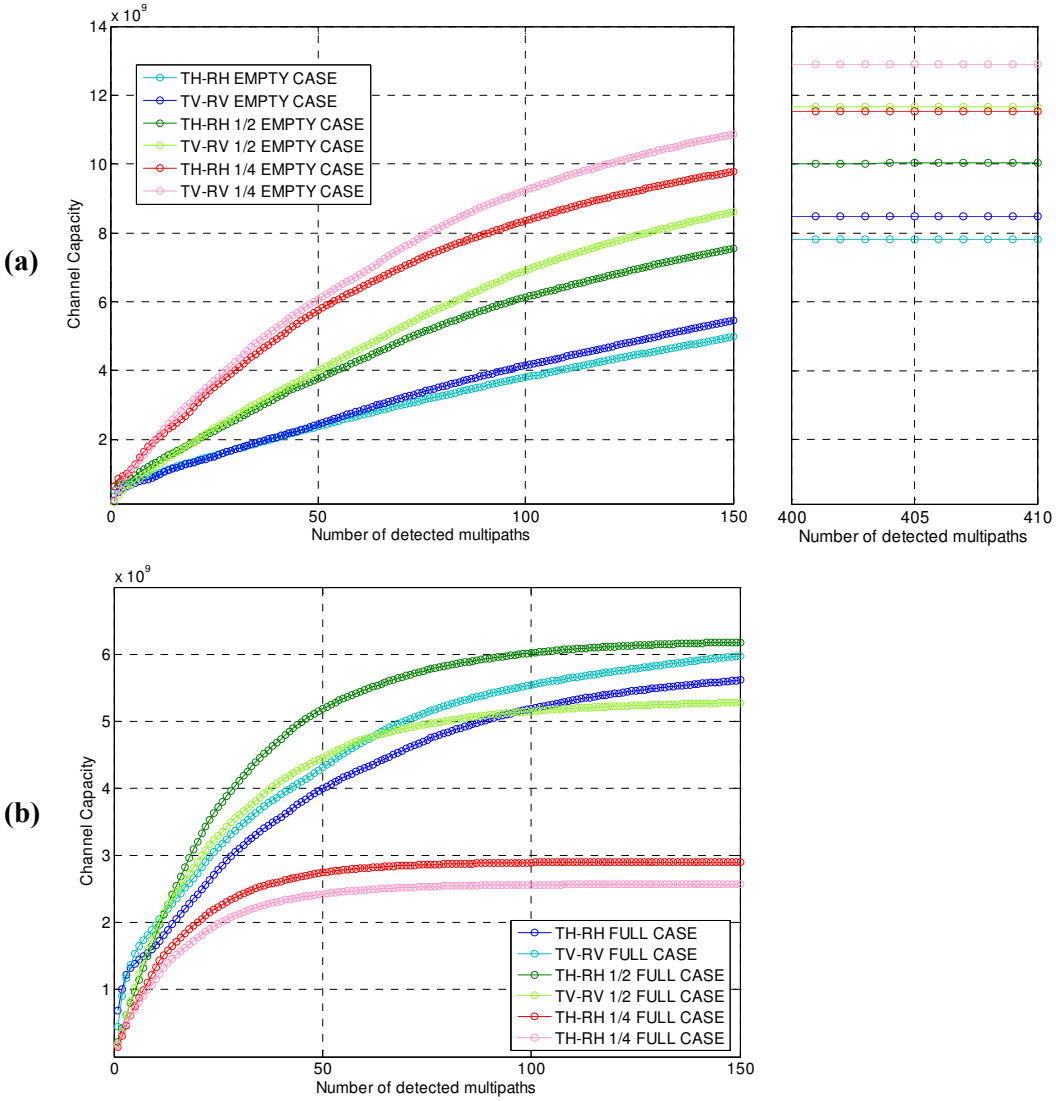


**Fig.6.13. Aggregated Shannon channel capacity, with the Aluminium Case being**

**(a) Empty**

**(b) Populated with 8 PCBs**

It was shown in section 6.4.1 that, with perfectly reflective walls, a very large number of multipaths (>250) are required to achieve the maximum capacity. Such a number is beyond the processing capacity of a rake receiver, for which more than 250 fingers would be required. Figure 6.13.a demonstrates the very significant number of multipath components needed to achieve maximum channel capacity inside an empty Aluminium box. The results from three different box sizes are included in the plot, each for both polarisations TH-RH and TV-RV. Figure.6.13.b shows the aggregate Shannon capacity once the empty Aluminium case is filled with the 8 PCBs cards, where an important change is expected in terms of the number of multipaths required to achieve its maximum value.

Maximal values of the Shannon capacity in Fig.6.13.a are, as expected, very high due to internal reflectivity (i.e., lack of internal absorbing material). An average maximum of at least 8 Gbps of Shannon capacity is seen with the empty box, with an increase of more than 30% when the case is populated with 8 PCBs (Fig.6.13.b), although an extra 100 multipaths are needed to achieve this maximum capacity. The difference in total channel capacity between the smaller and bigger case is due to the power threshold (i.e., related to the VNA limit). Only around 200 ns of transmission are recorded by the VNA (inverse of [bandwidth x freq. points]). Thus, in the empty case, not all the transmitted power has arrived to the RX once the VNA limit is reached, and, due to the high internal reflectivity and environment size, a longer transmission interval would be required for all power to be received. Although not essential to the objectives of this part of the study, this author believes that similar maxima channel capacities are achievable between empty case scenarios with a higher VNA limit.

Thus, Fig.6.13.a identifies a rapid increase in Shannon capacity with reduction of case size. This is because, with reduced size, the multipath components travel shorter distances to

reach the RX and a higher proportions of energy is carried by the same detected multipath for each case.

A number of observations are made from Fig.6.13.b. Firstly, the smaller the Aluminium case, the fewer multipath components are needed to achieve the maximum capacity. For example, the '1/2 Full Case' requires about 150 multipaths, whereas in the '1/4 Full Case' that number is halved. Thus, the smaller the enclosure, the overall multipath distance is lower, and the transmitted energy higher. Secondly, although similar maxima capacity are achievable despite halving the size of the case, once the size is further reduced to one quarter, the drop in total channel capacity is very significant. The decay in channel capacity for '1/4 Full Case' is around 50% compared to the other cases and a decay of 200% in comparison to the one when no PCBs were included in the ¼ case (see Fig.6.13.a). The probable reason is that in the "Full Case" and "1/2 Full Case" there remains empty space between the front wall and the PCBs where waveguide modes can be excited. However, in the "1/4 Full Case", the gap between this front wall and PCBs is less than 5cm and precludes signal propagation along this axis. Furthermore, the ratio of size to absorption between this "1/4 Full Case" and the other cases is much higher, translated to higher losses in energy.

Finally, from inspection of Fig.6.13, the different polarisations in the Aluminium box scenarios did not significantly affect overall channel capacity, in contrast to the PC Box. A possible explanation for this could be the absorbing effect of the actual MB covering one of the walls. This explanation can be verified by simulating a MB inside the Aluminium box by using an EMC absorber. Thus, Figure.6.14 compares the aggregated Shannon capacities for each size and polarisation including a $3M^{TM}$ AB-5050 absorber which covers the front wall of the metallic box (Z-Y plane). This absorber introduces a reflection loss of about 2.5 dB within the frequency range of interest.

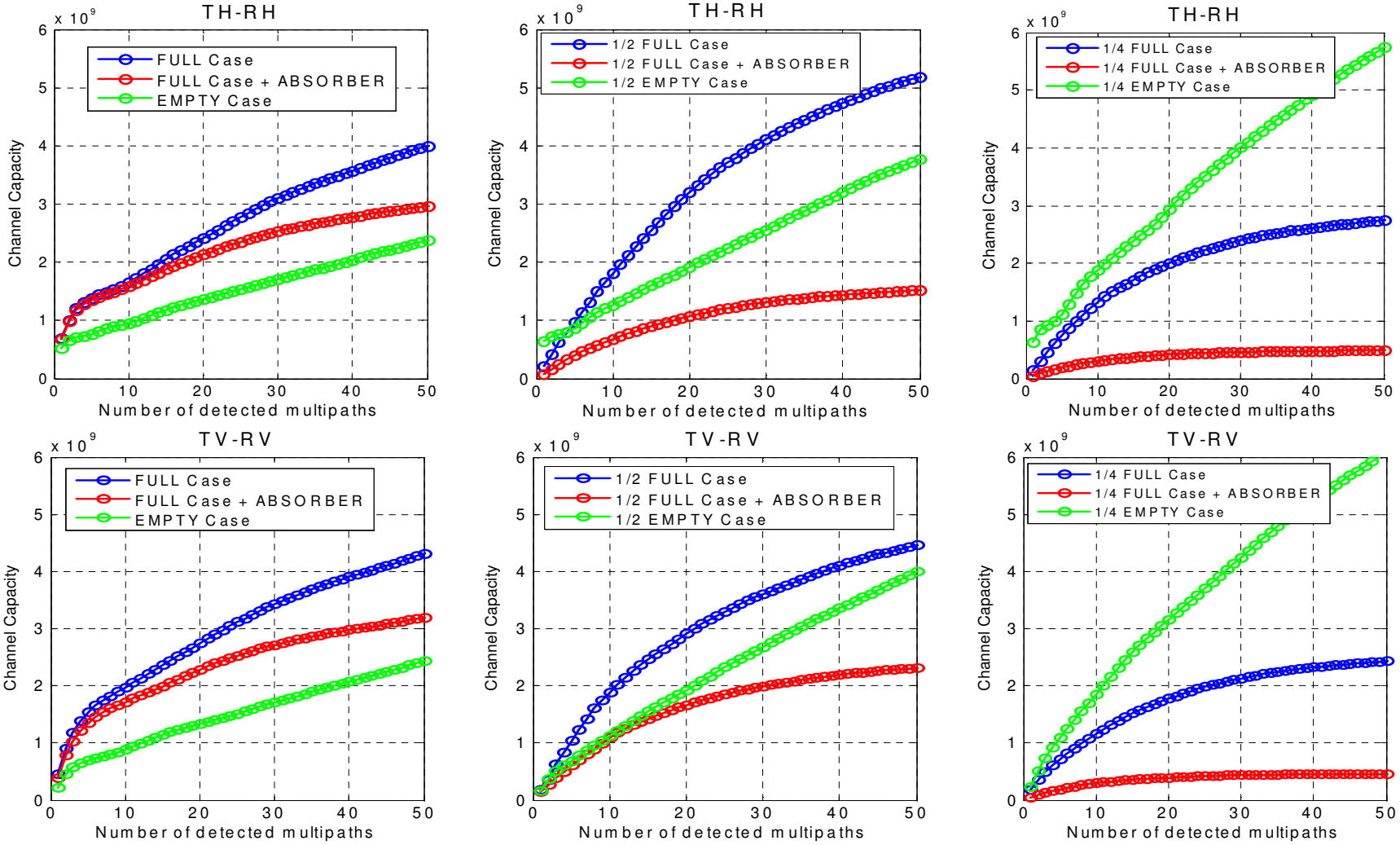


**Fig.6.14. Aggregate channel capacity comparison between different sizes of the Aluminium Case (Case, ½ Case and ¼ Case) corresponding to 'Full Case', 'Full case+ Absorber' and 'Empty case', for horizontal (TH-RH) and vertical polarisation (TV-RV)**

Every time the box becomes smaller, the actual percentage channel capacity loss increases when an absorber is present, as in the '1/4 Full case' scenario, with a 4-5 times larger reduction compared to the same scenario *without* the absorber. This can be explained by the fact that a higher number of multipaths are absorbed due to a *relative* increase in the absorber-to-box size ratio. However, with the absorber in place, only 25-30 multipaths are needed to achieve the maximum total capacity compared to a much higher number (up to 100 multipaths) without the absorber, this offering some potential for the use of rake receivers which have a limit in processing power.

Another further observation from Fig.6.14 is the difference in aggregate capacity for the *first* multipath in each case. Capacity follows a similar trend in the first 10 multipaths before any reduction is appreciated between the Aluminium case 'Full case' and 'Full case + Absorber' scenarios for each polarisation. However, once the case is reduced by at least half, the aggregate capacity follows a completely different trend just after the first path is detected. This finding becomes quite important since the EMC Absorber is in effect closer to the terminals. The aim of its inclusion was to modify the aggregate capacity trend, so fewer multipaths would be required to achieve the maximum capacity, and this aim was clearly not met for the larger case scenario ('Full case'). However, an effect was observed with decreasing distance between absorber and antennas (as the case size reduced), showing that in designing an UWB system, placement of these two elements (i.e. MB and antennas) can have a significant impact on channel capacity.

Finally, in terms of the effect of polarisation, a higher channel capacity reduction was *expected* where peak radiation gain is perpendicular to the absorber plane. However, in this study, no such observation was made, perhaps because of the suboptimal placement of the EMC absorber inside the case. This is mentioned in the final chapter, where recent work in this area is presented.

## 6.5. Summary of Findings

This Chapter has explored the issue of frequency-selective fading in small confined environments such as a standard PC Tower box and rectangular Aluminium case. Some of the findings can be summarized as follows:

i. Small scale fading was more significant than large scale fading (path loss), the latter being almost negligible inside a small confined environment. This may be due to the reduced size of the environment, where the mean power across the TX grid does not vary significantly with the distance between terminals. Therefore, path loss (PL) plays a small role in this type of channel, where waveguide modes become much more significant. PL only showed that the general trend of linear regression, adopted by other indoor models, is not appropriate due to its hybrid resonator behaviour, and that the actual mean power fit across the distances involved identified waveguide behaviour created by possible standing waves formed in the channel.

ii. In terms of small scale fading, a very high fade depth inside the small environment was found for narrowband signal (range between 20-40 dB). Simple comparisons of the experimental results showed that fading increases once the central frequency of the band decreases. This is because as the relative size of the environment becomes smaller, standing wave peaks become less dense. Thus, fading regions become larger in space, implying a much higher risk that the terminal locations will fall in a standing wave node for either polarisation. This phenomenon was demonstrated by electromagnetic simulations in Chapter 4.

iii. Wideband systems presented less standard deviation in power, which translates to more efficient signal transmission. Fade depth was reduced in almost all cases by more than 50% once the signal had a bandwidth higher than 500 MHz. Of interest

was the discovery that the actual integration of different devices and absorber did not substantially reduce fading, although in theory a more populated environment should result in fewer multipaths. A possible explanation is that the topography of the case created substantial random signal propagation, and thus other types of co-interference might be created due to the position of the PCBs.

iv. Nakagami-m distribution was considered the best fit for the amplitude [97] where lognormal distribution did not pass the Kolmogorov-Smirnov test. However, inspecting the results shows that this difference is negligent. The analysis on the impact of parameters *m* and Ω revealed that, for bandwidth greater than 500 MHz (i.e. wideband), the values were $m > 1.2$ and $\Omega < 1.15$.

v. Evaluation of the Shannon capacity showed that a very few number of multipaths are necessary to achieve the same data rates as the standard ones (SATA II and PCI Bus). A vertical antenna orientation within the PC Box appeared to be a better option in terms of avoiding signal interactions with the vertically-distributed electronics in the MB, and positioning the antennas away from the MB was also desirable. A maximum ideal capacity of 6.5 GHz was found for a SNR of 25 dB at the source when RX was located on top of another PCB card. On the other hand, inside the Aluminium box, where no MB was present, a vertical polarisation had a slightly better performance in terms of maximum data rate. A study of the spatial distribution of the channel capacity indicated that, once the antennas are integrated on the PCB cards, locating them at the front edge of the cards was the better choice.

vi. Finally, engineering the environment (reduction of size and inclusion of absorber) helped to reduce the number of multipaths necessary to achieve the required capacity. However, the inclusion of absorbers meant a massive reduction in total energy, even 4-5 times in the smallest Aluminium box. Therefore, it becomes very important that

the actual selection of the number of absorbers inside small cavities is carefully considered as well as their position.

# Chapter 7: Conclusions and Future Directions

This last chapter is divided into two parts. The first summarises the findings of the project and presents a précis of their significance. The second discusses current on-going studies and explores logical avenues for further investigation in the field of ultra-wideband (UWB) communications.

## 7.1. Summary of Findings

This thesis has explored theoretical and practical aspects of UWB communication inside ultra-small enclosed environments (<10λ) including a standard PC Tower Case and a rectangular Aluminium Case. Both simulated and empirical results of such enclosures have been analysed, and limitations of such a system addressed and possible solutions proposed. The high data-rate of short-range UWB channels has made UWB a promising technology in the fields of both wireless personal-area and wireless body-area networks (WBAN and WPAN respectively). Such wire-free transmissions, with the high bit rates of UWB channels, are well suited to very small enclosed environments. This writer believes that the work has brought new insights to the field, investigating the physical behaviour of UWB communications in a number of different small environments, in addition to exploring the relationships between bandwidth, cavity size, and frequency selectivity. The findings and contributions of this thesis can be summarized as follows:

### 7.1.1. Electromagnetic Interference (EMI) in the PC Tower case

Investigation into EMI within the PC Tower case identified the majority of spectral narrowband components to be of low frequencies, with the dominant one corresponding to interference from the microprocessor, at a frequency of 3.2 GHz. A very low decrease in

channel capacity was predicted due to EMI avoidance, suggesting that, with the correct SNR, EMI approaches insignificance.

### 7.1.2. Resonance

Simulations of wave propagation within a small enclosure verified the hypothesis of a hybrid resonator-like behaviour, where, depending on the wavelength of the signal, the environment could be treated as a resonator or modeled using a normal ray-like behaviour. This phenomenon was mainly due to the reduced volume ($V$) and high reflectivity present, where a very high density of multipath transmission in a short period of time was detected. This phenomenon was also explained with the help of a two ray model. The more populated the environment became the less resonance occurred in the overall system.

In the frequency domain analysis a repeated resonance nature for horizontal polarisation (TH-RH) was discovered, whereas for vertical polarisation (TV-RV), a more monotonic decrease in power was observed. This phenomenon was related to the correlation between radiation patterns of the antennas and the distribution of the PCBs. This author believes that the regularity in spacing of the cards results in a Bragg distribution [119], in which constructive interference, being every 2 GHz, coincides with double the inter-card distance. This discovery could significantly influence the optimum ultra-wide band frequency and inter-card separation in the planning of future PC Tower wireless communication systems. Future studies could calculate the actual reflection strength caused by this Bragg distribution.

Finally, the more modes excited inside the cavity the higher the probability that, in any of the three dimensions, the antennas would fall at an anti-node (A). Therefore, higher frequency selectivity suggests that better wireless communication could be established.

### 7.1.3. Influence of Polarisation on the Channel

Apart from the correlation between radiation patterns and distribution of PCBs (section 7.1.4), it was also found that a significant correlation existed between the internal orientation of the electronic components, which might influence dramatically the energy transmission, and the polarisation of the antennas. The explanation for that is the difference found between mean transmitted powers (~7 dBs) for each polarisation inside the PC Tower box. This difference was reduced significantly once a very similar experiment was carried put inside a less complex Aluminium case. Hence, this finding verified that complex structures inside the PC Tower (i.e. MB) were playing an important role in terms of absorption of energy. Also, different resonant modes will be excited depending of the sizes of the walls and the polarisation adopted by the antennas.

### 7.1.4. Relationship of Fade Depth to Volume, Bandwidth and Frequency

The fade depth model [105] predicted that frequency-selective fading is more severe inside this reduced indoor environment. This factor is expected to depend on bandwidth, frequency selectivity and volume of the enclosure; the analytical model showed that the bandwidth required to resolve all multipaths was scaled proportionally to $V^{-0.33}$, and ray tracing simulations of different rectangular environments predicted scaling proportional to $V^{-0.351}$. Thus, given the enclosure volumes used in this study, the required mean bandwidth to mitigate fading was found to be ~ 6 GHz. This result compared favourably with experimental data.

Simple comparisons of the experimental results showed that fading increases with decreasing central frequency of the band, where the difference in fade depth between low (3 GHz) and high (9 GHz) frequencies derived from simulated and empirical data was

approximately 1.5 dB. This is due to the *relative* size of the environment becoming smaller for lower frequencies (larger wavelength) and consequently wave peaks are not so dense. Thus, fading regions become larger in space, implying a much higher risk that the terminal locations will fall in a node of the standing wave pattern for either polarisation.

### 7.1.5. Small Scale Distribution Fitting

The Nakagami-m distribution was found to be the best distribution to fit small scale fading, following the standardised model of indoor environments from Molisch [26]. The analysis on the impact of parameters *m* and Ω revealed that, for bandwidth greater than 500 MHz (i.e. wideband), the values were $m > 1.2$ and $\Omega < 1.15$.

### 7.1.6. Averaged Power Delay Profile (APDP)

The linear decay (in semi-logarithmic scale) of the Averaged Power Delay Profile (APDP) was approached by a geometric model, where the impulse response decreases monotonically. The APDP inside the static environment of the PC Box presented an amplitude decay of 1 dB/ns, a significantly rapid decay time compared to the common indoor environments [26]. This model was found to predict with significantly high precision the results from time dispersion and Ricean K-factor.

### 7.1.7. RMS Delay Spread

Root mean square (RMS) delay spread was found to be in the order of nanoseconds due to the reduced size of the enclosures, where its values decreased once the cavities were engineered, hence a strong dependency was identified with the power decay of the channel (i.e. resonance of the channel).

### 7.1.8. Direct and Indirect Power Transmission (Ricen K-Factor)

The Ricean K-Factor verified the dominant non-light-of-sight (NLOS) nature of the environments, where an average of less than 10% of the power is transmitted by direct paths. This percentage decreased substantially once absorbing structures were included within the cavities. However, the attenuation caused by PCBs and associated components so significantly degraded the cavity resonances that the reflections and the interference arising from this resonance was no longer a significant limitation on the communication channel. Thus, the inclusion of absorbing materials such as PCBs and EMC absorbers helped to mitigate the reflectivity of the environment. In contrast, the inclusion of these devices increased power-loss within the system.

### 7.1.9. Optimal Wireless Bus Position

A huge variation in power was shown for small displacements of the antennas inside the grid once the bandwidth selected for transmission was in the narrow band. However, optimal data capacity between terminals for ultra-wide bands was achieved by positioning the antennas at the front edge of the cards. In this location they were able to excite the relative unobstructed line of sight (LOS) paths in empty sections of the box. Future designs for this type of communication may require the inclusion of this empty space to provide the wireless bus facility with a uniform capacity between all terminals. A maximum Shannon capacity of ~6 Gbps for an SNR of 25 dB at the source was calculated for this situation.

### 7.1.10. Use of an EMC Absorber

Finally, the inclusion of an electromagnetic compatibility (EMC) absorber reduced the required number of multipaths for maximum data rate, with a location close to the antennas proving optimal. However, the value of an absorber in a reduced-size environment,

in which power loss is high *per se*, remains unclear. Sections 7.2.5 and 7.2.6 explore this matter in further detail and present avenues for future work.

## 7.2. Recent Developments and Future Research Directions

The final section of this work considers the future for this field of research, and discusses certain studies which are currently being pursued.

### 7.2.1. Change of Polarisation

This author has identified the importance of antenna polarisation for data transmission in a UWB environment. However, other antenna orientations are possible, 'planar polarisation' (with opposing antennas co-planar with the PCBs) being one such example. In this orientation, very high power transmission can be achieved in the first LOS path. Preliminary measurements were conducted with an antenna located at the edge of each of two adjacent PCBs inside the Aluminium case. The measurement setup and calculated aggregate capacity is illustrated in Fig.7.1.

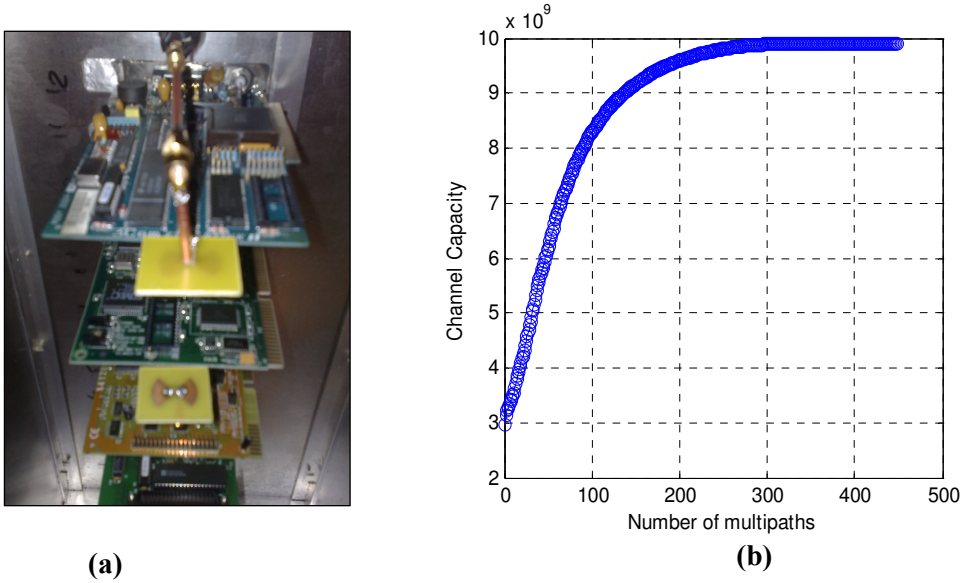


**(a)** **(b)**

**Fig.7.1. (a) Planar co-polarisation adopted by the bow-tie antennas inside the aluminium box (b) Calculated aggregate Shannon capacity per multipath**

Figure 7.1.b shows that 3 Gbps of channel capacity can be achieved in the first multipath alone, and already corresponds to 30% of the total capacity. Although the maximum capacity of 10 Gbps (with optimal antenna position and localisation) is carried in over 300 multipaths, a disproportionate quantum is transmitted in the first wavefront. This result compares with an equivalent maximum capacity of around 6 Gbps without planar polarisation (see Fig.6.13). Thus, although polarisation can profoundly affect channel capacity, the issue of numerous multipaths remains, and in a populated environment this will have a detrimental effect.

### 7.2.2. MIMO-UWB technology

Until about 2005, UWB investigations focused on single-antenna systems. In recent years, there has been an increasing interest in multiple transmitters and receivers as these arrangements allow beam-forming, increase the SNR at the receiver, and are more resistant to the effects of fading [125, 126]. Such set-ups include spatial multiple-input multiple-output (MIMO) and polarisation MIMO techniques, and these are discussed in detail elsewhere [127].

Figure.7.2 presents an example of measurements undertaken inside the Aluminium case when a linear array of two co-polarised TH-RH antennas (TX and RX) are located at the edge of two adjacent PCB cards. Because antenna-coupling effects become significant when the spacing between elements in the array is *less than* a half-wavelength [128], each array of antenna elements are spaced half of the maximum wavelength apart, that is, 5 cm at 3 GHz.

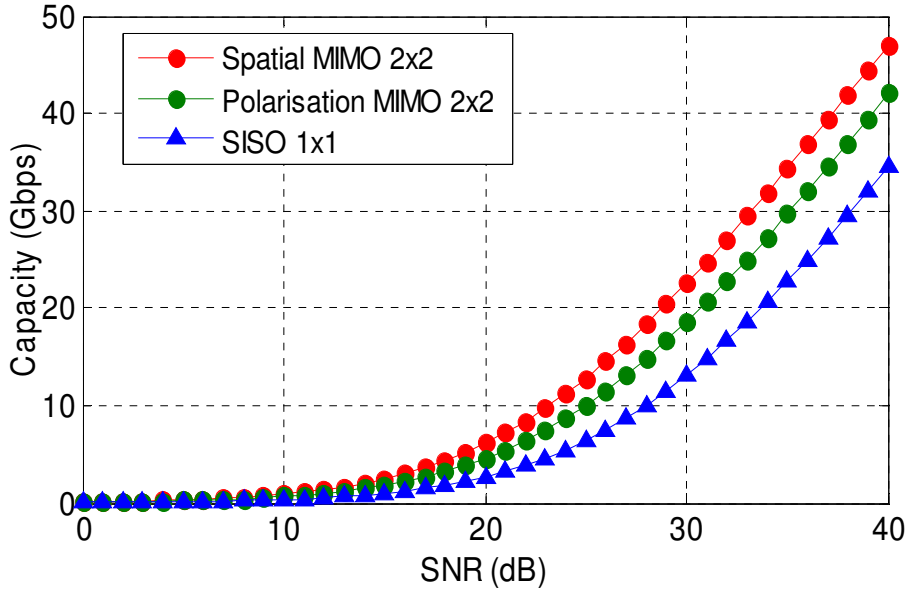


**Fig.7.2. Comparison of Shannon capacity for different antenna diversity schemes**

Three deductions can be drawn from Fig.7.2 for future UWB applications. Firstly, the channel capacity is enhanced by multiple antennas (MIMO) compared to single transmitter/receiver arrangements (SISO). Secondly, spatial antenna distribution outperforms dual-polarisation diversity. Thirdly is the observation that Shannon capacity is increased (as expected, given the previous discussion) with higher SNR values. Thus, a typical 6 Gbps achieved for a SNR of 25 dB increases almost six-fold to 35 Gbps if the SNR limit is lifted to 40 dB. Thus, transmission is significantly influenced not only by polarisation diversity and quantity of antennae, but also by the SNR: with a modest SNR increase of 5 dB from 25 dB to 30 dB, the Shannon capacity of a single transmitter arrangement surpasses that of a 2x2 spatial MIMO (Fig 7.2).

### 7.2.3. Use of different UWB Antennas

One avenue for future research is the nature of UWB antennae themselves. For the requirements of the studies undertaken for this work, bidirectional planar antennas were

adequate. However, an improved *omni-directional* pattern could be achieved using discone antennas with a similar distribution of peak power across the channel [129]. In contrast, unwanted aberrant reflections could be avoided by using more highly directional transmitters, such as vivaldi antennas [91]. Since the small environment such as a computer is static, once the ideal location is established, this option may also have a role.

### 7.2.4. Electromagnetic Analysis of PC Components

The variously-sized electronics within the MB and PCB cards all significantly affect UWB signal, especially at those frequencies which correspond in size to such components, when the power can be fortified or degraded, depending on the nature of the interference and absorption. It would, therefore, be of interest to subject each constituent component to separate electromagnetic analysis to analyse their contribution to the overall capacity. Ideally this sort of investigation would be undertaken in a 'free-space' scenario such as an anechoic chamber. It would be also useful to calculate the real reflectivity of the aluminium case to have a deeper knowledge of the environment.

### 7.2.5. Receiver Architecture: Rake Design

Due to the geometry of the environments the location and separation of the antennas, and the placement of obstructing objects and the properties of material used inside, the electromagnetic signal traverses a multitude of paths whose lengths are usually unequal. This multipath propagation has a negative effect on the system performance and link budget, and one of the solutions, apart from channel coding, equalisation and spectral shaping, is optimising multipath resolution of the Rake receiver.

A rake receiver consists of a number of channels ('rake fingers'), each with the function of tracking and selecting the power from the received multipath components. The output of the receiver is the sum of the instantaneous branch signals, and different combining

schemes have been proposed, such as selection combining (SC) and maximum ratio combining (MRC) [92, 121, 130-132]. Ideally, the rake receiver should have an equivalent number of fingers as the number of multipaths detected. Clearly such a complex solution is impractical and so a subset of available components within established thresholds are used instead. Figure 7.3.a presents the predicted number of multipaths necessary to achieve the total energy for a given power constant decay, and Fig.7.3.b shows the predicted loss of the total received energy once the power decay constant increases. The unit in Fig.7.3.b represents a perfect resonator environment.

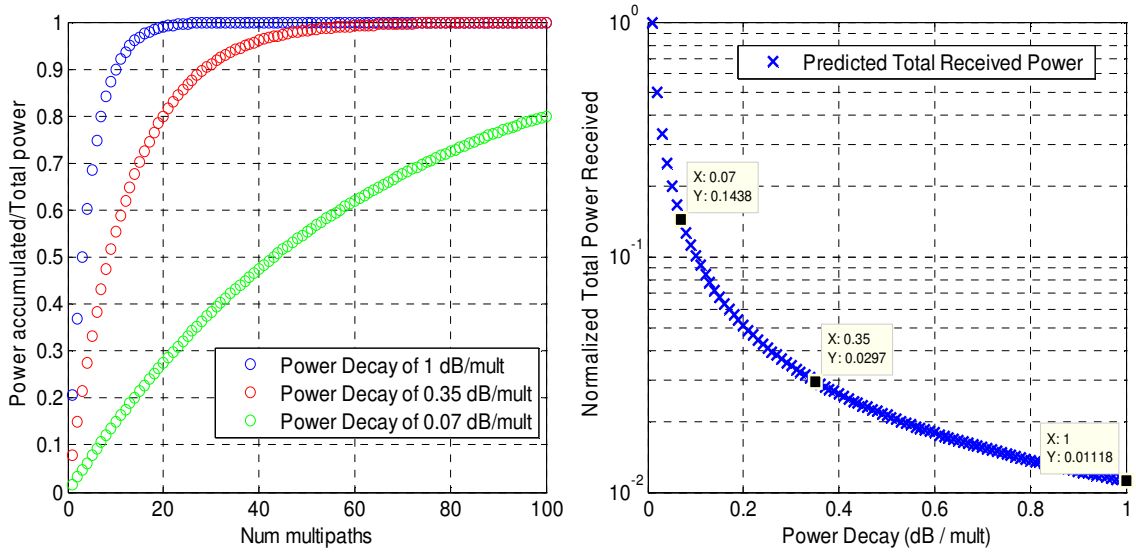


**(a)** **(b)**

**Fig.7.3. Prediction of the normalised accumulated Power per multipath (a) and Total Power for different values of power decay slope (b)**

Three different power decay profiles are shown in Fig.7.3, where 0.07 dB/multipath and 0.35 dB/multipath correspond to those for the Full Aluminium Case and PC Tower case respectively. The fewer the number of multipaths required for maximum transmission, the fewer the demands on the design of the rake receiver. Thus, the constant power decay profile of 0.35 dB/multipath (Fig.7.3.a) looks a better choice than 0.07 dB/multipath. However, the trade-off is a reduction in total energy received by 80 % (Fig.7.3.b). Future work will need to

investigate the influence of incorporating absorbers on power loss on maximum data rates for given power decay profiles and frequencies.

Finally, Malik described two different rake architectures: selective rake (S-Rake) and a partial rake (P-Rake) [121]. A P-Rake, has L fingers that track the first L paths of all the 'x' paths resolved, while an S-Rake selects the L best paths of all available. S-Rake requires fast adaptability, knowledge of instantaneous value of all multipaths and efficient channel estimation, and is therefore more complex than P-Rake. Figure.7.4 shows an example of comparison of both architectures (TH-RH), where the aim is to show the improvement achieved with an S-Rake receiver architecture, which has a higher complexity than P-Rake.

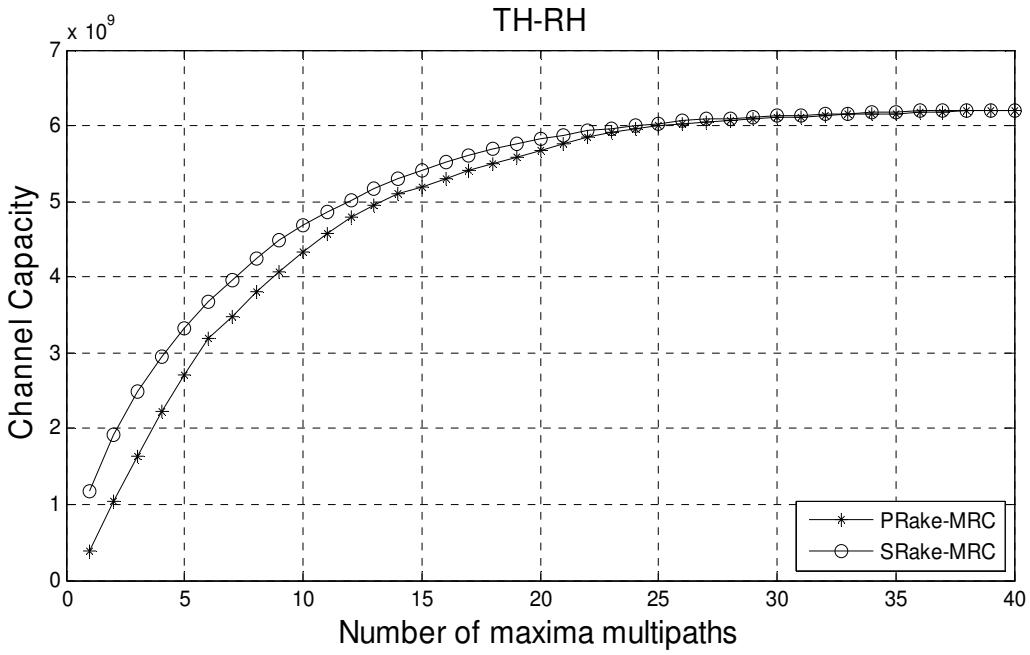


**Fig.7.4. Increase of the Shannon's capacity with MRC Rake Combining**

As shown in Figure 7.4, to process a channel capacity of 4 Gbps, there is a difference of 2 fingers (i.e., multipaths) between the rakes, with the P-Rake appearing to be less effective. A question for future investigation is the optimum architecture of the rake receiver for evaluation of tracking peaks in the received signal.

### 7.2.6. Impact on WiMedia UWB Systems: Engineered Environment

An important new development aspect is the investigation of the impact of a commercial WiMedia UWB kit inside small confined environments. This UWB development kit is a Wisair™ DV9110 controlled by Inoflex™ FPGA board with firmware from HW Communcations™. In essence, it generates and transmits packets and evaluates the packet error rate and achievable data. When used in a typical indoor environment (>10λ) its packet error rate is reported to be zero. Further details of its functionality are described elsewhere [87]. The aim of the measurement is to test this commercial kit inside a very small confined environment such as the Aluminium Box, once empty, and to include $3M^{TM}$ AB-5050 absorbers (reflexion loss of 2.5 dB). The system uses two small discone antennas [129], with a lower cut-off frequency of 2.5 GHz, and with two polarisations, vertical (TV-RV) along the z-axis and horizontal (TH-RH) along the y-axis. The location of the antennas is identical to the one showed in Fig.3.7 (section 3.3). The first measurements inside the empty aluminium box revealed a packet-error rate for both polarisations above 75%. This effectively precluded communication due to severe fading in such a confined environment, where the WiMedia standard does not posses sufficient counter-measures [87]. In this case TV-RV had better performance than TH-RH due to the LOS transmission. Subsequently, the measurements were repeated in a box that was enhanced by an absorber, covering one wall of the metallic box. This time, a significant improvement in packet-error rate appeared (>20%) and illustrated that a relatively poor absorber can still significantly reduce fading. Interestingly, the improvement was higher for horizontal polarisation (TH-RH), although remained poor *without* the absorber. This can be explained by the impact of antenna patterns [87], where the absorber does not remove reflections from the walls parallel to the XZ-plane for the vertical polarisation (TV-RV). These arrive shortly after the main direct path and may cause serious fading. An example of this phenomenon was presented in section 6.3.1, which showed that

the inclusion of the absorber did not reduce fading. To support this, another measurement was conducted where a second absorber was placed on one of the walls to reduce the impact of one of the dominant multipaths as illustrated in Fig. 7.5.

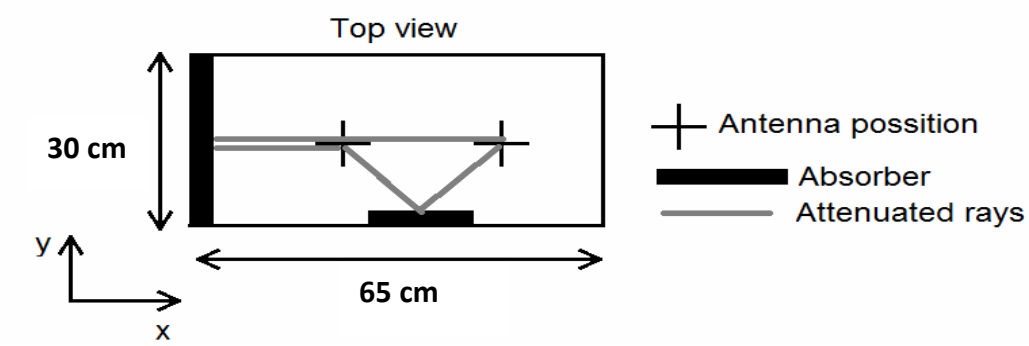


**Fig.7.5. Positions of absorber when antennas are TV-RV. The attenuated rays are highlighted**

This time, two absorbers were sufficient to secure reliable communication for all data rates (packet error rate < 7%). It is known that if the energy of a multipath arriving early after the dominant path is reduced, the system performance can significantly improve. Thus, for future UWB wireless communication systems in a confined environment, the antenna gain should be orientated for a selected dominant path. Thus fading reduction is a function both of the number of absorbers, and their location.

### 7.2.7. Investigation of UWB Wireless Communication inside Non-Cubic Environments

Lastly, future work should aim to conduct similar campaigns in other forms of enclosed environments. Since the work of this Thesis investigated USB campaigns inside cubic structures, logically future work would analyse UWB behaviour inside non cubic structures. These may include spherical or cylindrical ones with the development of different antenna design and polarisations required for structures which may in future differ from the classic PC or server shapes in current use. Of particular importance is the analysis of waveguide modes in such ‘atypical’ environments, in which the rules for antenna location, orientation, and polarisation might be quite different to those reported in this study.

# Appendix A

## List of Abbreviations and Acronyms

| | |
|---|---|
| UWB | Ultra Wide-Band |
| ISI | Intersymbol Interference |
| WPAN | Wireless Personal Area Network |
| MB | Mother Board (Main Board) |
| EIRP | Equivalent Isotropically Radiated Power |
| SATA II | Serial Advanced Technology Attachment 2 |
| FCC | Federal Communications Commission |
| EMI | Electromagnetic Interference |
| PCB | Printed Circuit Board |
| PC | Personal Computer |
| VNA | Vector Network Analyzer |
| PDP | Power Delay Profile |
| RMS | Root Mean Square |
| PCI | Peripheral Component Interface |
| FB | Fractional Bandwidth |
| GPRIC | Ground Penetrating Radar Industry Coalition |
| ECC | Electronic Communications Committee |
| EC | European Commission |
| RSC | Radio Spectrum Committee |
| TEM | Transverse-Electromagnetic |
| EIRP | Equivalent Isotropically Radiated Power |
| IEEE | Institute of Electrical and Electronics Engineers |
| ETSI | European Telecommunications Standards Institute |
| ECMA | European Computer Manufacturers Association |
| MB-OFDM | Multiband Orthogonal Frequency Division Multiplexing |
| DS-CDMA | Direct Sequence Code Division Multiple Access |
| PHY | Physical Layer |
| RF | Radio Frequency |
| SNR | Signal to Noise Ratio |

| | |
|---|---|
| MRI | Magnetic Resonant Imaging |
| CPU | Central Processing Unit |
| DoD | Department of Defence |
| RVC | Reverberating Chamber |
| LOS | Line-of-sight |
| NLOS | Non-Line-of-sight |
| RSC | Ratio Spectrum Committee |
| APDP | Average Power Delay Profile |
| CDF | Cumulative Distribution Function |
| CIR | Channel Impulse Response |
| DP | Direct Pulse |
| SC | Spread spectrum sliding Correlator |
| FS | Frequency Sweeping |
| TH-RH | Transmitter Horizontal- Receiver Horizontal |
| TV-RV | Transmitter Vertical- Receiver Vertical |
| TX | Transmitter Antenna |
| RX | Receiver Antenna |
| SV | Saleh-Valenzuela |
| Q | Quality Factor |
| TSA | Tapered-Slot Antenna |
| CMOS | Complementary Metal-Oxide-Semiconductor |
| RC | Reverberating Chamber |
| PL | Path Loss |
| AF | Attenuation Factor |
| MIMO | Multiple-Input Multiple-Output systems |
| SIMO | Single-Input Multiple-Output systems |
| RL | Return Loss |

## References


1. Ross, G. F., "The transient analysis of certain TEM mode four-port networks," *IEEE Trans. Microwave Theory and Tech*., Vol. MTT-14, No. 11, 1966, pp. 528-547.
2. G.F. Ross, "A time domain criterion for the design of wideband radiating elements", IEEE Trans. Antennas Propagat.", 1968, VOl.16, No.3, p.355.
3. J.M. Cramer, R.A Scholtz, and M.Z.Win., "On the analysis of UWB communication channels", in *IEEE Proc. Military Communications Conf*., vol.2, 1999, p.p. 1191-1195
4. W. Q. Malik and A. D. Adesnik, "Ultra-wideband technology: military applications and social implications", presented at 2nd UK National Student *Pugwash Conference*, Cambridge, UK, January 2003.
5. Y. Liuqing and G.B. Giannakis, "Ultra-wideband communications: an idea whose time has come", *IEEE Signal Processing Magazine,* vol. 22, issue 6, pp. 26-54, November 2004.
6. "Revision of Part 15 of the Commission's rules regarding ultra-wideband transmission systems: First report and order," *Federal Communications Commission*, Washington, DC, USA FCC 02-48, Feb. 2002.
7. A. Matsubara, T. Ichikawa, A.Tominiki, T. Toda, and T.Kobayashi, "Measurements and Characterization of UWB Propagation within Spacecrafts", in *Proc. Loughborough Antennas Propagat. Conf. (LAPC).* Loughborough, UK, Nov. 2009.
8. P. Chiang, et al., "Short-range, wireless interconnect within a computing chassis: Design challenges," *IEEE Design and Test of Computers*, vol. 27, no. 4, pp. 32-43, Jul. 2010.
9. Z.M. Chen, and Y. P. Zhang, "Inter-Chip Wireless Communication Channel: Measurement, Characterization, and Modelling", *IEEE Trans. Antennas Propag.*, vol. 55, no. 3, March 2007.
10. J. Karedal, A. P. Singh, F. Tufvensson, and A. Molish, "Characterization of Computer Board-to-Board UWB Channel", *IEEE Comm. Letters,* vol.11, No 6, June 2007.
11. S. Redfield et al., "Understanding the UWB channel characteristics within a computer chassis", *IEEE Antennas and Wireless Propagation Letters*, vol. 10, pp. 191-194, 2011.
12. *SATA-IO Releases SATA Revision 3.0 Specification,* Nereus for SATA-IO,Ann Jansen and Rachel Shaver.
13. Intel website. [Online accessed on 16 Feb 2012]. Avaliable: http://www.intel.com/pressroom/kits/quickreffam.htm/
14. Street, A.M., Lukama, L., Edwards, D.J.,"Use of VNAs for wideband propagation measurements", *IEE Proc.- Communications*, vol. 148, Dec 2001.
15. The Commission of European Communities, Commission Decision of 21 February 2007 on allowing the use of the radio spectrum for equipment using ultra wideband

technology in a harmonised manner in the Community. Official Journal of the European Union, 2007/131/EC, Feb. 23, 2007.

16. E. Thomas, "Walk Don't Run: The First Step in Authorizing Ultra-Wideband Technology", *IEEE Conference on Ultra Wideband Systems and Technologies (UWBST),* May 2002. Copyright © 2002 IEEE. Used with permission.

17. K.Pahlavan, P.Krishnamurthy and J. Beneat, "Wideband Radio Propagation Modelling for Indoor Geolocation Applications", *IEEE Commun. Mag.,36:4,* pp.60-65, 1998.

18. R. V. de Jongh, A. G. Yarovoy, L. P. Ligthart, I. V. Kaploun, and A. D. Schukin, "Design and analysis of new GPR antenna concepts," 7th Int. Conference on Ground Penetrating Radar, Vol. 1, Issue, May 27-30, 1998, pp. 81-86.

19. M. Hämäläinen, V. Hovinen, R. Tesi, J. H. J. Iinatti, and M. Latva-aho, "On the UWB system coexistence with GSM900, UMTS/WCDMA and GPS," *IEEE Journal on Selected Areas in Communications*, vol. 20, December 2002.

20. E. G. Farr, "Optimization of the feed impedance of impulse radiating antennas, part II: TEM horns and lens IRAs," *Sensor and Simulation Note 384*, November 1995.

21. M. Dunbar, "Plug-and-play sensors in wireless networks," *IEEE Instrumentation & Measurement Magazine*, vol. 4, issue 1, pp. 19-23, March 2001

22. M. Ho, L. Taylor, and G.R Aiello, "UWB technology for wireless video networking," in *Consumer Electronics ICCE International Conference*, pp. 18-19, June 2001.

23. White paper: "Ultra-Wideband (UWB) Technology: Enabling high speed wireless personal network*", Intel in Communications*, 2004.

24. B. Huang, "UWB Regulatory Overview", Sony AWT Group, October 2002.

25. WiMedia Alliance. [Online accessed on 16 Feb 2012]. Avaliable: http://www.wimedia.org

26. A. F. Molisch, K. Balakrishnan, D. Cassioli, C. C. Chong, S. Emami, A. Fort, J. Karedal, J. Kunisch, H. Shantz, U. Scuster, and K. Siwia, "IEEE 802.15.4a channel model—Final report ", Tech. Rep. Doc IEEE 802.15-04-0662-02-004a, 2005.

27. J. Bray, C. Sturman, "Bluetooth: Connect without Cables", Prentice Hall PTR, 2001.

28. E. Ferro, F. Potorti, "Bluetooth and Wi-Fi Wireless Protocols: A Survey and Comparison", *IEEE Wireless Communications*, Feb.2005.

29. E. Saberinia and A. H. Tewfik, "Multi-user UWB-OFDM Communications". In *Proc. IEEE Pacific Rim Conf. on Commun., Computers, and Sig. Processing (PACRIM),* vol. 1, Victoria, Canada, Aug. 2003, pp. 127-130.

30. Ecma International. [Online accessed on 16 Feb 2012]. Available: http://www.ecma-international.org.

31. W. Pam Siriwongpairat, K. J. Ray Liu, "Ultra-wideband communications systems: multiband OFDM approach", John Wiley & Sons, chap. 4, 2008.

32. J.Ahmadi-Shokouh, R. Caiming, “UWB Communications Channel Measurements –A Tutorial Review”, *International Journal of Ultra Wideband Communications and Systems,* 2009 - Vol. 1, pp. 11 - 31.

33. M. Hamalainen, J. Iinatti, V. Hovinen, and M. Latva-aho, “In-band interference of three kind of UWB signals in GPS L1 band and GSM900 uplink band Personal,” *12th IEEE Int. Symposium on Indoor and Mobile Radio Comm.*, vol. 1, Sept. 2001, pp. 76-80.

34. M. Hamalainen, V. Hovinen, J. Iinatti, and M. Latva-aho, “In-band interference power caused by different kinds of UWB signals at 211 UMTS/WCDMA frequency bands,” *IEEE Conf. on Radio and Wireless*, RAWCON’01, 2001, pp. 97-100.

35. L. Lundheim, “On Shannon and “Shannon’s formula”,” Department of Telecommunication, Norwegian University of Science and Technology (NTNU).

36. D.J. Daniels, “Surface-Penetrating Radar*”*, *The institution of Electrical Engineers*, London, United Kingdom, 1996.

37. M. Z. Win, R. A. Scholtz, “Ultra-Wide Bandwidth Signal Propagation for Indoor Wireless Communications*,*” *IEEE International Conference on Communication*, pp. 56-59, Montréal, Canada, June 1997.

38. J. J. Ely, T. W. Shaver, and G. L. Fuller, "Ultra wideband electromagnetic interference to aircraft radios," *NASA/TM-2002-211949*, October 2002.

39. F.R Gfeller and U. Bast, “Wireless In-house Data Communication via Diffuse Infrared Radiation”, IEEE Proceedings, vol.67, pp.1474-1486, 1979.

40. Laskar, J.; Pinel, S.; Dawn, D.; Sarkar, S.; Sen, P.; Perunama, B.; Yeh, D.; Barale, F., "60 GHz entertainment connectivity solution," *Ultra-Wideband, 2009. ICUWB 2009. IEEE International Conference on* , vol., no., pp.17-21, 9-11 Sept. 2009

41. A. Saleh and R. A Valenzuela, “A statistical model for indoor multipath propagation,” *IEEE J. Selected Areas Commun.*, vol. 5, pp.128-137, 1987.

42. H. Hashemi “The Indoor Radio Propagation Channel” *Proceeding of the IEEE*, vol. 81, no. 7, pp 943-968, July 1993.

43. H. Hashemi, “Impulse Response Modelling of Indoor Propagation Channels,” *IEEE Journal on Selected Areas in Communications*, vol. 11, No. 7, Sep. 1993.

44. C. R. Anderson, T. S. Rappaport, K. Bae, A. Verstak, N. Ramakrishnan, W. Tranter, C. Shaffer, and L. Watson, “In-Building Wideband Multipath Characteristics at 2.5 & 60 GHz,**”** *Proceedings of IEEE 56th Vehicular Technology Conference*, vol.1, 2002. pp. 97-101.

45. G. D. Durgin, and T. S. Rappaport, “Theory of Multipath Shape Factors for Small-Scale Fading Wireless Channels,” *IEEE Transactions on Antennas and Propagation*, vol. 48, no. 5, pp.682-693, May 2000.

46. T.S. Rappaport, “Characterization of UHF multipath radio channels in factory buildings,” *IEEE Transactions on Antennas and Propagation* , vol. 37, no. 8 , pp. 1058 –1069, Aug. 1989.

47. T. S. Rappaport and D. A. Hawbaker, "Wide-band microwave propagation parameters using circular and linear polarization antennas for indoor wireless channels," *IEEE Trans. Commun.,* vol. 40, no. 2, pp 1-6, Feb. 1992.

48. T.S. Rappaport, "Wireless Communications, Principles & Practice", 2nd edition, Prentice Hall, Inc. Feb 2009.

49. D. Cassioli, M. Win, A. Molisch, "The Ultra-Wide Bandwidth Indoor Channel: From Statistical Model to Simulations," *IEEE Journal on selected areas in Communications*, vol. 20, no. 6, pp. 1247-1257, August 2002.

50. D. Cassioli, M. Win, and A. Molisch, "A Statistical Model for the UWB Indoor Channel," *IEEE Conference on Vehicular Technology*, 53rd VTC 2001, vol. 2, 2001, pp. 1159-1163.

51. A. Molisch, "UWB Propagation Channels-Theory, Measurement, and Modelling" *IEEE Transactions on Vehicular Technology*, Vol. 54, No. 5, Sep 2005.

52. R. A. Scholtz, and M. Z. Win, "Impulse Radio," Invited paper, *IEEE PIMRC'97*-Helsinki, Finland. pp. 245-267.

53. Cramer R., Scholtz R., and Win M. "Evaluation of an Ultra-wide-Band Propagation Channel," *IEEE Transactions on Antennas and Propagation*, vol. 50, no. 5, pp. 561-570, May 2002.

54. Boashash B.,"Time-Frequency Signal Analysis and Processing: A Comprehensive Reference*"*, Oxford: Elsevier Science, ed. (2003), ISBN 0080443354.

55. J. Proakis, "Digital Communications", 4th Ed.,USA: McGraw-Hill, 2001

56. S. Ghassemzadeh, R. Jana, C. Rice, and W. Turin, "A Statistical Path Loss Model for In-Home UWB Channels" *IEEE Conference on Ultra Wideband Systems and Technologies*, May 2002, pp. 59-64.

57. C. Prettie, D. Cheung, L. Rusch, and M. Ho, "Spatial Correlation of UWB in a Home Environment," *IEEE Conference on Ultra Wideband Systems and Technologies*, May 2002, pp. 65-69.

58. J. Keignart and N. Daniele, "Subnanosecond UWB Channel Sounding in Frequency and Temporal Domain," *IEEE Conference on Ultra Wideband Systems and Technologies*, May 2002, pp. 25-29.

59. J. Kunisch and J. Pamp, "Measurement Results and Modelling Aspects for the UWB Radio Channels," *IEEE Conference on Ultra Wideband Systems and Technologies*, May 2002, pp. 19-23.

60. V. Hovinen, M. Hämäläinen, and T. Pätsi, "Ultra Wideband Indoor Radio Channel Models: Preliminary Results," *IEEE Conference on Ultra Wideband Systems and Technologies*, May 2002, pp. 75-79.

61. W. Turin, R. Jana, S. Ghassemzadeh, and C. Rice, "Autoregressive Modelling of Indoor UWB Channel," *IEEE Conference on Ultra Wideband Systems and Technologies*, May 2002, pp. 71-74.

62. A. P. Ariza, M. Bachhuber, R. Weigel, T. Fuss, R. Zetik, G. Shen, R. Muller, R. S. Thomä: "Ultrawideband Channel Sounding within an Airbus 319" . *VTC Fall 2010*: pp.1-5.

63. Thain, A.,"Simulated UWB Channel Modeling for Aircraft," *European Conference on Antennas and Propagation Conference (EUCAP), 2011 Rome* , 11-15 Apr. 2011

64. Manteuffel, D.; Ould, T.; Kempka, T.,"Antenna and Propagation Impairments of a UWB Localization System Integrated into an Aircraft Cabin," *Antennas and Propagation Conference (LAPC), 2010 Loughborough* , vol., no., pp.589-592, 8-9 Nov. 2010

65. W. Niu, J.Li, and T. Talty, "Ultra-Wideband Channel Modelling for Intravehicle Environment", *EURASIP Journal on Wireless Communications and Networking*, Vol. 2009, Article ID. 806209.

66. Kobayashi, T., "Measurements and Characterization of Ultra Wideband Propagation Channels in a Passenger-Car Compartment," *Spread Spectrum Techniques and Applications, 2006 IEEE Ninth International Symposium on* , vol., no., pp.228-232, 28-31 Aug. 2006.

67. Garcia Zuazola, I.J.; Elmirghani, J.M.H.; Batchelor, J.C.;"High-speed ultra-wide band in-car wireless channel measurements," *Communications, IET* , vol.3, no.7, pp.1115-1123, July 2009.

68. Schack, M.; Jemai, J.; Piesiewicz, R.; Geise, R.; Schmidt, I.; Kurner, T.; , "Measurements and Analysis of an In-Car UWB Channel," *Vehicular Technology Conference, 2008. VTC Spring 2008. IEEE* , vol., no., pp.459-463, 11-14, May 2008.

69. Schack, M.; Geise, R.; Schmidt, I.; Piesiewiczk, R.; Kurner, T.; "UWB channel measurements inside different car types," *Antennas and Propagation, 2009. EuCAP 2009. 3rd European Conference on* , vol., no., pp.640-644, 23-27, March 2009.

70. Alsindi N.A.,Birru D. and Wang D., "UWB Channel Characterization for Wireless MRI Applications", *Conference Information Science and Systems,* March 2007*,* pp. 135-140.

71. Y. Huang and D. J. Edwards, "A novel reverberating chamber: The source-stirred chamber," in *Proc. 8th Int. Conf. EMC*, Edinburgh U.K., 1992, pp. 120–124.

72. Y. Huang and D. J. Edwards, "An investigation of electromagnetic field inside a moving wall mode-stirred chamber**",** *Eighth International Conference on Electromagnetic Compatibility***,** 21-24 Sep 1992.

73. P. Corona, G. Latmiral, E. Paolini, and E. Piccioli, "Use of a reverberating enclosure for measurements of radiated power in the microwave range," *IEEE Trans. Electromagn. Compat*., vol. EMC-18, pp. 54–5.

74. A. Sorrentino; G. Ferrara; M. Migliaccio, "The reverberating Chamber as a LOS Wireless Channel Emulator", *IEEE Trans. Antennas Propag.,* Vol. 56, No. 6, June 2008.

75. C. Tepedelenlioglu, "The Ricean K Factor: Estimation and Performance Analysis*",* *IEEE Trans on Wireless Communications*, vol. 2, no.4, July 2003.

76. G.A. Conway & W.G. Scanlon, “Antennas for over-body-surface communication at 2.45 GHz,” *IEEE Trans. Antennas & Propagation*, Special Issue on Antennas & Propagation on Body-Centric Wireless Communications, pp. 844–855, Vol. 57, 4, Apr. 2009.

77. Pervez Khan, Md.Asdaque Hussain, Kyung Sup Kwak, ”Medical Applications of Wireless Body Area Networks”, *International Journal of Digital Content Technology and its Applications*, Vol. 3, Num. 3, Sept. 2009.

78. Compaq Computer Corporation “PCI Bus Numbering in a Microsoft Windows NT Environment”. December 2000 13UK-1200A-WWEN

79. *National Instruments Tutorial*, “PCI Express – An Overview of the PCI Express Standard”.

80. K. Y. Yazdandoost, R. Kohno, “Bow-tie antenna for UWB communication frequency,” in *Proc*. 2004 *Antennas and Propagation Society Int. Symop.,* vol. 3, Jun., 20-25 2004, pp.2520-2523.

81. Balanis C. A., “Antenna theory”, 3rd Edition, A John Wiley and Sons, Inc., Publication. Chapter 1.

82. J. Bahln and P. Bhartia, “Microstrip Antenna,” Dedham, Artech House, 1980.

83. Y.-L. Chen, C.-L. Ruan, and L. Peng, “A Novel UWB Bow-tie Slot Antennas in Wireless Communication Systems”, School of Physical Electronics, University of Electronic and Technology of China*, Progress In Electromagnetics Research Letters,* Vol. 1, 101–108, 2008.

84. Y.-D. Lin and S.-N. Tsai, “Analysis and design of broadband-coupled striplines-fed bow-tie antennas,” *IEEE Trans. Antennas Propagat.,* vol.46, no. 3, pp. 459-560, Mar. 1998.

85. S. Nikolau, L. Marcaccioli, G. E. Ponchak, J. Papapolymerou, and M. M. Tentzereis, “Conformal double exponentially tapered slot antennas (DETSA) for UWB communications systems,” in *Proc. 2005 IEEE-ICU Int. Conf. Ultrawideband Technolgies,* Zurich, Switzerland, Sep. 2005.

86. A. Eldek, A. Z. Elsherbeni, and C. E. Smith, “Wide-band modified printed bow-tie antenna with single and dual polarization for c- and X-band applications,” *IEEE Trans. Propagat.,* vol. 53, no. 9, pp. 3067-3072, sep. 2005.

87. Sipal V.**,** J. Gelabert, C. J. Stevens, B. Allen, D. J. Edwards, “Impact of Confined Environment on Performance of MB OFDM Systems”, *LAPC Conference 2011,* Loughborough, UK, Nov. 2011.

88. Trevor S. Bird, "Definition and Misuse of Return Loss", *IEEE Antennas & Propagation Magazine*, vol.51, iss.2, pp.166-167, April 2009.

89. R. Ye, S. Redfield, and H. Liu, “High-precision indoor UWB localization: Technical challenges and method,” in *Proc. IEEE UWB*, 2010, pp. 1–4.

90. Malik W.Q, Christopher Stevens, and David J. Edwards, “Synthetic aperture analysis of multipath propagation in the ultra-wideband communication channel”, *Signal*

*Processing Advances in Wireless Communications*, 2005 IEEE 6th Workshop on Volume 5, Issue 8, June 2005 Page(s): 375 – 379.

91. Li Tianming, Rao Yuping, and Niu Zhongxia, "Analysis and Design of UWB Vivaldi Antenna", *IEEE 2007 International Symposium on Microwave, Antenna, Propagation*, and EMC Technologies for Wireless Communications.

92. M. Z. Win, R. A. Scholtz, "On the Energy Capture of UWB signals in dense multipath environments", *IEEE Comm. Letters,* vol.2, Sep. 1998.

93. S. R. Saunders, "Antennas and Propagation for Wireless Communication Systems", Wiley & Sons Ltd, 1999.

94. S. M. Yano, "Investigating the Ultra-Wideband Indoor Wireless Channel," IEEE Vehi. Tech. Conf., pp. 1200-1204, Spring 2002.

95. K. Siwiak, H. Bertoni and S. M. Yano, "Relation between Multipath and Wave Propagation Attenuation," *IEE Elect. Letters*, vol. 39, no.1, pp. 142-143, Jan. 2003.

96. K. Siwiak and D. Mckeown, "Ultra-Wideband Radio Technology", West Sussex, England: John Wiley and Sons, 2004.

97. R. Qiu and I.-T. Lu, "Wideband wireless multipath channel modelling with path frequency dependence," in *IEEE International Conference on Communications* (ICC'96), pp. 277-281, 1996.

98. R. C. Qiu and I. Lu, "Multipath resolving with frequency dependence for broadband wireless channel modeling," *IEEE Trans.Veh. Tech*., 1999.

99. A. Kavatjikidis, "Measurement Analysis and Capacity Performance of UWB Radio Propagation Channels", Thesis for the Degree of dPhil at Oxford University, Sep 2008 Page(s): 77 - 80.

100. B. Allen, M. Dohler, E. Okon, W. Malik, A. Brown, and D. Edwards, "Ultra Wideband Antennas and Propagation for Communications, Radar and Imaging". John Wiley & Sons, 2006.

101. Pozar, D.M. *Microwave Engineering,* 2nd edition, John Wiley & Sons, 1998.

102. Romme, J.; Kull, B.; "On the relation between bandwidth and robustness of indoor UWB communication," *Ultra Wideband Systems and Technologies, 2003 IEEE Conference*, pp. 255- 259, 16-19 Nov. 2003.

103. Malik, W.Q.; Allen, B.; Edwards, D.J.; "Fade depth scaling with channel bandwidth," *Electronics Letters*, vol.43, no.24, pp.1371-1372, Nov. 22 2007.

104. Malik, W.Q., Allen, B., Edwards, D.J.; "Bandwidth-dependent modelling of small scale fade depth in wireless channels," *Microwaves, Antennas & Propagation, IET*, vol.2, no.6, pp.519-528, Sept. 2008.

105. Sipal, V.; Allen, B.; Edwards, D.J.; "Enhanced Fade Depth Model for Extremely Wideband Channels," *Modelling and Simulation 2010, AMSE Conference on*, June 2010, Prague.

106. G. Heidari, “WiMedia UWB - technology choice for wireless USB and Bluetooth.” John Wiley & Sons, 2008.

107. Sipal, V., J. Gelabert, B. Allen, C. Stevens, and D. Edwards, "Frequency-Selective Fading of Ultra wideband Wireless Channels in Confined Environments," *IET Microw. Antennas Propag*. -- Aug. 2011, Vol. 5, Issue 11, p.1328–1335.

108. Reinaldo A. Valenzuela, “Ray Tracing Prediction of Indoor Radio Propagation,” IEEE, PIMRC 1994, pp. 140-144.

109. Chang-Fa Yang, Boau-Cheng Wu, Chuen-Jyi Ko, “A Ray-Tracing Method for Modeling Indoor Wave Propagation and Penetration,” IEEE 1998.

110. Sakda Naruniranat, Yi Huang, David Parsons, “A three-dimensional Images Ray Tracing(3D-IRT) Method for Indoor Wireless Channel Characterisation,” IEEE, 1999.

111. Perter Kreuzgruber, Peter Unterberger, Rainer Gahleitner, “A Ray Splitting Model for Indoor Radio Propagation Associated with Complex Geometries,” IEEE 1993.

112. D.M.J. Devasirvatham, “Multipath Time Delay Spread in the Digital Portable Radio Environment”, *IEEE Comm. Mag*, Vol. 25, 1987.

113. A. Kavatjikidis, “Measurement Analysis and Capacity Performance of UWB Radio Propagation Channels”, Thesis for the Degree of dPhil at Oxford University, Sep 2008 Page(s): 88-92. Chapter 4.

114. H. Bertoni, et. al., “UHF propagation prediction for wireless personal communications”,Proc. IEEE, 1994, 82, (9), pp. 1333–1359.

115. I.Glover and P.Grant, “Digital Communications”, Prentice Hall, 1998, pp. 446-458.

116. High Rate Ultra Wideband PHY and MAC Standard ECMA-368 [Online]. Available: http://www.ecma-international.org/publications/files/ECMA-ST/ECMA-368.pdf

117. Garcia Zuazola, I.J.; Elmirghani, J.M.H.; Batchelor, J.C.;"High-speed ultra-wide band in-car wireless channel measurements," *Communications IET*, vol.3, no.7, pp.1115-1123, July 2009.

118. Blackstock, David T., “Fundamentals of Physical Acoustics”, *Wiley–IEEE,* ISBN 0471319791, chap. 6, pp. 236-250, 2000.

119. Carl. R. Nave, *Bragg's Law*, Hyper Physics, Georgia State. University. July 2008.

120. I. Marinovic, I. Zanchi, et al., “Estimation of channel parameters for Saleh-Valenzuela model simulation”, Faculty of Electrical Engineering, Mech. Eng. and Naval Arch (FESB).

121. Wasim Q.Malik, Christopher Stevens, and David J. Edwards, “Experimental Evaluation of Rake receiver Performance in a LOS UWB Channel”, *UWBST Conf.* 2004.

122. C. L. Holloway, D. A. Hill, J. M. Ladbury, P. F.Wilson, G. Koepke, and J. Coder, “On the use of reverberation chambers to simulate a Ricean radio environment for the testing of wireless devices,” *IEEE Trans. Antennas Propag.*, vol. 54, no. 11, pp. 3167–3177, 2006.

123. U.C.A.N., “Report on UWB basic transmission loss,” Tech. Rep. IST-2011-32710, Mar.2003.

124. Sipal, V.; Allen, B.; Edwards, D.J.; "Exploration of Nakagami fading in UWB Wireless Channels", *Electronic Letters,* vol.47, No 8, April 2011.

125. T. Kaiser, F. Zheng, and E. Dimitrov, “An overview of ultra-wide-band systems with MIMO,” *Proceedings of the IEEE*, vol. 97, no. 2, pp. 285–312, 2009.

126. A. Molisch, “MIMO-UWB Propagation Channels”, *EUCAP 2010, Barcelona,* April 2010, pp.1-6.

127. M.C. Mtumbuka, “MIMO Techniques for Future High Speed Wireless Communications Systems”, Thesis for the Degree of dPhil at Oxford University, T.T 2005, Chapter 4-5.

128. Wallace, J.,M.Jensen, “The Capacity of MIMO Wireless systems: A Rigorous Network Theory Analysis”, *IEEE Trans. Wireless Communications,* vol.3, pp. 1317-1325, 2002.

129. Balanis C. A., “Antenna theory”, 3rd Edition, A John Wiley and Sons, Inc., Publication. Chapter 9, pp.521-522.

130. Q. Li and L. A. Rusch, "Hybrid RAKE / multiuser receivers for UWB," in *Proceedings of the IEEE Radio and Wireless Conference*. Boston, MA, USA, August 2003.

131. B. Mielczarek, M.-0. Wessman, and A. Svensson, "Performance of coherent UWB Rake receivers with channel estimators," in *Proceedings of the IEEE Vehicular Technology Conference*. Orlando, FL, USA, October 2003.

132. A. G. Klein, D. R. Brawn, D. L. Gaeckel, and C. R. Johnson, "RAKE reception for UWB communication systems with intersymbol interference." *in Proceedings on the Processing on Wireless Communications Conference*. Rome, Italy, July 2003.